



UNIVERSITÀ DEGLI STUDI DI MILANO
FACOLTÀ DI SCIENZE MM. FF. NN.
DIPARTIMENTO DI CHIMICA FISICA ED ELETTROCHIMICA
CORSO DI DOTTORATO DI RICERCA IN SCIENZE CHIMICHE
CICLO XXIII
CHIM02

**“NANOSTRUCTURED TiO_2 AS A
MULTIFUNCTIONAL MATERIAL: FROM
PHOTOCATALYSIS TO BIOMEDICAL
APPLICATIONS”**

PH.D. STUDENT
ALBERTO NALDONI

TUTOR
PROF. CLAUDIA L. BIANCHI
Co-TUTOR
PROF. SILVIA ARDIZZONE

ACADEMIC YEAR 2009-2010

"...arts and sciences are branches of the same tree. All these aspirations are directed toward ennobling man's life, lifting it from the sphere of mere physical existence and leading the individual towards freedom."

Albert Einstein

ABSTRACT

The results presented in this Ph.D. thesis are focused on the use of nanostructured titanium dioxide for environmental remediation and for biomedical applications.

In the first part, the importance of the choice of a suitable and reliable synthetic route for obtaining nanomaterials with tailored properties for a specific application is highlighted. Several research projects on the design and sol-gel synthesis of TiO₂ nanoparticles have been carried out.

The experimental evidences suggest that sol-gel synthesis allow tailoring the morphological and superficial properties of the samples. The latter are strictly correlated to the photocatalytic activity of TiO₂ home-made samples for the degradation of pollutants in air (e.g., toluene and nitrogen oxides). Moreover, exploiting the capability of sol-gel synthesis, the light absorption of the photocatalyst is extended from UV to the visible spectrum *via* a nitrogen doping.

The morphology, bulk superficial properties, and photocatalytic activity of TiO₂ nanoparticle are also influenced by the direct physical/chemical effects of ultrasounds. Interestingly, using ultrasonic spray pyrolysis (USP), we can exploit indirect effects of ultrasounds to synthesized nanostructured materials. Here, it is presented the design, synthesis, characterization, and application in photocatalysis of porous TiO₂ microsphere with tunable physico-chemical properties obtained through USP.

The second part of this Ph.D. thesis is focused on the study of the interaction among inorganic surfaces and biomolecules or, in general, biological systems.

In a first work, we have synthesized sol-gel TiO₂ nanoparticles with different morphology and use them for preliminary study of acetyl salicylic acid delivery.

Moreover, the possibility to use TiO₂ as a material for scaffold for bone regeneration is reported. This study has led to unravel a new bio-inspired crystallization pathway toward the bioactivity of synthetic bone substitutes. Other examples in the biomedical field are reported in Appendix A.

ACKNOWLEDGEMENTS

A would like to acknowledge my Supervisor, Prof. Claudia L. Bianchi, for providing direction, enthusiasm and encouragement throughout this project. Also to Prof. Silvia Ardizzone and Dr. Giuseppe Cappelletti that have educated me in the design and synthesis of titanium dioxide nanoparticles.

I also have to thank all the scientists I had collaborate with such as Prof David Bremner, Dr. Vladimiro Dal Santo, Dr. Barbara Palazzo, Dr. Ismaela Foltran, Dr. Alessandro Minguzzi, and many others.

A special thank goes to Prof. Ken Suslick who gave me the inspiration to pursue my objectives and without which I would not have gained my current level of understanding of materials science.

Most of all, I would like to thank my parents for always supporting me in my decisions and studies. I dedicate this thesis to them.

I would like to thank all my friends with whom I shared smiles, ideas, or entertainment. Few of them are: Ivano, Giorgio, Simone, Elisa, Alessandra, Luca, Gianluca, Matteo, Luca, Chris, Evan, Agnieszka, Benjamin.

In particular, I would like to thank Michela, for her patience and continuous support.

CONTENTS

ABSTRACT.....	4
ACKNOWLEDGEMENTS	5
1 INTRODUCTION.....	13
1.1 NANOSTRUCTURED TiO ₂ AS A MULTIFUNCTIONAL MATERIALS.....	16
1.2 HETEROGENEOUS PHOTOCATALYTIC DEGRADATION OF ORGANIC POLLUTANTS OVER TiO ₂	18
1.2.1 <i>Basic principles of photocatalysis</i>	19
1.2.2 <i>Mechanism of titania-assisted photocatalytic degradation</i>	20
1.2.3 <i>The photocatalyst design</i>	24
1.3 BIOMEDICAL APPLICATIONS.....	26
1.3.1 <i>An overview on the interactions between nanomaterials and biological environments</i> 26	
1.3.2 <i>Nanotechnology in biomedical application</i>	28
1.4 REFERENCES.....	34
2 SYNTHESIS OF NANOSTRUCTURED TiO₂.....	39
2.1 SOL-GEL TECHNOLOGY.....	41
2.1.1 <i>Introduction</i>	41
2.1.2 <i>The general mechanism</i>	41
2.1.3 <i>Gelation, aging, drying and calcinations steps</i>	42
2.1.4 <i>Advantages and limitations of sol-gel technique</i>	45
2.2 APPLICATION OF ULTRASOUND TO THE SYNTHESIS OF NANOSTRUCTURED MATERIALS.....	46
2.2.1 <i>A brief introduction to ultrasound</i>	46
2.2.2 <i>Ultrasonic Spray Pyrolysis</i>	49
2.3 REFERENCES.....	63
2.4 DEGRADATION OF POLLUTANTS IN AIR BY PHOTOCATALYSIS ASSISTED BY TiO ₂	69
2.4.1 <i>Photocatalytic Degradation of Toluene in the Gas Phase: Relationship between Surface Species and Catalyst Features</i>	69
2.4.2 <i>N-doped TiO₂ from TiCl₃ for photodegradation of air pollutants</i>	81
2.4.3 <i>Photodegradation of Pollutants in Air: Enhanced Properties of Nano-TiO₂ Prepared by Ultrasound</i>	94
2.4.4 <i>Porous Titania microsphere with Tunable Properties</i>	107
2.5 DEGRADATION OF POLLUTANTS IN THE LIQUID PHASE BY ADVANCED OXIDATION PROCESSES.....	121
2.5.1 <i>Mineralisation of Surfactants Using Ultrasound and the Advanced Fenton Process</i>	121

2.6	BIOMEDICAL APPLICATION.....	135
2.6.1	<i>Absorption/Release of Acetylic Salicylic Acid by TiO₂ nanoparticles.....</i>	135
2.6.2	<i>Electrochemically-assisted Deposition on TiO₂ Scaffold for Tissue Engineering: an Apatite Bio-Inspired Crystallization Pathway.....</i>	141
3	CONCLUSION.....	163
	APPENDIX A: COLLOABORATIONS IN SCIENCE OF BIOMATERIALS.....	167
	APPENDIX A1: SURFACE ENAMEL REMINERALIZATION: BIOMIMETIC APATITE NANOCRYSTALS AND FLUORIDE IONS DIFFERENT EFFECTS.....	170
A.1.1	<i>Introduction.....</i>	170
A.1.2	<i>Materials and Methods.....</i>	171
A.1.3	<i>Results.....</i>	174
A.1.4	<i>Discussion.....</i>	183
A.1.5	<i>References.....</i>	184
	APPENDIX A2: ALKALINE PHOSPHATASE GRAFTING ON BIOACTIVE GLASSES AND GLASS CERAMICS.....	188
A.2.1	<i>Introduction.....</i>	188
A.2.2	<i>Materials and methods.....</i>	189
A.2.3	<i>Results.....</i>	195
A.2.4	<i>Discussion.....</i>	201
A.2.5	<i>Conclusions.....</i>	206
A.2.6	<i>References.....</i>	207
	APPENDIX A3: SURFACE ACTIVATION OF A FERRIMAGNETIC GLASS–CERAMIC FOR ANTINEOPLASTIC DRUGS GRAFTING.....	210
A.3.1	<i>Introduction.....</i>	210
A.3.2	<i>Materials and Methods.....</i>	212
A.3.3	<i>Results and Discussion.....</i>	215
A.3.4	<i>Conclusions.....</i>	226
A.3.5	<i>References.....</i>	227
	APPENDIX B: PHYSICO-CHEMICAL CHARACTERIZATIONS.....	231
	APPENDIX B1: X-RAY POWDER DIFFRACTION TECHNIQUE.....	233
B.1.1	<i>Introduction.....</i>	233
B.1.2	<i>Bragg's condition.....</i>	233
B.1.3	<i>Powder diffraction.....</i>	235
B.1.4	<i>Application.....</i>	237
B.1.5	<i>Limitation.....</i>	238
B.1.6	<i>Informations obtained by a diffraction line.....</i>	238

B.1.7	<i>Structure refinement and quantitative phase analysis of powder diffraction patterns</i>	239
APPENDIX B2: SURFACE AREA AND PORE STRUCTURE BY GAS ADSORPTION.....		242
B.2.1	<i>Introduction.....</i>	242
B.2.2	<i>Adsorption theory and methods of extracting information from the adsorption isotherm.....</i>	245
B.2.3	<i>Methods for characterizing mesoporous and macroporous materials.....</i>	248
APPENDIX B3: X-RAY PHOTOELECTRON SPECTROSCOPY.....		252
B.3.1	<i>Introduction.....</i>	252
B.3.2	<i>Physical Basis</i>	252
B.3.3	<i>XPS: the general features.....</i>	254
B.3.4	<i>Spin-Orbit Splitting</i>	256
B.3.5	<i>Chemical Shifts.....</i>	257
APPENDIX B4: SCANNING ELECTRON MICROSCOPY.....		259
B.4.1	<i>Introduction.....</i>	259
B.4.2	<i>How does the SEM work?</i>	259
B.4.3	<i>Sample preparation.....</i>	261
B.4.4	<i>X-Ray microanalysis</i>	262
APPENDIX B5: TRANSMISSION ELECTRON MICROSCOPY.....		270
APPENDIX B6: OTHERS CHARACTERIZATION TECHNIQUES.....		272
APPENDIX B7: REFERENCES.....		273

Chapter 1

Introduction

Nanotechnology is multidisciplinary and interdisciplinary and covers diverse fields including chemistry, physics, materials science, engineering, biology, and medicine (Fig. 1.1). Nanotechnology makes use of the unique chemical and physical properties (enhanced chemical reactivity and catalytic activity, high surface area, surface plasmon resonance properties, superparamagnetism, self-assembly, etc.) of nanoscale (1–100 nm) materials that cannot be achieved in their bulk counterparts. In this regard, nanostructured materials have been extensively studied since they offer an incomparable route to tailor materials properties and functionalities toward a specific application.¹

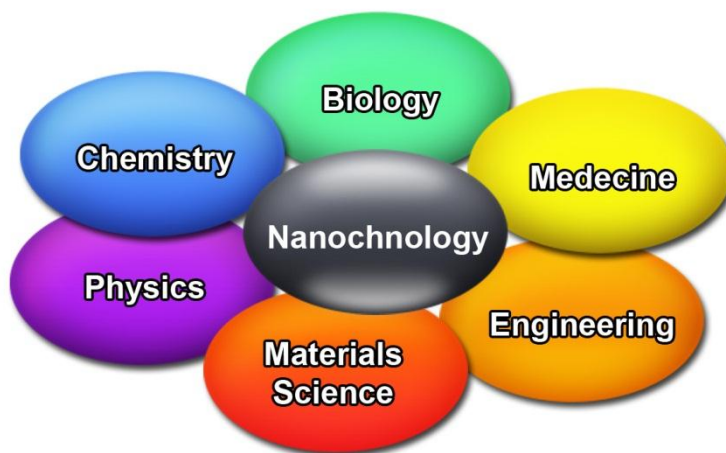


Figure 1.1: *Nanotechnology is a field of study at the intersection between many different basic sciences.*

Nanostructured materials have been prepared by a variety of synthetic methods, including sol-gel synthesis,² gas phase techniques (e.g., molten metal evaporation, flash vacuum thermal and laser pyrolysis decomposition of volatile organometallics), liquid phase methods (e.g., reduction of metal halides with various strong reductants, colloidal techniques with controlled nucleation), and mixed phase approaches (e.g., synthesis of conventional heterogeneous catalysts on oxide supports, metal atom vapor deposition into cryogenic liquids, explosive shock synthesis).³ One could claim that selecting an appropriate synthetic route ultimately determines the success or failure of nanostructured materials synthesis, because physical properties and applications of nanostructured materials are heavily dependent upon how they are prepared. The importance of choosing a proper synthetic route in designing nanostructured materials has been a driving force for the development of new methodologies for several decades. Indeed, this has led scientists' interest to the development of versatile and generalized synthetic methods readily adaptable for the preparation of a variety of nanostructured

materials. Among a variety of approaches, the sol-gel synthesis and the utilization of ultrasound for materials synthesis have been extensively examined over many years, and are now positioned as some of the most powerful and versatile tools in nanostructured materials synthesis. For all these reasons, during my Ph.D. I have study the synthesis and characterization of nanostructured titanium dioxide (TiO_2) for photocatalysis and biomedical applications obtained through these two synthetic methods.

1.1 Nanostructured TiO_2 as a multifunctional materials

If we go beyond the concept of synthesizing a nanostructured material with a specific functionality, we can think to assemble various nanostructured materials with different properties in order to obtain multifunctional nanoplatforms. These nano-objects could offer synergetic mechanisms to accomplish several functions simultaneously. There are many examples of such devices in nanobiotechnology where usually a multifunctional material is designed to perform at the same time multimodal imaging, diagnosis and therapy.⁴

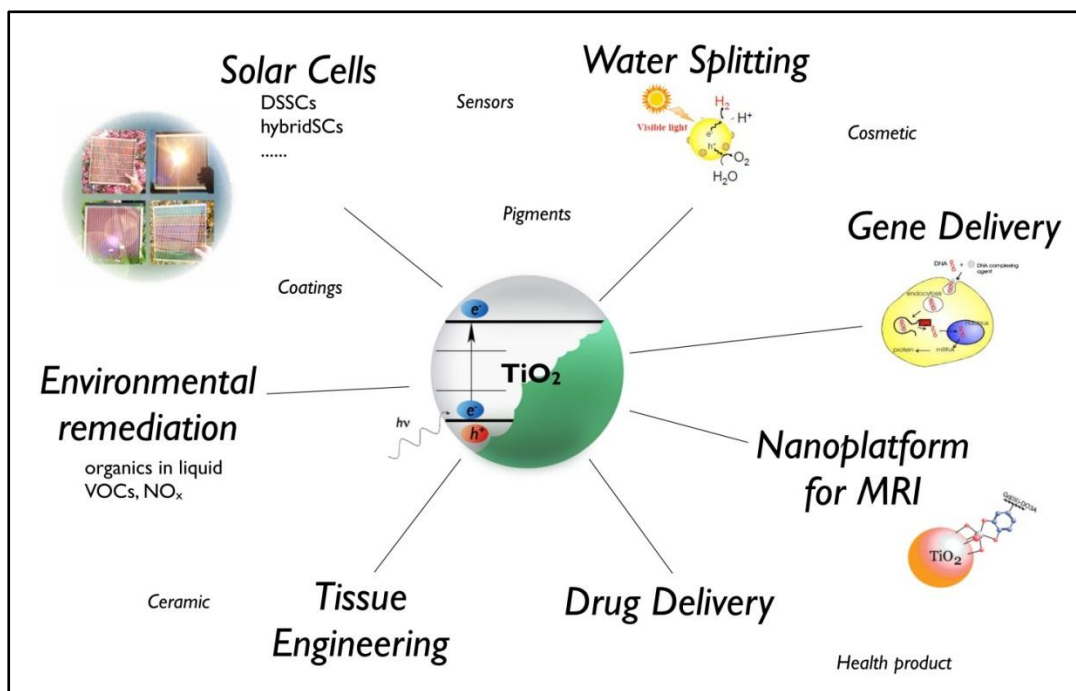


Figure 1.2: schematic representation of the many fields of application of nanostructured TiO_2 .

Similarly, nanomaterials having several functions that accomplish the requirements for being used in a wide range of applications can be considered multifunctional materials. Among these, titanium dioxide (TiO_2) is of primary interest for its

unusual electronic properties, cheapness, non-toxicity, and structural stability. It is already present in many different commercial products such as paints, cosmetics, ceramics, coatings, etc. Moreover, its potential applications range from photocatalysis in environmental remediation,⁵ water splitting,⁶⁻⁹ solar cells (e.g. dye-sensitized solar cells,¹⁰⁻¹¹ hybrid solar cells,¹² quantum dots solar cells¹³), gas sensors, to biomedical applications in tissue engineering,¹⁴ magnetic resonance imaging,¹⁵ and drug/gene therapy (Fig. 1.2).¹⁶⁻¹⁷

1.2 Heterogeneous photocatalytic degradation of organic pollutants over TiO_2

As recalcitrant organic pollutants continue to increase in air and wastewater streams, environmental laws and regulations become more stringent.¹⁸⁻¹⁹ As a response, the development of newer eco-friendly methods of destroying these pollutants became an imperative task. Ultimately, research activities centered on advanced oxidation processes (AOPs) for the destruction of synthetic organic species resistant to conventional methods. AOPs rely on in situ generation of highly reactive radical species, mainly $\text{HO}\cdot$ by using solar, chemical or other forms of energy.²⁰⁻²² The most attractive feature of AOPs is that this highly potent and strongly oxidizing radical allows the destruction of a wide range of organic chemical substrate with no selectivity. Among AOPs, heterogeneous photocatalysis has proved to be of real interest as efficient tool for degrading both aquatic and atmospheric organic contaminants.²³ Heterogeneous photocatalysis involve the acceleration of photoreaction in presence of semiconductor photocatalyst. One of the major applications of heterogeneous catalysis is photocatalytic oxidation to effect partial or total mineralization of gas phase or liquid phase contaminants to benign substances. Even though degradation begins with a partial degradation, the term ‘photocatalytic degradation’ usually refers to complete photocatalytic oxidation or photomineralization, essentially to CO_2 , H_2O , small inorganic acids and halide ions.²⁴

Titania (TiO_2) photocatalysis also referred to as the “Honda–Fujishima effect” was first unfolded by the pioneering research of Fujishima and Honda.⁶ They revealed the possibility of water splitting by photoelectrochemical cell having an inert cathode and rutile titania anode. Consequently, the application of titania photocatalysis extended to environmental frontiers. Frank and Bard²⁵ for the first time reported the application of TiO_2 in photocatalytic oxidation of CN^- and SO_3^{2-} in aqueous medium under sunlight. Subsequent reports of photocatalytic reduction of CO_2 by Inoue et al.²⁶ attracted more interest to titania photocatalysis. As part of the dawn, the photo-induced decarboxylation route to butane reported by Izumli et al.²⁷ and the suggestion of its reaction mechanism based on hydroxyl radical generation opened a new chapter in organic synthesis. The earliest description of photodecomposition of organic compounds and studies of effects of reaction parameters was reported by Kraeutler and Bard.²⁸

1.2.1 Basic principles of photocatalysis

Heterogeneous photocatalysis is a discipline which includes a large variety of reactions: organic synthesis, water splitting, photoreduction, hydrogen transfer, $O_2^{18}-O_2^{16}$ and deuterium–alkane isotopic exchange, metal deposition, disinfection and anti-cancer therapy, water detoxification, gaseous pollutant removal, etc.^{24,29} Among these appearances titania-assisted heterogeneous photocatalytic oxidation has received much attention for many years as alternative method for purification of both air and water streams. The basic photophysical and photochemical principles underlying photocatalysis are already established and have been reported in many literatures.³⁰ Vinodgopal and Kamat³¹ reported that the dependence of the rate of 1,3-diphenylisobenzofuran photodegradation on the surface coverage. In other words, only the molecules that are in direct contact with the catalyst surface undergo photocatalytic degradation.

Photocatalytic reaction (Fig. 1.3) is initiated when a photoexcited electron is promoted from the filled valence band of semiconductor photocatalyst to the empty conduction band as the absorbed photon energy, $h\nu$, equals or exceeds the band gap of the semiconductor photocatalyst leaving behind a hole in the valence band. Thus in concert, electron and hole pair (e^-h^+) is generated.

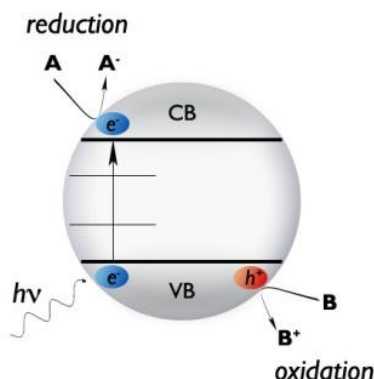
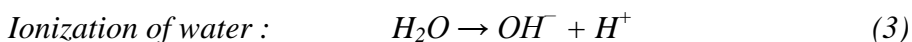
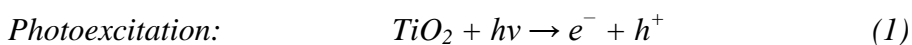
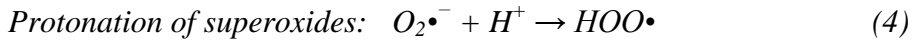


Figure 1.3: schematic representation of processes involved in photocatalysis assisted by TiO_2 .

The following chain reactions have been widely postulated.





The hydroperoxyl radical formed in (4) also has scavenging property as O_2 thus doubly prolonging the lifetime of photogenerated hole:



Both the oxidation and reduction can take place at the surface of the photoexcited semiconductor photocatalyst (Fig. 1). Recombination between electron and hole occurs unless oxygen is available to scavenge the electrons to form superoxides ($\text{O}_2^{\bullet-}$) its protonated form the hydroperoxyl radical (HO_2^{\bullet}) and subsequently H_2O_2 .

1.2.2 Mechanism of titania-assisted photocatalytic degradation

Titania has been widely used as a photocatalyst for generating charge carriers thereby inducing reductive and oxidative processes, respectively. Many elementary mechanistic processes have been described in the photocatalytic degradation of organic compounds over TiO_2 surface. The characteristic time for each elementary reaction has been reported in previous literature (Table 1.1).^{5,32}

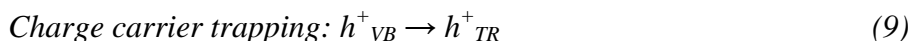
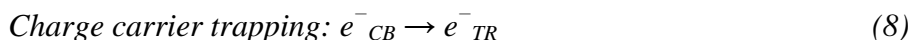
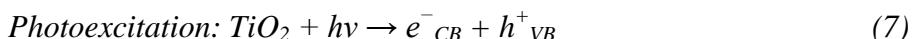
Table 1.1: Primary processes and time domains in titania-catalyzed mineralization of organic pollutant.

Primary process	Characteristic time
Charge carrier generation $\text{TiO}_2 + h\nu \rightarrow e^- + h^+$	fs (very fast)
Charge carrier trapping $h^+ + >\text{Ti}^{\text{IV}}\text{OH} \rightarrow \{>\text{Ti}^{\text{IV}}\text{OH}^{\bullet+}\}$ $e^- + >\text{Ti}^{\text{IV}}\text{OH} \rightleftharpoons >\text{Ti}^{\text{III}}\text{OH}\}$	10 ns (fast) 100 ps (shallow trap; dynamic equilibrium)
$e^- + >\text{Ti}^{\text{IV}} \rightarrow \text{Ti}^{\text{III}}$	10 ns (deep trap)
Charge carrier recombination $e^- + \{>\text{Ti}^{\text{IV}}\text{OH}^{\bullet+}\} \rightarrow >\text{Ti}^{\text{IV}}\text{OH}$ $h^+ + >\text{Ti}^{\text{III}}\text{OH} \rightarrow \text{Ti}^{\text{IV}}\text{OH}$	100 ns (slow) 10 ns (fast)
Interfacial charge transfer $\{>\text{Ti}^{\text{IV}}\text{OH}^{\bullet+}\} + \text{organic molecule} \rightarrow >\text{Ti}^{\text{IV}}\text{OH} + \text{oxidized molecule}$ $\{>\text{Ti}^{\text{III}}\text{OH}\} + \text{O}_2 \rightarrow >\text{Ti}^{\text{IV}}\text{OH} + \text{O}_2^{\bullet-}$	100 ns (slow) ms (very slow)

The $\{>\text{Ti}^{\text{IV}}\text{OH}^{\bullet+}\}$ and $\{>\text{Ti}^{\text{III}}\text{OH}\}$ represent the surface-trapped valence band electron and surface-trapped conduction band electrons, respectively. The surface-bound OH^{\bullet} radical represented by $\{>\text{Ti}^{\text{IV}}\text{OH}^{\bullet+}\}$ is chemically equivalent to the

surface-trapped hole allowing the use of the former and latter terms interchangeably. According to Lawless and Serpone³³ the trapped hole and a surface-bound OH• radical are indistinguishable species. A good correlation between charge carrier dynamics, their surface densities and the efficiency of the photocatalytic degradation over TiO₂ exit. In the last two decades, aqueous suspensions of TiO₂ have been probed by picosecond and more recently femtosecond absorption spectroscopies.³⁴⁻³⁵ Traditionally, an electron scavenger has been employed in such study. A femtosecond spectroscopic study of TiO₂/SCN⁻ aqueous system by Colombo and Bowman³⁴ indicated dramatic increase in the population of trapped charge carriers within the first few picoseconds.

The results also confirmed that for species adsorbed to TiO₂, the hole-transfer reaction can successfully compete with the picosecond electron-hole recombination process. The following interfacial photochemical reactions were described:



Electron-hole recombination:



Bahnemann et al.³⁶ provided evidence for the trapped charge carriers using flash radiolysis. Primarily, the fission of bonds in organic molecules is due to the interaction of the trapped e^-_{TR} (Ti³⁺) and h^+_{TR} (presumably •OH) pairs near TiO₂ particle. In agreement with the foregoing, Furube et al.³⁷ observed that trapped carriers mainly exist near the particle surface and do not undergo rapid (~1ps) recombination immediately after photoexcitation. The important consequences of surface trapped holes (h^+_{TR}) and electrons (e^-_{TR}) to the photooxidation of organic compounds have been highlighted by Serpone et al.³⁸

In most applications, photocatalytic degradation reactions are carried out in presence of water, air, the target contaminant and the photocatalyst. Photogenerated holes have great potential to oxidize organic species directly or indirectly via the combination with OH• predominant in aqueous solution:³⁹





The primary photoreactions (1)–(10) indicate the critical role of charge carriers (electron–hole pair) in photo-oxidative degradation. Essentially, hydroxyl radicals ($OH\bullet$), holes (h^+), superoxide ions (O_2^-) and hydroperoxyl radicals ($\bullet OOH$) are highly reactive intermediates that will act concomitantly to oxidize large variety of organic pollutants including volatile organic compounds (VOCs), nitrogen oxides and bioaerosols.

The reaction mechanism for the photo-oxidative degradation of many organic pollutants over titania particle has been extensively reviewed. The number of intermediates in the reaction and ease of decomposition depends upon the nature organic contaminant studied. The photocatalytic degradation of formaldehyde and phenol are interesting mechanistic examples on the role of hole, superoxide and hydroxyl radicals in titania-assisted photomineralization of aliphatic and aromatic organic templates. The mechanisms are illustrated in Figs. 1.4 and 1.5, respectively. In the degradation of phenol, several intermediates have been reported (Fig. 1.5). The $OH\bullet$ radical attacks the phenyl ring of the phenol (a), yielding catechol (b), resorcinol (c), benzene-1,2,3-triol (d) and hydroquinone (e), then the phenyl rings in these compounds break up to give maleic acid (f), then short-chain organic acids such as, 3-hydroxy propyl carboxylic acid (g), 2-hydroxy propanal (i), 2-hydroxy-ethanoic acid glycol acid (j), finally CO_2 and H_2O . Even though $H\bullet$ produced during the attack of bonds by $OH\bullet$ participates in the process, it is scavenged by oxygen to form $HO_2\bullet$ radicals, which finally convert to $OH\bullet$ radicals.

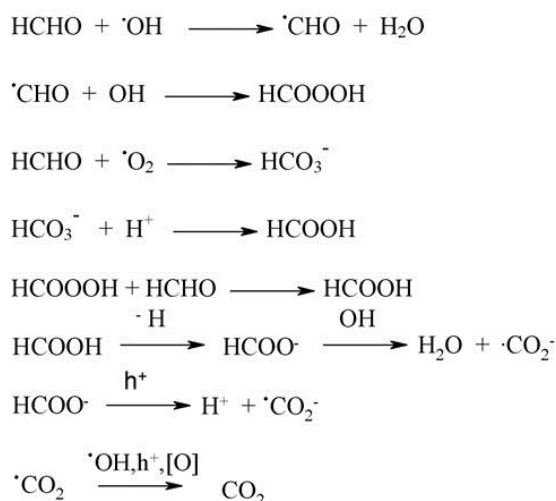


Figure 1.4: Photocatalytic oxidation of formaldehyde over TiO_2 .

The kinetics of photocatalytic degradation of organic compounds in the liquid phase usually follows the Langmuir–Hinshelwood scheme.³⁰

$$r = -\frac{dC}{dt} = \frac{kKC}{1+KC} \quad (15)$$

where r represents the initial rate of photooxidation, C the concentration of the reactant, t the irradiation time, k the rate constant of the reaction and K is the adsorption coefficient of the reactant. At mM concentrations $C \ll I$, the equation can be simplified to the apparent rate order equation:

$$C_t = C_0 e^{-K_{app}t} \quad (16)$$

where K_{app} is the apparent first order rate constant given by the slope of the graph of $\ln C_0/C$ versus t and C_0 is the initial concentration of the organic pollutant. Consequently under the same condition, the initial degradation rate could be written in a form conforming to the apparent first order rate law:

$$r_0 = K_{app}C \quad (17)$$

A quasi-exhaustive consideration of photodestruction studies of organic contaminants proved that the first order rate equation above holds true.⁴⁰⁻⁴³ At any rate, Langmuir–Hinshelwood model serves as a basis for the photodegradation of organic compounds even if it could not directly give adequate fitting.⁴⁴ Nevertheless, for suspended titania-mediated photocatalytic degradation of organic compounds pseudo-zeroth order is reported.⁴⁵

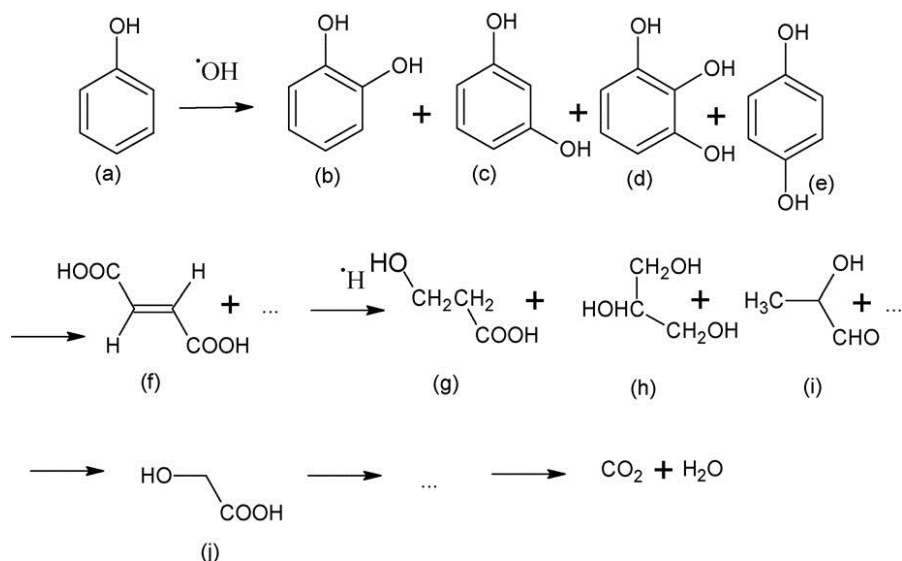


Figure 1.5: degradation of phenol in wastewater over TiO_2 .

1.2.3 The photocatalyst design

Many different processes are involved in the photocatalytic degradation of a pollutant over TiO_2 . However, it is possible consider the entire process of photocatalysis composed by three main processes (Fig. 1.6). The first one (i) is referred to the possibility to engineer the band-gap of the photocatalyst. The band structure is just a thermodynamic requirement but not a sufficient condition. The band gap of a visible-light-driven photocatalyst should be narrower than 3.0 eV ($\lambda=415$ nm). Therefore, suitable band engineering is necessary for the design of photocatalysts with visible light response. The second step (ii) in Fig. 1.6 consists of charge separation and migration of photogenerated carriers. Crystal structure, crystallinity and particle size strongly affect the step. The higher the crystalline quality is, the smaller the amount of defects is. The defects operate as trapping and recombination centers between photogenerated electrons and holes, resulting in a decrease in the photocatalytic activity. If the particle size becomes small, the distance that photogenerated electrons and holes have to migrate to reaction sites on the surface becomes short and this results in a decrease in the recombination probability. The final step (iii) in Fig. 1.6 involves the surface chemical reactions.

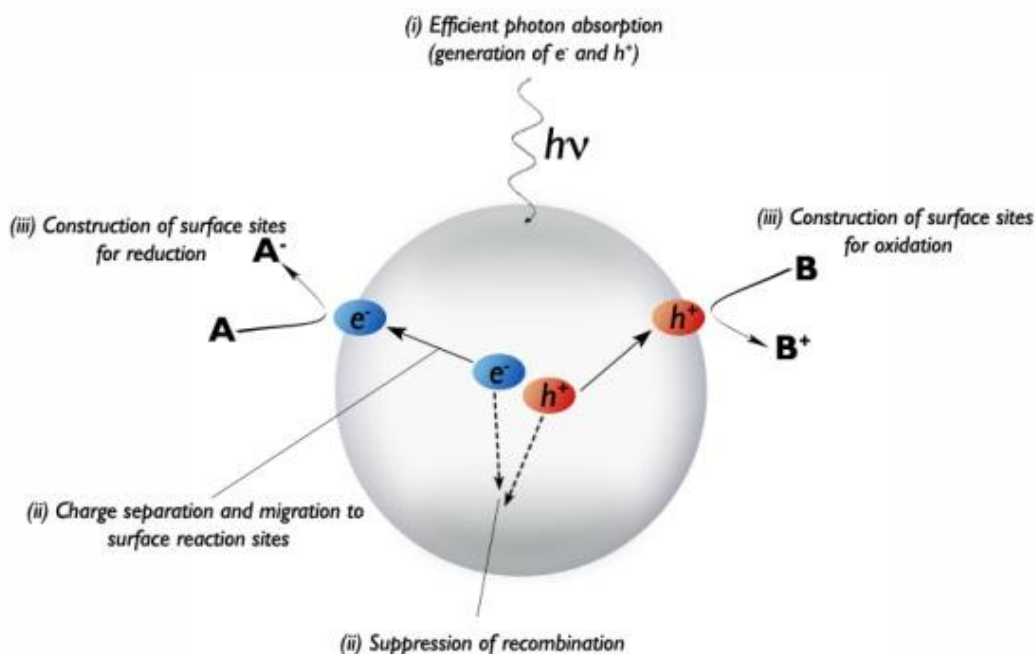


Figure 1.6: main processes involved in photocatalysis assisted by TiO_2 .

The important points for this step are surface character (active sites) and quantity (surface area). Even if the photogenerated electrons and holes possess

thermodynamically sufficient potentials for water splitting, they will have to recombine with each other if the active sites for redox reactions do not exist on the surface. The final goal in the study of photocatalytic processes should be obtaining as much information as possible on the relationship between the structure of the photocatalyst and the photocatalytic activity. In this way, we could design an efficient photocatalyst for a specific application in environmental remediation (also solar cells, water splitting, etc.). It is possible to optimize a photocatalyst working over the morphological and structural properties that influence the main processes involved in photocatalysis. For these reasons, the choice of the synthetic route to be employed in the synthesis of nanostructured TiO_2 is crucial.

Among the wide variety of synthetic methods reported in literature, during my Ph.D. I have focused my interest in the use of sol-gel synthesis and ultrasound (both high intensity and low intensity, e.g. ultrasonic spray pyrolysis) since they offer a great flexibility in the initial reaction conditions and .

1.3 Biomedical applications

1.3.1 *An overview on the interactions between nanomaterials and biological environments*

At the interface between nanomaterials and biological systems, the organic and synthetic worlds merge into a new science concerned with the safe use of nanotechnology and nanomaterial design for biological applications.

Table 1.2: *Main biophysicochemical influences on the interface between nanomaterials and biological systems.*

Nanomaterials
Size, shape and surface area
Surface charge, energy, roughness and porosity
Valence and conductance states
Functional groups
Ligands
Crystallinity and defects
Hydrophobicity and hydrophilicity
Suspending media
Water molecules
Acids and bases
Salts and multivalent ions
Natural organic matter (humics, proteins, lipids)
Surfactants
Polymers
Polyelectrolytes
Solid–liquid interface
Surface hydration and dehydration
Surface reconstruction and release of free surface energy
Ion adsorption and charge neutralization
Electrical double-layer formation, zeta potential, isoelectric point
Sorption of steric molecules and toxins
Electrostatic, steric and electrosteric interactions
Aggregation, dispersion and dissolution
Hydrophilic and hydrophobic interactions
Nano–bio interface
Membrane interactions: specific and nonspecific forces
Receptor–ligand binding interactions
Membrane wrapping: resistive and promotive forces
Biomolecule interactions (lipids, proteins, DNA) leading to structural and functional effects
Free energy transfer to biomolecules
Conformational change in biomolecules
Oxidant injury to biomolecules
Mitochondrial and lysosomal damage, decrease in ATP

The ‘nano-bio’ interface comprises the dynamic physicochemical interactions, kinetics and thermodynamic exchanges between nanomaterial surfaces and the

surfaces of biological components (e.g., proteins, membranes, phospholipids, endocytic vesicles, organelles, DNA and biological fluids).⁴⁶

The nano–bio interface comprises three dynamically interacting components: (i) the nanomaterial surface, the characteristics of which are determined by its physicochemical composition; (ii) the solid–liquid interface and the changes that occur when the material interacts with components in the surrounding medium; (iii) the solid–liquid interface’s contact zone with biological substrates (Table 1.2).

In a given medium, the most important nanomaterials characteristics that determine the surface properties are the material’s chemical composition, surface functionalization, shape and angle of curvature, porosity and surface crystallinity, heterogeneity, roughness, and hydrophobicity or hydrophilicity.^{47–49} Other quantifiable properties, such as effective surface charge (zeta potential), particle aggregation, state of dispersion, stability/biodegradability, dissolution characteristics, hydration and valence of the surface layer, are determined by the characteristics of the suspending media,⁴⁷ including the ionic strength, pH, temperature and the presence of large organic molecules (for example proteins) or detergents.⁵⁰

The particle characteristics contribute actively to the interactions with the medium through: (i) promoting the adsorption of ions, proteins, natural organic materials and detergents; (ii) double-layer formation; (iii) dissolution; or (iv) minimizing free surface energy by surface restructuring.^{51–52}

Many of these newly acquired particle properties or transformed states determine the forces that operate at the particle–medium interface with characteristic decay lengths. These forces include long-range forces arising from attractive van der Waals (VDW) and (generally) repulsive electrostatic double-layer interactions, plus short-range forces arising from charge, steric, depletion and solvent interactions (Table 1.3).^{52–53} Media interactions (e.g., protein interactions) could also induce large-scale changes, such as nanoparticle dissolution, ion leaching, phase transformation and agglomeration. Characterizing the solid–liquid interface is a key challenge in understanding the nano–bio interface. Although we often assume steady-state behaviour when assessing the bulk properties of suspensions (e.g., net charge, isoelectric point or average aggregate size), this approach must be adjusted when considering the nano–bio interface. The already metastable solid–liquid interface is subjected to an inhomogeneous and dynamic or transient environment that contributes to the formation of the nano–bio interface. Such interfacial inhomogeneity results from the distribution and distinct spatial localization of proteins, lipids and glycosylated structures on the surface membrane. Moreover, the interface is not at steady state. It undergoes continuous changes as a result of

cellular housekeeping and environmental influences; for example, secreted cell products may further change a suspending medium's properties,⁵⁴ and the nanomaterial may bind to these biomolecules in suspension or on the cell membrane. Likewise, the interacting biological components might be influenced by the nature of the particle, for example through binding to surface ligands, contact with hydrophobic or charged regions, changes in free surface energy inducing conformational changes or oxidant injury caused by reactive oxygen species (ROS).⁴⁷

The study of the interactions at the nano-bio interface is one the major issue in the field of biomedical application of nanotechnology. Only by a deep understanding of the forces that play at the nanoscale level between synthetic materials and biological environment we will be able to exploit the enormous potential behind the use of nanomaterials in imaging, therapy, diagnosis,^{55,56} and tissue engineering.⁵⁷

Table 1.3: Main force governing the interactions between nanomaterials and biological systems.

Force	Origin and nature	Range (nm)	Possible impact on the interface
Hydrodynamic interactions	Convective drag, shear, lift and Brownian diffusion are often hindered or enhanced at nanoscale separations between interacting interfaces	10 ² to 10 ⁶	Increase the frequency of collisions between nanoparticles and other surfaces responsible for transport
Electrodynamic interactions	VDW interactions arising from each of the interacting materials and the intervening media	1 to 100	Universally attractive in aqueous media; substantially smaller for biological media and cells owing to high water content
Electrostatic interactions	Charged interfaces attract counter-ions and repel co-ions through Coulombic forces, giving rise to the formation of an electrostatic double layer	1 to 100	Overlapping double layers are generally repulsive as most materials acquire negative charge in aqueous media, but can be attractive for oppositely charged materials
Solvent interactions	Lyophilic materials interact favourably with solvent molecules Lyophobic materials interact unfavourably with solvent molecules	1 to 10	Lyophilic materials are thermodynamically stable in the solvent and do not aggregate Lyophobic materials are spontaneously expelled from the bulk of the solvent and forced to aggregate or accumulate at an interface
Steric interactions	Polymeric species adsorbed to inorganic particles or biopolymers expressed at the surfaces of cells give rise to spring-like repulsive interactions with other interfaces	1 to 100 ^a	Generally increase stability of individual particles but can interfere in cellular uptake, especially when surface polymers are highly water-soluble
Polymer bridging interactions	Polymeric species adsorbed to inorganic particles or biopolymers expressed at the surfaces of cells containing charged functional groups can be attracted by oppositely charged moieties on a substrate surface	1 to 100	Generally promote aggregation or deposition, particularly when charge functionality is carboxylic acid and dispersed in aqueous media containing calcium ions

^aDepending on the length of adsorbed or expressed polymeric species

1.3.2 Nanotechnology in biomedical application

Nanotechnology is poised to make potentially revolutionary innovations in areas of biomedical science such as diagnostics, drug therapy, imaging, and tissue engineering (Table 1.4).

Table 1.4: Nanoscale application in medicine.⁵⁸

<i>Drug delivery</i>	Nanoscale delivery vehicles can (1) enhance the therapeutic efficacy and minimize adversities associated with available drugs; (2) enable new classes of therapeutics; and (3) encourage the re-investigation of pharmaceutically suboptimal but biologically active new molecular entities that were previously considered undevelopable.
<i>In vitro diagnostics</i>	Nanotechnology-based sensors (e.g., nanowires, nanotubes, nanoparticles, cantilevers, and micro/nanoarrays) can enable fast and high throughput detection of disease biomarkers with higher sensitivity and lower sample consumption. Nanotechnology also offers hope for the early detection of viruses, bacteria, and circulating tumor cells, as well as for single cell analysis.
<i>In vivo imaging</i>	Targeted imaging nanoprobe (e.g., magnetic nanoparticles, quantum dots, and carbon nanotubes) could provide a faster, less invasive, and more accurate way to diagnose diseases (e.g., cancer) at their earliest stages and monitor disease progression. Some other possible opportunities include reporting <i>in vivo</i> efficacy of therapeutics and tracking nanocarrier biodistribution in the body. In addition, imaging nanoprobe could help surgeons to locate tumors and their margins, identify important adjacent structures, and map sentinel lymph nodes.
<i>Therapy techniques</i>	Certain nanomaterials have unique therapeutic properties that differ from conventional drugs, and can, therefore, be directly used to treat diseases. For example, hafnium oxide- and gold-based nanoparticles can greatly enhance X-ray therapy; gold nanoshells/nanorods, carbon nanotubes, magnetic nanoparticles can induce hypothermia to kill cancer cells; and nanocrystalline silver is being used as an antimicrobial agent.
<i>Biomaterials</i>	Biocompatible nanomaterials that have optimal mechanical properties can be used as medical implants, such as dental restoratives and bone substitutes (also categorized as hard-tissue engineering.). Nanocoatings or nanostructured surfaces can also improve the biocompatibility and adhesion of biomaterials.
<i>Tissue engineering</i>	Nanotechnology can enable the design and fabrication of biocompatible scaffolds at the nanoscale and control the spatiotemporal release of biological factors, resembling native extracellular matrix, to direct cell behaviors, and eventually lead to the creation of implantable tissues.

In the future, nanotechnology using different biomarkers will be able to diagnose patients in much earlier stages of disease. Microchip-based diagnostic tests using biomarkers conjugated to nanoparticles or quantum dots can detect abnormalities at molecular levels that potentially can lead to disease progression. Nanotechnology can overcome anatomical and physiological barriers to deliver drugs more effectively to the target sites to reduce nonspecific effects. Many drugs, especially modern therapeutics, cannot be successful unless mechanisms for their effective delivery are developed. Nanotechnology can be a powerful tool to address delivery-related issues such as poor solubility or stability in biological environments. Imaging plays an important role in detection of pathologies such as tumors or vascular pathologies. Magnetic nanoparticles are under extensive investigation to enhance and improve the magnetic resonance imaging (MRI) capability for early detection of diseases.

Scientists have developed the ability to design new systems, smart bioresponsive polymers that respond to changes in the bioenvironment stimulated by disease conditions, and we have a better understanding of their action mechanisms, interactions with cells and tissue, body distribution, and clearance. The progress in the field of nanotechnology is evident from the range of nanotechnologies under various stages of clinical development from diagnostic to drug delivery applications. The field is certainly interdisciplinary by bringing together chemistry,

biology, medicine, physics, and materials science. Collaborative efforts address issues from various angles, and they may develop more effective solutions to exploit the enormous potential of nanotechnology in the health issue.

During my Ph.D. thesis I have worked on the possibility to use titania nanoparticles in drug delivery and on the synthesis and characterization of TiO_2 scaffold for tissue engineering for bone regeneration. The results obtained in this research work are presented in the *section 3.3*. This is just an example of the use of TiO_2 for biomedical application, but other research projects are ongoing such as the study of titania bioconjugates for targeted delivery.

1.3.2.1 Drug Delivery

Since liposomes were first described in the 1960s and proposed as carriers of proteins and drugs for disease treatment,⁵⁹ nanotechnology has made a significant impact on the development of drug delivery systems. A variety of organic/inorganic nanomaterials and devices have been used as delivery vehicles to develop effective therapeutic modalities. So far, there are over two dozen nanotechnology-based therapeutic products approved by Food and Drug Administration (FDA) for clinical use, and more are in clinical trials.⁶⁰⁻⁶² Of these products, the majority is composed of a nontargeted delivery system (e.g., liposomes and polymers) and a drug, and are therefore considered first generation nanotherapeutics.⁶³

Compared to conventional drug delivery, the first generation nanosystems provide a number of advantages. In particular, they can enhance the therapeutic activity by prolonging drug half-life, improving solubility of hydrophobic drugs, reducing potential immunogenicity, and/or releasing drugs in a sustained or stimuli-triggered fashion. Thus, the toxic side effects of drugs can be reduced, as well as the administration frequency. In addition, nanoscale particles can passively accumulate in specific tissues (e.g., tumors) through the enhanced permeability and retention (EPR) effect.⁶⁴ Beyond these clinically efficacious nanosystems, nanotechnology has been utilized to enable new therapies and to develop next generation nanosystems for “smart” drug delivery.

Targeted Delivery. It is widely believed that active targeting, through the modification of nanoparticles with ligands, has the potential to enhance the therapeutic efficacy and reduce the side effects relative to conventional therapeutics.⁶⁵ The ability to actively target specific cells rather than tissues also allows ligand-conjugated nanocarriers to outperform first generation, nontargeted nanosystems. While the necessity of targeted delivery depends on various factors

(e.g., delivery vehicles, drugs, and diseases), a myriad of important benefits have been demonstrated.^{62,65-68} In cancer therapy, the presence of targeting ligands can greatly enhance the retention and cellular uptake of nanoparticles via receptor-mediated endocytosis, even though tumor accumulation is largely determined by the physicochemical properties of nanoparticles.^{65,66} This can then lead to higher intracellular drug concentration and increase therapeutic activity, which is particularly important for bioactive macromolecules (e.g., DNA and siRNA) that require intracellular delivery for bioactivity.⁶⁵ In the case of endothelial targeting for cardiovascular diseases or immunological tissue targeting, nanoparticle localization is guided by ligand-receptor interactions rather than EPR.⁶⁸ Similarly, ligand-mediated targeting is of importance for the transcytosis of nanodrugs across tight epithelial and endothelial barriers (e.g., blood-brain barrier).⁶⁹ Additionally, targeted delivery has been applied, in some instances, to combat multidrug resistance (MDR).⁶² It is also envisioned that long-circulating targeted nanoparticles may be able to locate and fight migrating cancer cells.

Despite three targeted nanoparticle systems now in phase I/II clinical trials,⁶² the clinical translation of targeted delivery is not as smooth as we expect. One possible barrier stems from the complexity behind manufacturing viable targeted nanoparticles. Targeted nanoparticle fabrication usually requires multiple steps, including biomaterial assembly, ligand coupling/insertion, and purification, which could cause batch-to-batch variation and quality concerns. The recent development of single-step synthesis of targeted nanoparticles by self-assembling pre-functionalized biomaterials provides a simple and scalable manufacturing strategy.^{69,70} Another important consideration is targeting ligands. Among others, some variables that must be considered include ligand biocompatibility, cell specificity, binding affinity, mass production, and purity.⁷¹ For example, to achieve maximal specificity, the ideal ligand would be able to recognize the most overexpressed receptors on target cells relative to healthy ones. Other factors that could also affect cell targeting include ligand surface density and arrangement, as well as spacer type and length dividing ligand molecules and nanoparticles.⁷² Nevertheless, with advances in ligand engineering and screening, and nanoparticle optimization, targeted delivery will become a mainstay in the next generation of drug therapy.

Co-delivery. Combination therapy has shown several potential advantages (e.g., synergistic effects and reversal of drug resistance) and may prove more effective than single drug therapy.⁷³ However, due to the distinct pharmacokinetic profiles of individual drugs, the synergistic drug ratio optimized in vitro will undoubtedly change after the conventional administration of drug “cocktails”, an outcome that

could in turn lead to insufficient therapeutic results *in vivo*. To this end, lipid- and/or polymer-based nanoscale systems, previously developed for single drug delivery, have been applied to facilitate co-delivery. For some drug combinations, we can successfully tune the relative dosage of various drugs in single particle levels, and simultaneously deliver them to target sites with a maintained drug ratio.⁷⁴ For other combinations, we need to develop novel delivery vehicles with desired functionalities that enable co-encapsulation of hydrophobic and hydrophilic drugs, active targeting, and/or temporally controlled release.^{75,76} Such features are especially essential for the co-delivery of drugs and nucleic acids, which requires intracellular delivery to elicit bioactivity.^{77,78} For example, in the case of co-delivering chemotherapy and RNAi therapy to treat multidrug resistant cancers, the ideal nanoparticle would be expected to first release siRNA to reduce the expression of MDR transporters, followed by the release of anticancer drugs.

Another exciting advancement in co-delivery is the ability to combine targeted imaging and therapeutic agents within the same particle, allowing us to visualize sites of targeted drug delivery and deliver therapeutics simultaneously (“theranostics”).⁷⁹ This technology is innovative in concept and holds significant promise for making large medical impacts within the next few decades. It could provide us with critical information on intracellular targets, ensure that therapeutic agents are efficiently reaching their target sites, and enable the effective early detection and treatment of diseases. Current research is primarily focused on the design of such multifunctional nanosystems and proof-of-concept tests,⁸⁰⁻⁸³ but more systematic *in vivo* studies are needed.

Future research in this arena will also likely help us trace the absorption, distribution, metabolism, and excretion of nanoparticles *in vivo*. It is important that we understand the pharmacokinetics of a given drug delivery system to improve upon formulations, estimate clinical doses, and guarantee safety.⁸⁴ Currently, radionuclide labeling is the only technique that can be used to provide *in situ* quantitative information; but radio emitters may be too unstable to conjugate with nanomaterials. With the help of recently developed *in vivo* imaging probes like magnetic nanoparticles,⁶³ quantum dots,⁸⁵ gold nanoparticles,⁸⁶ and carbon nanotubes,⁸⁷ more imaging modalities may become available to track the distribution of nanotherapeutics in the body.

1.3.2.2 Tissue Engineering

Tissue engineering is an evolving interdisciplinary field integrating biology, engineering, materials science, and medicine, that focuses on the development of biological substitutes to restore, replace, maintain, or enhance tissue and organ

function.⁸⁸ Over the past few decades, continued progress in this specific field has led to the creation of implantable tissues, some of which are already used in humans (e.g., skin and cartilage) or have entered clinical trials (e.g., bladder and blood vessels).⁸⁹ Nevertheless, most tissue engineering strategies rely on the principle that under appropriate bioreactor conditions, cells seeded or recruited into three dimensional (3D) biocompatible scaffolds are able to reassemble into functional structures resembling native tissues. Early artificial scaffolds were designed to provide cells structural integrity on a macroscopic level, but only achieved moderate success. It is now widely accepted that to recapitulate proper tissue functionality, scaffolds should also establish a tissue specific microenvironment to maintain and regulate cell behavior and function.⁹⁰

Within tissues, cells are surrounded by extracellular matrix (ECM) which is characterized by a natural web of hierarchically organized nanofibers.⁹¹ This integral nanoarchitecture is important because it provides cell support and directs cell behavior via cell-ECM interactions. Furthermore, ECM plays a vital role in storing, releasing, and activating a wide range of biological factors, along with aiding cell-cell and cell-soluble factor interactions.⁹² Thus, the ability to engineer biomaterials that closely emulate the complexity and functionality of ECM is pivotal for successful regeneration of tissues. Recent advances in nanotechnology, however, have enabled the design and fabrication of biomimetic microenvironment at the nanoscale, providing an analog to ECM.⁹⁰

Notably, these technologies have been applied to create nanotopographic surfaces and nanofeatured scaffolds, and to encapsulate and control the spatiotemporal release of drugs (e.g., growth factors). In turn, these nanodevices offer a means to direct cellular behaviors that range from cell adhesion to gene expression.

1.4 References

- [1] A. S. Aricò, P. Bruce, B. Scrosati, J. M. Tarascon, W. Van Schalkwijk. *Nat. Mater.* **2005**, 4, 366-377.
- [2] B. B. Lakshmi, C. J. Patrissi, C. R. Martin. *Chem. Mater.* **1997**, 9, 2544-2550.
- [3] J. H. Bang, K. S. Suslick. *Adv. Mater.* **2010**, 22, 1039–1059.
- [4] J. Gao, H. Gu, B. Xu. *Acc. Chem. Res.* **2009**, 42, 1097-1107.
- [5] U. I. Gayaa, A. H. Abdullaha. *J. Photochem. Photobiol., C* **2008**, 9, 1-12.
- [6] A. Fujishima, K. Honda. *Nature*, **1972**, 238, 37.
- [7] J. Tang, J. R. Durrant, D. R. Klug. *J. Am. Chem. Soc.* **2008**, 130, 13885–13891.
- [8] A. Kudo, Y. Miseki. *Chem. Soc. Rev.* **2009**, 38, 253–278.
- [9] F. E. Osterloh. *Chem. Mater.*, **2008**, 20, 35-54.
- [10] B. O'Regan, M. Graetzel. *Nature* **1991**, 353, 737.
- [11] F. Sauvage, F. Di Fonzo, A. Li Bassi, C. S. Casari, V. Russo, G. Divitini, C. Ducati, C. E. Bottani, P. Comte, M. Graetzel. *Nano Lett.* **2010**, 10, 2562-2567.
- [12] E. Lancelle-Beltran, P. Prené, C. Boscher, P. Belleville, P. Buvat, C. Sanchez. *Adv. Mater.* **2006**, 18, 2579-2582.
- [13] A. Kongkanand, K. Tvrđy, K. Takechi, M. Kuno, P. V. Kamat. *J. Am. Chem. Soc.* **2008**, 130, 4007-4015.
- [14] A. Naldoni, A. Minguzzi, A. Vertova, V. Dal Santo, Laura Borgese, C. L. Bianchi. *J. Mater. Chem.* **2010**, DOI:10.1039/C0JM02446E.
- [15] P. J. Endres, T. Paunesku, S. Vogt, T. J. Meade, G.E. Woloschak. *J. Am. Chem. Soc.* **2007**, 129, 15760-15761.
- [16] T. Paunesku, S. Vogt, J. Maser, N. Stojicevic, K. T. Thurn, C. Osipo, H. Liu, D. Legnini, Z. Wang, C. Lee, G. E. Woloschak. *Nano letters*. **2007**, 7, 596-601.
- [17] T. Paunesku, T. Rajh, J. Maser, S. Vogt, N. Stojicevic, M. Protic, B. Lai, J. Oryhon, M. Thurnauer, G. E. Woloschak. *Nat. Mater.* **2003**, 2, 343-346.
- [18] P.R. Gogate, A.B. Pandit. *Adv. Environ. Res.* **2004**, 8, 501.
- [19] US EPA, National Emission Standards for Hazardous Air Pollutants, 40 CFR, part 63, **2006**.
- [20] T. Kudo, Y. Nakamura, A. Ruike. *Res. Chem. Intermed.* **2003**, 29, 631.
- [21] D. Bahnemann. *Solar Energy* **2004**, 77, 445.

- [22] A. Naldoni, A. Schibuola, C. L. Bianchi and D. H. Bremner. *Water Air Soil & Pollution* **2010**, DOI 10.1007/s11270-010-0493-y.
- [23] C. Guillard, J. Disdier, J.-M. Herrmann, C. Lehaut, T. Chopin, S. Malato, J. Blanco. *Catal. Today* **1999**, *54*, 217.
- [24] O. Carp, C.L. Huisman, A. Reller. *Prog. Solid State Chem.* **2004**, *32*, 33.
- [25] S.N. Frank, A.J. Bard. *J. Phys. Chem.* **1977**, *81*, 1484.
- [26] T. Inoue, A. Fujishima, S. Konishi, K. Honda. *Nature* **1979**, *277*, 637.
- [27] I. Izumi, F.-R. F. Fan, A. J. Bard. *J. Phys. Chem.* **1981**, *85*, 218.
- [28] B. Kraeutler, A. J. Bard. *J. Am. Chem. Soc.* **1978**, *100*, 5958.
- [29] J. M. Herrmann. *Catal. Today* **1999**, *53*, 115.
- [30] A. L. Linsebigler, G. Lu, J. T. Yates. *Chemical Reviews.* **1995**, *95*, 735-758.
- [31] K. Vinodgopal, P.V. Kamat. *J. Phys. Chem.* **1992**, *96*, 5053.
- [32] A. Mills, S. Le Hunte. *J. Photochem. Photobiol. A* **1997**, *108*, 1.
- [33] D. Lawless, N. Serpone. *J. Phys. Chem.* **1991**, *95*, 5166.
- [34] D.P. Colombo Jr., R.M. Bowman. *J. Phys. Chem.* **1996**, *100*, 18445.
- [35] X. Yang, N. Tamai. *Phys. Chem. Chem. Phys.* **2001**, *3*, 3393.
- [36] D. Bahnemann, A. Henglein, J. Lilie, L. Spanhel. *J. Phys. Chem.* **1984**, *88*, 709.
- [37] A. Furube, T. Asahi, H. Masuhara, H. Yamashita, M. Anpo. *J. Phys. Chem. B* **1999**, *103*, 3120.
- [38] N. Serpone, D. Lawless, R. Khairutdinov, E. Pelizzetti. *J. Phys. Chem.* **1995**, *99*, 16655.
- [39] A. Fujishima, T.N. Rao, D.A. Tryk. *J. Photochem. Photobiol. C* **2000**, *1*, 1.
- [40] J.P.S. Valente, P.M. Padilha, A.O. Florentino. *Chemosphere* **2006**, *64*, 1128.
- [41] A.F. Caliman, C. Cojocaru, A. Antoniadis, I. Poullos. *J. Hazard. Mater.* **2007**, *144*, 265.
- [42] H. Lachheb, E. Puzenat, A. Houas, M. Ksibi, E. Elaloui, C. Guillard, J.-M. Herrmann. *Appl. Catal. B: Environ.* **2002**, *39*, 75.
- [43] J. Beltran De Heredia, J. Torregrosa, J.R. Dominguez, J.A. Peres, *J. Hazard. Mater.* **2001**, *83*, 255.
- [44] K. Demeestere, A. De Visscher, J. Dewulf, M. Van Leeuwen, H. Van Langenhove. *Appl. Catal. B: Environ.* **2004**, *54*, 261.

- [45] M.F.J. Dijkstra, A. Michorius, H. Buwalda, H.J. Panneman, J.G.M. Winkelman, A.A.C.M. Beenackers. *Catal. Today* **2001**, 66, 487.
- [46] A. E. Nel, L. Mädler, D. Velegol, T. Xia, E. M. V. Hoek, P. Somasundaran, F. Klaessig, V. Castranova, M. Thompson. *Nature Mater.* **2009**, 8, 543-57.
- [47] A. Nel, T. Xia, L. Mädler, N. Li. *Science* **2006**, 311, 622–627.
- [48] Oberdorster, G. et al. *Part. Fibre Toxicol.* **2005**, 2, 8.
- [49] A. A. Vertegel, R. W. Siegel, J. S. Dordick. *Langmuir* **2004**, 20, 6800–6807.
- [50] W. Sigmund, G. Pyrgiotakis, A. Daga. *Chemical Processing of Ceramics* (CRC, **2005**).
- [51] B. Gilbert, F. Huang, H. Zhang, G. A. Waychunas, J. F. Banfield. *Science* **2004**, 305, 651–654.
- [52] Y. Min, M. Akbulut, K. Kristiansen, Y. Golan, J. Israelachvili. *Nature Mater.* **2008**, 7, 527–538.
- [53] D. Velegol. *J. Nanophoton.* **2007**, 1, 012502.
- [54] H. K. Baca, et al. *Science* **2006**, 313, 337–341.
- [55] J. Kim, Y. Piao, T. Hyeon. *Chem. Soc. Rev.* **2009**, 38, 372-90.
- [56] R. Hao, R. Xing, Z. Xu. *Adv. Mater.* **2010**, 22, 2729-2742.
- [57] P. X. Ma. *Adv. Drug Delivery Rev.* **2008**, 60, 184-98.
- [58] J. Shi, A. R. Votruba, O. C. Farokhzad, R. Langer. *Nano Lett.* **2010**, 10, 3223–3230.
- [59] A. D. Bangham, R. W. Horne. *J. Mol. Biol.* **1964**, 8, 660–668.
- [60] V. Wagner, A. Dullaart, A. K. Bock, A. Zweck. *Nat. Biotechnol.* **2006**, 24, 1211–1217.
- [61] L. Zhang, F. X. Gu, J. M. Chan, A. Z. Wang, R. S. Langer, O. C. Farokhzad. *Clin. Pharmacol. Ther.* **2008**, 83, 761–769.
- [62] M. E. Davis, Z. Chen, D. M. Shin. *Nat. Rev. Drug Discovery* **2008**, 7, 771–782.
- [63] K. Riehemann, S. W. Schneider, T. A. Luger, B. Godin, M. Ferrari, H. Fuchs, *Angew. Chem., Int. Ed.* **2009**, 48, 872–897.
- [64] Y. Matsumura, H. Maeda. *Cancer Res.* **1986**, 46, 6387–6392.
- [65] D. W. Bartlett, H. Su, I. J. Hildebrandt, W. A. Weber, M. E. Davis, *Proc. Natl. Acad. Sci. U.S.A.* **2007**, 104, 15549–15554.
- [66] K. F. Pirollo, E. H. Chang. *Trends Biotechnol.* **2008**, 26, 552–558.
- [67] O. C. Farokhzad, R. Langer. *ACS Nano* **2009**, 3, 16–20.

- [68] R. Gabathuler. *Neurobiol. Dis.* **2010**, 37, 48–57.
- [69] M. E. Davis. *Mol. Pharm.* **2009**, 6, 659–668.
- [70] F. Gu, L. Zhang, B. A. Teply, N. Mann, A. Wang, A. F. Radovic-Moreno, R. Langer, O. C. Farokhzad, *Proc. Natl. Acad. Sci. U.S.A.* **2008**, 105, 2586–2591.
- [71] T. M. Allen. *Nat. Rev. Cancer* **2002**, 2, 750–763.
- [72] H. Jung, T. Yang, M. D. Lasagna, J. Shi, G. D. Reinhart, P. S. Cremer. *Biophys. J.* **2008**, 94, 3094–3103.
- [73] F. Greco, M. J. Vicent. *Adv. Drug Delivery Rev.* **2009**, 61, 1203–1213.
- [74] L. D. Mayer, A. S. Janoff. *Mol. Interventions* **2007**, 7, 216–223.
- [75] S. Sengupta, D. Eavarone, I. Capila, G. L. Zhao, N. Watson, T. Kiziltepe, R. Sasisekharan, *Nature* **2005**, 436, 568–572.
- [76] L. Zhang, A. F. Radovic-Moreno, F. Alexis, F. X. Gu, P. A. Basto, V. Bagalkot, S. Jon, R. S. Langer, O. C. Farokhzad. *ChemMed-Chem* **2007**, 2, 1268–1271.
- [77] Y. Wang, S. Gao, W. H. Ye, H. S. Yoon, Y. Y. Yang. *Nat. Mater.* **2006**, 5, 791–796.
- [78] M. Saad, O. B. Garbuzenko, T. Minko. *Nanomedicine* **2008**, 3, 761–776.
- [79] P. Debbage, W. Jaschke. *Histochem. Cell Biol.* **2008**, 130, 845–875.
- [80] V. Bagalkot, L. Zhang, E. Levy-Nissenbaum, S. Jon, P. W. Kantoff, R. Langer, O. C. Farokhzad. *Nano Lett.* **2007**, 7, 3065–3070.
- [81] J. H. Park, G. von Maltzahn, E. Ruoslahti, S. N. Bhatia, M. J. Sailor. *Angew. Chem., Int. Ed.* **2008**, 47, 7284–7288.
- [82] N. Nasongkla, E. Bey, J. M. Ren, H. Ai, C. Khemtong, J. S. Guthi, S. F. Chin, A. D. Sherry, D. A. Boothman, J. M. Gao. *Nano Lett.* **2006**, 6, 2427–2430.
- [83] J. R. McCarthy, R. Weissleder. *Adv. Drug Delivery Rev.* **2008**, 60, 1241–1251.
- [84] W. R. Sanhai, J. H. Sakamoto, R. Canady, M. Ferrari. *Nat. Nanotechnol.* **2008**, 3, 242–244.
- [85] B. Dubertret, P. Skourides, D. J. Norris, V. Noireaux, A. H. Brivanlou, A. Libchaber. *Science* **2002**, 298, 1759–1762.
- [86] N. Chanda, V. Kattumuri, R. Shukla, A. Zambre, K. Katti, A. Upendran, R. R. Kulkarni, P. Kan, G. M. Fent, S. W. Casteel, C. J. Smith, E. Boote, J. D. Robertson, C. Cutler, J. R. Lever, K. V. Katti, R. Kannan. *Proc. Natl. Acad. Sci. U.S.A.* **2010**, 107, 8760–8765.
- [87] A. De La Zerda, C. Zavaleta, S. Keren, S. Vaithilingam, S. Bodapati, Z. Liu, J. Levi, B. R. Smith, T. J. Ma, O. Oralkan, Z. Cheng, X. Y. Chen, H. J. Dai, B. T. Khuri-Yakub, S. S. Gambhir, *Nat. Nanotechnol.* **2008**, 3, 557–562.

- [88] R. Langer, J. P. Vacanti. *Science* **1993**, *260*, 920–926.
- [89] A. Khademhosseini, J. P. Vacanti, R. Langer. *Sci. Am.* **2009**, *300*, 64–71.
- [90] M. Goldberg, R. Langer, X. Jia, *J. Biomater. Sci.* **2007**, *18*, 241–268.
- [91] M. M. Stevens, J. H. George. *Science* **2005**, *310*, 1135–1138.
- [92] J. Taipale, J. Keski-Oja. *FASEB J.* **1997**, *11*, 51–59.

Chapter 2

Synthesis of nanostructured TiO₂

2.1 Sol-gel technology

2.1.1 Introduction

A process that has, in the past years, gained much notoriety especially in the glass and ceramic fields is the sol-gel reaction.¹⁻¹¹ This chemistry produces a variety of inorganic networks from metal alkoxide monomer precursors. Although first discovered in the late 1800s and extensively studied since the early 1930s, a renewed interest^{2,13} surfaced in the early 1970s when monolithic inorganic gels were formed at low temperatures and converted to glasses without a high temperature melting process.¹⁴ Through this process, homogeneous inorganic oxide materials with desirable properties of hardness, optical transparency, chemical durability, tailored porosity, and thermal resistance, can be produced at room temperatures, as opposed to the much higher melting temperatures required in the production of conventional inorganic glasses.¹⁵⁻¹⁷ The specific uses of these sol-gel produced glasses and ceramics are derived from the various material shapes generated in the gel state, i.e., monoliths, films, fibers, and nanosized powders. Many specific applications include optics, protective and porous films, optical coatings, window insulators, dielectric and electronic coatings, high temperature superconductors, reinforcement fibers, fillers, and catalysts.¹⁷

2.1.2 The general mechanism

The sol-gel process, as the name implies, involves the evolution of inorganic networks through the formation of a colloidal suspension (sol) and gelation of the sol to form a network in a continuous liquid phase (gel).^{1-11,14} The precursors for synthesizing these colloids consist of a metal or metalloid element surrounded by various reactive ligands.

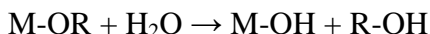
- the inorganic route with metal salts in aqueous solution (chloride, oxychloride, nitrate); much cheaper and easier to handle than metal alkoxides, but their reactions are more difficult to control;
- the metal-organic route with metal alkoxides in organic solvent; the alkoxides are most popular because they react readily with water. The most widely used metal alkoxides are the alkoxysilanes, such as tetramethoxysilane (TMOS) and tetraethoxysilane (TEOS). However, other alkoxides such as aluminates, titanates, and borates are also commonly used in the sol-gel process, often mixed with TEOS.

The general mechanisms in the metal-organic route are based on the growth of metal oxo-polymers in a solvent:

- inorganic step polymerization reactions through hydrolysis and condensation of metal alkoxides $M(OR)_Z$, where $M = Si, Ti, Zr, Al, Sn, Ce.$,

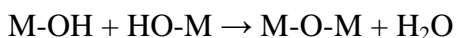
OR is an alkoxy group and Z is the valence or the oxidation state of the metal;

- first step: hydroxylation upon the hydrolysis of alkoxy groups

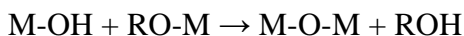


- second step: polycondensation process leading to the formation of branched oligomers and polymers with a metal oxo-based skeleton and reactive residual hydroxo and alkoxy groups; two competitive mechanisms

a) water condensation with the formation of oxygen bridges



b) alcohol condensation



Generally speaking, the hydrolysis reaction, through the addition of water, replaces alkoxide groups (OR) with hydroxyl groups (OH). Subsequent condensation reactions involving the M-OH groups produce M-O-M bonds plus the by-products water or alcohol. Under most conditions, condensation commences before hydrolysis is complete. However, conditions such as, pH, H₂O/M molar ratio, and catalyst can force completion of hydrolysis before condensation begins.^{4-8,16} Additionally, because water and alkoxides are immiscible, a mutual solvent such as an alcohol is utilized. With the presence of this homogenizing agent, alcohol, hydrolysis is facilitated¹⁵ due to the miscibility of the alkoxide and water. As the number of M-O-M bonds increases, the individual molecules are bridged and jointly aggregate in the sol. When the sol particles aggregate, or inter-knit into a network, a gel is formed. Upon drying, trapped volatiles (water, alcohol, etc.) are driven off and the network shrinks as further condensation can occur.

2.1.3 Gelation, aging, drying and calcinations steps

a) Gelation: for example, the mechanisms of the silicate systems are reported: under acid catalysed conditions there is the formation of a “polymeric” gel,¹⁴ as shown as in Fig. 2.1.

Under basic conditions and/or with higher additions of water: more highly branched clusters, which do not interpenetrate prior to gelation and thus behave as discrete species.

If the total concentration of alkoxysilane is low (< ~0.3 M) gelation leads to the formation of colloidal silica (Fig. 2.2). But for higher alkoxysilane concentrations there is the formation of a “colloidal” gel,¹⁴ as shown in Fig. 2.3.

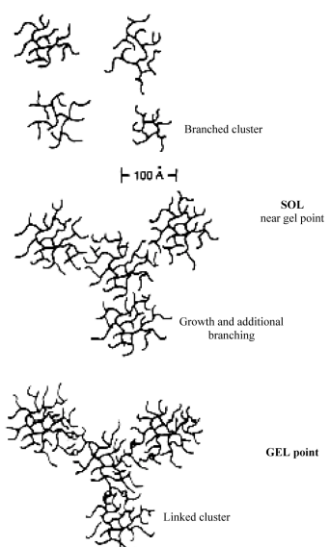


Figure 2.1: The formation of a “polymeric” gel.¹⁴

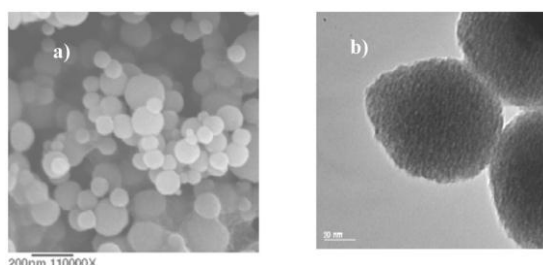


Figure 2.2: a) SEM and b) TEM image of “colloidal” silica.

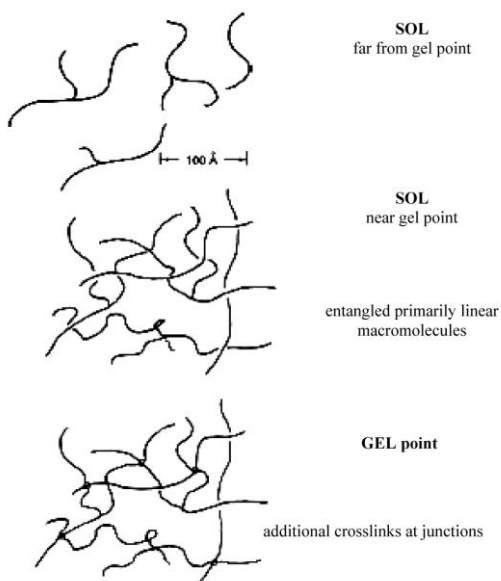


Fig. 2.3: The formation of a “colloidal” gel.¹⁴

- b) ageing: structure modifications with time depending on temperature, solvent and pH conditions:
- gel separation into regions of high and low polymer density because it is expected that as the critical point is approached (e.g. during a change in concentration), fluctuations in polymer density grow larger in amplitude (than those resulting merely from thermal motions);
 - promotion of additional crosslinking as unreacted terminal groups (-OH and -OR) come in contact in regions of higher polymer density;
 - acceleration of the phase separation process and creation of liquid-solid interfaces;
 - further structural changes attributed primarily to surface energy effects: it is well known that surfaces exhibiting positive radii of curvature dissolve more readily than surfaces exhibiting negative radii of curvature. Therefore as the dissolution rate is increased (e.g. by increased temperature or pH) dissolution-reprecipitation results in neck formation causing the gel structure to become fibrillar and the pore formation. Of course, when dissolution is extensive, the gel network would breakdown and ripens to form a colloidal sol.
- c) drying: this is the step of removing of the solvent from the gel-network. The methods adopted for the elimination of the residual solvent are influenced by the intended use of the dried material:
- if powdered ceramics are desired, no special care need be exercised to prevent fragmentation;
 - if monoliths from colloidal gels are desired, the drying procedures are largely determined by the need to minimize internal stresses associated with the volume changes on drying ;
 - if monoliths from polymeric gels are desired: the polymeric species are weakly cross-linked and as solvent is removed, they can deform readily and form a dense gel structure while polymer itself shrinks and forms more crosslinks.
- d) calcinations step: heating, in a different temperature range, to convert the dried gel to a crystalline material. For gels, the following reactions possibly occur:
- desorption of physically adsorbed solvent and water from the walls of micropores (100-200°C);
 - decomposition of residual organic groups into CO₂ (300-500°C);
 - collapse of small pores (400-500°C);
 - collapse of larger pores (700-900°C);
 - continued polycondensation (100-700°C).

Sintering and densification phenomena also take place, via typical sintering mechanisms such as evaporation condensation, surface diffusion, grain boundary and bulk diffusion. The small particle size of the powders lead to high reactivities

and enhanced sintering and/or coarsening rates (the principal process involved in densification is often viscous sintering).

2.1.4 Advantages and limitations of sol-gel technique.

a) Advantages: Sol-gel processes allow the synthesis of materials with:

- high purity, because organometallic alkoxy precursors can be purified by distillation or recrystallization;
- high degree of homogeneity, because reagents are mixed at the molecular level;
- the possibility to control simultaneously the bulk properties, such as the phase composition, and the surface characteristics, such as the surface area, the total pore volume distribution, etc;
- low or high porosity, by using appropriate heat treatment and firing times;
- the capability of obtaining fully-dense amorphous solids at temperatures lower by hundreds of centigrade degrees than those required for conventional compaction/densification or for melting;
- the ability to obtain materials with novel distributions of phases contained therein.

b) Drawbacks:

- high cost for the majority of alkoxide precursors;
- long processing steps.

2.2 Application of ultrasound to the synthesis of nanostructured materials

2.2.1 A brief introduction to ultrasound

Chemistry deals with the interaction between energy and matter, and chemical reactions require some form of energy (e.g., heat, light, radiation, electric potential, etc.) to proceed.¹⁸⁻²⁰ Precise control over chemical reactions is a key to the success of nanostructured materials synthesis, but currently such control is limited to the manipulations of various reaction parameters including time, energy input, and pressure. These parameters, however, are adjustable only within a certain boundaries defined by the energy source employed in reactions. Each type of energy has its own realm of reaction conditions determined by its inherent reaction parameters, as depicted in Fig. 2.4.²¹

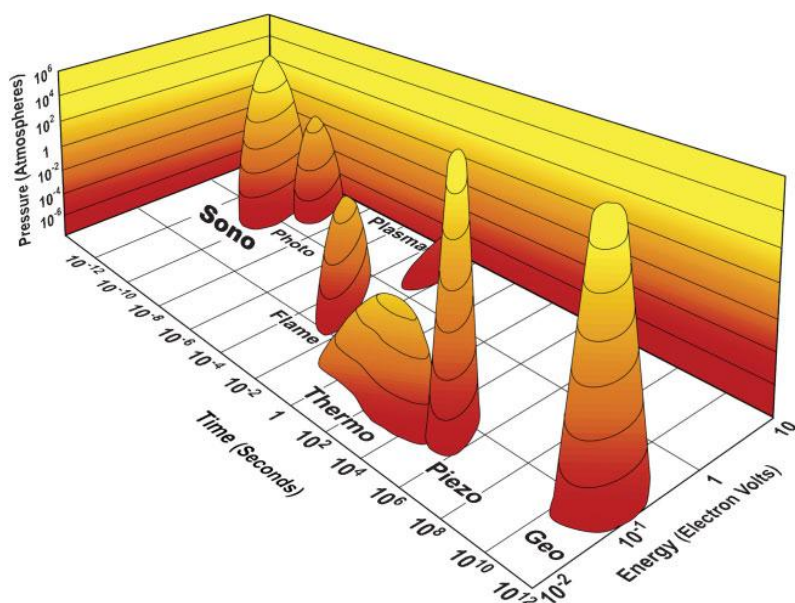


Figure 2.4: Islands of chemistry as a function of time, pressure, and energy.²⁰

Compared to traditional energy sources, ultrasonic irradiation provides rather unusual reaction conditions (a short duration of extremely high temperatures and pressures in liquids) that cannot be realized by other methods. Interestingly, such extraordinary conditions are not derived directly from ultrasound itself: acoustic wavelengths are much larger than molecular dimensions. Thus, no direct, molecular-level interaction between ultrasound and the chemical species takes place. Instead, acoustic cavitation (i.e., the formation, growth, and implosive collapse of bubbles in liquids), driven by high intensity ultrasound accounts for the chemical effects of ultrasound.²² When liquids are irradiated with ultrasound, the

alternating expansive and compressive acoustic waves creates bubbles (i.e., cavities) and makes the bubbles oscillate (Fig. 2.5). The oscillating bubbles can accumulate ultrasonic energy effectively while growing to a certain size (typically tens of *mm*). Under the right conditions, a bubble can overgrow and subsequently collapse, releasing the concentrated energy stored in the bubble within a very short time (with a heating and cooling rate of $>10^{10} \text{ K}\cdot\text{s}^{-1}$). This cavitation implosion is very localized and transient with a temperature of $\sim 5000 \text{ K}$ and a pressure of $\sim 1000 \text{ bar}$.²⁰ These extreme conditions created during acoustic cavitation can give rise to light emission. This intriguing physical phenomenon, known as sonoluminescence, was first observed during the ultrasonic irradiation of water in 1934 by Frenzel and Schultes,²³ and afterward, has been systematically investigated by several research groups. Because of the transient nature of acoustic cavitation, sonoluminescence has been explored as a spectroscopic probe to investigate reaction conditions (e.g., temperature and pressure) during ultrasonic irradiation.²⁴⁻³¹ A variety of sonochemical apparatuses are commercially available with several designs: ultrasonic cleaning baths, direct-immersion ultrasonic horns, and flow reactors are common examples.

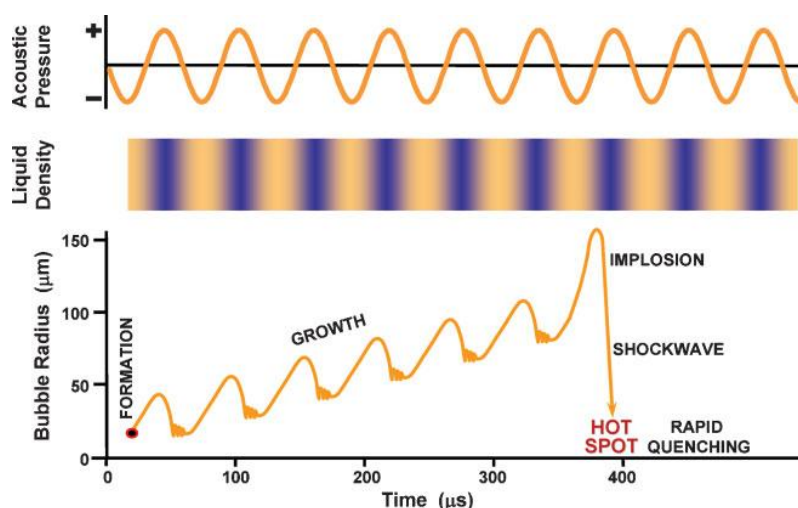


Figure 2.5: Schematic representation of transient acoustic cavitation.³⁶

Cleaning baths have insufficient intensity for most applications, but are useful for liquid-solid reactions with easily passivated but reactive solids (e.g., Li, Mg). A typical laboratory-scale sonochemical apparatus (Figure 2.6a) consists of a high-intensity ultrasonic titanium horn driven by a piezoelectric transducer which is directly introduced into a thermostated glass reactor having gas inlets and outlets.²⁰ Cavitation occurs over a very wide range of frequencies, from tens of *Hz* to tens of *MHz*; above that frequency regime, the intrinsic viscosity of liquids prevents

cavitation from occurring. Most high intensity ultrasonic horns operate at 20 or 40 kHz , most cleaning baths near 40 kHz , and there is specialized equipment available in the few hundred kHz to few MHz regime. In general, physical effects of ultrasound (e.g., emulsification and surface damage) are more dominant at lower frequencies, whereas cavitational heating of collapsing bubbles occurs over the full frequency range. The chemical effects of ultrasound were explored for many years, nearly always in water.³²⁻³⁵ Ultrasonic irradiation of aqueous liquids generates free radicals, and the formation of free radicals by sonolysis of water has been particularly well-studied.

Primary sonolysis products in water are $\text{H} \cdot$ and $\text{OH} \cdot$ radicals.³⁵ These radicals can recombine to return to their original form or combine to produce H_2 and H_2O_2 . They can also produce $\text{HO}_2 \cdot$ by combination with O_2 . These strong oxidants and reductants are utilized for various sonochemical reactions in aqueous solutions. Major advancements in sonochemistry have been achieved by moving to less volatile organic liquids, so that the bubble contents are dominated by the intended reactants rather than the solvent vapour.

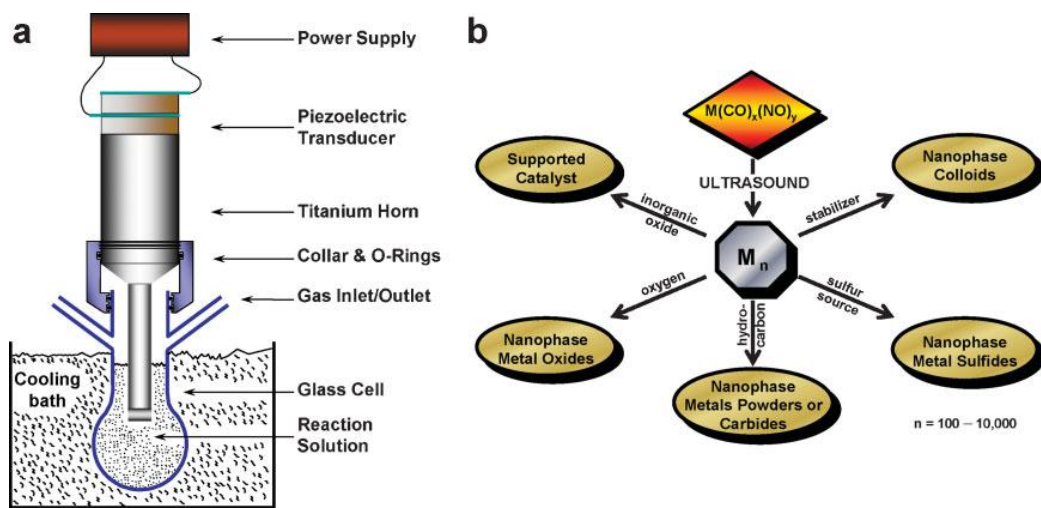


Figure 2.6: a) Typical high-intensity ultrasonic rig and b) sonochemical synthesis of various nanostructured inorganic materials.³⁷

Suslick and coworkers extensively explored the sonochemistry of metal carbonyl compounds (e.g., $\text{Fe}(\text{CO})_5$, $\text{Co}(\text{CO})_3\text{NO}$, $\text{Mo}(\text{CO})_6$, and $\text{W}(\text{CO})_6$) and utilized this non-conventional technique to produce unusual nanostructured inorganic materials.^{20-22,36,37} They observed that volatile organometallic compounds can fully dissociate their carbonyl ligands inside a bubble during acoustic cavitation, and the resulting metal atoms agglomerate to form a variety of nanostructured materials. A powerful aspect of the sonochemical synthesis resides in its versatility; various

forms of nanostructured metals, oxides, sulfides and carbides can be prepared simply by changing reaction conditions (Fig. 2.6b).^{20,22,36-38} For instance, sonochemical decomposition of $\text{Fe}(\text{CO})_5$ in hexadecane yields amorphous iron metal powder.^{39,40} In the presence of organic or polymeric stabilizers (e.g., oleic acid or polyvinylpyrrolidone), colloidal iron nanoparticles are obtained instead.⁴¹ Adding a sulfur source into the precursor solution produces nanophase iron sulfide, and replacing argon gas with oxygen as the purging gas leads to the formation of nanoscale iron oxide. Further, when $\text{Fe}(\text{CO})_5$ is irradiated with a solid support material (e.g., silica), nanometer-sized iron particles are deposited on the support.

2.2.2 Ultrasonic Spray Pyrolysis

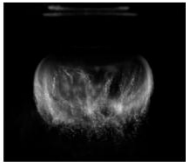

2.2.2.1 Introduction

In contrast with sonochemistry, where ultrasound directly induces chemical reactions, in Ultrasonic Spray Pyrolysis (USP), the ultrasound is not directly employed in chemical reactions, which are in fact thermally driven. Instead, the role of the ultrasound in USP is to provide the phase isolation of one microdroplet reactor from another. While high intensity ultrasound with a low frequency (typically 20 *kHz*) is used in sonochemistry, USP generally utilizes lower intensity ultrasound with a high frequency (e.g., ~ 2 *MHz*). In USP, ultrasound nebulizes precursor solutions to produce the micron-sized droplets that act as isolated, individual micron-sized chemical reactors. Both cavitation-induced sonochemistry and USP, in general, are involved phase-separated (i.e., two- and sometimes multiphase) chemical reactions. In USP, liquid droplets generated by ultrasonic nebulization are heated in a gas flow, and subsequently solid-phase or sometimes liquid-phase (when precursors melt prior to decomposition or when high boiling point liquids are used) chemical reactions occur. The major differences between two synthetic methods are summarized in Table 2.1.

Spray pyrolysis has been widely used in industry for ultrafine and nanoparticle production as well as film deposition, in part because the apparatus is simple and continuous and can be scaled easily for mass production. In general, spray pyrolysis involves the thermal decomposition of aerosols (i.e., solid or liquid particles suspended in a gas) generated by a nebulizer (e.g., pneumatic, ultrasonic, or electrostatic nebulizers) in a gas flow.⁴² Among the various nebulization techniques, the use of ultrasonic nebulizers has been favored because of their outstanding energy-efficiency in aerosol generation over other nebulization tools, affordability (e.g., the use of household humidifiers), and the inherently low velocity of the initial aerosol. As a synthetic tool, USP has several advantages over other traditional methods: production of micron- or submicron-sized spherical

particles, high product purity, continuous operation, and ease of controlling composition.⁴²⁻⁴⁴

Table 2.1: Comparison of the complementarities of sonochemistry and ultrasonic spray pyrolysis. Images: multi-bubble sonoluminescence in 85wt% phosphonic acid and ultrasonic mist produced at 1.7 MHz, respectively.

	Sonochemistry	Ultrasonic spray pyrolysis
		
Reaction site	Gas bubbles	Liquid microdroplets
Conditions	~5000 K, 1000 bar	500–1300 K, 1 bar
Reactants	Volatiles primarily	Nonvolatile solutes
Cooling rates	$> 10^{10} \text{ K s}^{-1}$	10^4 K s^{-1}
Templating	Easy	Easy, easy nanocomposites
Heating zone	Single extreme hot zone	Multiple hot zones possible
Scalability	Scalable: kg/day	Easily scalable: ton/day
Particle size control	Nano- and submicron-sized particles	Typically submicron-size, but nanoparticles possible
Composition control	Easy	Easy
Anisotropic shapes	Yes	No
Hollow structures	Yes	Yes
Core/shell structures	Yes	Yes

Unlike conventional solid- or liquid-phase synthetic methods (e.g., precipitation, hydrothermal method, and solid-state reaction) where batch reactions are performed to produce materials, the USP technique is a continuous flow process that enables both large and small scale production of products with excellent reproducibility. In addition, the facile control over chemical and physical compositions in the USP method makes USP particularly useful in the preparation of multicomponent or composite materials.⁴²

The droplet formation by low frequency ultrasound was first described by Wood and Loomis in 1927.⁴⁵ In 1962, Lang experimentally established the relationship between ultrasonic frequency and droplet size.⁴⁶ Ultrasonic nebulization (Fig. 2.7) is a result of capillary waves (i.e., waves travelling along the interface between two fluids) at the surface of liquids; in other words, nebulization is a result of momentum transfer. The capillary waves generated by ultrasonic vibrations at the liquid's surface consist of crests and troughs. When the amplitude of the surface capillary waves is sufficiently high, the crests (peaks) of the capillary waves can break off, resulting in liquid droplets. Since the capillary wavelength is inversely proportional to frequency, finer droplets can be produced at higher frequencies. Several other parameters (e.g., surface tension and density) also affect the droplet size along with frequency, which is well-described by the Lang equation:⁴⁶

$$D_{DROPLET} = 0.34 \left(\frac{8\pi\gamma}{\rho f^2} \right)^{\frac{1}{3}}$$

where D is mean droplet diameter, γ ($N\ m^{-1}$) is surface tension, ρ ($kg\ m^{-3}$) is solution density, and f (MHz) is the ultrasonic frequency. For nanomaterial synthesis, high frequencies (e.g., $>1\ MHz$) are generally used, but commercial large scale nebulizers are also available in the $25\ kHz$ region and are used for spray drying and painting. A typical USP apparatus consists of an ultrasonic transducer at the base of a vessel containing precursor solutions and fitted with a gas stream to carry the mist into a tubular furnace; a collector is positioned at the furnace outlet (e.g., bubbler, filter, electrostatic precipitator, etc); for film deposition, substrates such as silicon and glass are usually placed inside the furnace (Fig. 2.8a). The liquid droplets generated by ultrasonic nebulization are carried through a heated zone by a gas flow (e.g., Ar, N_2 , O_2 , etc). Often, additional furnaces are attached to the end of the single furnace to increase residence time of the droplets in the heated zone or to achieve multi-zone temperatures. In a laboratory-scale USP rig used in the Suslick research group, for example, an inexpensive high frequency ultrasound generator from a household humidifier can be used to create a useful source for USP, eliminating the need for expensive, commercial ultrasonic nebulizers. The USP synthetic process involves droplet generation, evaporation of solvents, diffusion of solutes, precipitation, decomposition, and densification (Fig. 2.8b).⁴² The entire USP process, however, is more complicated, and some of the processes are still poorly understood. A simplified and qualitative description of the USP process will be discussed here; more detailed descriptions are available in several excellent books and reviews.^{42-44,47,48} The first process that occurs during USP is the formation of liquid droplets by ultrasonic nebulization. As previously mentioned, the size of the droplets can be controlled by changing several parameters, but typically, in the case of water, spherical droplets with an initial diameter of $\sim 5\ \mu m$ are obtained at a frequency of $\sim 2\ MHz$. The liquid droplets are then carried into a heated zone by a gas flow with subsequent solvent evaporation from the surface of the droplets. During solvent evaporation, the droplets rapidly shrink, and further heating leads to supersaturation, at which point precipitation of solute takes place, often at the surface of the droplet. Decomposition of precursors may follow to produce porous or hollow intermediate particles, which may subsequently undergo densification to yield solid particles. The formation of dense solid particles versus hollow shells is intimately related to solvent evaporation rate and solubility of precursors.^{42,44,47} These factors can affect the degree of supersaturation, which significantly influences the morphology of final products.



Figure 2.7: Photograph of an ultrasonic fountain and mist produced at 1.7 MHz.⁴⁹

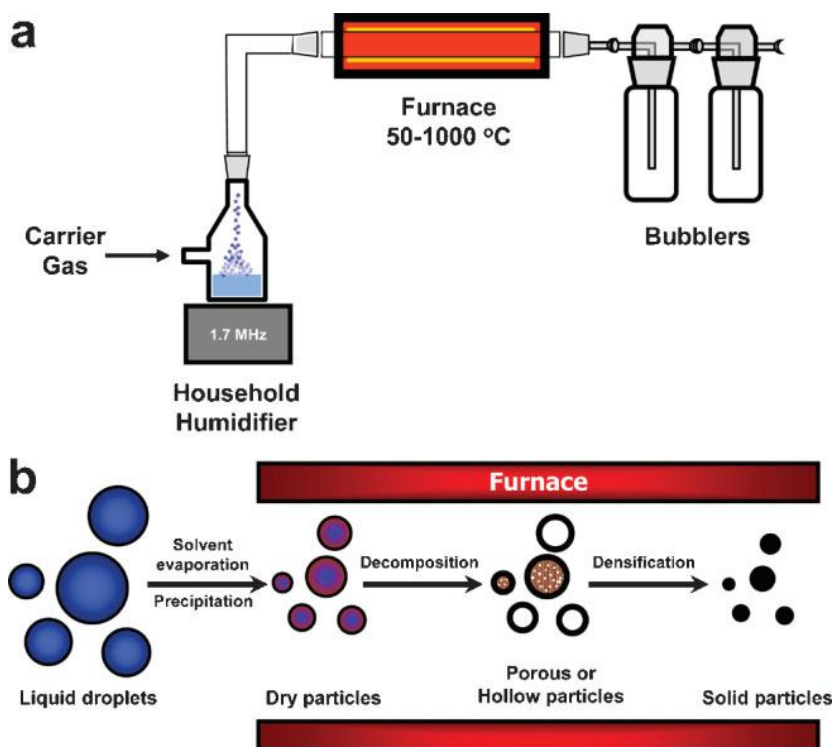


Figure 2.8: Schematic illustration of (a) typical USP apparatus and (b) a simplified USP process.⁴²

2.2.2.2 *Preparation of nanostructured materials by USP*

Despite the advantages of the USP technique, its utilization had long been confined to the production of micron-sized powders and thin films. During the last 10 years, however, USP has been revived by several research groups as a generalized synthetic method for the preparation of nanostructured materials. This conspicuous transformation of the USP technique into a powerful synthetic tool has originated from its outstanding ability to produce nanocomposites. In a majority of cases, the nanocomposites are composed of desired materials (e.g., metal oxides, sulfides, or carbon) combined with sacrificial materials (e.g., surfactants, colloidal silica, polymers, or metal salts). The sacrificial materials are subsequently removed by several methods (e.g., chemical etching, calcination, or dissolution), introducing various nanostructures (e.g., porosity) into final products.

In the following paragraphs will be reported some examples of materials that have been synthesized by USP.

a) Nanostructured Materials from Organic-Inorganic Hybrid Nanocomposites

Mesostructured framework solids consist of nanometer-sized, thin walls integrated continuously in an orderly fashion. Well-ordered mesoporous materials often have unique properties with important applications to catalysis, sorption, gas sensing, optics, and photovoltaics.⁵⁰⁻⁵² Often, the physical and chemical properties of the well-ordered mesoporous materials are significantly different from their nonporous, solid counterparts.⁵³ Typical synthetic procedures for mesostructured materials are batch reactions where self-assembled organic-inorganic hybrid nanocomposites are produced with the assistance of pre-organized organic species (e.g., surfactants and amphiphilic block copolymers), which are then burnt out of the final mesoporous material. Despite their versatility and reproducibility, the batch synthetic routes possess several critical drawbacks: tedious and time-consuming templating processes, difficulties of their use to produce thin films, and limited utilization for the production of patterned nanocomposites.⁵⁴ Brinker and coworkers addressed such problems by combining an evaporation-induced self-assembly (EISA) process and aerosol techniques.⁵⁵⁻⁵⁶ In this pioneering work, they sprayed homogeneous water/ethanol mixture solutions containing silica precursors and surfactants whose initial concentrations were considerably less than the critical micelle concentration into a heated zone. As the aerosol droplets are heated in the furnace, rapid solvent evaporation takes place, causing the surfactant concentration to exceed the critical micelle concentration at the droplet surface.

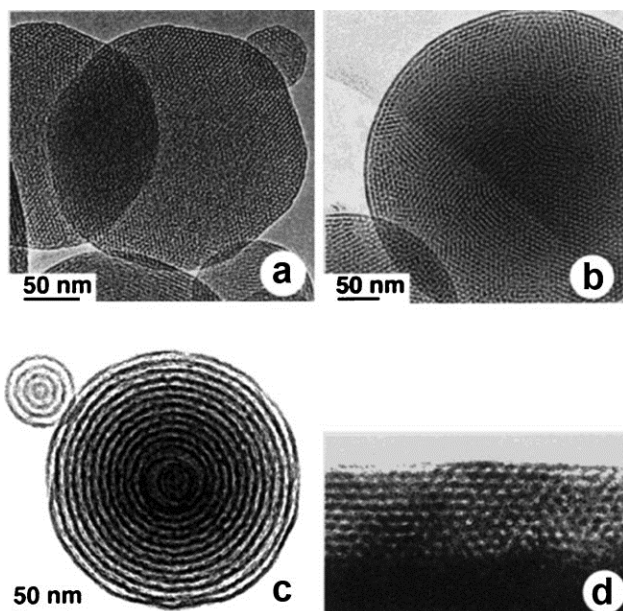


Figure 2.9: Representative TEM images of mesostructured silica particles and film. (a) faceted, calcined silica particles with a hexagonal mesophase; (b) calcined silica particles showing cubic mesostructure; (c) calcined particles showing a vesicular mesophase; (d) cross-section of porous silica film deposited on a silicon substrate.⁵⁴

Further solvent evaporation renders the entire surfactant concentration greater than the critical micelle concentration throughout the droplet, initiating micelle formation. The micelles subsequently organize into liquid-crystalline mesostructures. Strictly speaking, this synthetic process should not be called USP because no decomposition (i.e., pyrolysis) is involved in this aerosol process; rather, this is more accurately an aerosol-assisted sol-gel reaction. Heat-treatment (i.e., calcination under oxygen) of the obtained organic-inorganic hybrid nanocomposites produces various forms of mesostructured silica spheres, depending on the surfactant used in the synthesis (Fig. 2.9a–c).⁵⁵ For instance, when cetyltrimethylammonium bromide (CTAB), a cationic surfactant, was used as a structure-directing agent, spherical particles with a highly ordered hexagonal mesophase were produced. Non-ionic surfactants, on the other hand, produced silica particles showing a layered, vesicular mesostructure. Interestingly, adding swelling agents (e.g., polypropylene glycol dimethylacrylate and polypropylene oxide) into the precursor solutions gave control over the mesopore diameters.⁵⁷ Along with the powder production, this aerosol-assisted synthetic route proved to be very useful even for the formation of ordered mesostructured thin films (Fig. 2.9d); the droplet coalescence on substrates results in the formation of uniformly well-ordered thin films.⁵⁸ Another advantage of this synthetic route is the ability to

incorporate metal species, organic dye molecules, or polymers within the mesostructured framework.^{55,59-62} With metal complexes added to precursor solutions, for instance, metal/silica nanocomposites (e.g., gold/silica and palladium/silica) can be easily obtained.^{55,59} Simultaneous control over metal loadings and pore structures provides sophisticated level of control with this synthetic approach unavailable through other conventional methods such as incipient wetness.

b) Nanostructured Materials from Silica-based Nanocomposites

Hard templates, especially colloidal silica, have also proven useful in the USP preparation of nanostructured materials. Silica nanoparticles will close-pack in an evaporating droplet and can provide a nanostructured scaffold *in situ*. Suslick and Skrabalak utilized silica particles as a sacrificial component in USP-produced nanocomposites to prepare porous MoS₂ via USP.⁶³ While USP without templating produces only submicron-sized, spherical solid MoS₂ spheres, USP with templating yields SiO₂/MoS₂ nanocomposite from the decomposition of a single-source MoS₂ precursor dissolved in an aqueous suspension of nanometer-sized, colloidal silica particles. Subsequent HF etching selectively leaches silica nanostructures out of the nanocomposite, resulting in porous MoS₂ network. The nature of the resulting MoS₂ nanostructure (e.g., porosity and surface area) can be easily tuned by changing the size and concentration of silica particles. The porous MoS₂ produced by the USP technique was shown to be an extremely active catalyst for hydrodesulfurization reaction compared to its nonporous counterpart. Upon doping with cobalt, the porous MoS₂ exhibits a superior catalytic activity and selectivity than even RuS₂, known as the most intrinsically active catalyst for hydrodesulfurization.

Recently, nanostructured ZnS:Ni²⁺ photocatalysts were prepared in a similar manner and evaluated for hydrogen evolution under visible light (Fig. 2.10).⁶⁴ Because of their high energy conversion efficiency and the relatively negative redox potential of their conduction band, ZnS photocatalysts have been examined for a variety of applications, including degradation of water pollutants, reduction of toxic heavy metals, and water-splitting for H₂ evolution. In the USP synthesis of ZnS:Ni²⁺ photocatalysts, mesoporous hollow microspheres (Fig. 2.10a and b) were obtained at a low temperature after silica template removal, whereas nanoparticles (Fig. 2.10c and d) are produced at a high temperature. This temperature-dependent morphology change is related to the rapid crystal growth of ZnS at high temperatures, which results in ZnS nanoparticles larger than the silica colloid template; such composites are not sufficiently strongly held together to sustain the hollow microsphere structure after the silica template is removed. In addition to the

rapid crystal growth, gas released during the decomposition of the ZnS precursors may also lead to the destruction of the porous microspheres. Photocatalytic activity of USP products of ZnS:Ni^{2+} toward water-splitting under visible light was examined in the presence of sacrificial electron donors (K_2SO_3 and Na_2S). The most efficient of the ZnS:Ni^{2+} morphologies are nanoparticles, which are well-balanced between crystallinity and surface area. The USP nanoparticles were further compared to conventional powders, and it was found that the photocatalytic activity of the USP nanoparticles for H_2 production is substantially superior to those of ZnS:Ni^{2+} powders. These results clearly demonstrate that USP is a robust and efficient method for production of highly active photocatalysts.

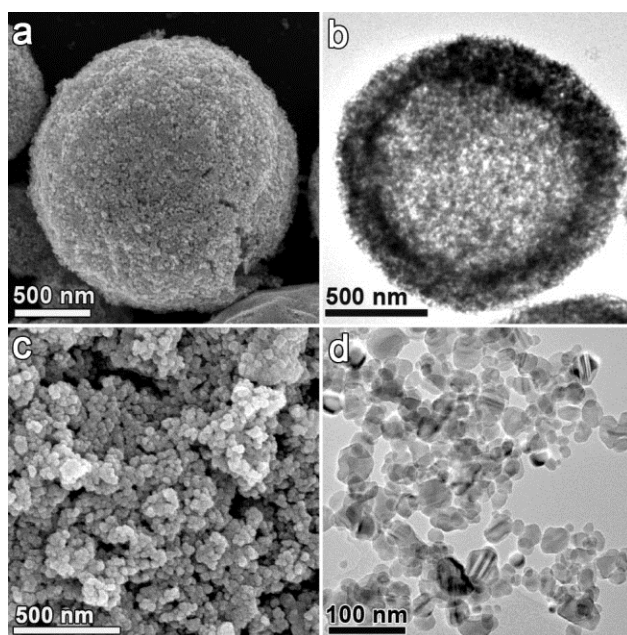


Figure 2.10: Electron micrographs of nanostructured ZnS:Ni^{2+} hollow microspheres and nanoparticles produced by USP.⁶⁴

The utilization of a silica template has been further extended for the synthesis of nanostructured metal oxides. Suslick and coworkers reported the USP synthesis of various forms of titania nanostructures, including porous, hollow, and ball-in-ball architectures (Fig. 2.11).⁶⁵ When an aqueous solution containing a titanium complex and silica nanoparticles is nebulized and decomposed via the USP process, a titania/silica nanocomposite is produced (Fig. 2.11a). This normally produces a porous titania microsphere after the silica is selectively etched with HF from the nanocomposite (Fig. 2.11b). In the presence of some transition metal ions in the precursor solution, however, an unusual phase separation occurs during USP

with the formation of an outer titania enriched shell and an inner silica core. Upon etching, this generates initially a ball-in-ball with an inner silica core and an outer porous titania shell (Fig. 2.11c and d); on full etching, the core is gone and only a porous titania spherical shell remains; the exact mechanism by which the transition metal ions induce the phase separation remains unknown. Cytotoxicity studies revealed that these nanostructured microspheres possess negligible effects on the viability of various cell lines, which led to the further examination of these materials as potential drug delivery agents. The microspheres loaded with a potential drug for Alzheimer's disease showed an outstanding ability to selectively deliver the drug to cytosol rather than cell nuclei. In another use of silica colloid templating, Lu and coworkers synthesized various kinds of porous carbon spheres from silica/ sucrose nanocomposites.⁶⁶⁻⁶⁷ By changing the type of silica template and manipulating the ratio of template to sucrose, they were able to simply control the pore structures of carbon spheres and their macroscopic morphology. Hydrogen physisorption on these carbon materials has been recently evaluated, presenting a potential use of these USP carbons for hydrogen storage applications.⁶⁷

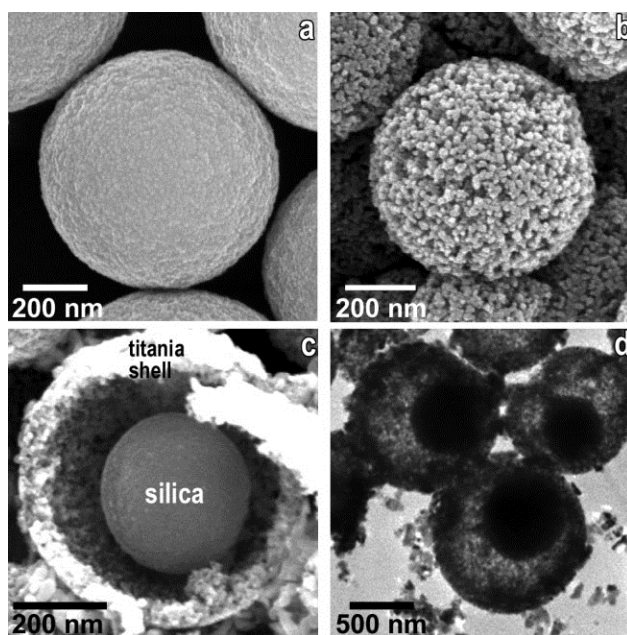


Figure 2.11: Electron micrographs of (a) silica-titania composite produced by USP and (b) porous titania obtained by HF treatment; (c) SEM and (d) TEM image of ball-in-ball silica-titania composite decorated with Co oxide nanoparticles after partial etching with HF.⁶⁵

c) Nanostructured Materials from Metal Salt-based Nanocomposites

In the traditional USP process, one initial droplet yields one final particle. While multiple nucleation occur at an early stage of the USP process, the resulting multiple nanocrystallites grow and aggregate into a larger micron-sized single particle as thermal heating in the droplet proceeds. This distinctive nature of the USP process has excluded the use of USP for the production of nanoparticles. There have been some attempts to produce nanometer-sized particles by USP (e.g., low-pressure spray pyrolysis);⁶⁸⁻⁷⁰ however, the requirement of a vacuum system and the difficulties in controlling experimental parameters in this method have prevented its wide spread use for nanoparticle production. To address such issues, Okuyama and coworkers proposed a facile, rapid, and generalizable USP method. In their synthetic strategy named “salt-assisted aerosol decomposition”, metal salts (e.g., chlorides or nitrates of Li, Na, K) or their eutectic mixtures are simply introduced into precursor solutions to prevent the agglomeration of nanocrystallites produced at the early stage of USP process.⁷¹ The added metal salts play a role as hot liquid solvents where nanocrystallites can dissolve and precipitate during USP process. Such multiple series of dissolution/ precipitation events occurring in the molten droplets lead to the production of separated nanoparticles trapped in a salt matrix. The molten salts and the non-agglomerated nanoparticles then solidify as the aerosol droplets are cooled, and the salt matrix is subsequently removed by several cycles of washing, resulting in separated nanoparticles. A wide variety of nanoparticles have been prepared, including Ni, Ag–Pd, NiO, CeO₂, ZnO, LiCoO₂, Y₂O₃–ZrO₂, (Ba_{1-x}Sr_x)TiO₃, CdS, and ZnS.^{72,71,73-76} In addition to the versatility of this novel route, the molten salts serve as an effective liquid flux to improve mass transport.⁷¹ Due to the greatly enhanced mass transfer rates, the materials produced via the salt-assisted aerosol decomposition method are often much more crystalline than the USP products obtained by the conventional USP method, which can improve their physical properties substantially. Judicious control over the quantity of metal salts can create porous architectures (e.g., mesopores or hollow interiors) into the final USP products rather than producing fully separated nanoparticles.

Unlike the salt-assisted methods discussed above where pre-existing metal salts are employed to create pore structures, a newly devised USP method for porous carbons utilizes in situ generated metal salts as a template. Suslick and Skrabalak reported USP synthesis of various nanostructured carbons from the decomposition of alkali halocarboxylates (Fig. 2.12).⁷⁷ While traditional procedures for porous carbon synthesis require a series of tedious steps (e.g., creation of porous framework, infiltration of carbon precursors, carbonization, and template removal), the new approach is a one-step process and does not require relatively expensive

template materials. Depending on the types of alkali halocarboxylates, a variety of nanostructures (mesoporous, macroporous, and hollow) are created (Fig. 2.12a-f). The USP products of an aqueous solution of alkali metal chloroacetates ($\text{H}_2\text{ClCCO}_2\text{M}$, $\text{M} = \text{Li}, \text{Na}, \text{K}$) are hollow carbon spheres (Fig. 2.12a) and macroporous carbon cages (Fig. 2.12c-f), whereas the pyrolysis of a lithium dichloroacetate ($\text{HCl}_2\text{CCO}_2\text{Li}$) solution yields mesoporous carbon spheres (Fig. 2.12b).

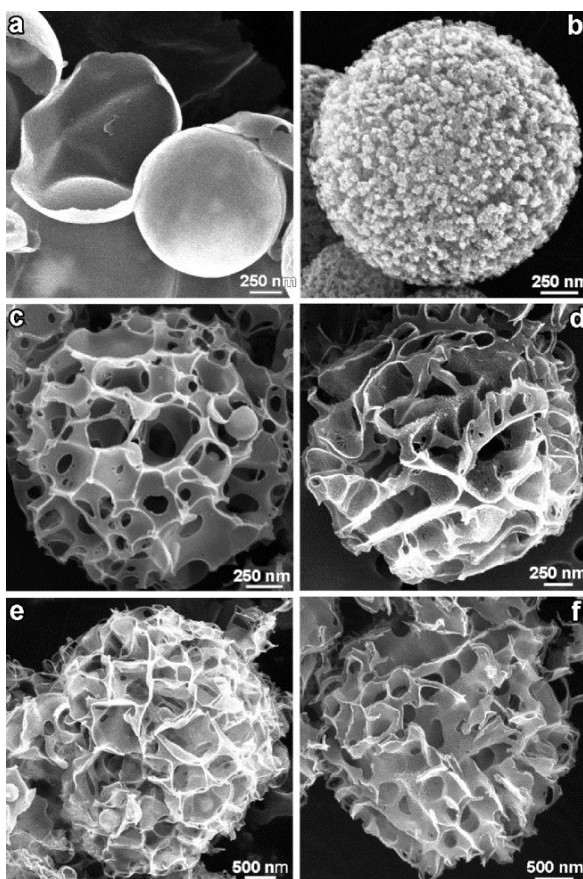


Figure 2.12: SEM images of USP porous carbons from various precursors: a) lithium chloroacetate, b) lithium dichloroacetate, and c) sodium chloroacetate, d) sodium dichloroacetate, e) potassium chloroacetate, and f) potassium dichloroacetate.⁷⁷

In-depth studies on a decomposition pathway of precursor solutions (using differential scanning calorimetry and thermal gravimetric analysis) revealed that the formation of pore structures is intimately related to the relative order of precursor melting and decomposition processes. In case of mesoporous carbon shown in Fig. 2.12b, for instance, the decomposition of lithium dichloroacetate generates LiCl , which then acts as a temporary pore template as carbon network growth occurs. In the macroporous carbon shown in Fig. 2.12bc-f, on the other

hand, no melting occurs before precursor decomposition; as a result, the carbon network forms through solid-state reactions, resulting in macropore formation. USP decomposition of aqueous solutions of substituted alkali benzoate salts also produced various porous or hollow carbon spheres.⁷⁸ Interestingly, the size of the carbon spheres is linearly correlated to the concentration of precursor solutions. In addition, both the cation and the ring substituents of a given precursor influence product morphology. In contrast with the porous carbons produced from the decomposition of alkali halocarboxylates, electron micrographs revealed that *in situ* generated salts do not account for pore or bowl formation, suggesting that their formation is involved in different mechanisms. Thermogravimetric analysis of precursors suggests that the relative temperature of decomposition steps releasing gas determines morphology differences. Porous carbon powders produced by USP were evaluated as catalyst supports for a direct methanol fuel cell (DMFC) catalyst and as pore formers in a membrane electrode assembly (MEA).⁷⁹ The effect of these materials on unit cell performance was compared to traditional Vulcan XC-72 carbon nanoparticle powder. It has been demonstrated that the inclusion of these carbon microspheres in electrodes is a simple, effective way to facilitate the mass transport of air and methanol during fuel cell operation.

d) Semiconductor Nanoparticles from Chemical Aerosol Flow Synthesis

Despite the success of the salt-assisted aerosol decomposition method for nanoparticle production, it had remained a serious challenge to produce high quality semiconductor nanoparticles (or quantum dots). Traditional synthetic routes (e.g., high-temperature decomposition of organometallic compounds) in general require rapid nucleation through thermal or concentration spikes to produce monodispersed nanoparticles.⁸⁰ In this respect, USP would be a suitable synthetic approach because the rapid heating and cooling of nebulized droplets that occurs during the USP process (with a timescale of seconds) can easily create the rapid nucleation required. Despite this potential advantage of USP method, however, the production of highly luminescent quantum dots via the USP route had not been realized until recently, mainly because of the use of aqueous precursor solutions in semiconductor preparation.⁸¹

To address this long-standing problem, Didenko and Suslick proposed a novel synthetic concept named “chemical aerosol flow synthesis”,⁸² using organic solutions of high boiling point liquids (e.g., octadecane) containing nanoparticle precursors instead of aqueous precursor solutions. Prior to ultrasonic nebulization, the organic precursor solutions are diluted with a low boiling point liquid (e.g., toluene) to make them less viscous. Nebulized droplets of the organic solutions

first lose the low boiling point solvent as they pass through a heating zone, leaving a concentrated precursor solution in the high boiling point solvent behind. At this point, chemical reactions take place in high boiling point organic liquid to produce highly crystalline nanoparticles, and the reactions are then rapidly quenched in cold, solvent-filled bubblers. Highly fluorescent Cd-based quantum dots (e.g., CdS, CdSe, and CdTe as well as mixed chalcogenides) have been successfully prepared via this method (Fig. 2.13a), and their particle size and consequently their photoluminescent emission can be easily tuned by simply changing the furnace temperature (Figure 20b). With this approach, one droplet is capable of yielding thousands of nanoparticles and high boiling point liquids containing surfactants prevent the agglomeration of nanoparticles. In addition, highly reproducible, gram-scale synthesis became possible (with a production rate of ~100 mg/h even with a laboratory-scale experimental setup), which had been significant limitations with traditional syntheses of quantum dots.

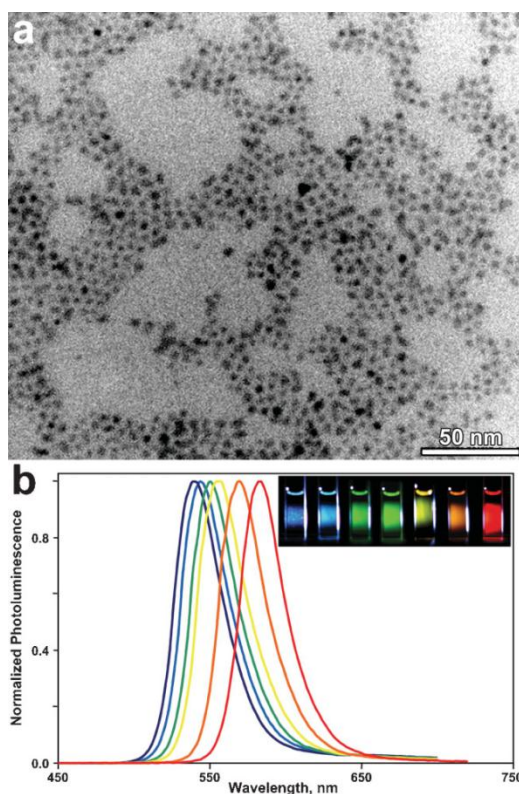


Figure 2.13: a) TEM image of CdSe QDs produced by USP at 340 °C and b) photoluminescence spectra of CdSe QDs obtained at temperatures of 240, 260, 280, 300, 320, and 340 °C (from left to right) in toluene solution (Inset: photograph of photoluminescence of the corresponding QDs in toluene solution).⁸²

Very recently, this synthetic method has been further extended to prepare ternary CdTeSe and CdTeS quantum dots emitting at far-red and near-infrared (NIR) wavelength regions.⁸³ Far-red and NIR emitting QDs have the advantage that in biological systems the NIR is a clear window for *in vivo* imaging because autofluorescence, light absorption, and scattering from cells and cellular components is minimized. In the previous report,⁸⁴ CdTe nanocrystals stabilized by octadecylphosphonic acid (ODPA) with ~40% quantum efficiency had been successfully synthesized; the emission, however, could not be shifted further into the red than ~610nm. The strong coordination bond in Cd-ODPA precursors significantly decreases the reactivity of the monomers, and the residence time of aerosolized precursors during the flow synthesis was insufficient for CdTe QDs to grow to the large-sized particles necessary for far-red and NIR emission. Furthermore, it has been noted that the stability of the ODPA-stabilized CdTe QDs in air is relatively poor compared to the fatty-acid-coated QDs. In this recent study, oleic acid was used as a stabilizer instead of octadecylphosphonic acid to provide greater stability. Also, upon adding a third element (Se) to the CdTe precursor solution and changing the reaction temperature, the photoluminescence of CdTe can be tuned from red to near-IR. The quantum efficiency of CdTe QDs was greatly improved by adding sulfur instead of selenium to the precursor solution because of better surface passivation of the CdS outer shell, which is grown during the flow synthesis over the initially formed CdTe core.

2.3 References

- [1] Wang, C.C.; Ying, J.Y. *Chem. Mater.* **1999**, *11*, 3113.
- [2] Mayo, M.J.; Ciftcioglu, M. *Mater. Res. Soc. Symp. Proc.* **1991**, *206*, 545.
- [3] Ocana, M.; Garcia_Ramos, J.V.; Serna, C.J. *J. Am. Ceram. Soc.* **1992**, *75*, 2010.
- [4] Ardizzone, S.; Bianchi, C.L.; Galassi, C. *J. Electroanal. Chem.* **2000**, *490*, 48.
- [5] Melada, S.; Signoretto, M.; Ardizzone, S.; Bianchi, C.L. *Catal. Lett.* **2001**, *75*, 199.
- [6] Ardizzone, S.; Binaghi, L.; Cappelletti, G.; Fermo, P.; Gilardoni, S. *Phys. Chem. Chem. Phys.* **2002**, *4*, 5683.
- [7] Ricceri, R.; Ardizzone, S.; Baldi, G.; Matteazzi, P. *J. Europ. Ceram. Soc.* **2002**, *22*, 629.
- [8] Ardizzone, S. *Chim. Ind.* **1999**, *81*, 599.
- [9] Boiadjeva, T.; Cappelletti, G.; Ardizzone, S.; Rondinini, S.; Vertova, A. *Phys. Chem. Chem. Phys.*, **2003**, *5*, 1689.
- [10] Boiadjeva, T.; Cappelletti, G.; Ardizzone, S.; Rondinini, S.; Vertova, A. *Phys. Chem. Chem. Phys.*, **2004**, *6*, 3535.
- [11] Del Nero, G.; Cappelletti, G.; Ardizzone, S.; Fermo, P.; Gilardoni, S. *J. Europ. Ceram. Soc.* **2004**, *24(14)*, 30603.
- [12] Hench, L.L.; West, J.K. *Chem. Rev.* **1990**, *90*, 35.
- [13] Lev, O. *Anal. Chem.* **1995**, *67(1)*, 22.
- [14] Brinker, C.J.; Scherer, G.W. *Sol-Gel Science: The Physics and Chemistry of Sol-Gel Processing* Academic Press, Inc.: New York, **1990**.
- [15] Brinker, C.J.; Scherer, G.W. *J. Non-Crystalline Solids* **1985**, *70*, 301.
- [16] Keefer, K.D. *Silicon Based Polymer Science: A Comprehensive Resource*; American Chemical Society Washington, DC, **1990**, 227.
- [17] Prassas, M.; Hench, L.L. *Ultrastructure Processing of Ceramics, Glasses, and Composites* John Wiley & Sons New York, **1984**, 100.
- [18] JH Bang, KS Suslick. *Adv. Mater.* **2010**, *22*, 1039-59.
- [19] K. S. Suslick, *Ultrasound: Its Chemical, Physical, and Biological Effects*, Wiley-VCH, New York **1988**.
- [20] K. S. Suslick, *Science* **1990**, *247*, 1439.
- [21] K. S. Suslick, *Sci. Am.* **1989**, *260*, 80.

- [22] K. S. Suslick, S. J. Doktycz, in *Advances in Sonochemistry*, Vol. 1 (Ed.: T. J. Mason), JAI Press, New York **1990**, pp. 197.
- [23] H. Frenzel, H. Schultes, *Z. Phys. Chem.* **1934**, 27b, 421.
- [24] E. B. Flint, K. S. Suslick, *Science* **1991**, 253, 1397.
- [25] W. B. McNamara, III, Y. T. Didenko, K. S. Suslick, *Nature* **1999**, 401, 772.
- [26] Y. Didenko, W. B. McNamara, III, K. S. Suslick, *Nature* **2000**, 407, 877.
- [27] Y. T. Didenko, K. S. Suslick, *Nature* **2002**, 418, 394.
- [28] D. J. Flannigan, K. S. Suslick, *Nature* **2005**, 434, 52.
- [29] N. C. Eddingsaas, K. S. Suslick, *J. Am. Chem. Soc.* **2007**, 129, 3838.
- [30] D. J. Flannigan, S. D. Hopkins, C. G. Camara, S. J. Putterman, K. S. Suslick, *Phys. Rev. Lett.* **2006**, 96, 204301.
- [31] D. J. Flannigan, K. S. Suslick, *Phys. Rev. Lett.* **2005**, 95, 044301.
- [32] A. Weissler, *J. Am. Chem. Soc.* **1959**, 81, 1077.
- [33] A. Weissler, *Nature* **1962**, 193, 1070.
- [34] M. Anbar, I. Pecht, *J. Phys. Chem.* **1964**, 68, 352.
- [35] K. Makino, M. M. Mossoba, P. Riesz, *J. Am. Chem. Soc.* **1982**, 104, 3537.
- [36] K. S. Suslick, *MRS Bull.* **1995**, 20, 29.
- [37] K. S. Suslick, G. J. Price, *Annu. Rev. Mater. Sci.* **1999**, 29, 295.
- [38] A. Gedanken, *Ultrason. Sonochem.* **2004**, 11, 47.
- [39] K. S. Suslick, S. B. Choe, A. A. Cichowlas, M. W. Grinstaff, *Nature* **1991**, 353, 414.
- [40] M. W. Grinstaff, A. A. Cichowlas, S. B. Choe, K. S. Suslick, *Ultrasonics* **1992**, 30, 168.
- [41] K. S. Suslick, M. Fang, T. Hyeon, *J. Am. Chem. Soc.* **1996**, 118, 11960.
- [42] T. T. Kodas, M. Hampden-Smith, *Aerosol Processing of Materials*, Wiley-VCH, New York **1999**.
- [43] K. Okuyama, W. Lenggoro, *Chem. Eng. Sci.* **2003**, 58, 537.
- [44] G. L. Messing, S.-C. Zhang, G. V. Jayanthi, *J. Am. Ceram. Soc.* **1993**, 76, 2707.
- [45] R. W. Wood, A. L. Loomis, *Phil. Mag.* **1927**, 7, 417.
- [46] R. J. Lang, *J. Acoustical Soc.* **1962**, 34, 6.
- [47] I. W. Lenggoro, T. Hata, F. Iskandar, M. M. Lunden, O.K., *J. Mater. Res.* **2000**, 15, 733.

- [48] P. S. Patil, *Mater. Chem. Phys.* **1999**, *59*, 185.
- [49] W. H. Suh, K. S. Suslick, *J. Am. Chem. Soc.* **2005**, *127*, 12007.
- [50] M. E. Davis, *Nature* **2002**, *417*, 813.
- [51] G. J. d, A. Soler-Illia, C. Sanchez, B. Lebeau, J. Patarin, *Chem. Rev.* **2002**, *102*, 4093.
- [52] S. W. Boettcher, J. Fan, C.-K. Tsung, Q. Shi, G. D. Stucky, *Acc. Chem. Res.* **2007**, *40*, 784.
- [53] M. G. Kanatzidis, *Adv. Mater.* **2007**, *19*, 1165.
- [54] C. J. Brinker, Y. Lu, A. Sellinger, H. Fan, *Adv. Mater.* **1999**, *11*, 579.
- [55] Y. Lu, H. Fan, A. Stump, T. L. Ward, T. Rieker, C. J. Brinker, *Nature* **1999**, *398*, 223.
- [56] X. Ji, Q. Hu, J. E. Hampsey, X. Qiu, L. Gao, J. He, Y. Lu, *Chem. Mater.* **2006**, *18*, 2265.
- [57] H. Fan, F. Van Swol, Y. Lu, C. J. Brinker, *J. Non-Crystalline Solids* **2001**, *285*, 71.
- [58] Y. Lu, B. F. McCaughey, D. Wang, J. E. Hampsey, N. Doke, Z. Yang, C. J. Brinker, *Adv. Mater.* **2003**, *15*, 1733.
- [59] J. E. Hampsey, S. Arsenault, Q. Hu, Y. Lu, *Chem. Mater.* **2005**, *17*, 2475.
- [60] X. Ji, J. E. Hampsey, Q. Hu, J. He, Z. Yang, Y. Lu, *Chem. Mater.* **2003**, *15*, 3656.
- [61] J. H. Bang, S. H. Lim, E. Park, K. S. Suslick, *Langmuir* **2008**, *24*, 13168.
- [62] L. Li, C.-K. Tsung, T. Ming, Z. Sun, W. Ni, Q. Shi, G. D. Stucky, J. Wang, *Adv. Funct. Mater.* **2008**, *18*, 2956.
- [63] S. E. Skrabalak, K. S. Suslick, *J. Am. Chem. Soc.* **2005**, *127*, 9990.
- [64] J. H. Bang, R. J. Helmich, K. S. Suslick, *Adv. Mater.* **2008**, *20*, 2599.
- [65] W. H. Suh, A. R. Jang, Y.-H. Suh, K. S. Suslick, *Adv. Mater.* **2006**, *18*, 1832.
- [66] J. E. Hampsey, Q. Hu, L. Rice, J. Pang, Z. Wu, Y. Lu, *Chem. Commun.* **2005**, 3606.
- [67] Q. Hu, Y. Lu, G. P. Meisner, *J. Phys. Chem. C* **2008**, *112*, 1516
- [68] Y. C. Kang, S. B. Park, *J. Aerosol Sci.* **1995**, *26*, 1131.
- [69] I. W. Lenggoro, Y. Itoh, N. Iida, K. Okuyama, *Mater. Res. Bull.* **2003**, *38*, 1819.
- [70] W.-N. Wang, I. W. Lenggoro, Y. Terashi, Y.-C. Wang, K. Okuyama, *J. Mater. Res.* **2005**, *20*, 2873.
- [71] B. Xia, W. Lenggoro, K. Okuyama, *Adv. Mater.* **2001**, *13*, 1579.
- [72] I. W. Lenggoro, Y. Itoh, K. Okuyama, T. O. Kim, *J. Mater. Res.* **2004**, *19*, 3534.
- [73] B. Xia, I. W. Lenggoro, K. Okuyama, *J. Mater. Chem.* **2001**, *11*, 2925.

- [74] Y. Itoh, I. W. Lenggoro, K. Okuyama, L. *Mat. Res.* **2003**, 5, 191.
- [75] C. Panatarani, I. W. Lenggoro, K. Okuyama, *J. Nanopart. Res.* **2003**, 5, 47.
- [76] Y. Itoh, M. Abdullah, K. Okuyama, *J. Mater. Res.* **2004**, 19, 1077.
- [77] S. H. Kim, B. Y. H. Liu, M. R. Zachariah, *Chem. Mater.* **2002**, 14, 2889.
- [78] S. E. Skrabalak, K. S. Suslick, *J. Phys. Chem. C* **2007**, 111, 17807.
- [79] J. H. Bang, K. Han, S. E. Skrabalak, H. Kim, K. S. Suslick, *J. Phys. Chem. C* **2007**, 111, 10959.
- [80] C. B. Murray, C. R. Kagan, M. G. Bawendi, *Annu. Rev. Mater. Sci.* **2000**, 30, 545.
- [81] K. Okuyama, I. W. Lenggoro, N. Tagami, S. Tamaki, N. Tohge, *J. Mater. Sci.* **1997**, 32, 1229.
- [82] Y. T. Didenko, K. S. Suslick, *J. Am. Chem. Soc.* **2005**, 127, 12196.
- [83] J. H. Bang, W. H. Suh, K. S. Suslick, *Chem. Mater.* **2008**, 20, 4033.
- [84] S. H. Kim, B. Y. H. Liu, M. R. Zachariah, *Chem. Mater.* **2002**, 14, 2889.

Chapter 3

Applications of nanostructured TiO₂

2.4 Degradation of pollutants in air by photocatalysis assisted by TiO_2

2.4.1 *Photocatalytic Degradation of Toluene in the Gas Phase: Relationship between Surface Species and Catalyst Features*

S. Ardizzzone, C. L. Bianchi, G. Cappelletti, A. Naldoni, C. Pirola, *Environmental Science & Technology* **2008**, 42 (17), 6671-6676.

2.4.1.1 Introduction

Toluene is a common solvent, able to dissolve paints, paint thinners, many chemical reactants, rubber, printing ink, adhesives, lacquers, leather tanners, and disinfectants. Toluene is used as an octane booster in gasoline fuels for internal combustion engines: in the United States this use covers up to the 95% of the entire toluene industrial production. EPA (Environmental Protection Agency) reported that toluene was found in well water, surface water, or soil and its relative vapors are also present in air. Because of its usage in consumer products, toluene concentrations in indoor air may exceed those in outdoor air. When exposure to both indoor levels of toluene from consumer products and outdoor levels due to releases from vehicle exhaust or unburned gasoline vapors are taken into account, an average absorbed dose from inhalation exposure is estimated at about 300 $\mu\text{g}/\text{day}$. Heterogeneous photocatalysis, in the presence of semi-conductor oxides, is becoming one of the most promising fields in environmental remediation, especially in the case of organic pollutants in both water and air. TiO_2 is, up to now, one of the most attractive and efficient semiconductor materials for the photodegradation of pollutants as it provides photogenerated holes with high oxidizing power due to its wide band-gap energy, its stability toward photocorrosion, insolubility in water, low toxicity, and costs.¹⁻³ Many papers are present in the recent literature on the photodegradation of toluene by TiO_2 in the gas phase.⁴⁻¹⁶ Some of the different studied aspects can be mentioned: conditions of the reaction and the photodegradation mechanism,⁵ catalyst deactivation and regeneration,⁶ use of different kinds of UV sources,⁷ and combination of photocatalytic degradation with other oxidation processes.⁸ A significant proportion of literature results concerning toluenephotodegradationby TiO_2 are performed by adopting P25 or other commercial brands. Less reported are instead studies in which homemade TiO_2 samples are used. Keller et al.⁴ report the comparison between different synthesized samples and show that promotion by sulfates and the use of nanosized anatase TiO_2 strongly increase the toluene

removal efficiency. Inaba et al.,¹⁶ in the case of nanosized anatase prepared in reverse micelle systems, show that when the particles are submitted to heat treatments, the activity for toluene degradation is improved even though the surface area decreased. No results could be found in the literature concerning, instead, the role played by the particle features (phase composition, crystallite size, hydrophilicity, etc.) on the nature of intermediate products or on the possible reaction pathway. Palmisano and co-workers,^{10,11} in comparing the activity of two commercial TiO₂ samples, P25 and a pure anatase sample (Merck), with respect to the photocatalytic degradation of toluene in both gas and liquid phases, suggest the occurrence of different degradation pathways depending on the kind of photocatalyst. In the present case the photodegradation of toluene in the gas phase is performed by adopting as photocatalysts both commercial and homemade TiO₂ samples.^{17,18} Pure anatase samples with small (9 nm) and large crystallites (86 nm) and anatase/brookite composites with varying degree of hydrophilicity are employed together with the well-known P25 by Degussa. The degradation is performed at room temperature, with both UV and solar irradiation, with a high concentration of toluene (1000ppm) to verify the photoactive material efficiency in extreme conditions of pollutant concentration (accidental pourings). On the grounds of HPLC studies of surface species washed from the deactivated catalysts and of Fourier transform infrared attenuated total reflectance (FTIR-ATR) spectroscopic results obtained on selected samples, possible reaction pathways as a function of the catalysts features are proposed.

2.4.1.2 Experimental Section

Sample Preparation. All the chemicals were of reagent-grade purity and were used without further purification; doubly distilled water passed through a Milli-Q apparatus was used to prepare solutions and suspensions. Titania samples, except for the well-known P25 Degussa commercial sample (anatase-rutile composite), were named as follows: the letters indicate the polymorphs and the ensuing value the surface area of the samples. Synthesis of the anatase-brookite mixed powders (AB_200, AB_145) was reported previously by us.^{2,17} The sol-gel precursor obtained by the hydrolysis of a solution of Ti(OC₃H₇)₄ and 2-propanol (water/alkoxide molar ratio = 49 and water/propanol molar ratio = 15) was dried as a xerogel. One fraction of the xerogel was submitted to a hydrothermal treatment in water for 500h (spontaneous pH, T=60 °C) (AB_200), and a second fraction was submitted to thermal treatment at 300 °C for 5 h in O₂ stream (AB_145). The samples prepared in the laboratory are compared with pure-phase commercial samples A_287 and A_9 (Alfa Aesar).

Sample Characterization. Room-temperature X-ray powder diffraction (XRPD) patterns were collected between 10° and 80° (2θ range, $\Delta 2\theta = 0.02^\circ$) with a Siemens D500 diffractometer using $Cu\ K\alpha$ radiation. Rietveld refinement has been performed with the GSAS software suite and its graphical interface EXPGUI.¹⁹ The average diameter of the crystallites, d , was estimated from the most intense reflection (101) of the TiO_2 anatase phase by use of the Scherrer equation.² Specific surface areas were determined by the classical Brunauer-Emmett-Teller (BET) procedure with a Coulter SA 3100 apparatus. Diffuse reflectance spectra of the powders were measured on a UV-vis scanning spectrophotometer (Perkin-Elmer, Lambda 35), which was equipped with a diffuse reflectance accessory. A TiO_2 thin film was placed in the sample holder on integrated sphere for the reflectance measurements. A “total white” Perkin-Elmer reference material was used as the reference.²⁰ X-ray photoelectron spectra were taken in an M-probe apparatus (Surface Science Instruments). The source was monochromatic $Al\ K\alpha$ radiation (1486.6 eV). The binding energies (BE) were corrected for specimen charging by referencing the C $1s$ peak to 284.6 eV, and the background was subtracted by Shirley’s method, as reported previously.¹⁸ The chemical structure of the organic compounds remaining on the TiO_2 surface was analyzed by using Fourier transform infrared spectroscopy [FTIR; Jasco 4200, accessorized by attenuated total reflectance (ATR) module].

Photocatalytic Experiments. Photocatalytic degradations of toluene were conducted in a Pyrex glass cylindrical reactor with diameter of 200 mm and effective volume of 5 L. The amount of catalyst (in the form of powder deposited from 2-propanol slurry on flat glass disk) used in the tests was 0.5 g. However, previous studies demonstrated that only the exposed/external fraction of the catalyst works in the photocatalytic degradation of the pollutant.² The gaseous mixture in the reactor was obtained by mixing hot chromatographic air, humidified at 37%, and a fixed amount of volatilized (250 °C) toluene, in order to avoid condensation. The actual concentration of toluene in the reactor is determined directly by micro-GC sampling. The initial concentration of toluene in the reactor was 1000 ppm. Photon sources were provided by a 500 W iron halogenide lamp (Jelosil, model HG 500) emitting in the 315-400 nm wavelength range (UV-A) and by a 300 W solar lamp (Radium Sanolux HRC 300-280) emitting in the 380-600 nm wavelength range. Toluene and its intermediate oxidation products were analyzed on the eluate solution obtained by washing the catalyst with Milli-Q water, by means of HPLC (Agilent, Model HP1100; column: ACE 5C18, 150×4 mm, 60/40 methanol/ H_2O , toluene peak at 10.3 min). Toluene adsorption onto the TiO_2 layer was determined through dark experiments: no appreciable amount was

detected. The accuracy of the analytical determination of CO₂ by gas chromatography was not such as to provide reliable data concerning CO₂ levels at the end of the reaction time.

2.4.1.3 Results and Discussion

Choice of Reaction Conditions and Catalyst Regeneration.

The present project presents some significantly different aspects with respect to the major part of literature data. The first aspect concerns the light source. Two different irradiation devices were adopted: a classical UV 500 W lamp (315-400 nm) and a lamp simulating solar emission (360-600 nm). This aspect is considered to be relevant in relation to the possible use of photocatalytic TiO₂ in open-air paints, cements, and asphalts. A second aspect regards the toluene level in the reacting chamber. The major part of literature results pertain to several hundred parts per billion (ppb) levels or to a few parts per million (ppm).^{6,7,10,11} In this work, significantly higher toluene levels (1000 ppm) were adopted in order to bring to light catalyst deactivation processes on a short timescale, to precisely identify the nature of the reaction intermediates and also to evaluate the possible feasibility of a photocatalytic degradation process even in severe pollution conditions. The preliminary part of the work, dedicated to the choice of reaction conditions, was performed by adopting as the photocatalyst the commercial P25 TiO₂ Degussa. Figure 1 reports the trend of percent degradation of toluene for the two different irradiation sources and for dry and humid conditions.

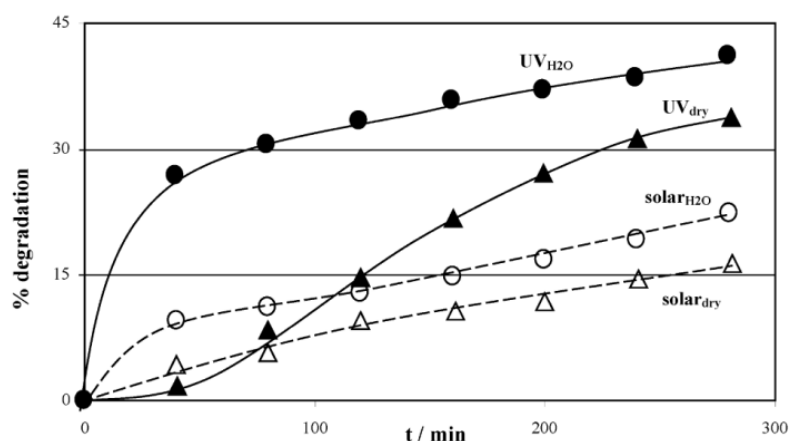


Figure 1. UV and solar P25-assisted photodegradation of toluene in humid and dry conditions. $[C_7H_8]^0 = 1000 \text{ ppm}$, $T = (30 \pm 3)^\circ\text{C}$, 0.5 g of TiO_2 .

The figure shows that irradiation by the UV lamp leads to a conversion about twice that by the solar lamp, for both dry and humid conditions. This observation is in

agreement with results by Keller et al.,⁴ who observed very low toluene removal efficiency by TiO₂ upon visible light irradiation. It is immediately evident that reactions performed in dry conditions are much slower and that, in the case of UV irradiation, the degradation curve shows a sort of initial induction time for the reaction to start. The central role played by humidity in the photodegradation of toluene observed in the present case is in agreement with the great part of literature results. Ibusuki and Takeuchi²¹ found that the presence of water vapor was beneficial in order to achieve the almost complete mineralization of toluene by TiO₂ at room temperature. Also, Marci` et al.¹¹ show that the absence of water greatly affects the performance of the given TiO₂ catalyst as it continuously deactivates. Furthermore, Einaga et al.⁹ show that an exhaust photocatalyst is significantly regenerated by simply irradiating it in humidified air. In the present case, XPS analyses of the C 1s region, obtained on exhaust catalysts at the end of the reaction time, show different C/Ti ratios: dry sample 1.7, wet sample 1.2. These values show that the amount of carbon-containing species (including toluene) is larger in the absence of humidity. Furthermore, in the case of the wet sample it is interesting to observe (Figure 2) the different shape of C 1s region: four peaks, including a new species at higher binding energy (D component) are present, indicating the formation of a larger amount of oxidized carbon-containing species as the result of a faster course of the reaction.

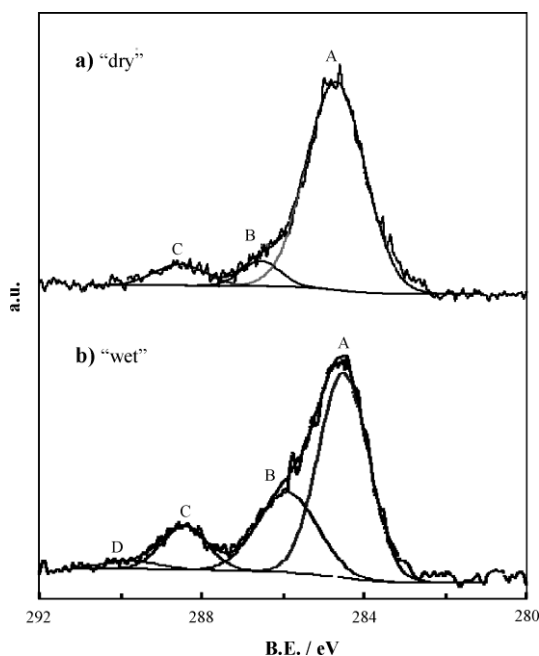


Figure 2. XPS spectra: C1s region for (a) dry and (b) wet exhaust P25. For the different components, see ref 18.

A very important aspect, in the study of toluene degradation, concerns catalyst deactivation and possible regeneration. The use, in a second run, of the exhaust catalyst leads to a lower percent degradation with respect to the fresh catalyst (24.6 vs 41.2). The deactivation of photocatalysts in toluene degradation has been reported by several authors.^{6,7,10,11} In the present case, deactivation is also surely justified by the high toluene levels adopted in the experiments. Different regenerating treatments are reported in the literature to restore the activity of TiO₂.^{6,7,10,11} In the present case only washings by water were employed, in order to simulate the effect of rain on outdoor paints, concrete, or asphalts. A relevant improvement, with respect to the exhaust catalyst, is produced on the activity by simple water treatment (24.6 to 34.2).

Role of Photocatalyst Features.

The features of the present TiO₂ samples, both commercial and homemade, are reported in Table 1. Two high-purity, commercial anatase samples, A_287 and A_9, are analyzed, showing largely different specific surface areas (fifth column) and crystallite sizes (sixth column). The anatase-brookite composites (AB_200 and AB_145) are obtained in the laboratory by a single sol-gel reaction and, subsequently, submitted either to a prolonged hydrothermal treatment (AB_200) or to a mild thermal treatment at 300 °C (AB_145).

The phase enrichment obtained by elaborating the diffractograms by the Rietveld method is very similar for the two samples (Table 1). Comparable crystallite sizes of 6 and 8 nm and large surface areas are obtained. The table also includes data concerning the commercial P25, very often used in literature as a reference sample. The surface state of the TiO₂ particles was analyzed by XPS. No significant differences could be appreciated in the Ti 2*p* region among all the present samples concerning the binding energies (BE) and the full width at half-maximum (FWHM) values. The peak Ti 2*p*^{3/2} was regular and the BE (458.3 eV) compared well with data for Ti(IV) in TiO₂.¹⁸ Analysis of the oxygen peaks showed, as often reported in the case of oxides, the presence of more than one component, which could be attributed respectively to lattice oxygen in TiO₂ (529.9 eV), and to surface OH species (531.9 eV).² The eighth column of Table 1 reports the OH/O_{tot} surface ratio obtained by elaborating the XPS oxygen peak for all the present samples to get indications concerning the hydrophilicity/hydrophobicity of the TiO₂ surfaces. The values can be significantly different from one another and range from 0.28 for the sample hydrothermally grown (AB_200) to 0.12 for the large crystallite anatase (A_9). In order to obtain some information concerning the light absorption features of the various samples, experimental data of diffuse reflectance were elaborated to absorption coefficient values $F(R)$ according to the Kubelka-Munk equation.²⁰ The

corresponding band-gap values obtained by this procedure for all samples are reported in Table 1 (ninth column).

TABLE 1. Quantitative Phase Composition, BET Surface Area, Crystallite Anatase and Rutile Diameter, OH/O_{tot}, and Band Gap

sample ^a	% A ^b	% B ^b	% R ^b	S _{BET} , m ² g ⁻¹	d _A ¹⁰¹ , ^c nm	d _R ¹¹⁰ , ^c nm	OH/O _{tot} ^d	band gap, ^e eV
A_287 (C)	100			287	9 ± 1		0.24	3.35
A_9 (C)	100			9	86 ± 18		0.12	3.20
AB_200 (H)	65	35		200	6 ± 1		0.28	3.24
AB_145 (H)	68	32		145	8 ± 1		0.21	3.13
P25 (C)	80		20	50	25 ± 5	35 ± 8	0.14	3.28

^a C = commercial sample; H = homemade sample. ^b A = anatase, B = brookite, R = rutile. ^c Determined by XRD (Scherrer equation). ^d Determined by XPS analysis. ^e Determined by the Kubelka–Munk equation from diffuse reflectance spectra.

The obtained band-gap values do not show large differences among the various samples and fall in the range expected for TiO₂ photocatalysts; only sample AB_145 shows a band-gap value (3.13 eV) slightly smaller than the other values. For all the present TiO₂ photocatalysts, the reaction of toluene degradation was performed in humid conditions (37%). The reaction kinetics can be described for all samples, with the exception of P25, by a pseudo-first-order rate equation. The rate constant (κ) values for the different catalysts, evaluated by linear fitting of the logarithmic plot, are listed in Table 2. The rate constants show different values among the various photocatalysts and appreciably drop in passing from UV to solar irradiation, except for AB_145, which shows only a slight decrease. Just in the case of solar irradiation, the initial sigmoidal shape of the degradation curve of A_287 does not allow the rate constant to be obtained. In the case of P25, instead, elaboration by a pseudo-first-order rate equation did not yield significant results for both UV and solar irradiation.

Figure 3 shows the direct comparison among the data pertaining respectively to AB_145 and P25. In the case of this latter sample, apparently, a fast initial conversion is soon followed by an early deactivation with respect to the other samples. The comparison among the degradation, at 280 min reaction time, produced by the present samples is reported in Table 2. It can be immediately observed that the sequence in final degradation follows the same order of the rate constants reported in the same table. In general it can be observed that the widely used commercial P25 is not the best catalyst and that the most efficient samples are the anatase-brookite composites. Samples with small crystallite sizes and large surface area are more active than samples with large crystallite sizes, for the same TiO₂ polymorph; see, for example, the comparison between A_287 and A_9 for pure anatase.

The sample surface area is not, however, the only relevant parameter in imposing the performance. The commercial pure anatase, A_287, presenting the largest

surface area is not the sample showing the best performance. This result is interesting since anatase is generally considered the more active polymorph of TiO₂. Also, in the case of the anatase-brookite composites, AB_200 and AB_145, the sample surface area is not the main factor imposing the performance: under solar irradiation, AB_145 shows a degradation efficiency more than twice that of AB_200 (Table 2, fifth column), probably to be traced back to the smaller value of band gap (Table 1, ninth column).

TABLE 2. Photocatalytic Percent Degradation and Pseudo-First-Order Kinetic Constants^a

sample	UV			solar		
	% deg	$k \times 10^3 \text{ (min}^{-1}\text{)}$	R^2	% deg	$k \times 10^3 \text{ (min}^{-1}\text{)}$	R^2
A_287	41.6	1.87 ± 0.06	0.988	33.5	nd	
A_9	27.0	1.16 ± 0.03	0.983	10.0	0.31 ± 0.05	0.977
AB_200	50.2	2.58 ± 0.09	0.990	17.3	0.62 ± 0.03	0.986
AB_145	52.4	2.87 ± 0.03	0.996	40.2	1.86 ± 0.04	0.990
P25	41.2	nd		22.1	nd	

^a Values are given together with relative standard deviation and regression coefficient for all samples. nd = not determined.

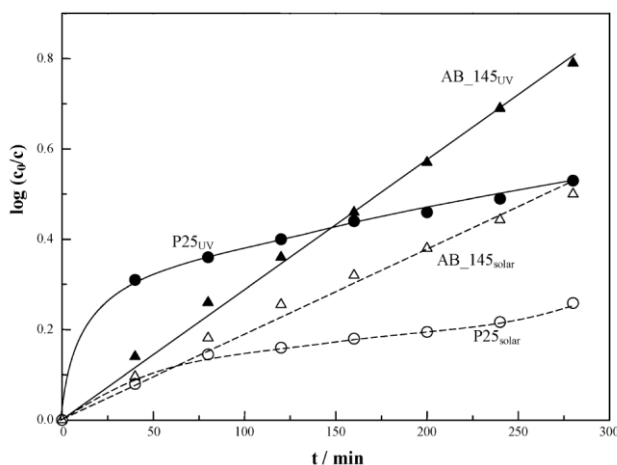


Figure 3. Logarithmic conversion plot as a function of the reaction time for P25 and AB_145 samples.

It is our opinion that the best efficiency of AB_145 with respect to AB_200 is related also to the hydrophilic/hydrophobic character of the surface. The OH/O_{tot} ratio, as obtained by elaboration of the O 1s XPS peak (Table 1, eighth column), is generally considered to be a measure of the hydrophilicity/hydrophobicity of an oxide.¹ In the present case, the two samples prepared by sol-gel and submitted to thermal/hydrothermal treatments (AB_145 and AB_200) show OH/O_{tot} values differing by 25%. Efficient adsorption of the pollutant molecule at the semiconductor surface may promote the photocatalytic reaction. The adsorption of toluene on oxide surfaces has been shown to be a key factor determining the subsequent photocatalytic efficiency. In the present case it can be suggested that a

less hydrophilic surface, that is, the one showing a lower OH/O_{tot} ratio (AB_145), can adsorb toluene more easily and give rise of different reaction intermediates, than a more hydroxylated surface.

TABLE 3. HPLC Intermediates Detected for All Investigated Samples^a

sample	intermediates (UV lamp)				
	BZAc	BZOH	BZH	HQ	p-Cr
A_287	++			t	
A_9	++		t	t	
AB_200	++	t	t	+	t
AB_145	++	+	+++	++	t
P25	+++	++	+	+	t

^a BZAc, benzoic acid; BZOH, benzyl alcohol; BZH, benzaldehyde; HQ, hydroquinone; p-Cr, *p*-cresol. (+++, most abundant; ++, abundant; +, appreciable; t, traces).

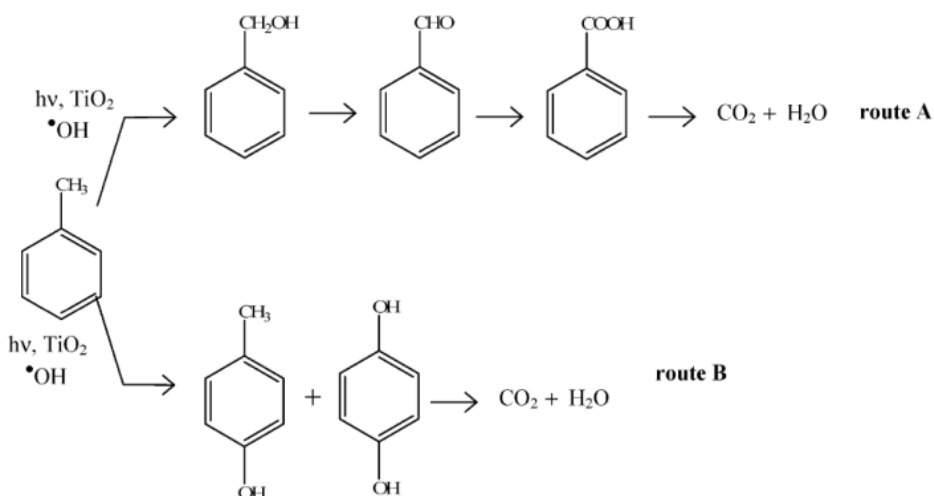


Figure 4. Possible TiO₂-assisted toluene degradation schemes.

These considerations are in agreement with results by Inaba et al.,¹⁶ who observed that the calcined samples were more active than the hydrothermally aged samples, although showing lower surface area. There is a further aspect, related to the sample phase composition that should be considered. The top performance presented by the two composite anatase-brookite samples (AB_200 and AB_145) with respect to all the other samples can be attributed to an increase in charge separation efficiency due to interfacial electron transfer via the junction between anatase and brookite nanocrystals, by analogy with what was directly shown in

anatase-rutile systems by electron paramagnetic resonance (EPR) spectroscopy, as mentioned in *ref 2*. This effect, apparently, becomes more relevant under less efficient and powerful irradiation conditions.

Table 3 reports the data obtained by HPLC concerning the eluate products obtained by washing the catalyst with water at the end of the reaction performed under UV irradiation. Due to the very high toluene initial level (1000 ppm), degradation is not complete at the end of the reaction time; consequently, reaction intermediates are still present at the surface of the catalysts. Since washing by water may produce only partial removal of the adsorbed species, only qualitative evaluations are present in the table.

It can be immediately observed that the intermediates are largely different for the various catalysts, indicating different degradation pathways and also different adsorption behavior of the oxides. For example, in the case of the nanocrystalline pure anatase sample (A_287), only the presence of benzoic acid can be appreciated, while the mixed-phase commercial P25 and AB_145 give rise to all the observed intermediate products

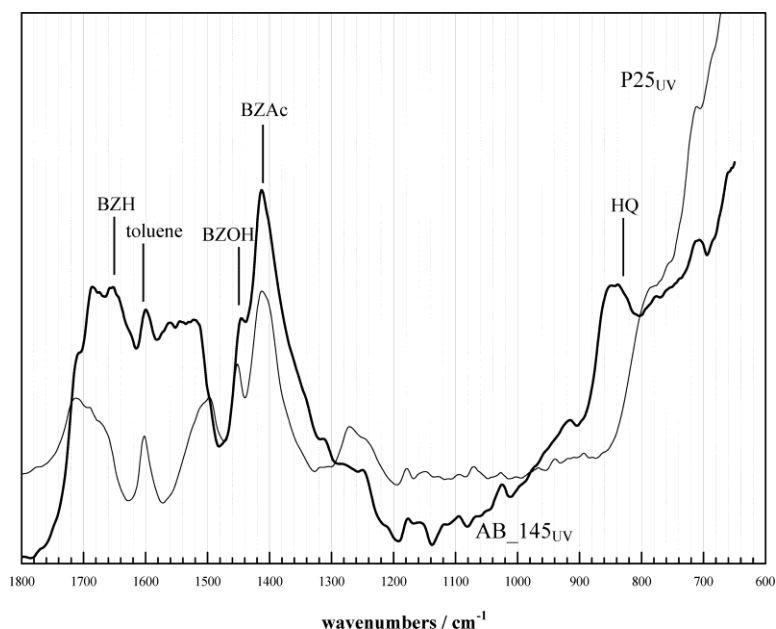


Figure 5. IR spectra of (---) P25 and (----) AB_145 sampled at the end of the photocatalytic run. For each oxide, the curve of the relative pure TiO_2 was subtracted. Only the major (or most appreciable) bands of the adsorbed species are shown.

The reaction profile for the toluene degradation may proceed through the main mechanisms, sketched in Figure 4. The role played by humidity and the presence of benzoic acid and of hydroquinone (and in some cases of traces of cresols), as reaction intermediates (Table 3), indicate that the more frequent mechanisms of

degradation are either the direct attack of $\text{OH}\cdot$ to CH_3 (route A) or/and the attack of $\text{OH}\cdot$ to the para position of the aromatic ring (route B) or [less frequently, see Palmisano and co-workers¹¹] to the meta and ortho positions. On the grounds of data in Table 3, it could be suggested that in the case of pure anatase samples (A_287 and A_9) the main reaction path is through route A, while the attack to other positions of the ring does not occur significantly. Sample AB_145, instead, shows the presence of all intermediates, indicating on one hand that both route A and B occur simultaneously and on the other hand that no intermediate is so strongly adsorbed as to deactivate all the surface sites. Possibly this is one of the reasons why this sample is so efficient. These hypotheses are supported by the comparison between FTIR-ATR spectra of AB_145 and of P25 withdrawn at the end of the toluene degradation reaction (Figure 5). For each catalyst the “blank” curve pertaining to the pure oxide was subtracted. In the figure only a few of the most intense bands are shown for the sake of clarity.^{14,15,22} Although the two spectra show the presence of several common bands (toluene, benzoic acid, and benzyl alcohol), significant differences are appreciable in the pattern of the two curves. The shoulder at about 840 cm^{-1} , for example, is appreciable only in the case of AB_145 (hydroquinone?); the same can be said of the bands in the two regions $1520\text{--}1580\text{ cm}^{-1}$ (benzoic acid, cresols?) and $1640\text{--}1690\text{ cm}^{-1}$ (benzaldehyde?). Straightforward attribution of these bands to definite species is not possible, but it is clear that the surface species and their relative abundance are very largely different in the case of the two photocatalysts. Several different components concur to build up the efficiency of a given photocatalyst with respect to a specific degradation reaction. Small crystallite sizes and large surface areas are promoting factors; the contemporary presence of different polymorphs, grown on the same particle, seems to introduce a positive component. The hydrophilic/hydrophobic character of the surface plays a key role with respect to the adsorption of toluene and of its intermediate products. The degradation route appears to be imposed by the photocatalyst features. Pure anatase samples appear to follow a simple degradation route starting with the attack of the $\text{OH}\cdot$ radical to the methyl group of toluene. Mixed-phase samples, anatase-rutile and anatase-brookite, instead follow a more complex pathway, implying both the attack of the $\text{OH}\cdot$ radical on the methyl group and also the attack of the $\text{OH}\cdot$ on other positions of the aromatic ring.

2.4.1.4 Literature Cited

- (1) Wu, L.; Yu, J. C.; Wang, X.; Zhang, L.; Yu, J. J. *Solid State Chem.* 2005, 178, 321–328.

- (2) Ardizzone, S.; Bianchi, C. L.; Cappelletti, G.; Gialanella, S.; Pirola, C.; Ragaini, V. J. *Phys. Chem. C* 2007, 111, 13222–13231.
- (3) Lin, H.; Huang, C. P.; Li, W.; Ni, C.; Ismat Shah, S.; Tseng, Y.-H. *Appl. Catal., B* 2006, 68, 1–11.
- (4) Keller, N.; Barraud, E.; Bosc, F.; Edwards, D.; Keller, V. *Appl. Catal., B* 2007, 70, 423–430.
- (5) Sekiguchi, K.; Yamamoto, K.; Sakamoto, K. *Catal. Commun.* 2008, 9, 281–285.
- (6) Ao, C. H.; Lee, S. C.; Mak, C. L.; Chan, L. Y. *Appl. Catal., B* 2003, 42, 119–129.
- (7) Jeong, J.; Sekiguchi, K.; Sakamoto, K. *Chemosphere* 2004, 57, 663–671.
- (8) Kuo-Pin, Y.; Lee, G. W. M. *Appl. Catal., B* 2007, 75, 29–38.
- (9) Einaga, H.; Futamura, S.; Ibusuki, T. *Appl. Catal., B* 2002, 38, 215–225.
- (10) Addamo, M.; Augugliaro, V.; Coluccia, S.; Di Paola, A.; Garcia- Lopez, E.; Loddo, V.; Marci`, G.; Martra, G.; Palmisano, L. *Int. J. Photoenergy* 2006, 39182, 1–12.
- (11) Marci`, G.; Addamo, M.; Augugliaro, V.; Cosuccia, S.; Garcia-Lopez, E.; Loddo, V.; Martra, G.; Palmisano, L.; Schiavello, M. *J. Photochem. Photobiol., A* 2003, 160, 105–114.
- (12) Zuo, G.-M.; Cheng, Z.-X.; Chen, H.; Li, G.-W.; Miao, T. *J. Hazard. Mater.* 2006, B128, 158–163.
- (13) Irokawa, Y.; Morikawa, T.; Aoki, K.; Kosaka, S.; Ohwaki, T.; Taga, Y. *Phys. Chem. Chem. Phys.* 2006, 8 (9), 1116–1121.
- (14) Blount, M. C.; Falconer, J. L. *J. Catal.* 2001, 200, 21–33.
- (15) Mendez-Roman, R.; Cardona-Martinez, N. *Catal. Today* 1998, 40, 353–365.
- (16) Inaba, R.; Fukahori, T.; Hamamoto, M.; Ohno, T. *J. Mol. Catal. A: Chem.* 2006, 260, 247–254.
- (17) Boiadjieva, T.; Cappelletti, G.; Ardizzone, S.; Rondinini, S.; Vertova, A. *Phys. Chem. Chem. Phys.* 2004, 6, 3535–3539.
- (18) Cappelletti, G.; Bianchi, C. L.; Ardizzone, S. *Appl. Surf. Sci.* 2006, 253, 519–524.
- (19) Larson, A. C.; Von Dreele, R. B. Los Alamos National Laboratory, Los Alamos, NM, 1994.
- (20) Cappelletti, G.; Bianchi, C. L.; Ardizzone, S. *Appl. Catal., B* 2008, 78, 193–201.
- (21) Ibusuki, T.; Takeuchi, K. *Atmos. Environ.* 1986, 20, 1711–1715.
- (22) <http://webbook.nist.gov/chemistry/vib-ser.html>.

2.4.2 *N-doped TiO₂ from TiCl₃ for photodegradation of air pollutants*

C. L. Bianchi, G. Cappelletti, S. Ardizzone, S. Gialanella, A. Naldoni, C. Oliva, C. Pirola, *Catalysis Today* **2009**, *144*, 31–3.

2.4.2.1 *Introduction*

Photocatalysis is raising much attention owing to its potential applications in environmental remediation, the photo-electrochemical splitting of water and the conversion of solar energy to electric power. TiO₂ is the most frequently employed photocatalyst owing to its cheapness, non-toxicity, and structural stability.^{1,2} To date, a great number of attempts have been made to promote the practical photocatalytic applications of TiO₂ by extending the spectral response from the UV area to the visible region and enhancing quantum efficiency. The doping of TiO₂ with non-metal ions has raised recently an enormous interest especially in the case of nitrogen-doped samples.³⁻¹³ The biggest advantage of N-doped TiO₂ samples, compared to pure TiO₂, is their lower excitation energy, which not only allows the absorbance of the UV portion of solar light, but also of the visible portion, which covers >50% of the solar energy. Several points are still open to debate in the understanding of N-doped samples behaviour. One of the main debated questions concerns the electronic structure of these systems, i.e. whether the enhanced visible-light absorbance is due to a narrowed band gap or mainly to the introduction of localized impurity states in the band gap. Further questions regard the actual localization of N species in the TiO₂ lattice either interstitial or substitutional and their interactions with oxygen vacancies.³⁻¹³ Different methods are presented in the literature to incorporate nitrogen in titanium dioxide, and different sources of N are adopted (NH₃/NH₄⁺, amines, nitrides, etc.).⁷⁻¹⁴ The different synthetic procedures may lead to materials showing even significantly different properties. In this work TiO₂ samples were prepared through a composite route starting from strongly acid TiCl₃ aqueous solutions. N species are loaded by NH₃ in the liquid phase. A final calcination step at mild temperatures promotes the crystallization of the amorphous precursors. The synthetic reaction implies an accurate control of the suspension pH during the formation of the TiO₂ precursors. The structure, morphology and chemical composition of the nitrogen-doped sub-surface region are investigated by X-ray diffraction, TEM and XPS. Moreover, EPR spectra are obtained to characterize paramagnetic centres. The doping effect on the photoactivity is measured in the case of the photodegradation of toluene; the nature of the surface species adsorbed onto exhaust catalysts is investigated by FTIR-ATR in order to evaluate the progress of the oxidation reaction.

2.4.2.2 Experimental

Sample preparation. All the chemicals were of reagent grade purity and were used without further purification; doubly distilled water passed through a Milli-Q apparatus was used to prepare solutions and suspensions. N-doped samples were obtained starting from a TiCl_3 salt solution (12% in hydrochloric acid) by successive addition of ammonia solutions at different concentrations (2, 4 and 6 M) in order to achieve pH 4 (TN4), 7 (TN7) and 9 (TN9), and with a starting N/Ti molar ratio of 6.6, 7.6 and 9.2, respectively. The mixture was kept stirred under O_2 stream (10 nL/h) till the disappearance of the blue colour of the slurry (about 5 h) due to the oxidation of $\text{Ti}(\text{OH})_3$. The wet precursors were dried in oven at 80 °C overnight and subsequently calcined at 300 °C for 6 h. Then the calcined powders were washed with a solution of ethanol/water (80:20) to eliminate the salt, reaching conductivity values in the washing solutions of about 1 mS. The un-doped reference sample (T9) was obtained by the same procedure at pH 9, using KOH instead of ammonia. Homemade powders were compared with different commercial samples: A_287 (Alfa Aesar), PC105 (Millennium Inorganic Chemicals), P25 (Degussa) and NanoActive (NanoScale Corporation).

Sample characterization. Room-temperature X-ray powder diffraction (XRPD) patterns were collected between 20° and 90° with a Siemens D500 diffractometer, using Cu $\text{K}\alpha$ radiation. For all studied samples, powder patterns were collected with a counting time of 20 s for each a 0.088 step. Rietveld refinement has been performed using the GSAS software suite and its graphical interface EXPGUI.¹⁵ The average diameter of the crystallites, d , was estimated from the most intense reflection (101) of the TiO_2 anatase phase using the Scherrer equation.¹⁶ Specific surface areas were determined by the classical BET procedure using a Coulter SA 3100 apparatus. Diffuse reflectance spectra of the powders were measured on UV–vis scanning spectrophotometer (PerkinElmer, Lambda 35), which was equipped with a diffuse reflectance accessory, as reported previously.² X-ray photoelectron spectra were taken in an M-probe apparatus (Surface Science Instruments). The source was monochromatic Al $\text{K}\alpha$ radiation (1486.6 eV) as in reference.¹⁷ EPR spectra have been collected at room temperature by means of a Bruker Elexsys spectrometer at the working frequency of ca. 9.4 GHz. The spectral simulations were obtained by the Bruker SimFonia programme. Transmission electron microscopy (TEM) observations were conducted at 120 keV using an analytical microscope equipped with an energy dispersive X-ray spectrometer (EDXS). The powder samples were ultrasonically suspended in alcohol and then spread onto a copper grid covered with an amorphous carbon film.

Photocatalytic experiments. Photocatalytic degradations of toluene were conducted in a Pyrex glass cylindrical reactor with diameter of 200 mm and effective volume of 5 L, as already described.¹⁸ The gaseous mixture in the reactor was obtained by mixing hot chromatographic air, humidified at 60%, and the fixed amount of volatilized (250 °C) toluene, in order to avoid condensation. The initial concentration of toluene in the reactor was 500 ppm. Photon source was provided by a 300 W solar lamp (Radium Sanolux HRC 300-280) emitting in the 380–600 nm wavelength range (radiation intensity of $I = 1.2 \times 10^{-5} \text{ Einstein dm}^{-3} \text{ s}^{-1}$).

2.4.2.3 Results and discussion

Structural and morphological characterization

Fig. 1 reports the X-ray diffractograms of the three, nitrogen doped, samples prepared starting from TiCl_3 , at different pH values. By analyzing the features of the diffractograms, it can be immediately observed that pH plays a key role in imposing the sample phase composition, in terms of relative enrichment in the three TiO_2 polymorphs. The phase composition of the various samples, obtained by the Rietveld method, is reported in Table 1. At pH 4 rutile is the prevailing phase, although also anatase and brookite are present as minor components. In the presence of chlorides and at acid pH the formation of nanocrystalline rutile is reported to be promoted.² At neutral pH, anatase is the main component in the presence of traces of rutile, while only at pH 9 the pure anatase phase can be obtained. In the case of the sample obtained at pH 9 in the absence of N species (T9), the pattern of the diffractogram (not reported for reasons of space) shows that the sample, although calcined at the same temperature of the samples containing N species, is still amorphous. Due to the presence of the large amount of KCl coprecipitated with the oxide the specific surface area and pore volume appear to be very low (Table 1, columns 7,8). Apparently the presence of N species promotes crystallization in otherwise identical conditions. The anatase unit cell parameters obtained by the Rietveld refinement are reported in Fig.1 for each sample.

Table 1. Quantitative phase composition (*A* = anatase, *B* = brookite, *R* = rutile), crystallite anatase and rutile diameter by XRD (Scherrer equation), BET surface area; total pore volume, N/Ti by XPS analysis.

Sample	%A	%B	%R	d_A^{101} (nm)	d_R^{110} (nm)	S_{BET} ($\text{m}^2 \text{ g}^{-1}$)	V_{pore} (ml g^{-1})	N/Ti
T9	–	–	–	–	–	2	0.014	–
TN4	14	11	75	–	11 ± 2	103	0.355	0.016
TN7	97	–	3	9 ± 1	–	97	0.356	0.037
TN9	100	–	–	11 ± 2	–	102	0.439	0.028
NanoActive	–	–	–	–	–	>500	>0.400	–
A_287	100	–	–	9 ± 1	–	287	0.442	–
PC105	100	–	–	20 ± 4	–	73	0.384	–
P25	80	–	20	25 ± 5	35 ± 8	50	0.256	–

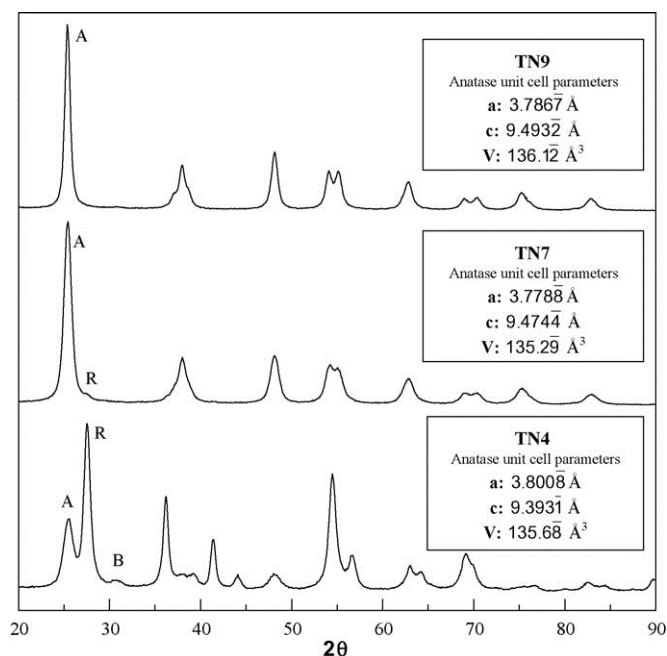


Figure 1. Powder X-ray diffraction lines and relative anatase cell parameters of TN4, TN7 and TN9 samples (A = anatase, B = brookite and R = rutile). Theoretical anatase unit cell parameters: a , $b = 3.7845$ Å, $c = 9.5143$ Å and $V = 136.27$ Å³.

Parameters pertaining to the sample obtained at pH 9 match closely the theoretical values while in the case of the sample obtained at pH 7 an appreciable shrinking of the unit cell volume is observed. Di Valentin et al.,¹⁶ on the grounds of DFT calculations, report slightly longer Ti–N bond lengths (1.964 and 2.081 Å) with respect to Ti–O ones (1.942 and 2.002 Å). Experimental data on the effects of N-doping on unit cell parameters of anatase are very scanty in the literature. The only pertinent result is that by Song et al.¹⁹ reporting “slightly smaller” lattice parameters of N-doped samples with respect to pure TiO₂. The present lattice parameters of TN7 might suggest, also on the grounds of XPS data presented in the following, a location, at least in part, substitutional for N species in the TiO₂ lattice in the case of this sample. The minority presence of anatase in sample TN4 does not allow straightforward conclusions to be drawn in the case of this sample. Table 1 reports the crystallite size obtained by elaboration of the most intense diffraction peak by the Scherrer’s equation. The modulation of pH, although relevantly affecting the phase composition, does not significantly modify either the crystallite size or the specific surface area. Further, the values of specific surface areas show, when compared with the crystallite sizes, the occurrence of a relevant degree of aggregation between the crystallites in the actual particles. Table 1 reports also

results of characterizations of commercial TiO_2 samples to be used as reference systems in the analysis of the photodegradation results.

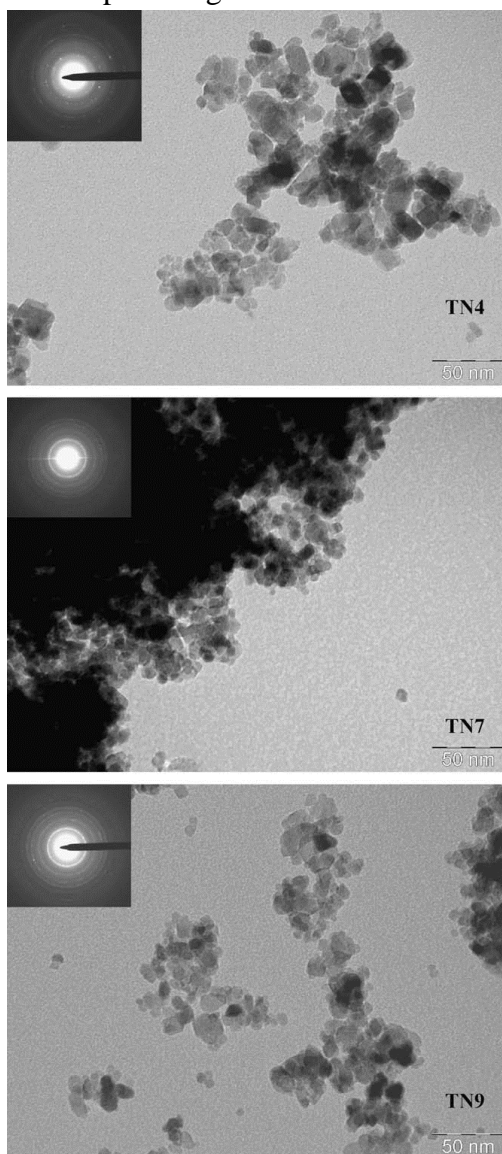


Figure 2. TEM images and the relevant SAED pattern (inset) for TN4, TN7 and TN9 samples.

TEM characterization

TN4 (Fig. 2) displays well-crystallized grains with size ranging from 10 nm up to 30 nm approximately. The grains show quite different morphologies: from round shaped to prismatic, although in all cases rather isotropic. The relevant diffraction pattern (inset) displays the presence of the characteristic lines of all three polymorphs of the titanium oxide, in agreement with the XRD results. In the case

of TN7 the observed microstructure shows mostly equiaxed domains with an average size close to 10 nm, in agreement with the predictions of XRD analyses, as concerns anatase. The other expected polymorph (rutile) has not been detected, since, as indicated by the XRD results, its concentration is too low. The typical grain morphology of TN9 is shown in the figure, where the mostly equiaxed grains of the powder have size ranging from a few nanometers up to 30 nm or so. In this respect the grain size distribution looks comparatively broader than in the former sample (TN7). The corresponding SAED pattern (inset) confirms the presence, as the only phase in this material, of the anatase polymorph.

Optical absorption

Fig. 3 reports the comparison among the diffuse reflectance (DR) UV–vis spectra of N-doped TiO_2 prepared from TiCl_3 , of the reference sample T9 and of an undoped commercial pure anatase sample. The curve relative to TN9 essentially differs from that of bare TiO_2 for the broad absorption in the visible region centered at about 450 nm, in analogy with what reported by other authors for N-doped TiO_2 .^{6,7} The spectra relative to TN7 and TN4 show increased absorption in the visible region, the more so in the case of the sample prepared at pH 4. This effect is to be related, besides to the presence of N species, also to the absorption in the visible region typical of rutile, which is present in these samples, reaching 75% of the phase abundance in the case of the TN4.

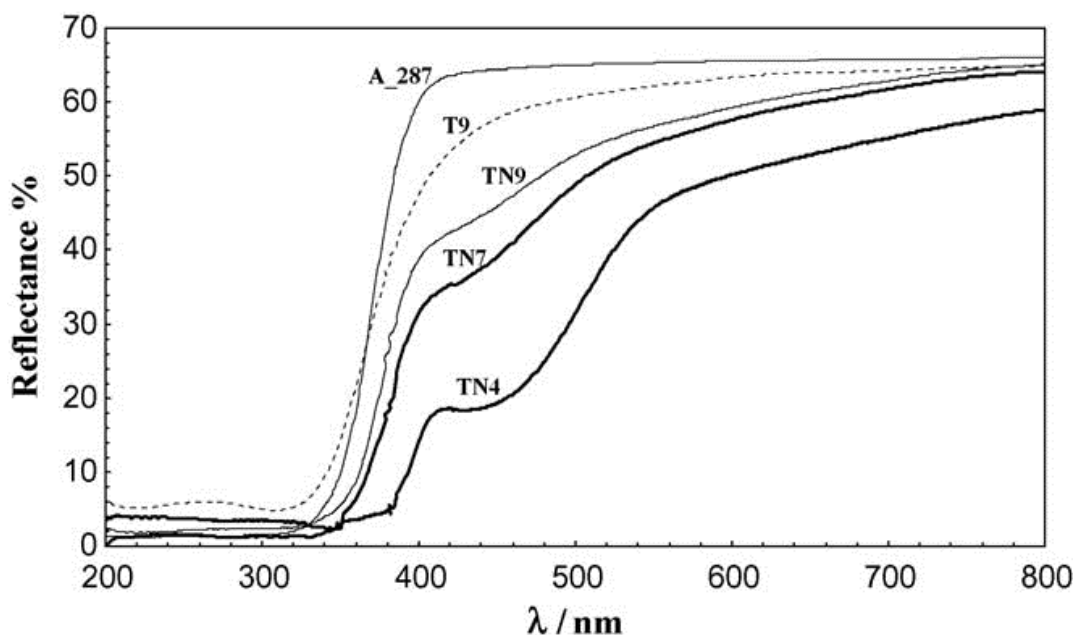


Figure 3. Diffuse reflectance spectra for commercial (A_287) and homemade (T9, TN4, TN7 and TN9) samples.

XPS analyses

Table 1 reports the N/Ti atomic ratios obtained by XPS on the present N-doped samples. The trend is not monotonically varying with pH, the sample showing the largest N content is the sample obtained at intermediate pH (TN7). The sample obtained at pH 4 shows the lowest N content and a broad N *1s* peak which is difficult to fit.

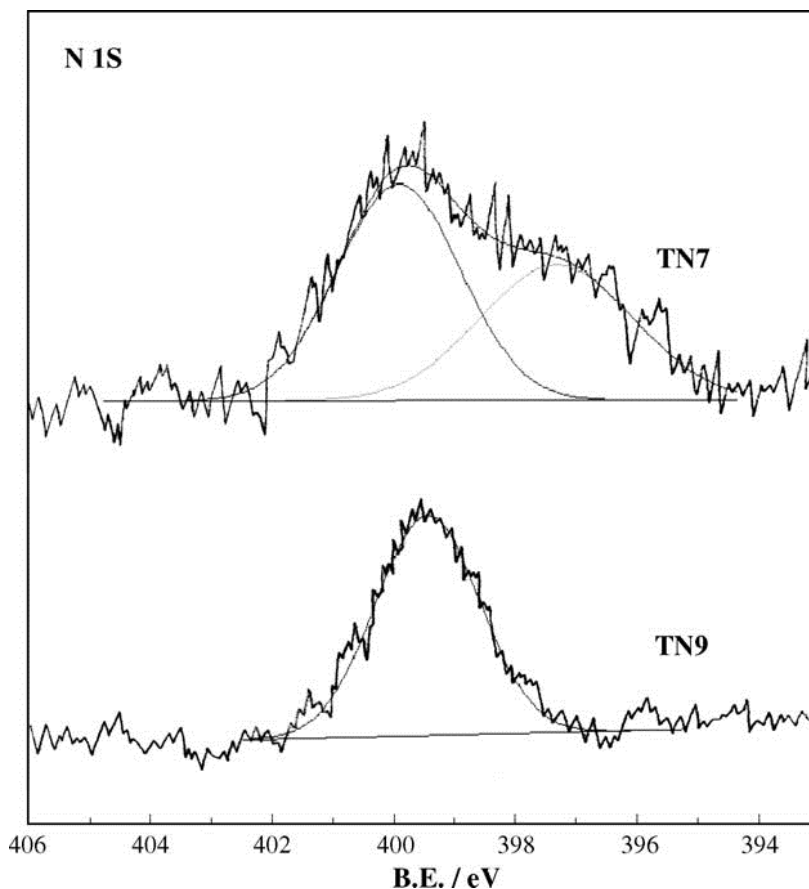


Figure 4. XPS spectra: N *1s* region for TN7 and TN9 samples.

The N *1s* region of the two samples obtained respectively at pH 7 and 9 is instead more defined and is reported in Fig. 4. It can be observed that the fitting procedure allows in the case of TN9 the identification of only one component centered at 400.1 eV while in the case of sample TN7 two components respectively at 396.1 and 399.9 eV are clearly appreciable. The debate on the attribution of XPS N *1s* peak components to specific species or structures (O–Ti–N, N– O–Ti–O or O–N–Ti–O, etc.) is definitely open and well discussed in *Ref. 20*. XPS N *1s* peaks in the range (396–404 eV) were observed by several authors and generally peaks at 396–397 eV were attributed to substitutional nitrogen while peaks at higher binding

energies (e.g. 400 eV) were attributed to interstitial locations. In the present case the attribution of the component at 396.1 eV to substitutional N, in the case of sample TN7, could be supported by the values of the cell parameters obtained by elaboration of XRD data. Just in the case of this sample the cell parameters show appreciable shrinking with respect to both theoretical and experimental values obtained for the samples prepared at different pH. In the case of sample TN9 a sole interstitial location of N species could be proposed also on the grounds of the almost un-modified cell parameters. The convergence between XPS and XRD data suggests, in the case of the present samples, a homogeneous distribution of N species between particle surface/sub-surface and bulk. It is interesting to recall that in the case of TiO₂ prepared by a sol-reaction and N doped by different inorganic compounds, Di Valentin et al.¹¹ never observed peaks at 396 eV. Again, therefore, the specific conditions of the TiO₂ preparative reactions are found to play a key role on the features of the N-doped samples.

EPR results

The most intense EPR feature has nearly the same shape for the three N-doped samples with relative intensities respectively of 1:2.1:2.9 for TN4, TN7 and TN9. The large width of the lines employed in the spectral simulation in the *xy* plane could suggest the presence of either unresolved interactions with N nuclei or that of many different coordinative environments around each paramagnetic center. These spectra are rather similar to those elsewhere attributed to NO with the unpaired electron confined in the *2p* antibonding orbital with lower energy.⁸ However in that case the spectrum was observable only at *T* < 170 K and interactions with N nuclei were also determined. Similar spectra were also reported for N-doped TiO₂ photocatalysts⁹ and attributed to the overlapping contributions of Ti³⁺ “trapped electrons” and of O^{•-} “trapped holes”.²¹ Indeed, both these species would form with TiO_{2-x}N_x.^{10,22} Ti³⁺ ions are characterized by very short relaxation time, so that their EPR spectrum is observable at very low temperature only or, at room temperature, with Ti⁴⁺ coupled with species like O^{•-}.^{22,23} In any case it can be noted that the last interpretation, as well as that based on the presence of NO, would indicate an increasing amount of N doping with increasing pH. Furthermore, in the present case, a second EPR component is appreciable, the intensity increasing in the order TN4 < TN7 < TN9. Fig. 5 and inset show, as an example, the spectrum obtained by subtracting TN7 from TN9 spectrum. This difference spectrum (Fig. 5, inset) is composed by three lines due to an unpaired electron interacting with a nuclear spin *I* = 1, and can be univocally attributed to Nb[•] centres formed by an unpaired *2p* electron belonging to an (interstitial or

substitutional) N atom.^{7,8,11} Systems of this kind are typical of N–TiO₂ submitted to oxidation⁷ and are of great interest for visible-light absorption.⁷ Furthermore, their importance resides also in the fact that their presence would reduce from 4.2 to 0.6 eV the cost of V₀ formation in bulk TiO₂.^{7,11} All these EPR patterns are not observable with the T9 sample (TiO₂ without N radicals), which displays only a less intense EPR pattern centered approximately at $g = 2.003$ (Fig. 5(d)).

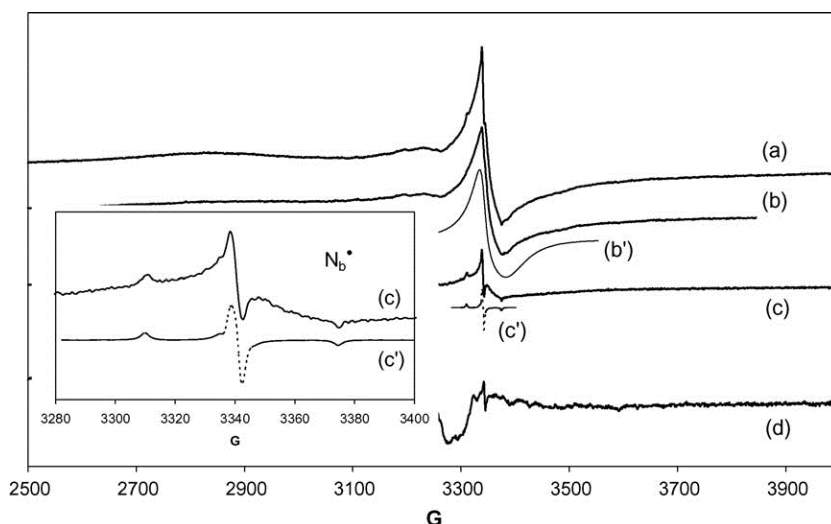


Figure 5. EPR spectra obtained at room temperature with (a) TN9, (b) TN7 and (d) T9 samples, respectively. The difference between tracks (a) and (b) multiplied by 1.38 gives (c). (b') is the simulation of (b) with $g_x \approx 1.978$; $g_y \approx 1.993$; $g_z \approx 2.003$ (i.e. $\langle g \rangle \approx 1.99$) and Lorentzian-component lines with peak-to-peak widths $\Delta H_{pp} \approx 60$; 60; 12 G along the x, y, z axis, respectively. (c') is the simulation of (c) with $g_x \approx 2.005$; $g_y \approx 2.004$; $g_z \approx 2.003$ and $A_z = 32.3$ G.

Photocatalytic activity

Table 2. Photocatalytic % degradation, pseudo-first-order kinetic constant together with relative standard deviation and regression coefficient for all samples (n.d. = not determined).

Sample	%Degradation	κ ($\times 10^3 \text{ min}^{-1}$)	R^2
T9	13.7	0.6 ± 0.3	0.980
TN4	56.2	2.9 ± 0.1	0.991
TN7	65.0	4.2 ± 0.1	0.987
TN9	79.6	6.0 ± 0.2	0.990
NanoActive	35.2	1.0 ± 0.3	0.991
A_287	55.8	n.d.	–
PC105	47.7	n.d.	–
P25	56.0	n.d.	–

For all the present TiO_2 samples the photocatalytic activity was tested with respect to the degradation of toluene. The reaction kinetics can be described for all the synthesized samples by a pseudo-first-order rate equation. The rate constant (k) values for the different catalysts, evaluated by linear fitting of the logarithmic plot of the residual toluene amounts (determined by GC) as a function of the reaction time, are listed in Table 2. In the case of three of the commercial samples elaboration by a pseudo-first order rate equation did not yield significant results as observed previously in the case of P25.¹⁸ Fig. 6 reports the trend of percent degradation of toluene, in humid conditions, for the present TiO_2 photocatalysts. It can be immediately observed that the sequence in the final degradation follows the same order of the rate constants reported in Table 2.

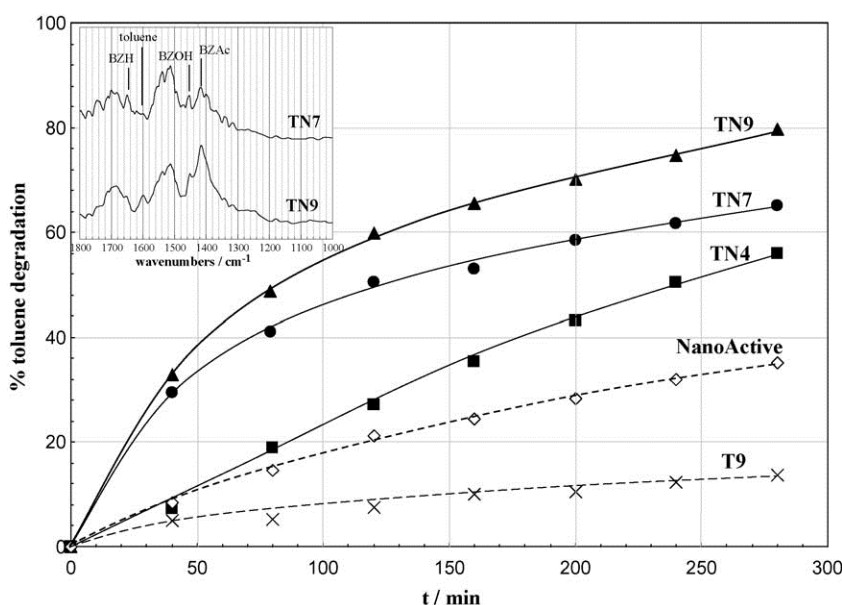


Figure 6. Toluene photodegradation for amorphous (T9 and NanoActive) and crystalline (TN4, TN7 and TN9) samples. Inset: IR spectra of TN7 and TN9 sampled at the end of the photocatalytic run. For each oxide, the curve of the relative pure TiO_2 was subtracted. Only the major (or most appreciable) bands of the adsorbed species are evidenced (see Ref. 18).

The commercial samples, not promoted by N species, both the pure anatase (A_287 and PC105) and the mixed phase P25, show relatively low efficiencies with respect to N-doped ones. An increase in the photocatalytic activity for N-doped samples has been reported for different photocatalytic reactions.²⁴ Livraghi et al.,⁷ for example, report that the activity of N- TiO_2 in the photodegradation of methylene blue is definitely although not largely higher than that of the bare oxide. The three N-doped samples obtained from TiCl_3 , show increasing conversion with increasing

the pH of the synthetic reaction. The sample obtained at pH 9 shows a top conversion reaching a degradation of around 80% after 280 min reaction time and showing the largest rate constant. FTIR-ATR spectra of TN7 and TN9 withdrawn at the end of the toluene degradation reaction are reported in Fig. 6 (inset). For each catalyst the “blank” curve pertaining the pure oxide was subtracted. In the figure only few of the most intense bands are evidenced for the sake of clarity.¹⁸ The two spectra show the presence of several common bands (toluene, benzoic acid, benzaldehyde and benzyl alcohol), but with different relative intensities.

In the case of sample TN9, in agreement with the faster kinetics (sample TN9, $k = 6.0 \times 10^{-3} \text{ min}^{-1}$; sample TN7, $k = 4.2 \times 10^{-3} \text{ min}^{-1}$, see Table 2), the BZAc (benzoic acid) component appears the most abundant adsorbed species with respect to TN7, showing a more advanced oxidation reaction. In fact the degradation sequence implies the progressive degradation from toluene to benzoic acid species, passing through benzylic alcohol and benzaldehyde. It is interesting to observe that the sequence in degradation, among the TiCl_3 samples, does not match the sequence in optical absorption reported in Fig. 3. Since the present three N-doped samples show fully comparable surface areas and crystallite sizes effects different from morphology or microstructure have to be invoked to interpret the observed trend. No systematic results could be found in the literature concerning the role played by the TiO_2 polymorph hosting N species on the photocatalytic efficiency of TiO_2 by solar irradiation. Data by model representation show that rutile and anatase accommodate differently N species.⁶ No results could be found concerning brookite. Results in Fig. 6 may indicate that pure anatase hosting N species is more active than a mixture of anatase and rutile. Further the comparison between the activity of samples TN7 and TN9 may suggest that substitutional N sites yield less active photocatalysts than interstitial ones. Data in the literature are controversial on this point. Di Valentin et al.,⁶ in the case of films prepared by chemical vapour deposition observed no evidence of photocatalytic activity in the visible in the case of N substitutional sites. Asahi et al.,³ instead, in the case of powdered samples prepared with NH_3/Ar as the source of N attributed visible photoactivity to substitutional sites associated with an XPS peak at 396 eV. The sequence in photocatalytic activity seems to correlate simply with EPR results which show an increasing amount of paramagnetic centres with increasing the reaction pH, the sample prepared at pH 9 containing an additional amount of paramagnetic N centres even with respect to sample TN7.

2.4.2.4 Conclusions

The first aspect which can be commented regards the role played by the pH of the synthetic reaction on the features of the obtained photocatalysts. Actually pH intervenes in modifying all the investigated features of the material, including the photo-catalytic activity. The photoactivity with respect to toluene degradation follows the order of increasing pH; this sequence does not match either the trend shown by XPS for the surface/sub-surface N amount or the possible presence of substitutional N in the TiO₂ lattice. The origin of the best performance of TN9 is to be sought in the largest amount of paramagnetic centres present in this sample as reported by EPR results.

2.4.2.5 References

- [1] M. Anpo, Bull. Chem. Soc. Jpn. 77 (2004) 1427.
- [2] G. Cappelletti, C.L. Bianchi, S. Ardizzone, Appl. Catal. B: Environ. 78 (2008) 193.
- [3] R. Asahi, T. Morikawa, T. Ohwaki, K. Aoki, Y. Taga, Science 293 (2001) 269.
- [4] Y. Huo, Z. Bian, X. Zhang, Y. Jin, J. Zhu, H. Li, J. Phys. Chem. C 112 (2008) 6546.
- [5] A.V. Emeline, G.N. Kuzmin, N. Serpone, Chem. Phys. Lett. 454 (2008) 279.
- [6] C. Di Valentin, E. Finazzi, G. Pacchioni, A. Selloni, S. Livraghi, M.C. Paganini, E. Giamello, Chem. Phys. 339 (2007) 44.
- [7] S. Livraghi, M.C. Paganini, E. Giamello, A. Selloni, C. Di Valentin, G. Pacchioni, J. Am. Chem. Soc. 128 (2006) 15666.
- [8] S. Livraghi, A. Votta, M.C. Paganini, E. Giamello, Chem. Commun. (2005) 498.
- [9] S.K. Joung, T. Amemiya, M. Murabayashi, K. Itoh, Appl. Catal. A: Gen. 312 (2006) 20.
- [10] N. Serpone, J. Phys. Chem. B 110 (2006) 24287.
- [11] C. Di Valentin, G. Pacchioni, A. Selloni, S. Livraghi, E. Giamello, J. Phys. Chem. B 109 (2005) 11414.
- [12] S. Sakthivel, M. Janczarek, H. Kisch, J. Phys. Chem. B 108 (2004) 19384.
- [13] S. Sato, R. Nakamura, S. Abe, Appl. Catal. B 284 (2005) 131.
- [14] T. Morikawa, R. Asahi, T. Ohwaki, K. Aoki, Y. Taga, Jpn. J. Appl. Phys. 40 (2001) L561.
- [15] A.C. Larson, R.B. Von Dreele, GSAS: General Structural Analysis System, Los Alamos National Laboratory, Los Alamos, NM, 1994.

- [16] S. Ardizzone, C.L. Bianchi, G. Cappelletti, S. Gialanella, C. Pirola, V. Ragaini, J. Phys. Chem. C 111 (2007) 13222.
- [17] G. Cappelletti, C.L. Bianchi, S. Ardizzone, Appl. Surf. Sci. 253 (2006) 519.
- [18] S. Ardizzone, C.L. Bianchi, G. Cappelletti, A. Naldoni, C. Pirola, Environ. Sci. Technol. 42 (2008) 6671.
- [19] K. Song, J. Zhou, J. Bao, Y. Feng, J. Am. Ceram. Soc. 91 (2008) 1369.
- [20] A.V. Emeline, V.N. Kuznetsov, V.K. Rybchuk, N. Serpone, Int. J. Photoener. (2008), doi:10.1155/2008/258394.
- [21] J.E. Wertz, J.R. Bolton, Electron Spin Resonance. Elementary Theory and Applications, McGraw-Hill, 1972, p. 317.
- [22] R.F. Howe, M. Grätzel, J. Phys. Chem. 89 (1985) 4495.
- [23] C. Oliva, L. Bonoldi, S. Cappelli, L. Fabbrini, I. Rossetti, L. Forni, J. Mol. Catal. A: Chem. 226 (2005) 33.
- [24] J.L. Gole, J.D. Stout, C. Burda, Y. Lou, X. Chen, J. Phys. Chem. B 108 (2004) 1230.

2.4.3 Photodegradation of Pollutants in Air: Enhanced Properties of Nano-TiO₂ Prepared by Ultrasound

G. Cappelletti, S. Ardizzone, C. L. Bianchi, S. Gialanella, A. Naldoni, C. Pirola, V. Ragaini, *Nanoscale Research Letters* **2009**, 4, 97–105.

2.4.3.1 Introduction

The use of ultrasonic sources in environmental remediation has been extensively studied, both in combination with other processes and also by itself.¹⁻⁴ The principal mode of action of continuous ultrasound is the production of hydroxyl radicals from water sonolysis, that can promote the degradation process of pollutants. Sonochemical processing to obtain materials with improved or unusual properties is, instead, relatively recent.⁵⁻¹¹ The chemical effect of ultrasound arises from acoustic cavitation, that is, the formation, growth, and implosive collapse of bubbles in a liquid. The implosive collapse produces high temperatures and pressures with localized hot spots, characterized by transient temperatures up to about 5000 K and pressures up to 1800 atm. The involved heating and cooling rates may be larger than 108 K s^{-1} . Nanoparticles showing a more uniform size distribution, higher surface area, a more controlled phase composition are some of the interesting features resulting from the application of sonication as a synthetic method. The synthesis of TiO₂ with tailored features widens the field of applications of the semiconductor oxide, among which the photocatalytic processes aimed at degrading environmental pollutants.¹²⁻¹⁹ It is well known that the morphology and structure of a nanosized material can deeply affect the semiconductor performance.^{14,20} Previously reported results^{15,16} have shown that the photocatalytic performance of TiO₂, in reactions performed both in water solution and in gas phase, is the result of a complex balance between diverging effects (e.g., crystallinity, surface area) and that the surface state plays a key role in determining the kinetics of the relevant reactions. Results present in the literature concerning the synthesis of TiO₂ assisted by US are rather difficult to rationalize since very different experimental conditions are adopted and the specific power of the US source is not reported in all cases. Meskin et al.¹⁰ report the hydrothermal synthesis of TiO₂ in an autoclave, coupled with ultrasonic activation. The results demonstrate that ultrasonic activation markedly accelerates the crystallization rates and raises the rutile content with respect to the values obtained in synthesis carried out under identical conditions, but without sonication. Similarly, Arami et al.⁸ produced nanostructured rutile with 15–20 nm crystallite size, which is usually difficult to be obtained at low temperatures, by simply treating in ultrasonic bath the product of dissolution of TiO₂ pellets in 10 M NaOH. Other authors, instead,

observe opposite effects. Kim et al.¹¹ combine a short aging of a TiCl_4 hydro-alcoholic solution with a sonication treatment performed in a conventional low power sonifier. In this case US depresses rutile formation, induces smaller particle size and larger surface areas. Yu et al.⁶ by a similar procedure based on the combination of a sol–gel synthesis with a treatment in a conventional ultrasonic bath, observe that ultrasonic irradiation enhances the crystallization rate of the TiO_2 gel. Gedanken et al.^{7,9} report the beneficial effects of ultrasonic irradiation on the template synthesis of worm-like TiO_2 in presence of a long chain amine. The authors measured very high surface areas ($853 \text{ m}^2 \text{ g}^{-1}$) for un-calcined products and a higher thermal stability of the mesoporous structures as compared to those samples that were not ultrasonically treated. To gain some new evidence on the key role played by US in the formation and growth of nanocrystalline TiO_2 , in the present work US treatments are applied during the aging of sol–gel precursors. Both continuous and pulsed US treatments are used. In the case of these latter treatments, both the on/off time and the power were modulated. To the authors best knowledge, no data are present in the literature so far concerning the use of pulsed US on the growth of TiO_2 particles. The structural and morphological features of the synthesized samples are investigated using different experimental techniques. The surface state of both Ti 2p and O 1s are analyzed by XPS and the value of the band gap of the semiconductor oxide estimated for all samples. The photocatalytic activity in the gas phase degradation of NO_x is also investigated. Various processes are studied in the literature to abate the emissions of NO into the environment. The photocatalytic oxidation by a semiconductor, mainly TiO_2 , is very promising and the tailoring of its features may promote the efficiency of the process.

2.4.3.2 Experimental

All the chemicals were of reagent grade purity and were used without further purification; bi-distilled water passed through a Milli-Q apparatus was used to prepare solutions and suspensions.

Sample Preparation. The sol–gel precursor (T), obtained by the hydrolysis ($t = 90$ min, $T = 65$ °C) of a solution of $\text{Ti}(\text{OC}_3\text{H}_7)_4$ and 2-propanol (water/alkoxide molar ratio = 49 and water/ propanol molar ratio = 15) was dried as a xerogel.²¹ A fraction of precursor was treated at 300 °C for 5 h in O_2 flux (T_300); the remaining part of the precursor was submitted to either pulsed (Bandelin, Ti horn, 20 kHz) for 1 h, or continuous (NTS Italia, Ti horn, 20 kHz) ultrasound water treatment for 30 min. The acoustic intensity, as determined calorimetrically, is 9 W cm^{-2} for continuous and 140 W cm^{-2} (maximum value) for pulsed ultrasound. In the case of PW treatment, two acoustic intensities were used: 49 and 84 W cm^{-2} (35%

and 60% of the maximum intensity, respectively). See Table 1 for the experimental parameters of the acoustic treatment. Three samples were obtained during the growth assisted by pulsed ultrasound, by varying both the “time on” and the acoustic intensity (TP0.5on49W, TP0.9on49W, and TP0.5on84W). The sample obtained using continuous US treatment is labeled TC9W.

Sample Characterization. Room-temperature X-ray powder diffraction (XRPD) patterns were collected with a Siemens D500 diffractometer over the 2θ range 10° – 80° , with a step scan of $\Delta 2\theta = 0.02^\circ$, and a Cu $K\alpha$ radiation. Rietveld refinement has been performed using the GSAS software suite and its graphical interface EXPGUI.¹⁵ Specific surface areas were determined by the classical BET procedure using a Coulter SA 3100 apparatus. Scanning electron microscopy (SEM) photographs are acquired with a LEO 1430. TEM samples were prepared by spreading a suspension of powder in ethylic alcohol onto a carbon coated copper grid. A Philips 400T electron microscope operated at 120 keV was used for imaging and for acquiring selected area electron diffraction (SAED) patterns. Diffuse reflectance spectra of the powders were measured on UV–vis scanning spectrophotometer (Perkin Elmer, Lambda 35), which was equipped with a diffuse reflectance accessory. A TiO_2 thin film was placed into the sample holder on integrated sphere for the reflectance measurements. A “total white” Perkin Elmer reference material was used as an internal reference. The experimental absorption versus lambda plot was elaborated by differentiation to better highlight the different optical features of the catalyst spectra. X-ray photoelectron spectra were acquired in an M-probe apparatus (Surface Science Instruments). The source was a monochromatic Al $K\alpha$ radiation (1486.6 eV). The binding energies (BEs) were corrected for specimen charging by referencing the C $1s$ peak to 284.6 eV. For the background subtraction the Shirley’s method was used.¹⁶ The relevant fittings were performed using only Gaussian line shapes, without BE or FWHM (full width at half maximum) constraints. The accuracy of the reported BE can be estimated to be ± 0.1 eV.

Photocatalytic Experiments. In the photocatalytic oxidation of nitrogen, oxide immobilized particulate TiO_2 layers (ca. 0.1 g) were prepared on glass sheets (7 cm^2) by deposition from a suspension of the oxide in isopropanol. The immobilized photocatalyst was placed into a pyrex glass reactor (with a volume of 20 L) and irradiated with an halogenide lamp (Jelosil, model HG500) emitting in the 340–400 nm wavelength range, with a nominal power of 500 W, at room temperature. The relative humidity was kept constant in all the runs (50%). Air, NO_x , and N_2 gas streams were mixed to obtain the desired NO_x concentration (400 ppb), inside the photoreactor. The photodegradation products concentrations (NO and NO_2) were

continuously monitored by an online chemiluminescent analyzer (Teledyne Instruments M200E). The NO_x adsorption onto the TiO₂ layer was determined through dark experiments. Degradation time was limited to 120 min.

2.4.3.3 Results and Discussion

Acoustic waves are known to cause the following effects in liquids:¹⁰ (1) activation of mass transport, (2) heating, and (3) cavitation, i.e., generation of bubbles, which then collapse, giving rise to high local temperatures and pressures. Consequently, the growth of an oxide assisted by ultrasound can be differently affected by diverging processes: (1) formation of additional nucleation centers in the vicinity of bubbles; (2) increased growth rate of the particles owing to accelerated mass transport; and (3) disintegration of aggregates and agglomerates of primary crystallites by the shock waves resulting from bubble collapse.

Table 1 General conditions adopted for the US treatment in suspension

	Instrumental features				Experimental conditions		
	US source	d_{horn} (cm)	S_{horn} (cm ²)	Acoustic intensity (W cm ⁻²)	t (s)	E_{tot} (kJ)	E_{tot}/V (kJ L ⁻¹)
TP _{0.5on} 49W	Pulsed	1.3	1.3	49	3600	117	470
TP _{0.5on} 84W	Pulsed	1.3	1.3	84	3600	202	808
TP _{0.9on} 49W	Pulsed	1.3	1.3	49	3600	210	840
TC9W	Continuous	5.6	24.6	9	1800	414	414

To evaluate separately the different effects provoked by US, in the present case both continuous and pulsed ultrasound were used during the aging of a TiO₂ precursor obtained by sol–gel reaction. Table 2 reports data concerning the synthesized samples. The specific surface area ranges from 215 to 280 m² g⁻¹. Sample T_300, not submitted to US treatment and calcined at 300 °C shows the lowest surface area. Variable effects are introduced by the different US treatments. Pulsed US, with the highest total energy per volume (TP0.9on49W and TP0.5on84W, see Table 1), produce an increase in surface area even with respect to the untreated precursor. This suggests that, in these cases, the prevailing effect of the US treatment may be the disintegration of aggregates. The continuous US treatment, instead, provokes a slight reduction in the surface area, with respect to the precursor, which suggests either a more pronounced grain growth or a less dispersed sample. The total pore volume and size are not significantly affected by the US treatment (Fig. 1a). The sample showing the largest pore volume is the pulsed one (TP0.5on84W), the increase concerning the largest pore sizes. All the samples are mesoporous; the shape of the N₂ adsorption hysteresis loops (Fig. 1b) changes from H2 (prevailing “bottleneck” shape) in the precursor sample (T) to a prevailing slit-shaped shape (H3) for the US-aged and thermally treated samples.

X-ray diffraction data show the presence of anatase and brookite polymorphs for all samples. The formation of the metastable brookite polymorph for small TiO_2 crystallite sizes is a well-established finding, often reported in the literature.²¹

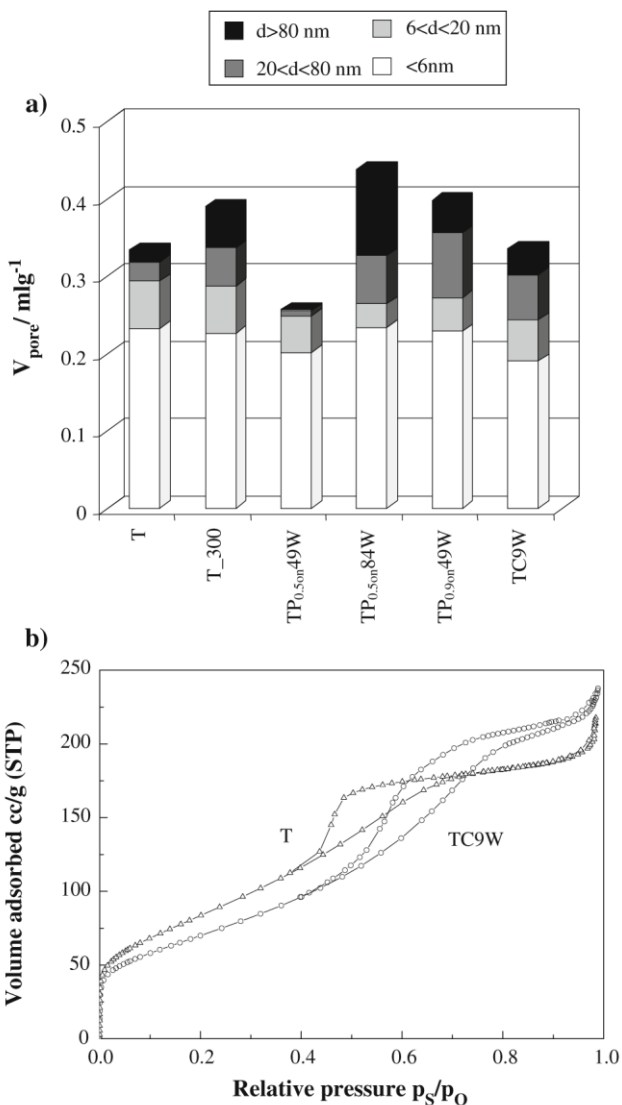


Figure 1. (a) Distribution of pore volume of all samples and (b) BET isotherm, hysteresis loop of the precursor sample (T) and of the sample submitted to CW treatment.

Pulsed US treatment promotes the formation of the brookite polymorph, particularly in the two samples showing the largest surface area. On the other hand, in the case of the CW US (sample TC9W), the treatment provokes a decrease in the brookite content of the sample. The thermal treatment at 300 °C (sample T_300) results in the lowest brookite content; the crystallite size, as estimated by the

Sherrer's equation, applied to the breadth of the most intense anatase peak, is of 8 nm. The crystallite size for all the other samples is ranges around 4 nm.

Table 2 Quantitative phase composition (*A* = anatase, *B* = brookite) and BET surface area

Sample	US source	% <i>A</i>	% <i>B</i>	S_{BET} , m ² g ⁻¹
T	–	60.2	39.8	254
T_300	–	67.0	33.0	215
TP _{0.5on} 49W	Pulsed	55.6	44.4	231
TP _{0.5on} 84W	Pulsed	53.0	47.0	268
TP _{0.9on} 49W	Pulsed	53.5	46.5	278
TC9W	Continuous	63.0	37.0	242

Figure 2 reports the anatase cell volume as evaluated from X-ray diffraction data for selected samples. It is interesting to observe that, the CW US treatment leads to samples showing cell volumes closer to the theoretical values, indicating the formation of a more ordered and regular structure, even more ordered than the sample calcined at 300 °C but with no US treatment. It is worth observing that the US treatment provokes in any case a more regular spatial reticular organization since even the sample TP0.9on49W, characterized by the largest surface area, shows a cell volume smaller than the precursor sample one.

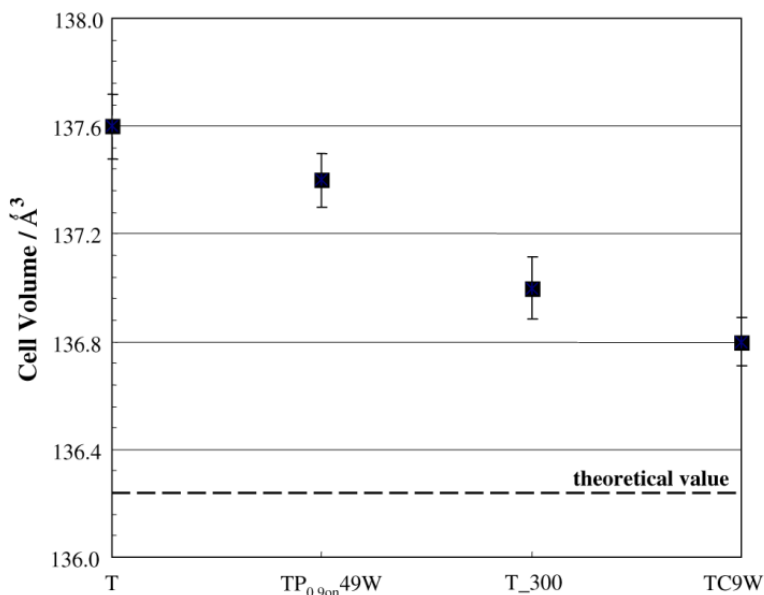


Figure 2. Anatase cell volume of selected samples obtained by elaboration of experimental diffraction data.

Spectroscopic Characterization

To obtain information on the light absorption features of the various samples, experimental data of diffuse reflectance were elaborated to give absorption coefficient values $F(R)$ according to the Kubelka–Munk equation.¹⁶ The corresponding band-gap values obtained by this procedure for all samples are reported in Table 3 (first column).

Table 3. Band gap values calculated by Kubelka–Munk equation of diffuse reflectance spectra and $\text{OH}/\text{O}_{\text{tot}}$, $\text{Ti}^*/\text{Ti}^{4+}$ by XPS analysis for all samples.

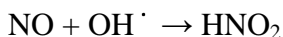
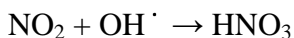
Sample	Band gap, eV	$\text{Ti}^*/\text{Ti}^{4+}$	$\text{OH}/\text{O}_{\text{tot}}$
T	3.19	–	0.17
T_300	3.20	–	0.12
TP _{0.5on} 49W	3.13	–	0.29
TP _{0.5on} 84W	3.16	–	0.26
TP _{0.9on} 49W	3.18	–	0.21
TC9W	3.42	0.87	0.27

The band gap values fall in the range expected for TiO_2 photocatalysts, with the only exception of the CW US sample, that shows a slightly higher value of band-gap with respect to the other ones. This point will be commented on further in the following.

Photodegradation of NO_x

Figure 3a displays the general trend of the NO_x degradation curves of some TiO_2 photocatalysts selected among those produced in the present study. The NO_x concentration is the sum of the NO and NO_2 concentrations.

The general mechanism for NO_x degradation by photocatalysis implies the oxidation of the nitric monoxide to nitric or nitrous acid induced by oxygen species produced at the TiO_2 surface.¹⁵ The reaction path for NO_x conversion is generally mediated by OH radicals:



In the present case, no increase in activity was observed upon increasing the catalyst amount. Therefore, it was concluded that only the exposed/external fraction of the catalyst was irradiated.

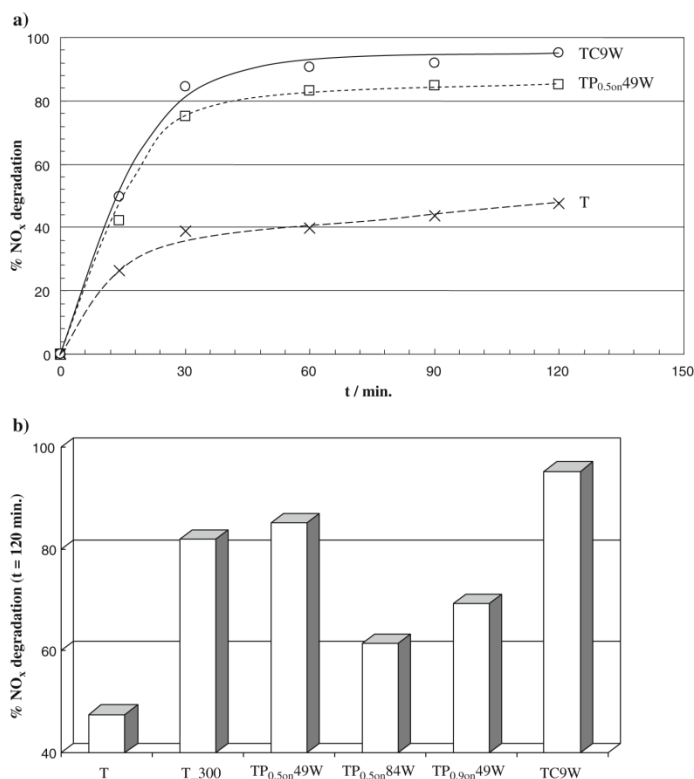


Figure 3. (a) NO_x percent degradation as a function of reaction time for selected samples and (b) final percent degradation after 120 min for all the samples.

All samples reach in a short time (30 min) a plateau region as concerns NO_x degradation, with values falling in a wide range: from 40% to about 90%. The final sequence in efficiency, shown by the various samples, is displayed in Fig. 3b. It can be seen that the conversion of the precursor not submitted to sonication is very poor. All sonicated samples show better performances than the untreated T sample. Two US treated samples show the best conversions, higher than the thermally treated sample (T₃₀₀). In the case of the CW treated sample, the increase with respect to T₃₀₀ is significant (about 15%).

An improvement of the photocatalytic efficiency of samples submitted to US treatment has been reported previously in the literature. Kim et al.,¹¹ for example, observe an improvement in methylene blu degradation in samples submitted to US treatments. In general, the increase in the photocatalytic performance is attributed to an increase in the samples surface area, produced by the US treatment. This is not the case for the present samples, since those showing the best performances (TC9W and TP_{0.5on}49W) are the ones showing the lowest surface area, besides T₃₀₀. The interpretation of the origin of the better photocatalytic conversion is

not straightforward. Further investigations of the surface state and of the microstructure may bring new evidence to elucidate the trend apparent in Fig. 3b.

XPS Analyses

The literature regarding XPS analyses of nanocrystalline TiO₂ samples obtained by ultrasound is not large, specifically concerning the region of Ti 2*p*. Yu et al.^{5,6} show no significant effects on the BE of Ti 2*p* (458.2 eV) in the case of nanosized TiO₂ powders obtained by sol–gel combined with US-treatment performed in a conventional ultrasonic bath. Gedanken et al.⁷ measured the BE of Ti 2*p* at 457.1 eV in the case of un-calcined product and at 459.2 eV for the same sample calcined at 450 °C.

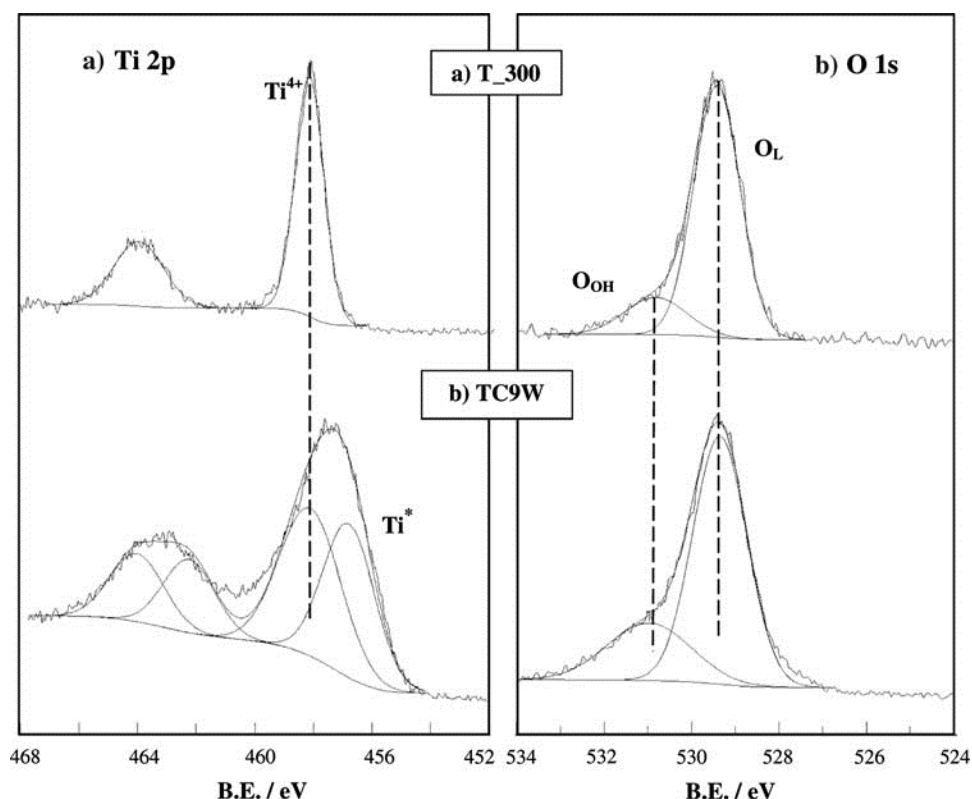


Figure 4. XPS of (a) Ti 2*p* and (b) O 1*s* regions for T₃₀₀ and TC9W.

The authors interpreted the shifts in the Ti 2*p* peak position, from the regular 458.2 eV, as due to the interaction of octadecylamine with TiO₂ in the templated synthesis of the mesoporous oxide.⁷ Figure 4 shows the region of Ti 2*p* (a) and O 1*s* (b) of precursor (T) and CW US aged samples. In all samples, the peaks in the Ti 2*p* region are regular and the BEs (Ti 2*p*^{3/2} 458.3 eV) compare well with data of Ti(IV) in TiO₂.¹⁵ In the case, instead, of sample TC9W a second component (Ti*) at lower BE (Fig. 4a) can be appreciated (Table 3, second column). The presence of

two components in the Ti 2*p* spectrum is not frequently observed in TiO₂ samples. Zhu et al. [22], reported this effect in TiO₂ particles prepared by a nonhydrolytic sol–gel reaction, without any US treatment. They attributed the component at lower BE to Ti(III). In the present case, the best fit of the Ti 2*p* region yields two components at 456.8 and at 458.3 eV, respectively. The component at lower BE might be interpreted, according to Zhu et al.,²² as due to the presence of defective titanium surface sites, these in turn being the result of the interactions of the oxide surface with the OH radicals produced by the CW US treatment. It is interesting to observe that TC9W is just the most photocatalytically performing sample with respect to the degradation of NO_x. The O 1*s* peaks of the present samples show, in any case, a regular pattern (Fig. 4b) and show two components, corresponding, respectively, to oxygen in the oxide lattice (O_L), and to surface hydroxyl (O_{OH}). The ratio between O_{OH} and total oxygen components (O_{OH} + O_L) is reported in Table 3 (third column) and can be considered as an indication of the degree of hydrophilicity of each sample.¹⁵ The two samples showing top photocatalytic performances are the ones showing the highest OH/O_{tot} ratio.

SEM and TEM Observations

SEM images (Fig. 5) show that the samples submitted to US are, in general, more disperse than those obtained in the absence of US. The sample submitted to CW US, besides being much more disaggregated than the precursor, appears to be composed by smaller particles. To obtain further indications concerning the microstructure of the samples, TEM images of the best photocatalysts were obtained and compared with those of the untreated precursor. Figure 6a, referring to the untreated precursor sample (T), shows aggregates in which the size of the crystallites is extremely reduced. The figure also shows the typical microstructure of this sample and in the SAED pattern the presence of reflections due to anatase and brookite phases, although largely overlapping, appear clearly, in agreement with the XRD data in Table 1. The diffraction rings are uniform and with homogeneous intensity supporting the nanometric size of the crystallites and their spatial isotropy. The microstructure of the pulsed sample (TP0.5on49W) is shown in Fig. 6b. The SAED pattern, also in this case, supports the presence of the two TiO₂ polymorphs. Crystallite clusters appear to be relatively dense, so that only the peripheric regions can be analyzed in detail. Crystallite size even in this case compares well with the XRD value. The microstructure of the TC9W sample is shown in Fig. 6c. Also in this case the presence of the A and B polymorphs is well appreciable in the SAED spectrum. In the case of this sample, the crystallite

agglomerates appear to be densely packed, possibly as a consequence of their reduced size, which can be estimated to be around 1–2 nm. The crystallites appear to be rather homodisperse concerning both shape and size. The extremely small size of the crystallites would justify the larger value of the band gap of this sample and the relevant blue shift, reported by other researchers for very small crystallite sizes.¹³

2.4.3.4 Conclusions

Two main features, promoted by US treatments, can be assumed to support a better photocatalytic performance: reduction in the crystallite sizes and larger surface coverage by OH. Reduction in the crystallite size of a semiconductor can usually lead to enhancement in the photocatalytic degradation. It is believed that enhanced quantum yields are achievable for the nanosized catalysts due to more efficient transfer of the photogenerated charge carriers from the interior to the particle surface [23]. Moreover, in these catalysts the very small size of the crystallites is also accompanied by a more ordered crystalline structure and the samples appear to be more regular and can be considered to contain a relatively low concentration of lattice defects. These features result in a lower recombination rate between electrons and holes and, therefore, in an overall better photocatalytic performance. The OH population of the surface is a key feature in NO_x photodegradation [15]; a more hydroxylated surface promotes both the formation of OH radicals and also the adsorption of the pollutant molecules prior to the degradation. The analysis of the present data seems to suggest that the relevant parameter imposing the final features of the oxides is the US total energy per volume (E_{tot}/V) and not the acoustic intensity or the pulsed or continuous mode of US. The two samples obtained at the higher E_{tot}/V (808, 840 kJ L⁻¹) show the largest surface area and highest brookite content. The other way round, the two samples obtained at around half E_{tot}/V (414, 470 kJ L⁻¹) show very similar features between each other and display the top photocatalytic activity. The continuous mode induces, further, the presence of surface defects and consequently yields the best photocatalyst.

2.4.3.5 References

- [1] C. Petrier, D.J. Casadonte, *Advances in Sonochemistry*, vol. 6 (JAI Press, London, 2001), pp. 91–110.
- [2] G. Zhang, I. Hua, *Environ. Sci. Technol.* 34(8), 1529 (2000). doi: 10.1021/es981127f.
- [3] C. Petrier, A. Jeunet, J.L. Luche, G. Reverdy, *J. Am. Chem. Soc.* 114, 3148 (1992). doi:10.1021/ja00034a077.

- [4] A. Kotronarou, G. Mills, M. Hoffmann, *Environ. Sci. Technol.* 26(7), 1460 (1992). doi:10.1021/es00031a026.
- [5] L. Wu, J.C. Yu, L. Zhang, X. Wang, W. Ho, *J Solid State Chem.* 177, 2584 (2004). doi:10.1016/j.jssc.2004.03.033.
- [6] J.C. Yu, J. Yu, L. Zhang, W. Ho, *J. Photochem. Photobiol. A: Chem. (Easton)* 148, 263 (2002).
- [7] Y. Wang, S. Chen, X. Tang, O. Palchik, A. Zaban, Y. Koltypin, A. Gedanken, *J. Mater. Chem.* 11, 521 (2001). doi:10.1039/b006070o.
- [8] H. Arami, M. Mazloumi, R. Khalifehzadeh, S.K. Sadrnezhad, *Mater. Lett.* 61, 4559 (2007). doi:10.1016/j.matlet.2007.02.051.
- [9] Y. Wang, X. Tang, L. Yin, W. Huang, Y. Rosenfeld Hachon, A. Gedanken, *Adv. Mater.* 12, 1183 (2000). doi :10.1002/1521- 4095(200008)12:16\1183::AID-ADMA1183[3.0.CO;2-X.
- [10] P.E. Meskin, A.E. Baranchikov, V.K. Ivanov, D.R. Afanasev, A.I. Gavrilov, B.R. Churagulov, N.N. Oleinikov, *Inorg. Mater.* 40, 1058 (2004). doi:10.1023/B:INMA.0000046468.73127.f5.
- [11] S.Y. Kim, T.S. Chang, C.H. Shin, *Catal. Lett.* 118, 224 (2007). doi:10.1007/s10562-007-9174-x.
- [12] J. Yu, J.C. Yu, M.K.-P. Leung, W. Cheng, B. Ho, X. Zhao, A.I. Gavrilov, B.R. Churagulov, N.N. Oleinikov, *Inorg. Mater.* 40, 1058 (2004). doi:10.1023/B:INMA.0000046468.73127.f5.
- [13] H. Lin, C.P. Huang, W. Li, C. Ni, S. Ismat Shah, Y.-H. Tseng, *Appl. Catal. B* 68, 1 (2006). doi:10.1016/j.apcatb.2006.07.018.
- [14] S. Bakardjieva, V. Stengl, L. Szatmary, J. Subrt, J. Lukac, N. Murafa, D. Niznansky, K. Cizek, J. Jirkovskyc, N. Petrova, *J. Mater. Chem.* 16, 1709 (2006). doi:10.1039/b514632a.
- [15] S. Ardizzzone, C.L. Bianchi, G. Cappelletti, S. Gialanella, C. Pirola, V. Ragaini, J. *Phys. Chem. C* 111, 13222 (2007). doi:10.1021/jp0741096.
- [16] G. Cappelletti, C.L. Bianchi, S. Ardizzzone, *Appl. Catal. Environ.* 78, 193 (2008). doi:10.1016/j.apcatb.2007.09.022.
- [17] J. Sicha, D. Herman, J. Musil, Z. Stryhal, J. Pavlik, *Nanoscale Res. Lett.* 2(3), 123 (2007). doi:10.1007/s11671-007-9042-z.
- [18] V. Vega, V.M. Prida, M. Herna Aranda, E. Ruiz-Hitzky, M. Vandez-Velez, E. Manova, P. ´zquez, *Nanoscale Res. Lett.* 2(7), 355 (2007). doi:10.1007/s11671-007-9073-5.

- [19] S. Watson, D. Beydoun, J. Scott, R. Amal, J. Nanopart. Res. 6(2), 193 (2004). doi:10.1023/B:NANO.0000034623.33083.71.
- [20] J. Rajeswari, P.S. Kishore, B. Viswanathan, T.K. Varadarajan, Nanoscale Res. Lett. 2(10), 496 (2007). doi:10.1007/s11671-007-9088-y.
- [21] T. Boiadjeva, G. Cappelletti, S. Ardizzzone, S. Rondinini, A. Vertova, Phys. Chem. Chem. Phys. 6, 3535 (2004). doi:10.1039/b402370f.
- [22] J. Zhu, J. Yang, Z.F. Bian, J. Ren, Y.-M. Liu, Y. Cao, H.-X. Li, H.-Y. He, K.-N. Fan, Appl. Catal. B Environ. 76, 82 (2007). doi: 10.1016/j.apcatb.2007.05.017.
- [23] M. Benmami, K. Chhor, A.V. Kanaev, J. Phys. Chem. B 109(42), 19766 (2005). doi:10.1021/jp051396+.

2.4.4 Porous Titania microsphere with Tunable Properties

A. Naldoni, C. Pirola, C. L. Bianchi and K. S. Suslick, submitted to *Chemistry of Materials*.

2.4.4.1 Communication

The synthesis of nanomaterials with desired morphologies and functionality has attracted an intense recent interest. Among the various morphologies explored (e.g., nanotubes, nanowires, nanorods, core-shell nanoparticles), hierarchically porous nanostructures have received a much attention¹ not only for their unique or enhanced physicochemical properties, but also for their widespread potential applications, including use for drug delivery, photonic materials, batteries and membrane fuel cells, and photocatalysis.^{2,3}

Titania is a multifunctional material whose unusual electronic properties make it an especially important material for photoelectrochemical solar cell applications and environmental remediation. Nanostructured TiO₂ exhibits superior photocatalytic activity compared to traditional bulk materials, and numerous strategies have been developed to synthesized hollow and porous TiO₂ nano/micro spheres.⁴⁻⁵ Control over the physical properties of the resulting porous nanostructures, however, remains a scientific challenge.

-
- (1) (a) Lakes, R. *Nature* **1993**, *361*, 511-515. (b) Caruso, F.; Caruso, R. A.; Möhwald, H. *Science* **1998**, *282*, 1111. (c) Bigi, A.; Boanini, E.; Walsh, D.; Mann, S. *Angew. Chem. Int. Ed.* **2002**, *41*, 2163. (d) Yang, J.; Sasaki, T. *Chem. Mater.* **2008**, *20*, 2049. (e) Zhou, H.; Fan, T.; Ogawa, H. *Chem. Mater.* **2007**, *19*, 2144. (f) Suh, W. H.; Suslick, K. S.; Stucky, G. D.; Suh, Y.-H. *Prog. Neurobiol.* **2009**, *87*, 133.
- (2) (a) Mo, M. S.; Yu, J. C.; Zhang, L. Z.; Li, S.-K. A. *Adv. Mater.* **2005**, *17*, 756. (b) Dinsmore, A. D.; Hsu, M. F.; Nikolaidis, M.; Weitz, D. A. *Science* **2002**, *298*, 1006. (c) Gao, S.; Yang, S.; Shu, J.; Li, Z.; Jiang, K. *J. Phys. Chem C* **2008**, *112*, 19324. (d) Cao, A. M.; Hu, J. S.; Liang, H. P.; Wan, L. J. *Angew. Chem. Int. Ed.* **2005**, *44*, 4391.
- (3) (a) Fang, B.; Kim, J. H.; Kim, M.; Yu, J.-S. *Phys. Chem. Chem. Phys.* **2009**, *11*, 1380. (b) Shan, Z. W.; Adesso, G.; Alivisatos, A. P. *Nat. Mater.* **2008**, *7*, 947. (c) Song, X.; Gao, L. *J. Phys. Chem. C* **2008**, *12*, 15299. (d) Cao, S.-W.; Zhu, Y.-J. *J. Phys. Chem. C* **2008**, *112*, 6253. (e) Fei, J.; Cui, Y.; Yan, X.; Li, J. *Adv. Mater.* **2008**, *20*, 452.
- (4) (a) Li, X.; Xiong, Y.; Xie, Y. *Inorg. Chem.* **2006**, *45*, 3493. (b) Li, H.; Bian, Z.; Lu, Y. *J. Am. Chem. Soc.* **2007**, *129*, 8406. (c) Yu, J.; Liu, W.; Yu, H. *Cryst. Growth Des.* **2008**, *8*, 930. (d) Song, X.; Ding, X.; Zhang, L. *J. Phys. Chem. C* **2009**, *113*, 5455. (e) Li, D.; Haneda, H.; Ohashi, N. *Chem. Mater.* **2005**, *17*, 2588.
- (5) (a) Suh, W. H.; Jang, A. R.; Suh Y.-H.; Suslick, K. S. *Adv. Mater.* **2006**, *18*, 1832. (b) Iskandar, F.; Nandiyanto, A.; Yun, K.; Hogan, C.; Okuyama, K.; Biswas, P. *Adv. Mater.* **2007**, *19*, 1408. (c) Nandiyanto, A.; Iskandar, F.; Okuyama, K. *Chem. Eng. J.* **2009**, *152*, 293.

As a synthetic tool, ultrasonic spray pyrolysis (USP) has several advantages over other traditional methods: production of micron- or submicron-sized spherical particles, high product purity, continuous operation, and facile control over chemical and physical compositions.^{5-6b,d,e}

Here, we use USP⁶⁻⁷ as a phase separated process for the synthesis of porous TiO₂ microspheres with tunable properties and examined its photocatalytic activity for the decomposition of NO_x. Porous TiO₂ spheres were prepared by USP employing a modification of the synthesis previously reported by Suslick and co-workers.^{5a} An aqueous solution of a Ti^{IV} complex (titanium(IV)bis(ammonium lactato)dihydroxide) containing colloidal silica was nebulized using a home-made ultrasonic generator (1.65 MHz) (cf. Supporting Information (SI) for details).

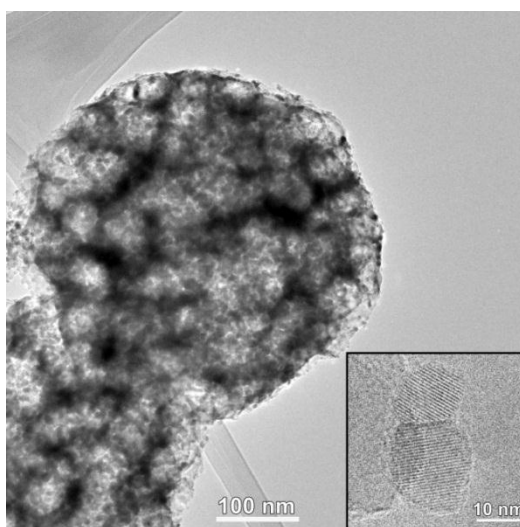


Figure 1. Transmission electron microscopy (TEM) image of a TiO₂ USP prepared porous microsphere (T13M) and (inset) at higher magnification, two building blocks.

-
- (6) (a) Bang, J. H.; Suslick, K. S. *Adv. Mater.* **2010**, *22*, 1039–1059. (b) Okuyama, K.; Lenggoro, W. *Chem. Eng. Sci.* **2003**, *58*, 537. (c) Patil, P. S. *Mater. Chem Phys.* **1999**, *59*, 185. (d) Kudas, T.T.; Hampden-Smith, M. *Aerosol Processing of Materials*, Wiley-VCH, New York: **1999**. (e) Messing, G. L.; Zhang, S. C.; Jayanthi, G. V. *J. Am. Ceram. Soc.* **1993**, *76*, 2707. (f) Iskandar, F; Okuyama, K. *Nano Lett.* **2001**, *1*, 231. (g) Nandiyanto, A.; Kim, S.; Iskandar, F; Okuyama, K. *Microporous Mesoporous Mater.* **2009**, *120*, 447.
- (7) (a) Suh, W. H.; Suslick, K. S. *J. Am. Chem. Soc.* **2005**, *127*, 12007. (b) Didenko, Y.T.; Suslick, K.S. *J. Am. Chem. Soc.* **2005**, *127*, 12196. (c) Skrabalak, S. E.; Suslick, K. S. *J. Am. Chem. Soc.* **2006**, *128*, 12642. (d) Bang, J. H.; Helmich, R. J.; Suslick, K. S. *Adv. Mater.* **2008**, *20*, 2599. (e) Dunkle, S. S.; Suslick, K. S. *J. Phys. Chem., C*, **2009**, *113*, 10341. (f) Fortunato, M. E.; Rostam-Abadi, M.; Suslick, K. S. *Chem. Mater.* **2010**, *22*, 1610.

The resulting mist was carried into a furnace by an air flow (1 SLPM), the SiO₂/TiO₂ nanocomposite microspheres so produced were collected in water-filled bubblers, isolated by centrifugation, and the silica template finally removed by etching with HF 10 wt.% in water. As a control, USP of the same aqueous solution of the Ti^{IV} complex in the absence of colloidal silica was performed, generating solid TiO₂ spheres (abbreviated T_USP, etched with HF is T_USP_HF).

Table 1. BET Surface area and phase composition analysis* of solid and porous titania microspheres.

Sample	Si:Ti molar ratio	silica size (nm)	initial SiO ₂ surf. area [§] (m ²)	surf. area of titania microsphere (m ² /g)	Anatase %
T_USP	—	—	0	<1	36
T_USP	—	—	0	<1	37
T15L	1:5	70-100	9	6	81
T15M	1:5	35-50	12	16	93
T15S	1:5	12	56	32	100
T13L	1:3	70-100	14	9	89
T13M	1:3	35-50	20	19	96
T13S	1:3	12	92	48	100
T11L	1:1	70-100	42	14	100
T11M	1:1	35-50	59	—	100
T11S	1:1	12	276	—	100

*Anatase ref. JCPDS 21-1272, Rutile ref. JCPDS 21-1276

[§]details are reported in SI, Figure S5

The porous nanostructure of USP particles was confirmed by TEM analysis (Figure 1); abbreviations for the various microspheres based on the preparation conditions are given in Table 1 together with relevant properties. The titania microspheres were few hundreds of nanometers in diameter; their nanostructure is built up of assembled individual nanoparticles between 20 and 40 nm in average size (SI, Table S1). The inter-aggregations of these building blocks are due to condensation reactions among the hydroxyl groups on their surface,^{4e} which results in the formation of the porous nanostructures. We can control the morphology of the titania porous spheres by varying colloidal silica to titanium precursor molar ratio (Figure 2).

In addition, by using SiO₂ nanoparticles with different sizes (12, 35-50, 70-100 nm), we obtain TiO₂ porous spheres characterized by meso- or macroporosity (SI, Figure S3).^{4e} The BET surface areas of the microspheres show a monotonical trend directly related to surface area of the template silica originally present (Table 1). If the silica content, however, was too high (SiO₂/Ti=1:1, SiO₂ size 12 or 35-50 nm), the superstructure was lost, presumably because of insufficient interactions among the TiO₂ nanoparticles (SI, Figure S2).

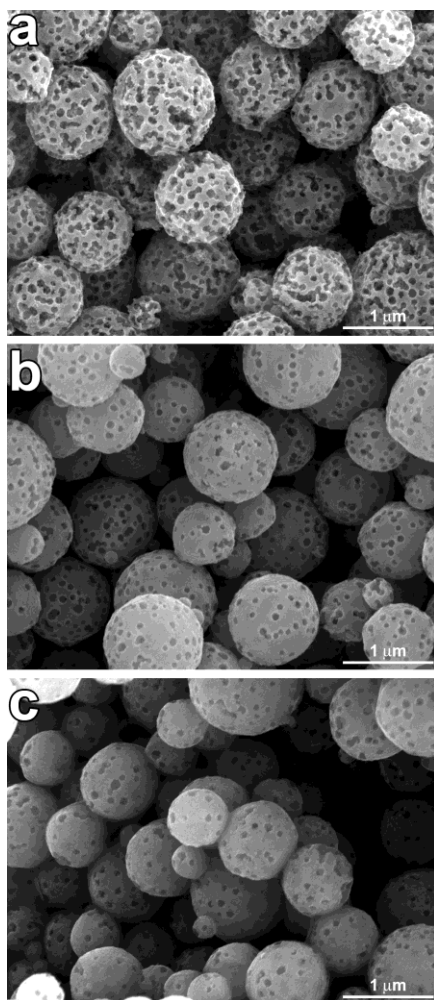


Figure 2. Scanning electron microscopy (SEM) images showing the effect of silica/titanium molar ratio on the particle morphology. Sample names and SiO_2/Ti ratios are (a) T11L, 1:1; (b) T13L, 1:3; (c) T15L, 1:5; all with initial silica colloid template of 70-100 nm diameter.

For all samples, the microspheres' composition was confirmed by bulk elemental analysis, which showed only about 0.3% of Si left after etching. Moreover, XPS analysis revealed the absence of Si on the material surface (SI, Figure S1) and the presence of surface traces of fluorine ($\text{F}/\text{Ti} \leq 0.12$ at/at) as fluoride species (683.7 eV)^{8a} remaining from the etching step.

USP process is substantially different from batch reactions in terms of the physicochemical interactions that occur during reaction. The USP process is unique in its continuous production of isolated sub- μm microreactors (i.e., each droplet formed by the nebulizer) in a hot-gas steam. Inside the droplets, after water evaporation, precursor precipitation and decomposition take place.^{4d-e,5-6} At this stage, the interactions between hot SiO_2 template particles surface and TiO_2

precursor become crucial in the material formation process, and especially the preferential formation of anatase vs. rutile.

We were particularly struck by the increasing concentration of anatase over rutile phases as a function of increasing silica surface area in the initial formulations shown in Table 1. As determined from the XRD, the solid microspheres produced by USP in the absence of a silica template are only 36% anatase (64% rutile). The porous microspheres, however, have a much greater fraction of anatase. Strikingly, the fraction of anatase increases monotonically with the initial colloidal silica template surface area (Table 1 and plotted in Supporting Information, Figure S5).

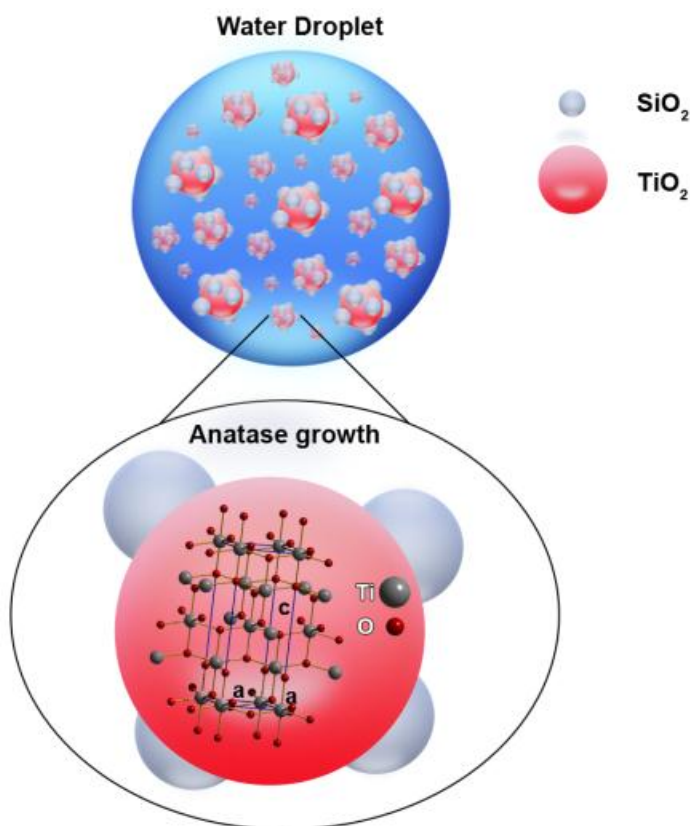


Figure 3. Schematic illustration of preferential anatase growth on the silica (e.g. 12 nm of diameter) surface inside a USP generated water droplet.

We suggest that the formation mechanism of the microspheres proceeds through a competition between homogeneous and heterogeneous nucleation. In the T_USP sample (i.e., in the absence of a silica template), TiO₂ is produced mainly by homogeneous nucleation thus promoting the growth of solid spheres mainly composed from the thermodynamically most stable phase, i.e., rutile. In the presence of colloidal SiO₂, however, the sites for heterogeneous nucleation

increase. We propose that the SiO₂ surface creates preferential growth of anatase phase titania from the decomposition of our Ti^{IV} salt (Figure 3). There is some limited precedent for this hypothesis: SiO₂ precursors (e.g., TEOS) enhance the phase stability of anatase in batch reactions.⁸ There are also a few studies of titania growth on silica particles, yielding amorphous TiO₂ coating,⁹ anatase particles deposition,^{4e} and or ion-directed anatase growth.^{10b,c}

In addition to the XRD data, the rutile/anatase ratios were qualitatively confirmed by the samples' band-gap (SI, Table S1). Diffuse reflectance data were converted to absorption coefficient values $F(R)$ according to the Kubelka-Munk equation.¹⁰ As expected, the band gap values so obtained correlate with the anatase content in the samples: the larger the rutile component, the smaller the band gap, which ranges from 2.92 eV for T_USP (36% anatase) to 3.31 eV for T13S (100% anatase). For comparison, titania nanoparticles of rutile and anatase have reported band gaps of 3.00 and 3.21 eV, respectively, whereas thin films of titania on alumina show band gaps of 3.25 and 3.75 eV, respectively.¹¹

In order to test the chemical reactivity of our porous titania microspheres, we examined the photocatalytic activities using gas phase catalytic degradation of NO_x degradation as a probe reaction (SI, Experimental Section).^{11b} T15M and Degussa P25 (used as a reference photocatalyst) show the lowest activity (~85% NO_x degradation after 150 min), while T_USP, T_USP_HF and T13L show only slightly higher activities (SI, Figure S6). However, considering the % NO_x degradation at 30 min per unit surface area, the best catalyst are T_USP and T_USP_HF, while all microsphere samples show an higher specific activity that by

-
- (9) (a) Yoshinaka, M.; Hirota, K.; Yamaguchi, O. *J. Am. Ceram. Soc.* **1997**, *80*, 2749. (b) Okada, K.; Yamamoto, N.; Kameshima, Y.; Yasumori, A.; MacKenzi, K. J. D. O. *J. Am. Ceram. Soc.* **2001**, *84*, 1591. (c) Kominami, H.; Kohno, M.; Matsunaga, Y.; Kera, Y. *J. Am. Ceram. Soc.* **2001**, *84*, 1178. (d) Anderson, C.; Bard, A. J. *J. Phys. Chem. B* **1997**, *101*, 2611. (e) Hirano, M.; Ota, K.; Iwata, H. *Chem. Mater.* **2004**, *16*, 3725.
- (10) (a) Hanprasopwattana, A.; Srinivasan, S.; Sault, A. G.; Datye A. K. *Langmuir* **1996**, *12*, 3173. (b) Yue, W.; Randorn, C.; Attidekou, P. S.; Zhou, W. *Adv. Funct. Mater.* **2009**, *19*, 2826. (c) Vermury, S.; Pratsinis, S. E. *J. Am. Ceram. Soc.* **1995**, *78*, 2984.
- (11) (a) Cappelletti, G.; Bianchi, C. L.; Ardizzone, S. *Appl. Catal. B* **2008**, *78*, 193. (b) Cappelletti, G.; Ardizzone, S.; Bianchi, C. L.; Gialanella, S.; Naldoni, A.; Pirola, C.; Ragaini, V. *Nanoscale Res. Lett.* **2009**, *4*, 97.
- (12) (a) Reyes-Coronado, D.; Rodriguez-Gattorno, G.; Espinosa-Pesqueira, M. E.; Cab, C.; de Coss, R.; Oskam, G. *Nanotech.* **2008**, *19*, 145605. (b) Young Ran Parka, Y. R.; Kim, K. J. *Thin Solid Films*, **2005**, *484*, 34-38

P25. Importantly, this trend appear to be directly related to the hydrophilicity vs. hydrophobicity of the samples (SI, Table S2 and Fig. S7).

In conclusion, we have used ultrasonic spray pyrolysis to prepare porous titania microspheres with tunable porosity and nanostructures and resulting control over their phase composition. We can tailor properties of the microspheres' by adjusting both the silica to titanium molar ratio and the silica particle sizes. Importantly, the silica template induces preferential growth of the anatase phase of titania from pyrolysis of the Ti^{IV} precursor. The porous titania microspheres also show a high photocatalytic activity in the gas phase for the decomposition of NO_x .

2.4.4.2 Supporting information

Experimental Section

Materials.

All chemicals were handled in air and are available commercially. Silica colloid Ludox AS-30 (30 wt.% suspension in water; 12 nm diameter), titanium(IV)bis(ammonium lactato)dihydroxide (50 wt.% water solution) were purchased from Aldrich Chemicals. Hydrofluoric acid (49 wt.%) was obtained from Acros Organics. Two SNOWTEX silica colloids (ST-XL: 35–50 nm, and ST-ZL: 70–100 nm) 40 wt.% water suspension were provided by Nissan Chemical Industries (Japan), while TiO_2 P25 was purchased from Degussa (Germany). Water was purified and filtered using a Barnstead Nanopure system.

Synthesis.

Porous TiO_2 Microspheres. The precursor solution was composed by titanium(IV) bis(ammonium lactato) dihydroxide (0.02 mol), purified water (50 mL, Barnstead Nanopure ion exchange) and colloidal silica variable in amount (Si : Ti molar ratio 1:1, 1:3, 1:5) and particle size (12 nm, 35-50 nm, 70-100 nm). A piezoceramic transducer operating at 1.65 MHz was used to nebulize the starting solution through a polyethylene membrane into a glass apparatus. The mist was then carried by an air flow rate of 1 standard liter per minute (SLPM) into a furnace where the temperature was set at 1000 °C. After 8 h of collection into water-filled bubblers, the white colloidal particles were obtained by centrifugation at $9000 \times g$. The products were washed with purified water three times and sampled for analysis.

TiO_2 Solid Microspheres (T_{USP}). Titanium dioxide spheres were synthesized using the same procedure as for porous titania microspheres but without adding colloidal silica as template.

Etching procedure. For all etched microspheres, removal of silica was done with HF 10 wt.% in water at room temperature. After 75 min., the particles were

centrifuged and washed three times with purified water and once with 100% ethanol.

Characterization.

Structural features of the prepared titanium dioxide microspheres have been determined by X-ray Diffraction powder (XRD) on a Siemens-Bruker D5000 diffractometer operating at 40 kV and 30 mA using a Cu K α radiation source ($\lambda = 1.5418 \text{ \AA}$). In a typical experiment, a scan rate of 1 deg./min. and a step size of 0.05 deg. was used. All data was worked out using Jade X-ray analysis software package. The powder morphology was observed with a JEOL 7000F field emission SEM operating at an acceleration voltage of 15 kV. Samples were prepared for analysis by the deposition of an absolute ethanol TiO $_2$ suspension on a silicon wafer, subsequently sputtered with a Pd-Au alloy. TEM micrographs were taken using a JEOL 2100 Cryo microscope operating at 200 kV. X-Ray Photoelectron Spectroscopy (XPS) was performed by a M-Probe Instrument (SSI) equipped with a monochromatic Al K α source (1486.6 eV) with a spot size of $200 \times 750 \text{ }\mu\text{m}$ and a pass energy of 25 eV, providing a resolution for 0.74 eV. With a monochromatic source, an electron flood gun was used to compensate for the build-up of positive charge on the insulator samples during the analysis.

The surface area of materials was investigated by nitrogen adsorption studies using the Brunauer-Emmett-Teller (BET) method. Measurements have been performed using a Nova 2200e Surface Area and Pore Analyzer (Quantachrome Instruments) at liquid nitrogen temperature (-196 °C). A UV-vis spectrometer (LAMBDA 35, Perkin-Elmer Co.), was used to perform UV-vis diffuse reflectance measurements of powders.

Photocatalytic testing.

In the photocatalytic oxidation of nitrogen oxides (NO $_x$), immobilized particulate TiO $_2$ layers (ca. 50 mg) were prepared on glass sheets by deposition from a suspension of the samples in isopropanol. The immobilized photocatalyst was placed into a pyrex glass reactor (with a volume of 25 L) and irradiated with an halogen lamp (Jelosil, model HG500) emitting in the 340–400 nm wavelength range, with a nominal power of 500 W, at room temperature. The distance between the light source and the reactor was properly adjusted so that the UV irradiance at the sample surface is $10 \text{ W/m}^2 \pm 0.5 \text{ W/m}^2$. The relative humidity was kept constant in all the runs (50%). Air, NO $_x$ (NO = 10%, NO $_2$ = 90%), and N $_2$ gas streams were mixed to obtain the desired NO $_x$ concentration (300 ppb) inside the photoreactor. The photodegradation products concentrations (NO and NO $_2$) were continuously monitored by an online chemiluminescent analyzer (Teledyne

Instruments M200E). The NO_x adsorption onto the TiO₂ layer was determined through dark experiments.

Table S1. X-Ray Photoelectron spectroscopy analysis (at/at %), band gap values and anatase crystallite size of the porous microspheres samples and reference sample (P25, T_USP, T_USP_HF).

Sample	F/Ti	O/Ti	OH/O _{tot}	band gap (eV)	Anatase crystallite size (nm) [§]
P25	—	2.6	0.18	3.17	25
T_USP	—	3.8	0.30	2.92	41
T_USP_HF	0.25	5.7	0.29	2.94	35
T15L	0.08	3.0	0.20	2.91	41
T15M	0.06	2.8	0.17	2.97	39
T15S	0.10	2.8	0.22	3.13	27
T13L	0.03	2.9	0.19	3.05	40
T13M	0.12	2.7	0.13	3.20	35
T13S	0.07	2.6	0.21	3.31	23
T11L	0.05	2.9	0.18	3.23	33
T11M	—	—	—	—	28
T11S	—	—	—	—	14

[§] calculate by Sherrer's equation applied to the anatase (101) peak.

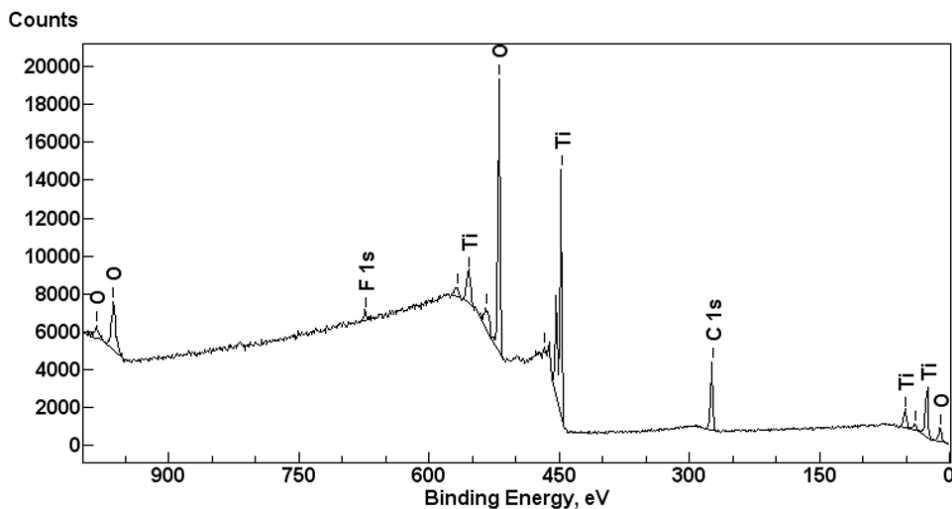


Figure S1. XPS Survey spectra of TiO₂ porous micro spheres synthesized with molar ratio SiO₂/Ti=1:1 and silica size 70-100 nm.

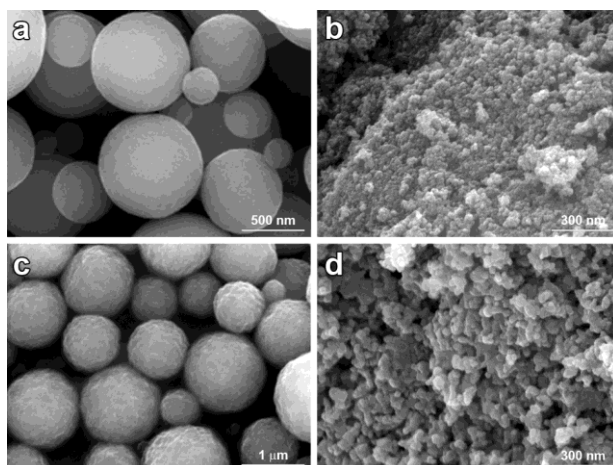


Figure S2. SEM micrographs shown microspheres' morphologies before etching (a, T11S) (c, T11M) and after 75 min. etching (b, T11S) (d, T11M) with HF 10 wt.%.

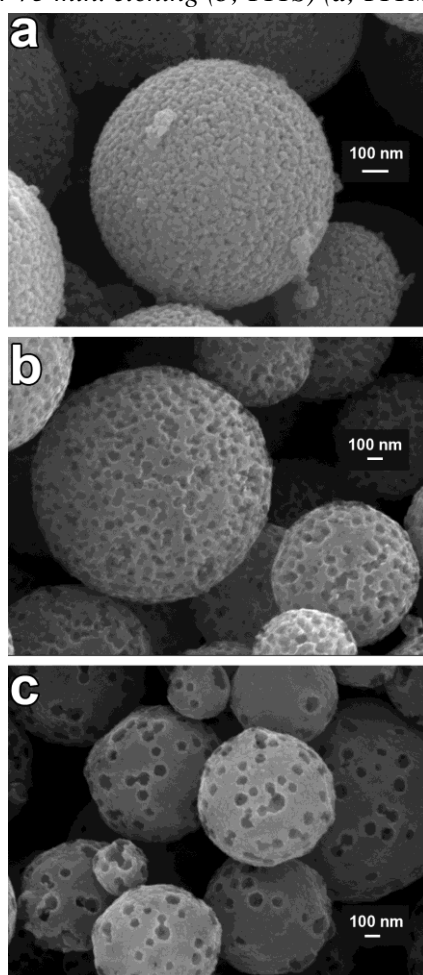


Figure S3. SEM micrographs shown microspheres' porosity of the sample (a) T13S (b), T13M, (c) T13L.

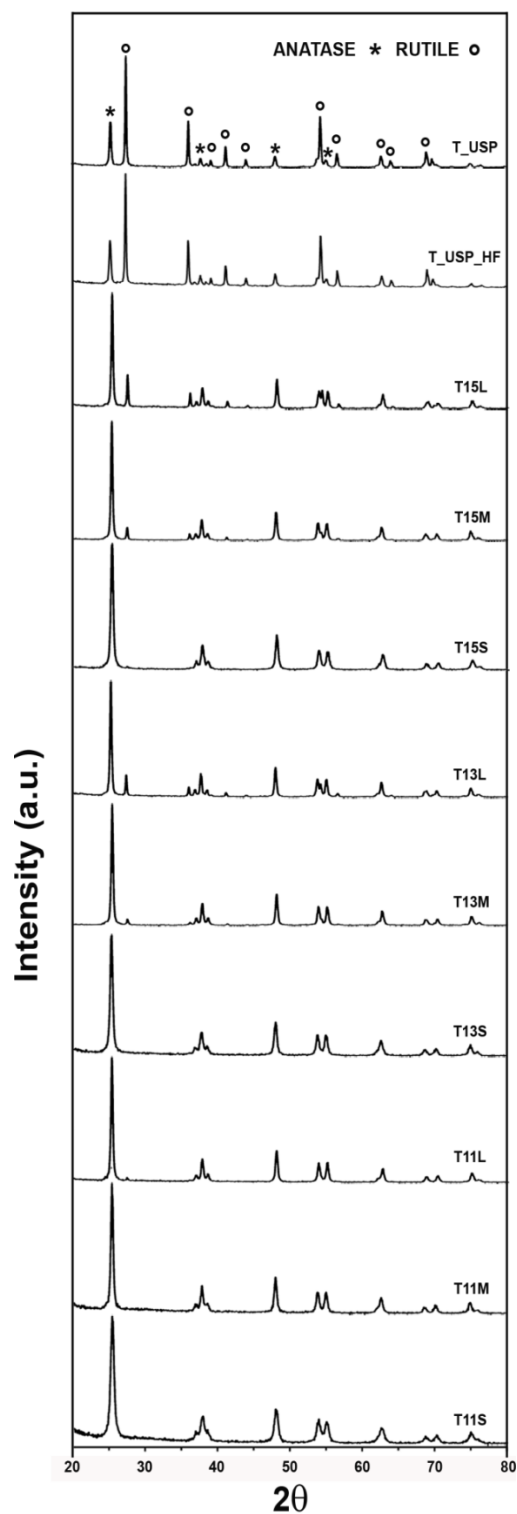


Figure S4. X-ray powder diffraction patterns of all USP titania samples synthesized.

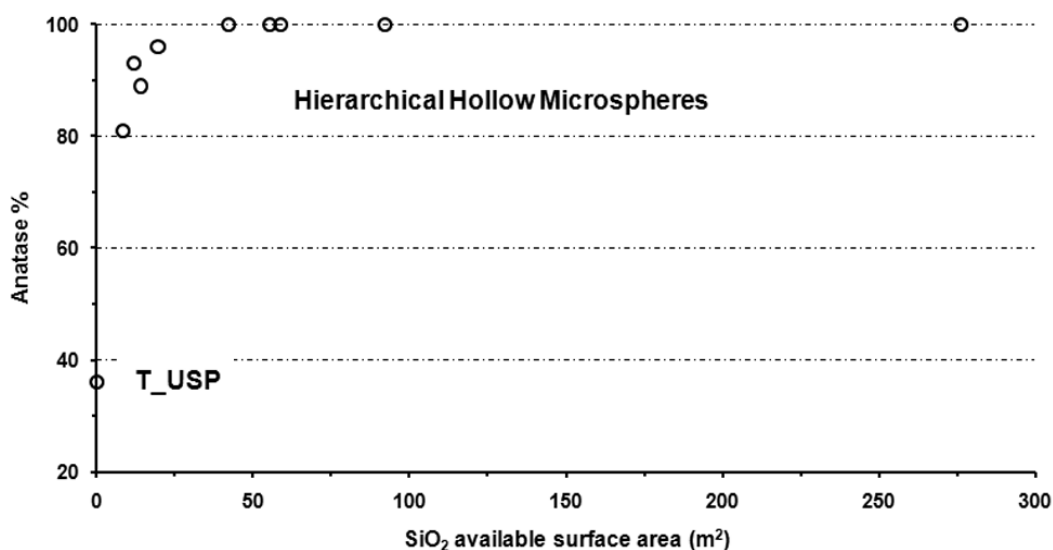


Figure S5. Anatase content of the porous microspheres as a function of initial SiO₂ template surface area. Silica available surface area was calculated as following: amount of SiO₂ added to the precursor solution \times B.E.T. surface area of SiO₂. Ludox AS-30 silica colloid has a surface area of 230 m²/g (according to Sigma Aldrich product specifications); SNOWTEX ST-XL and ST-ZL silica colloids have surface areas of 49 m²/g and 35 m²/g, respectively (Glazer, M.; Fidanza, J.; McGall, G.; Frank, C. *Chem. Mater.* **2001**, 13, 4773).

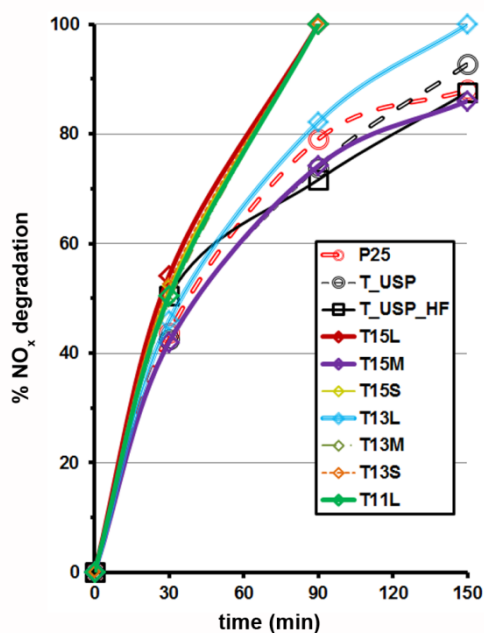


Figure S6. Photocatalytic activity of porous microspheres and reference samples on the degradation of NO_x after 150 minutes of reaction time.

Table S2. Photocatalytic activity of USP microspheres and reference samples for the degradation of NO_x after 30 min of reaction (% Conversion_{@30}) and $\text{OH}/\text{O}_{\text{tot}}$ (XPS, at/at %) per unit surface area.

Sample	% degradation _{@30}	(% degradation _{@30}) $\times \text{m}^{-2}$	$(\text{OH}/\text{O}_{\text{tot}}) \times \text{m}^{-2} \times 10^{-3}$
P25	43.8	0.89	3.7
T_USP	42.5	42.50 [†]	300 [†]
T_USP_HF	50.5	50.50 [†]	290 [†]
T15L	54.2	9.03	33.3
T15M	38.0	2.38	10.6
T15S	51.2	1.60	6.9
T13L	45.9	5.10	21.1
T13M	49.4	2.60	6.8
T13S	52.4	1.09	4.4
T11L	50.4	3.60	12.9
T11M	—	—	—
T11S	—	—	—

[†] T_USP and T_USP_HF surface area was approximated to 1 m²/g.

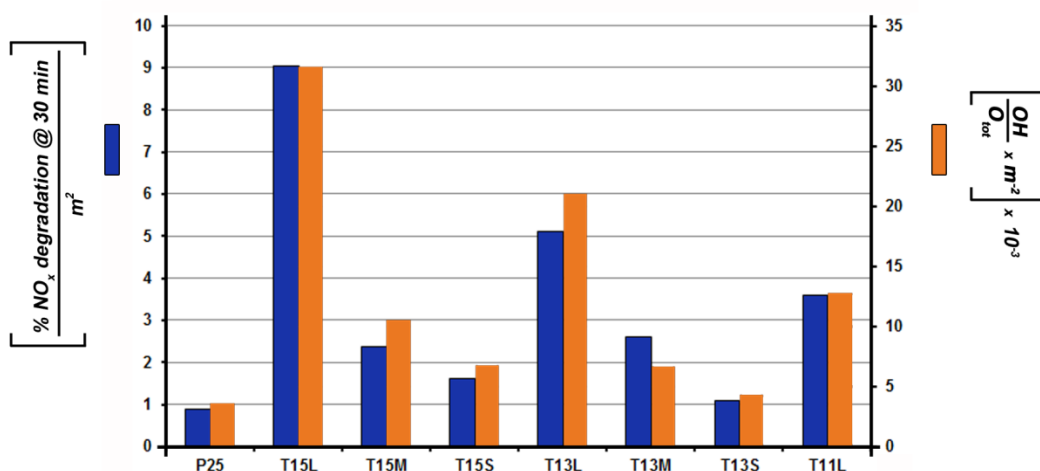


Figure S7. Bar chart of representing the % NO_x degradation at 30 min per unit surface area in comparison with the hydrophilicity vs hydrophobicity ($\text{OH}/\text{O}_{\text{tot}}$) per unit surface area. The values are reported for P25 by Degussa and all the microsphere samples.

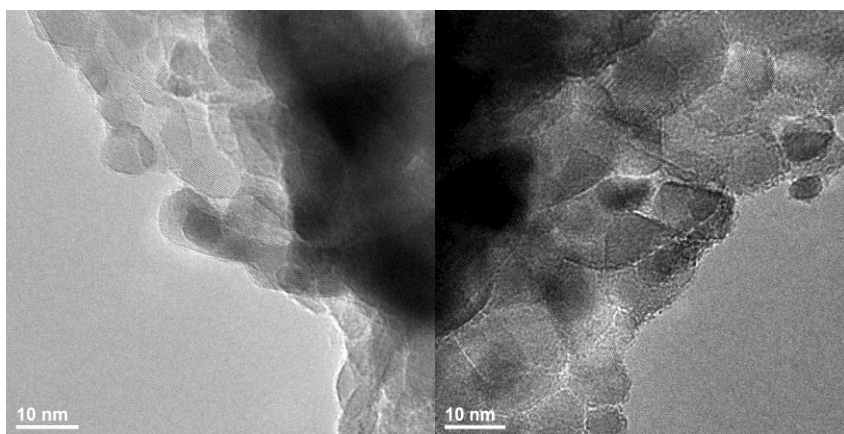


Figure S8. TEM images of the porous titania microspheres T13M, showing the assembly of individual single crystalline nanoparticles with an average diameter of 20 nm.

2.5 Degradation of pollutants in the liquid phase by Advanced Oxidation Processes

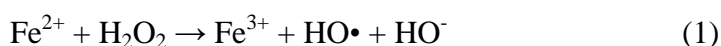
2.5.1 Mineralisation of Surfactants Using Ultrasound and the Advanced Fenton Process

A. Naldoni, A. Schibuola, C. L. Bianchi and D. H. Bremner, *Water Air Soil & Pollution* **2010**, DOI 10.1007/s11270-010-0493-y.

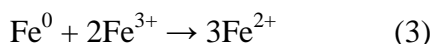
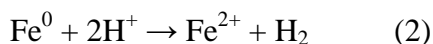
2.5.1.1 Introduction

Surfactants are amphiphilic molecules that accumulate at interfaces, decrease interfacial tension and form aggregate structures such as micelles. Due to these properties, surfactants alter interfacial behaviour and impact on the way other molecules behave at interfaces and in solution. Surfactants are used in a number of applications and products in the petroleum, food, pharmaceuticals and therapeutics, cosmetic, environmental bioremediation, agricultural and biocatalysis industries (Singh et al. 2007). Although they are generally not directly toxic, these compounds have intrinsic structural properties which can induce different environmental problems such as hindering both the dissolution of atmospheric oxygen into natural waters and the sedimentation of floating particles, having potential to disrupt hormonal systems of aquatic organisms and might subsequently alter the ecosystem (Ikehata and El-Din 2004). Surfactants can normally be removed from water using the activated sludge technique, but complete elimination cannot be guaranteed. Traditional techniques for such contaminants in soil include landfill, air stripping/carbon adsorption, incineration, biological processing and chemical treatment. However, incineration, adsorption and landfill merely transfer the contaminant to another phase or location and produce a potentially dangerous and toxic secondary disposal requirement. Biodegradation is very sensitive to numerous environmental factors, is slow, often produces unpredictable results and is uneconomical for highly concentrated waste effluents. For these reasons, in the past few decades, Advanced Oxidation Processes (AOPs) have been used as alternative techniques in the degradation of surfactants and, generally, for wastewater treatment. AOPs are based on the generation of the hydroxyl radical ($\text{HO}\cdot$), one of the most powerful oxidants known ($E_0 = 2.73 \text{ V}$), and which are capable of reacting non-selectively with virtually all organic compounds. Several authors report surfactant remediation experiments using several oxidising agents (Mendez- Diaz et al. 2009) and AOPs such as photocatalysis supported by TiO_2 (Hidaka et al. 1995; Ohtaki et al. 2000; Zhang et al. 2003; Vohra and Tanaka 2003;

Zhang et al. 2004; Horvath et al. 2005), ultrasound (US; Manousaki et al. 2004; Yim et al. 2002; Yang et al. 2005) and Fenton or Fenton-like processes (Lin et al. 1999; Bandala et al. 2008; Amat et al. 2004), and most of these achieve good remediation in short reaction times (a few hours instead of days as happens using conventional wastewater treatment with activated sludge). The classical Fenton oxidation process (Fenton 1894; Haber and Weiss 1934; Barb et al. 1949, 1951a, b) utilises the reaction of aqueous iron (II) salt with hydrogen peroxide to generate hydroxyl radicals, which are then used to carry out chemical oxidation or to degrade recalcitrant organic pollutants in wastewater treatment Eq. 1. The characteristics and uses of Fenton and Fenton-like processes have been extensively reviewed (Pignatello et al. 2006). The usual Fenton process is applied in the degradation of industrial wastewater treatment, and it has also been investigated as a pre-treatment process for surfactants (Wang et al. 2008).



The classic Fenton process has been used extensively for the degradation of organic pollutants (Pignatello et al. 2006), but this methodology suffers from a number of drawbacks. An improvement on the Fenton process is the advanced Fenton process (AFP), which uses zero valent iron (ZVI) instead of expensive iron salts, which need to be removed later in the usual Fenton process. In the AFP, hydrogen peroxide and ZVI in acidic conditions react to generate hydroxyl radicals and ferric ions (Bremner and Burgess 2004; Namkung et al. 2005). These ferric ions are then recycled back to ferrous ions by further interaction with the ZVI surface in a pseudo catalytic process (Eqs. 2 and 3). Furthermore, the use of ultrasound in conjunction with AFP activates the catalyst and helps clean the metal surface and also induces cavitation, which enhances the production of hydroxyl radicals.



The degradation of organic pollutants by ultrasound in conjunction with AFP has been described (Bremner et al. 2006, 2008; Namkung et al. 2008; Zhang et al. 2009; Devi et al. 2009), but to our knowledge, there has been no report on the degradation of aqueous surfactants using this methodology. Therefore, in this study, we describe the degradation of two surfactants, sodium dodecylbenzene sulfonate (DBS) and dodecyl pyridinium chloride (DPC) using the AFP in combination with ultrasonic irradiation. DBS, an anionic surfactant, is an example

of a linear alkylbenzene sulfonate which is the major type of surfactant produced industrially. Also studied was the cationic surfactant, DPC, which has bactericidal and fungicidal properties and was chosen for investigation because of its high resistance towards classical wastewater treatment. The purpose of the present investigation was to examine the effects of operating conditions such as temperature, the presence or absence of ultrasound, the effect of the addition of ZVI and/or hydrogen peroxide, the pH and reaction time. The extent of mineralisation of DBS and DPC was determined by measuring the decrease in total organic carbon (TOC) content.

2.5.1.2 Experimental

Materials

Sodium DBS, DPC hydrate, ZVI powder (325mesh) and hydrogen peroxide (30% w/w in water) were purchased from Aldrich and were used as received. Water was purified using an Elga Option 3 de-ioniser and was used to prepare all solutions.

Apparatus

The TOC content of the initial surfactant (DBS and DPC) aqueous solution and the samples taken from the reaction medium were measured by oxidation analysis (Model 1020 TOC Analyzer from OI-Analytical). The sono-Fenton experiments were performed in a cylindrical glass reactor making use of a commercial ultrasonic processor (Cole-Parmer, 400Wmodel) equipped with a titanium probe with a 1 cm diameter tip capable of operating either continuously or in a pulse mode at a fixed frequency of 20 kHz. In the present work, the experiments were carried out with the probe working in pulses, 4.0 s on and 2 s off, which allows the system to dissipate some of the heat generated by the ultrasonic waves. The intensity of the irradiation was adjusted to 50% of ultrasonic power amplitude, which corresponds to a calorimetric measurement of 18W.

Experimental Methodology

In a typical run, the probe was immersed in a 1000 mL cylindrical glass reactor filled with 500 mL of aqueous surfactant stock solution (1 mM is equivalent to $[\text{TOC}]_0$ of DBS = 216 ppm and $[\text{TOC}]_0$ of DPC = 204 ppm). The pH was adjusted to 2.5 with appropriate amounts of H_2SO_4 (1 mM). The temperature was kept constant at $20 \pm 5^\circ\text{C}$ or $40 \pm 5^\circ\text{C}$ during all reactions by an external cooling bath as necessary. The appropriate amounts of hydrogen peroxide (2.38 g/L) and ZVI (0.6 g/L) were added to the reactor just before beginning the reaction. Aliquots of the reaction mixture (10 mL) were removed by syringe every 15 min during the

reaction and filtered through 0.45- μ m polycarbonate membranes before being analysed (pH and total organic carbon measurement). Silent experiments were carried out in an identical manner without the input of ultrasound but with an overhead stirrer (250 rpm). All reactions were performed in triplicate, and the error bars are shown on the graphs.

2.5.1.3 Results and Discussion

DBS Degradation with 20 kHz Ultrasound

DBS although, relatively benign, can give rise to toxic oxidation products on traditional biological or chemical treatments (Kirmele and Swisher 1977; Beltran et al. 2000). A recent review (Mendez-Diaz et al. 2009) compared the effectiveness of different oxidising agents for removal of DBS but only measured the rates of removal and did not determine the extent of mineralisation. In the current work, we wished to examine the effect of the advanced Fenton process on the conversion, by hydroxyl radicals, of DBS into low carbon containing organics as measured by TOC content. When DBS (1 mM) in 500 mL of de-ionised water, with pH adjusted to 2.5 with dilute sulphuric acid, was stirred at 250 rpm with hydrogen peroxide (2.38 g/L), no decrease in TOC was observed over 60 min. A similar result was obtained when ZVI (0.6 g/L) replaced the hydrogen peroxide. The amounts of hydrogen peroxide and ZVI used were based on previous work (Chand et al. 2009) where they were optimised for the degradation of phenol and consequently were chosen at these levels for this investigation. However, when both hydrogen peroxide (2.38 g/L) and ZVI (0.6 g/L) were present (the AFP; Namkung et al. 2005) at the beginning of the reaction, a 51% decrease in TOC was seen after 15 min stirring at 20°C, indicating that stirring alone is reasonably efficient for mineralisation of DBS using the AFP (Fig. 1). The reaction probably ceases at this time as the hydrogen peroxide which was added initially is used up. Interestingly, around half of the mineralisation occurs in the first 5 min of treatment and may be even faster than this, as seen from the inset in Fig. 1. The additional effect of introducing ultrasound is illustrated in Fig. 2 where the reaction was stirred for 60 min at 20°C, and then 20 kHz ultrasound was applied for 4 s on and 2 s off for a further 60 min. After an induction period of about 15 min, the TOC content dropped to 50% and remained reasonably constant for the next 45 min. When ultrasound was introduced, there was little effect for 10 min, but then the TOC dropped to about 40% after 120 min. This increased mineralisation with the addition of US may be due to the generation of additional hydrogen peroxide from sonication of water though generally this is not a very efficient process. However, other effects such as mass transfer and enhanced corrosion of the iron surface

cannot be discounted. In an attempt to increase the amount of mineralisation even further, the reaction was carried out at 40°C, and the comparison between the two temperatures is shown in Fig. 2.

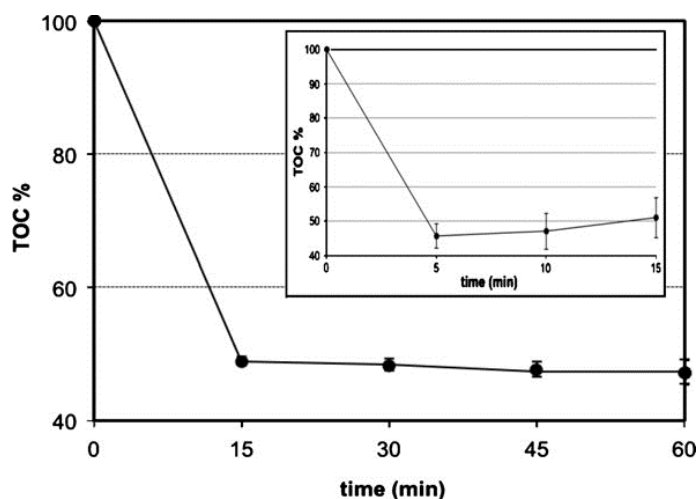


Fig. 1 Mineralisation of DBS with AFP and stirring at 20°C. Inset: kinetics in the first 15 min of reaction.

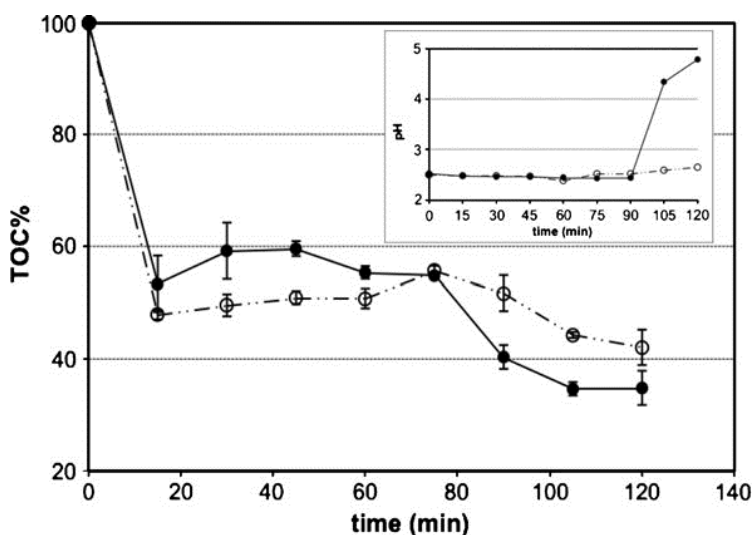


Fig. 2 Mineralisation of DBS using the AFP with stirring for 1 h and then US 1 h at 20°C (dashed line) and AFP with stirring for 1 h and then US 1 h at 40°C (solid line); change of pH (inset).

It can be seen that there is a slight difference between the degradation at the two temperatures with the rates being similar but the remaining TOC, after 120 min, was 40% at 20°C and 35% at 40°C, respectively. At the higher temperature (40°C), there was a significant change in pH going from 2.5 at the beginning of reaction to 4.8 at the end of the degradation (inset Fig. 2). To obtain high mineralisation,

ultrasound was introduced from the beginning (in combination with AFP) at 40°C, and various other reaction conditions were investigated. When the initial amounts of hydrogen peroxide and ZVI were maintained as above but when the pH reached 4, extra sulphuric acid was added to return the pH to 2.5 (pH control), the extent of mineralisation was 61%. If extra H₂O₂ (1.19 g) was added after 75 min with maintenance of pH at 2.5, then the extent of mineralisation increased to 71% after 120 min.

However, if the pH was maintained at 2.5 throughout and extra amounts of ZVI (0.3 g) and H₂O₂ (1.19 g) were both added at 75 and 90 min, then the extent of mineralisation of DBS was increased, substantially, to 93% (data not shown). Advanced oxidation processes have been investigated previously for surfactant wastewater treatment using Fenton oxidation (Lin et al. 1999; Bandala et al. 2008); electrochemical oxidation (Gu et al. 2006), ozone and/or UV irradiation (Amat et al. 2007) and ozone along with powdered activated carbon (Rivera- Utrilla et al. 2006). Beltran and co-workers (2000) have also reported the kinetics of decomposition of DBS with ozone, but most of these studies have concentrated on the kinetics of removal of the surfactant rather than the decrease in total organic carbon. It is well known that hydroxyl radicals are exceptionally powerful oxidants, and the oxidative mechanism proceeds by electrophilic attack on the aromatic ring of the substrates. In the case of the model compound phenol, there are a number of oxidised aromatic intermediates before the ring is broken open, leading eventually to small organic entities such as maleic, acetic and formic acids along with CO₂ and H₂O (Santos et al. 2002; Bremner et al. 2006). In the case of DBS, it is expected that the aromatic ring is hydroxylated by HO• several times before ring opening, and then further oxidation by hydroxyl radical/hydrogen peroxide will produce β-dicarboxylic acids which will decarboxylate to give mono acids and CO₂ (Fig. 3). Continuing oxidation will afford small organic acids and CO₂ which accounts for the residual organic content in the case of the former and a decrease in TOC from the latter. This mechanism is partially supported by the work of Fernandez et al. (2004) who examined the products of photodegradation and ozonation of alkyl benzene- sulphonates. With the conditions used in the AFP, merely stirring with H₂O₂ and ZVI produces a reasonable flux of hydroxyl radicals giving a 50% decrease in TOC. This is augmented slightly by application of US as a result of enhanced mass transfer and possibly sonochemical production of hydrogen peroxide. There is a slight improvement in mineralisation by increasing the reaction temperature to 40°C, but this may be due to faster kinetics resulting in hydrogen peroxide being available for a slightly longer time. The increase in pH is noteworthy and is ascribed to production of hydrated iron salts which are no longer

ultrasound, in combination with AFP, was introduced from the beginning at 40°C with pH control, then the extent of mineralisation was around 50%. If extra H₂O₂ was added at 45 min with pH control, then 57% mineralisation was seen (Fig. 5).

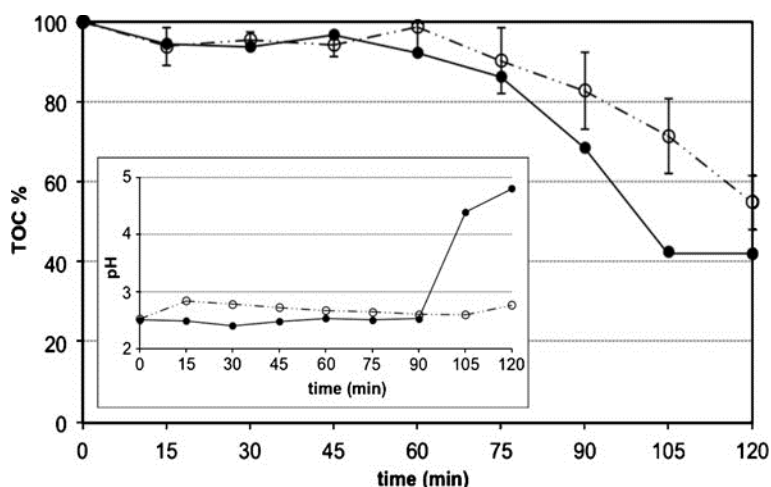


Fig. 4 Mineralisation of DPC using the AFP with stirring for 1 h and then US 1 h at 20°C (dashed line) and AFP with stirring for 1 h and then US 1 h at 40°C (solid line); change of pH (inset).

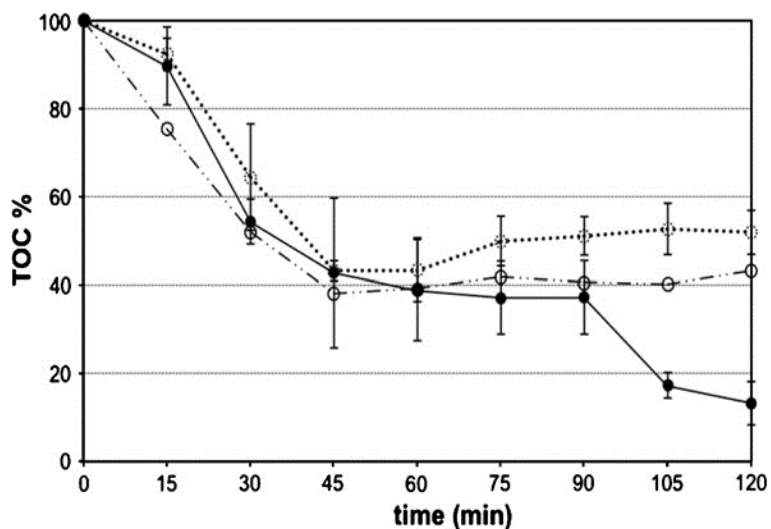


Fig. 5 Mineralisation of DPC with AFP and US from the beginning at 40°C: pH control (dotted line), pH control and H₂O₂ additions (dashed line), pH control and ZVI/H₂O₂ additions (solid line).

If extra ZVI (0.3 g) and hydrogen peroxide (1.19 g) were introduced at 45, 60, 75, and 105 min at 40°C and the pH was maintained at 2.5 by addition of H₂SO₄ (1 mM), then 87% mineralisation of DPC was observed after 120 min. Thus, it can be seen that the addition of all the extra reagents are required to gain this high removal

of carbon although these conditions have not been optimised. Little work has been reported on the oxidation of DPC using hydroxyl radicals. However, it is expected that the reaction will proceed in a similar manner to that described in section 3.1. In this case little reaction was observed at 20°C with just stirring with the reagents (unlike for DBS), and only 45% removal of TOC was seen on the additional application of ultrasound. If the full range of excess oxidants, extra ZVI and with stirring and US were used, then only 13% TOC remained after treatment at 40°C. The lack of reaction at 20°C is a reflection of the relative stability to hydroxyl attack on the positively charged pyridinium ring in DPC compared to the benzene ring in DBS.

Latent Remediation of DBS and DPC

In order to minimise energy input during the mineralisation process, it was decided to investigate the effect of minimal ultrasonic treatment along with silent processing in a process termed latent remediation (Chakinala et al. 2009). In this procedure the pollutant is irradiated for a short time with ultrasound in the presence of iron and hydrogen peroxide, and then the solution is left silent for 24 h and the TOC content then measured. When DBS was stirred with ZVI (0.6 g/L) and hydrogen peroxide (2.38 g/L) at pH 2.5 for 60 min at 20°C, then 51% mineralisation occurred. If the stirring was stopped after 60 min and the sample left undisturbed with no added reagents for a further 24 h, the amount of mineralisation increased to 83%. A similar result was obtained if the sample containing ZVI and H₂O₂ stirred for 1 h at 20°C was irradiated with 20 kHz ultrasound for further hour of treatment (58%) and then left for 24 h (77%). Interestingly, performing the same experiment at 40°C for the first hour and then leaving the solution at room temperature overnight resulted in no improvement in mineralisation (65%) possibly due to the higher initial temperature decomposing some of the hydrogen peroxide. The effect of latent remediation was also examined for DPC. Merely stirring DPC with ZVI and hydrogen peroxide for 60 min at 20°C resulted in only 2% mineralisation. If the stirring was stopped after 60 min and the sample left undisturbed for a further 24 h, the amount of mineralisation increased to 18%. If the DPC solution was stirred using the usual AFP conditions for 1 h and ultrasound applied for further 1 h, then 45% mineralisation was seen. If this solution was then left silent for 24 h, the TOC reduced to 70%. Again the higher temperature had a negative effect on the latent remediation: At 40°C, the extent of mineralisation observed was constant (58%) after 2 and 24 h. Further work on the exact mechanism involved in latent remediation is ongoing.

2.5.1.4 Conclusions

Generally, surfactants are relatively resistant to degradation using conventional oxidation processes. However, when sodium DBS and DPC are separately treated with ZVI and hydrogen peroxide at pH = 2.5 along with the application of 20 kHz ultrasound, extensive mineralisation is observed. DBS is partially decomposed at 20°C, but if the temperature is raised to 40°C, then the extent of mineralisation is increased to 93%. When the oxidation of DPC is attempted at 20°C, under identical conditions to DBS, it proves to be recalcitrant, but at 40°C, then 87% mineralisation of DPC is obtained. A novel energy saving process (latent remediation) is also described where mineralisation continues even after energy input has ceased, and future work will concentrate on establishing the mechanism of this process. Although the concentrations of surfactants used in this study are well above those normally found in water, the current work illustrates the high effectiveness of the advanced Fenton process and acts as a model for mineralisation studies. Indeed our previous work has shown that highly dilute solutions of pollutants (as found in wastewater) are even more readily mineralised.

2.5.1.5 References

- Amat, A., Arques, A., Miranda, M. A., & Segui, S. (2004). Photo-Fenton reaction for the abatement of commercial surfactants in a solar pilot plant. *Solar Energy*, 77, 559–566.
- Amat, A. M., Arques, A., Miranda, M. A., Vincente, R., Segui, S. (2007). Degradation of two commercial anionic surfactants by means of ozone and/or UV irradiation. *Environmental Engineering Science*, 24, 790–794.
- Bandala, E. R., Pelaez, M. A., Salgado, M. J., & Torres, L. (2008). Degradation of sodium dodecylbenzene sulphate in water using solar driven Fenton-like advanced oxidation processes. *Journal of Hazardous Materials*, 151, 578–584.
- Barb, W. G., Baxendale, J. H., George, P., & Hargrave, K. R. (1949). Reactions of ferrous and ferric ions with hydrogen peroxide. *Nature*, 163, 692–694.
- Barb, W. G., Baxendale, J. H., George, P., & Hargrave, K. R. (1951a). Reactions of ferrous and ferric ions with hydrogen peroxide. Part 1—the ferrous ion reaction. *Transactions of the Faraday Society*, 47, 462–500.
- Barb, W. G., Baxendale, J. H., George, P., & Hargrave, K. R. (1951b). Reactions of ferrous and ferric ions with hydrogen peroxide. Part 2—the ferric ion reaction. *Transactions of the Faraday Society*, 47, 591–616.

- Beltran, F. J., Garcia-Araja, J. F., & Alvarez, P. M. (2000). Sodium dodecylbenzenesulfonate removal from water and waste-water. 1. Kinetics of decomposition by ozonation. *Industrial & Engineering Chemistry Research*, 39, 2214–2220.
- Bremner, D. H., & Burgess, A. E. (2004). US Patent 6,692,632, University of Abertay Dundee.
- Bremner, D. H., Burgess, A. E., Houlemare, D., & Namkung, K.-C. (2006). Phenol degradation using hydroxyl radicals generated from zero-valent iron and hydrogen peroxide. *Applied Catalysis B: Environmental*, 63, 15–19.
- Bremner, D. H., Di Carlo, S., Chakinala, A. G., & Cravotto, G. (2008). Mineralisation of 2,4-dichlorophenoxyacetic acid by acoustic or hydrodynamic cavitation in conjunction with the advanced Fenton process. *Ultrasonics Sonochemistry*, 15, 416–419.
- Chakinala, A. G., Gogate, P. R., Burgess, A. E., & Bremner, D. H. (2009). Industrial wastewater treatment using hydrodynamic cavitation and heterogeneous advanced Fenton processing. *Chemical Engineering Journal*, 152, 498–502.
- Chand, R., Ince, N. H., Gogate, P. R., & Bremner, D. H. (2009). Phenol degradation using 20, 300 and 520 kHz ultrasonic reactors with hydrogen peroxide, ozone and zero valent metals. *Separation and Purification Technology*, 67, 103–109.
- Devi, L. G., Kumar, S. G., Reddy, K. M., & Munikrishnappa, C. (2009). Photo degradation of methyl orange an azo dye by advanced Fenton process using zero valent metallic iron: Influence of various reaction parameters and its degradation mechanism. *Journal of Hazardous Materials*, 164, 459–467.
- Fenton, H. J. H. (1894). Oxidation of tartaric acid in presence of iron. *Journal of the Chemical Society*, 65, 899–910.
- Fernandez, J., Riu, J., Carcia-Calvo, E., Rodriguez, A., Fernandez-Alba, A. R., & Barcelo, D. (2004). Determination of photodegradation and ozonation by products of linear alkylbenzene sulfonates by liquid chromatography and ion chromatography under controlled laboratory experiments. *Talanta*, 64, 69–79.
- Gu, L., Wang, B., Ma, H., & Kong, W. (2006). Catalytic oxidation of anionic surfactants by electrochemical oxidation with CuO–Co₂O₃–PO₄
- Haber, F., & Weiss, J. (1934). The catalytic decomposition of hydrogen peroxide by iron salts. *Proceedings of the Royal Society A*, 134, 332–351.

- Hidaka, H., Nohara, K., Zhao, J., Pellizzetti, E., & Serpone, N. (1995). Photodegradation of surfactants XIV. Formation of NH_4^+ and NO_3^- ions for the photocatalyzed mineralization of nitrogen-containing cationic, non-ionic and amphoteric surfactants. *Journal of Photochemistry Photobiology A: Chemistry*, 91, 145–152.
- Horvath, O., Bodnar, E., & Hegyi, J. (2005). Photoassisted oxidative degradation of surfactants and simultaneous reduction of metals in titanium dioxide dispersions. *Colloids and Surfaces A: Physicochemical Engineering Aspects*, 265, 135–140.
- Ikehata, K., & El-Din, M. G. (2004). Degradation of recalcitrant surfactants in wastewater by ozonation and advanced oxidation processes: A review. *Ozone Science and Engineering*, 26, 327–343.
- Kirmele, R. A., & Swisher, K. D. (1977). Reduction of aqueous toxicity of linear alkylbenzene sulfonate (LAS) by biodegradation. *Water Research*, 11, 31–37.
- Lin, S. H., Lin, C. M., & Leu, H. G. (1999). Operating characteristics and kinetic studies of surfactants wastewater treatment by Fenton oxidation. *Water Research*, 33, 1735–1741.
- Manousaki, E., Psillakis, E., Kalogerakis, N., & Mantzavinos, D. (2004). Degradation of sodium dodecylbenzene sulfonate in water by ultrasonic irradiation. *Water Research*, 38, 3754–3759.
- Mendez-Diaz, J. D., Sanchez-Polo, M., Rivera-Utrilla, J., & Bautista-Toledo, M. I. (2009). Effectiveness of different oxidizing agents for removing sodium dodecylbenzene sulphonate in aqueous systems. *Water Research*, 43, 1621–1629.
- Namkung, K.-C., Burgess, A. E., & Bremner, D. H. (2005). A Fenton-like oxidation process using corrosion of iron metal sheet surfaces in the presence of hydrogen peroxide: A batch process. *Environmental Technology*, 26, 341–352.
- Namkung, K. C., Burgess, A. E., Bremner, D. H., & Staines, H. (2008). Advanced Fenton processing of aqueous phenol solutions: A continuous system study including sonication effects. *Ultrasonics Sonochemistry*, 15, 171–176.
- Ohtaki, M., Sato, H., Fujii, H., & Eguchi, K. (2000). Intramolecularly selective decomposition of surfactant molecules on photocatalytic oxidative degradation over TiO_2 photocatalyst. *Journal of Molecular Catalysis A: Chemistry*, 155, 121–129.

Pignatello, J. J., Oliveros, E., & MacKay, A. (2006). Advanced oxidation processes for organic contaminant destruction based on the Fenton reaction and related chemistry. *Environmental Science and Technology*, 36,1–84.

Rivera-Utrilla, J., Mendez-Diaz, J., Sanchez-Polo, M., Ferro- Garcia, M. A., & Bautista-Toledo, I. (2006). Removal of the surfactant sodium dodecylbenzenesulphonate from water by simultaneous use of ozone and powdered activated carbon: Comparison with systems based on O₃ and O₃/H₂O₂. *Water Research*, 40, 1717–1725.

Santos, A., Yustos, P., Quintanilla, A., Rodriguez, S., & Garcia- Ochoa, F. (2002). Route of the catalytic oxidation of phenol in aqueous phase. *Applied Catalysis B: Environmental*, 39,97–113.

Singh, A., Van Hamme, J. D., & Ward, O. D. (2007). Surfactants in microbiology and biotechnology: Part 2. Application aspects. *Biotechnology Advances*, 25,99–121.

Vohra, M. S., & Tanaka, K. (2003). Photocatalytic degradation of aqueous pollutants using silica-modified TiO₂. *Water Research*, 37, 3992–3996.

Wang, X.-J., Song, Y., & Mai, J.-S. (2008). Combined Fenton oxidation and aerobic biological processes for treating a surfactant wastewater containing abundant sulphate. *Journal of Hazardous Materials*, 160,344–348.

Yang, L., Rathman, J. F., & Weavers, L. K. (2005). Degradation of alkylbenzene sulfonate surfactants by pulsed ultrasound. *Journal of Physical Chemistry B*, 109, 16203–16209.

Yim, B., Okuno, H., Nagata, Y., Nishimura, R., & Maeda, Y. (2002). Sonolysis of surfactants in aqueous solutions: An accumulation of solute in the interfacial region of the cavitation bubbles. *Ultrasonics Sonochemistry*, 9,209–213.

Zhang, T., Oyama, T., Horikoshi, S., Zhao, J., Serpone, N., & Hidaka, H. (2003). Photocatalytic decomposition of the sodium dodecylbenzene sulfonate surfactant in aqueous titania suspensions exposed to highly concentrated solar radiation and effects of additives. *Applied Catalysis B: Environmental*, 42,13–24.

Zhang, R., Gao, L., & Zhang, Q. (2004). Photodegradation of surfactants on the nanosized TiO₂ prepared by hydrolysis of the alkoxide titanium. *Chemosphere*, 54, 405–411.

Zhang, H., Zhang, J., Zhang, Liu, F., & Zhang, D. (2009). Degradation of C.I. Acid Orange 7 by the advanced Fenton process in combination with ultrasonic irradiation. *Ultrasonics Sonochemistry*, 16, 325–330.

2.6 Biomedical application

2.6.1 Absorption/Release of Acetylic Salicylic Acid by TiO_2 nanoparticles

2.6.1.1 Introduction

Major advances have been made in the development of novel materials such as ceramics and polymers to be used for the delivery of drugs to a local region of pathology. The advantages of such a system are twofold: the ability to deliver the concentrations for a relatively long period of time, whilst minimizing the concentrations of the drug in the bloodstream and other organs and the potential side effects produced by systemic administration.

In the last decade, many different inorganic or metallic materials have been studied in controlled drug delivery, such as gold nanoparticles, quantum dots, hybrid nano-objects, silica microspheres, and so on. However, very little is known about the possibility to use titania based nanomaterials as drug carrier. Only few attempts have been made in this direction, mostly through the use of titania bioconjugate for use in magnetic resonance imaging or gene delivery.

Here, we present a study focused on the relationship between bulk and morphological properties of titania nanoparticles and the adsorption/release of acetyl salicylic acid (aspirin). The TiO_2 nanoparticles were prepared *via* a sol-gel method. They present an interesting behavior in the release of aspirin, showing a quasi-linear trend over a week of release.

2.6.1.2 Materials and method

Sample Preparation.

All the chemicals were of reagent-grade purity and were used without further purification; doubly distilled water passed through a Milli-Q apparatus was used to prepare solutions and suspensions. Titania nanoparticles with variable water/alkoxide molar ratio were synthesized. The samples were named as follows: the letter *T*, the ensuing value the /alkoxide molar ratio, and the letter *c* if the sample was submitted to thermal treatment. The sol-gel precursor obtained by the hydrolysis ($T = 25^\circ\text{C}$, $t = 90$ min) of a solution of $\text{Ti}(\text{OC}_3\text{H}_7)_4$ and 2-propanol (water/alkoxide molar ratio = 49, 75, 100 and water/propanol molar ratio = 15) was dried as a xerogel ($T = 80^\circ\text{C}$, $t = 24$ h). One fraction of the xerogel was submitted to thermal treatment at 300°C for 5 h in O_2 stream (e.g., T49c), and a second fraction was used for the absorption/release experiments (e.g., T49) without further

treatment. Absorption tests were conducted using P25 by Degussa (80% anatase, 20% rutile, crystallite size ~20 nm) as a reference samples.

Adsorption of aspirin by TiO₂ nanoparticles.

Adsorption experiments were carried out in water using TiO₂ nanoparticles obtained through sol-gel synthesis. 10 mL of an aqueous solution of acetyl salicylic acid (aspirin) were put in vials containing a certain amount of TiO₂ nanoparticles. Initially, a number of vials equal to the number of samplings were prepared and then the kinetics was started. At the time of a sampling (e.g., 1 day) the stirring was stopped, the suspension contained in a vial was centrifuged (13000 rpm for 5 min), and the liquid was examined by means of total organic carbon analyzer evaluating the amount of aspirin adsorbed onto the TiO₂ surface.

Release of TiO₂-bound aspirin.

Desorption of the acetylic salicylic acid from TiO₂ nanocrystals in aqueous solutions was measured as follows: suspensions of the TiO₂ crystals (5 mg/mL) complexed with aspirin were dispersed in aqueous solution, at the time of sampling they were centrifuged at 13000 rpm for 5 min, the supernatant discarded and replaced by the same volume of fresh solution. The crystals were re-dispersed by rapid mixing and the process repeated for every sampling.

Characterization techniques.

Room-temperature X-ray powder diffraction (XRPD) patterns were collected between 10° and 80° (2θ range, $\Delta 2\theta = 0.02^\circ$) with a Siemens D500 diffractometer using *Cu K α* radiation. Rietveld refinement has been performed with the QUANTO software suite. The average diameter of the crystallites, d , was estimated from the most intense reflection (101) of the TiO₂ anatase phase by use of the Scherrer equation. Specific surface areas were determined by the classical Brunauer-Emmett-Teller (BET) procedure with a Coulter SA 3100 apparatus.

The percentage of acetylic salicylic acid adsorbed/released in aqueous solution was measured by total organic carbon (TOC) analysis (Model Shimadzu TOC-5000A analyzer).

2.6.1.3 Results and discussion

Characterization of TiO₂ nanoparticles

TiO₂ nanoparticles were synthesized using the sol-gel method to obtain samples characterized by different morphological features. The sol-gel process allows tailoring the physical-properties of materials through the control over the initial reaction conditions. In the present case, we have synthesized 3 samples of TiO₂ nanoparticles using a different water/alkoxide molar ratio. We have used a

water/titanium alkoxide molar ratio of 49, 75, and 100 (samples T49, T75, T100). A part of these precursors were submitted to thermal treatment and the samples were called T45c, T75c, and T100c respectively.

The TiO₂ powders so obtained had similar phase composition (Table 1) and low degree of crystallinity. The samples were composed by anatase and brookite in a ratio of about 60/40 as indicated in Table 1. The average crystallite size computed on the most intense peak of anatase were around 5 nm for the precursor sample and of around 7-8 nm for the sample treated at 300 °C. Therefore, the crystallite size was not strongly affected by the thermal treatment. Differently, the thermal step had a great influence on the BET surface area of all samples (Table 2).

Table 1: phase composition and crystallites size calculated by the Sherrer equation for the TiO₂ home-made nanoparticles.

Sample	Heat treatment	% Anatase	% Brookite	Crystallite size (nm)
T49	-	61	39	5
T49c	300°C, 5h	63	37	7
T75	-	59	41	6
T75c	300°C, 5h	62	38	8
T100	-	61	39	5
T100c	300°C, 5h	63	37	7

Indeed, once the TiO₂ nanoparticles were submitted to the thermal treatment a remarkable shrinking of the BET surface area was observed. For T49 and T75 the surface area decreased of ~40%, while for T100 only a 28% shrinking was measured.

Table 2: BET surface area and pore size distribution of the samples tested in adsorption of aspirin.

Sample	BET surface area (m ² /g)	Pore size (nm)			
		<6	6<d<20	20<d<80	>80
T49	243	90	7	2	1
T49c	144	26	69	3	2
T75	232	79	18	2	1
T75c	142	n.d.	n.d.	n.d.	n.d.
T100	250	66	25	6	3
T100c	180	39	53	5	3
P25	50	n.d.	n.d.	n.d.	n.d.

n.d. = not determined.

The TiO₂ nanoparticles were mainly characterized by mesoporosity. All samples had ~95% of pores below 20 nm and an opposite trend composition was observed for precursor and thermal treated samples. Specifically, the TiO₂ not treated at 300 °C had an abundance of pore <6 nm in size, while the samples submitted to the

thermal treatment presented a major component of pore size ranging between 6 and 20 nm. In addition, increasing the water/alkoxide molar ratio, a decrease in the % of these pores was observed (Table 2).

In Figure 2 are represented TiO₂ nanoparticles of T100 and P25 by Degussa after immersion in water for 48 h. Both the nanoparticles are characterized by an outer amorphous layer that is induced by the immersion in water. We assume that the immersion in water induced a partial superficial reconstruction of the crystalline samples with the final result to obtain a thin layer of amorphous oxide enclosing the nanoparticles.

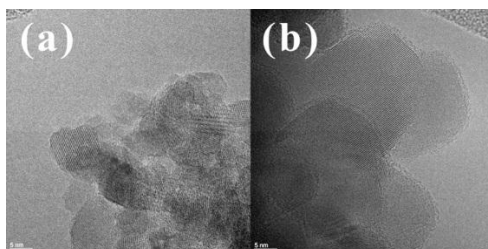


Figure 2: TEM picture of the samples (a) T100; and (b) P25 after immersion in water for 48 h.

Optimization of the experimental conditions: adsorption tests

In order to optimize the experimental condition of drug delivery, we initially tested all home-made TiO₂ nanocrystals and P25 by Degussa (Figure 4) in different amount at constant concentration of aspirin (1×10^{-3}). The adsorption of aspirin was studied over a time of 14 days. All the sol-gel titania sample presented an increased % of adsorption of the drug in comparison with the value obtained for P25 (Figure 3d). Using 5 mg/mL we have observed a marked increase in the adsorption over the home-made sample in comparison with that one in presence of 0.7 mg/mL. T49 (Figure 3a) and T75 (Figure 3b) had a similar adsorption (~60%) and the greater amount of aspirin adsorbed onto the titania surface was observed in the first day of reaction.

Differently, T100 (Figure 3c) presented an increase of activity up to ~80% and after the first day it increased from 50 to 80% with a linear trend. No remarkable difference was observed for TiO₂ nanoparticle untreated and treated at 300 °C. For these reason we have selected this carrier amount (5 mg/mL) for the following study of adsorption and release.

Thereafter we have study the influence of aspirin concentration on the adsorption over TiO₂. From Figure 4 it is clear that the range of concentration tested here does not influence in a significant manner the % of aspirin loaded on the TiO₂

nanoparticles. We have used $1 \times 10^{-3} \text{ M}$ of aspirin in the preliminary adsorption experiment before the release of aspirin.

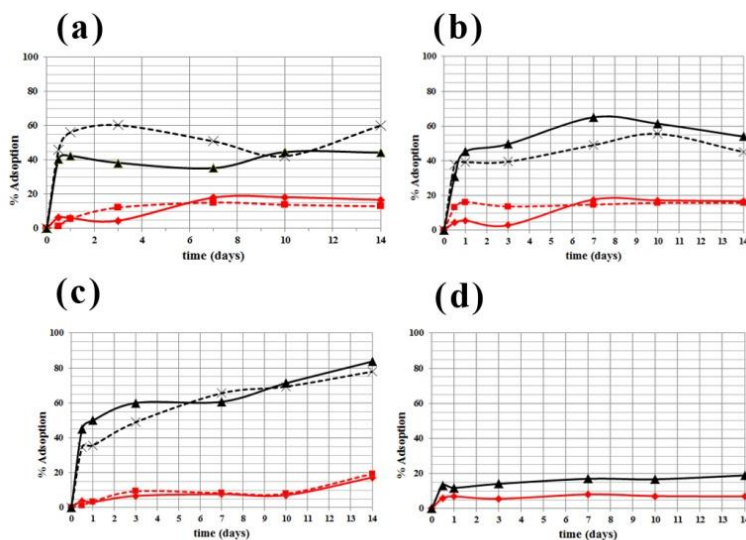


Figure 3: adsorption experiments for the samples of TiO_2 nanoparticles (a) T49; (b) T75; (c) T100; (d) P25. Red lines indicate the experiment conducted with 0.7 mg/mL of carrier, while the black lines shown experiments run in the presence of 5 mg/mL of TiO_2 . Otherwise, dotted lines are for untreated precursor; continuous lines are for samples submitted to thermal treatment.

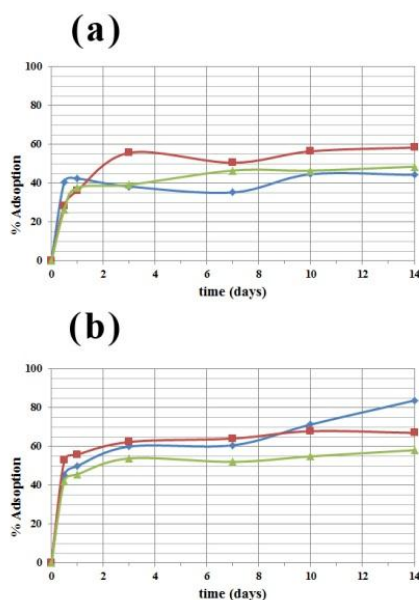


Figure 4: adsorption behavior of (a) T49; (b) T100 at different concentration of aspirin. Blue line: $1 \times 10^{-3} \text{ M}$. Red line: $2 \times 10^{-3} \text{ M}$. Green line: $3 \times 10^{-3} \text{ M}$.

Aspirin release

The adsorption/release behavior of the titania samples could be possibly regulated by the outer amorphous layer observed in the TEM images (Figure 2). To better understand the mechanism behind the process of adsorption/release, we are performing FTIR analysis and NMR study on the surface of the TiO₂-aspirin conjugate.

The release profile reported in Figure 4 show that T100 (red line) had a faster release reaching 100% of cumulative release after 7 days, while T49 presented a slower release reaching 80% of the total amount of drug loaded after 8 days. In the latter case, after the first day of release, the sample follow a linear kinetic of release of aspirin.

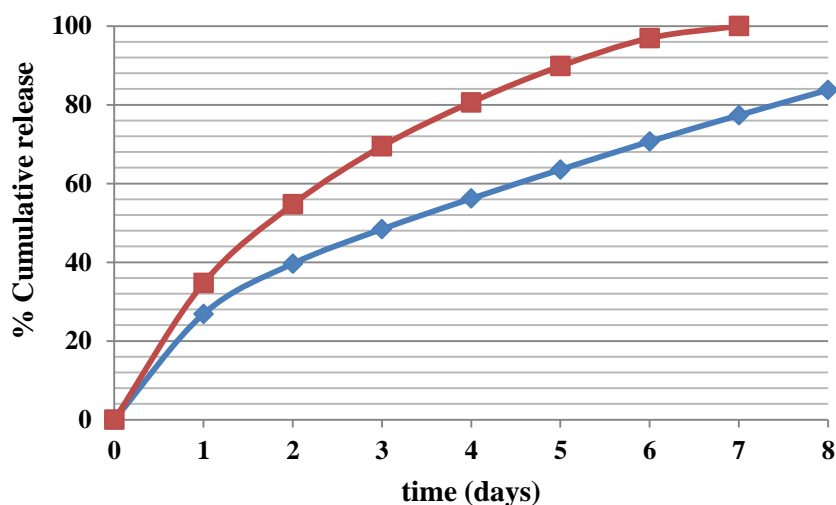


Figure 4: release curve referred to the samples (blue) T100, (red) T49.

2.6.1.4 Conclusion

We have presented a preliminary study on the use of TiO₂-based nanomaterials for drug delivery applications. The initial condition of adsorption of acetylic salicylic acid (carrier amount and drug concentration) were optimized and subsequently the release of aspirin by two selected samples were studied in aqueous solution. Interestingly, the release kinetic follow a linear trend, highlighting the possibility to use TiO₂-based nanomaterials as efficient carrier for controlled drug delivery.

The use of nanomaterials in biomedical applications is strictly related to the understanding of the interaction between the inorganic surface of the carrier and the drug molecule that adsorbs onto its surface. For this reasons, NMR and FTIR experiments are ongoing in order to enable the design of more sophisticated carrier and the study of more complex molecule, such as cisplatinum and other antitumoral agents.

2.6.2 Electrochemically-assisted Deposition on TiO₂ Scaffold for Tissue Engineering: an Apatite Bio-Inspired Crystallization Pathway

A. Naldoni, A. Minguzzi, A. Vertova, V. Dal Santo, L. Borgese, C. L. Bianchi, *Journal of Materials Chemistry*, **2010**, DOI: 10.1039/c0jm02446e

2.6.2.1 Introduction

Tissue Engineering (TE) represents today one of the most attractive and interdisciplinary field of nanoscience since it enables the design of artificial or natural biological substitutes that restore, maintain or improve the original tissue functions. In this field, bone regeneration represents a major issue. In particular, the research for a suitable scaffold which serves as a structural support and substrate for cell adhesion, differentiation and neo tissue genesis is now a fundamental topic.¹ Hence, artificially designed scaffolds should have several requirements, including biocompatibility, mechanical properties similar to those of the bone replaced, biodegradability and biomimetic porosity. Among these features, the porosity is a key property of a biomaterial² and interconnected hierarchical micro-/meso-/macroporous networks become, therefore, natural candidates for bone TE. Pores are necessary for bone regeneration because they allow migration and proliferation of osteoblasts and mesenchymal cell, as well as the delivery of cytokines and cellular nutrients *via* an enhanced vascularization. Macropores enhance mass transfer, while micro-/mesopores provide a large surface area thus promoting a strong adhesion at the scaffold/naturally grown bone interface.^{3,4}

A wide range of different materials have been tested for TE such as metals, natural and synthetic polymers, ceramics, polymer/inorganic composites.^{1,5} Among these, oxide ceramics (e.g. Al₂O₃, ZrO₂, TiO₂) are bioinert materials designed to be used as bone, joint or dental implants.^{6,7} Only few papers reported on the use of titanium dioxide (TiO₂) scaffolds as potential materials for implants, although it already showed good biocompatibility and the capability to enhance bone ingrowth.⁸⁻¹⁰ Differently, hydroxyapatite (HA, Ca₁₀(PO₄)₆(OH)₂), the main inorganic component of natural bone and all calcified tissues, was widely used both as a structural material¹¹⁻¹³ or as a coating onto metallic prosthesis to enhance their bioactivity.¹⁴⁻¹⁵

The aim of the current study was to explore the properties and the functionalization of TiO₂-based scaffolds for TE. We synthesized pure TiO₂ and TiO₂/HA macroporous scaffolds by a modification of the well-known polymeric sponge method.¹⁶ Instead of producing a negative replicate of the sponge, we

used it as an organic template in the sol-gel synthesis of TiO_2 to direct the growth of nanoparticles preferentially on the sponge surface.

Moreover, we tuned up a versatile electrochemically-assisted deposition method for non-conductive substrates (Scheme 1) to coat the scaffold pores of both nanocrystallites and amorphous species, precursors for stable HA.

Electrochemistry-based methods have been already adopted for HA synthesis on conductive substrates¹⁷⁻¹⁸ and consist in the local and controlled generation of OH^- ions (because it is directly related to the current passing through the circuit), products of the water reduction reaction occurring at the cathode.

Electrochemical methods were selected since they typically lead to higher selectivity, milder reaction conditions and simpler process design and operation than the respective chemical methods.¹⁹ To our best knowledge, electrochemically-assisted deposition on an electrically insulating substrate has never been reported in the literature, except for methods only aiming to the migration of the precursors into the scaffold.²⁰

Interestingly, the composition and morphology of the growing phases were strictly correlated to the physico-chemical properties of the scaffolds surface, indicating the capability of the method to obtain tailored coating onto non-conductive materials. The *in vivo* bone bioactivity of the TiO_2 -based scaffolds were then predicted examining the apatite formation on their surface in simulated body fluid (SBF) and the transformation of amorphous calcium carbonate into crystalline hydroxyapatite was proposed as a novel bio-inspired pathway toward the bioactivity of scaffold for TE.

2.6.2.2 Experimental

Synthesis of TiO_2 scaffolds. Macroporous scaffolds were prepared by an organic template-directed method. Cellulose sponges (Spontex; diameter 12 mm, height 10 mm) were soaked in a solution containing $\text{Ti}(\text{OC}_3\text{H}_7)_4$ (0.2 mol) in 2-propanol (50 mL) for 30 min, in order to allow the complete diffusion of the TiO_2 precursor inside the porous bodies. Then, Milli-Q water (9.8 mol) was added, drop by drop, to obtain a water/alkoxide molar ratio of 49 and a water/propanol molar ratio of 15.²¹ The slurry was stirred for 120 min at 300 rpm to complete the hydrolysis and then left standing for 120 min without stirring, allowing the titanium dioxide nanoparticles to growth onto the surface of the cellulose templates. Subsequently, the sponges were removed from the suspension and dried for 24 h at 80°C.

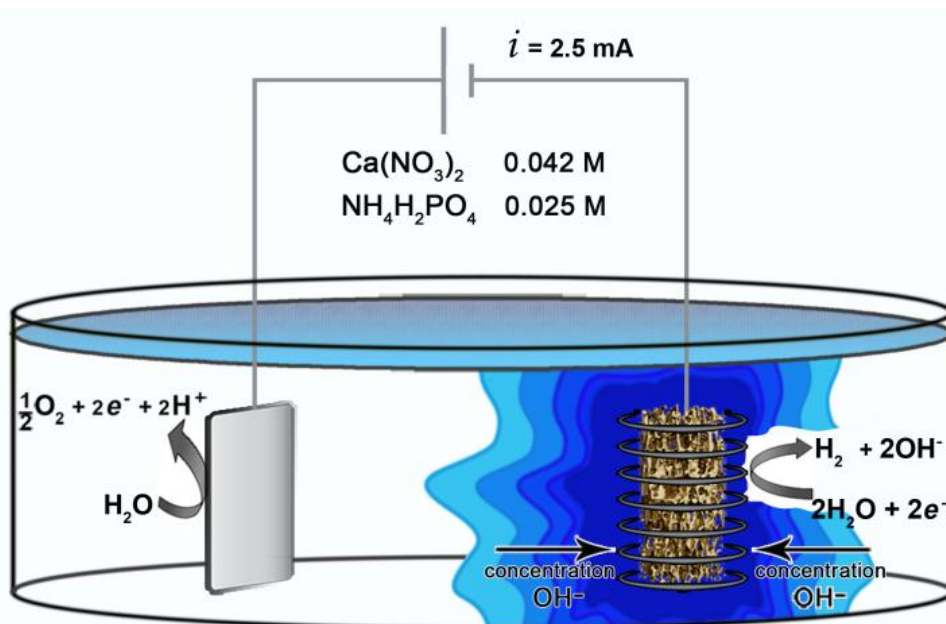
Synthesis of TiO_2 -Hydroxyapatite scaffolds. We prepared TiO_2 /HA scaffolds following the same procedure described for the TiO_2 scaffolds. The addition of biomimetic HA crystals, during the soaking period of the sponges in the TiO_2

precursor, was the only exception. Needle-shaped HA nanocrystals were synthesized as previously reported by Palazzo et al.²² The fraction having a granular dimension ranging between 40-100 μm was selected for the scaffold synthesis.

Sintering process. After the mild thermal treatment at 80°C, both the TiO_2 and TiO_2/HA soaked sponges were sintered for three times at a heating/cooling rate of 2.5 °C/min. Initially, the temperature was increased from 25°C to 500 °C, where the samples were kept for 20 hours to allow the complete emission of organic combustion products. In the second step the temperature was increased up to 1200 °C, inducing sintering processes. After 2 h at 1200 °C, the samples were cooled using the same thermal steps described above.

Electrochemically assisted depositions. Electrochemically-assisted deposition was carried out at room temperature in a single compartment electrochemical cell containing $\text{Ca}(\text{NO}_3)_2$ (42 mM) and $\text{NH}_4\text{H}_2\text{PO}_4$ (25 mM) aqueous solutions. In each experiment, 2.5 mA current intensity was applied by using an AMEL 555B potentiostat/galvanostat and a Keithley 199 multimeter as amperometer. A Pt coil (geometric surface area approximately 2.5 cm^2) served as working electrode while a dimensionally stable anode (DSA[®]) was used as counter electrode.

The general process involves an electrolyte solution containing a Ca to P molar ratio of 1.67 (equal to the theoretical ratio in stoichiometric HA) and a conductive sample (Ti, steel) employed as a cathode. When a potential difference between the material and a counter electrode is applied, the reduction of water to hydrogen leads to the local increase of the hydroxyl ions concentration. This process results in the precipitation of HA crystals both in solution and on the metallic surface. We adopted an electrochemical set-up slightly different to those usually reported for conductive substrates: a platinum coil was bent to host the scaffold like into a conductive cage with the aim of producing a local increase of OH^- concentration, centered on the scaffold (Scheme 1). Before the deposition, the scaffold was immersed in the electrolyte solution and then treated in an ultrasonic bath (2 min) in order to allow ions diffusion into the pores. Deposition was conducted by application of a constant current for 3 h. During the process, a white colloid formed around the Pt coil, together with the evolution of hydrogen bubbles. After the deposition, the scaffold was immersed in a 1 M NaOH aqueous solution for 22 h, dried for 2 h at 80 °C, soaked with water for 30 min to wash away the unreacted reagents and then dried again. Alternatively, the scaffold was directly dried at 80 °C without undergoing the NaOH treatment.



Scheme 1 Schematic representation of the electrochemical set-up employed for the depositions onto non-conductive porous substrates.

Bioactivity tests. The in vivo bone bioactivity of the ceramic scaffolds were tested by examining apatite formation on their surface in SBF. SBF solutions were prepared by dissolving NaCl (137.5 mM), NaHCO₃ (4.2 mM), KCl (3 mM), K₂HPO₄·3H₂O (1 mM), MgCl₂·6H₂O (1.5 mM), 1.0 M HCl (39 ml), CaCl₂ (2.6 mM), Na₂SO₄ (0.5 mM) in de-ionized water (MilliQ grade), following the procedure reported by Kokubo et al.²³ The pH of solutions was adjusted to 7.40 by adding tris(hydroxymethyl)aminomethane and HCl (1.0 M) at 36.5±0.5°C. Samples were immersed in SBF solutions with composition similar to human blood plasma under static condition at 36.5±0.5°C. The SBF solutions were renewed every 7 days to replicate the physiological conditions of ions exchange. After a soaking time of 14 days, the samples were removed from the SBF solutions, gently rinsed with distilled water, and then dried at room temperature.

Characterization. Scanning electron microscopy (SEM) analysis of scaffolds were acquired by using a LEO 1430 at a voltage of 20 kV and a working distance of 15 mm. XRD measurements of powder samples were performed with a Panalytical X'Pert Pro diffractometer equipped with the X'Celerator detector and Cu anode. Operating values were 40 kV and 40 mA. For phase quantification Rietveld refinement was performed after identification of crystallized minerals (ICCD cards) and consequently their basic crystal structures (CIF files).

Diffuse Reflectance Infrared Fourier Transformed (DRIFT) spectra were recorded on a Digilab FTS-60A spectrometer equipped with a KBr beam-splitter and a N₂-

cooled linearized broad band MCT detector operating between 400 and 4000 cm^{-1} . The samples were finely grounded in a mortar and a small portion was loaded in a sample holder that was then inserted in a Harrick DRA-2C1 diffuse reflectance accessory. DRIFT spectra were recorded operating at 4 cm^{-1} resolution and collecting 50 scans against a KBr background.

The micro hardness measurements were conducted using a Fisherscope HCU Micro Hardness control Unit (Fischer) with a dwell time of 10 s and a 10 mN load. The specimens were embedded in epoxy resin to provide support for the porous network and then polished (to produce the smooth surfaces needed for the testing) with silicon carbide abrasive papers of decreasing grit size (120, 320, 600 and 1200 grit). The Characteristic material parameters were obtained according to DIN 50359/ISO 14577. Tests were conducted in replicates of five. During the calculation of the indentation hardness (MPa), indentation modulus (GPa) and elastic part of indentation work (%), the shape correction for the indenter was always taken into account.

2.6.2.3 Results

2.6.2.3.1 Characterization of macroporous scaffolds: SEM, XRD, DRIFTS and mechanical properties

Monoliths with highly interconnected pores were obtained by the organic-template synthesis and subsequent thermal treatment. The general morphology of the bioceramic scaffolds is shown in Fig. 1a and 1b. The pore sizes distribution for both TiO_2 and TiO_2/HA (hereafter referred as composite one) scaffolds was not homogeneous with pores diameter ranging from 1 μm to 1mm. The average macroporosity observed by SEM measurements (Fig. 1b) was around 100 μm , that is generally considered the minimum pore size required to regenerate mineralized bone.⁴

When TiO_2 was the only structural component, grains have grown randomly creating a fine texture with crystallites dimension ranging from few hundreds nanometers to 10 μm in size (Fig. 3a₁). Differently, if HA crystals were added to the TiO_2 precursor solution, the distribution of crystallites dimension narrowed dramatically (Fig. 3c₁) and the mean grains diameter became smaller (about 1 μm) than in the case of pure TiO_2 scaffolds.

XRD patterns of the titania-based scaffolds indicate the presence of well crystallized samples with various phase compositions (Fig. 2a-b). As expected, TiO_2 scaffolds were composed by 100% in rutile; otherwise, the scaffolds initially containing HA presented a more complex phase composition with the presence of

rutile (81.1%), Whitlockite $\beta\text{-Ca}_3(\text{PO}_4)_2$ ($\beta\text{-TCP}$, 14.5%) and perovskite CaTiO_3 (4.4%).

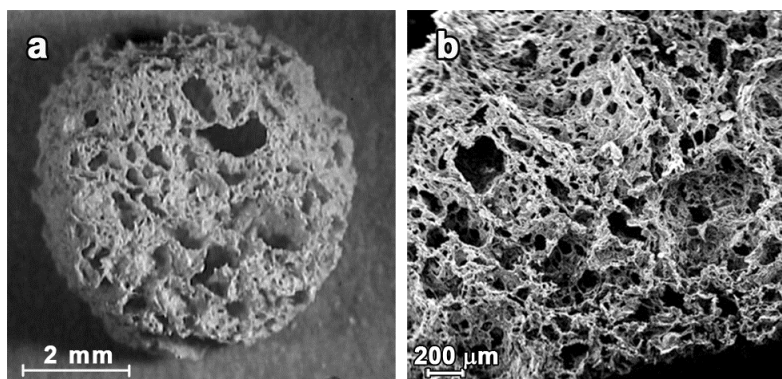


Figure 1 General morphology obtained for TiO_2 and TiO_2/HA scaffolds. (a) Optical microscopy image shows the top view of the porous bodies. (b) SEM image shown a low magnification view of the biomimetic porosity of the scaffolds.

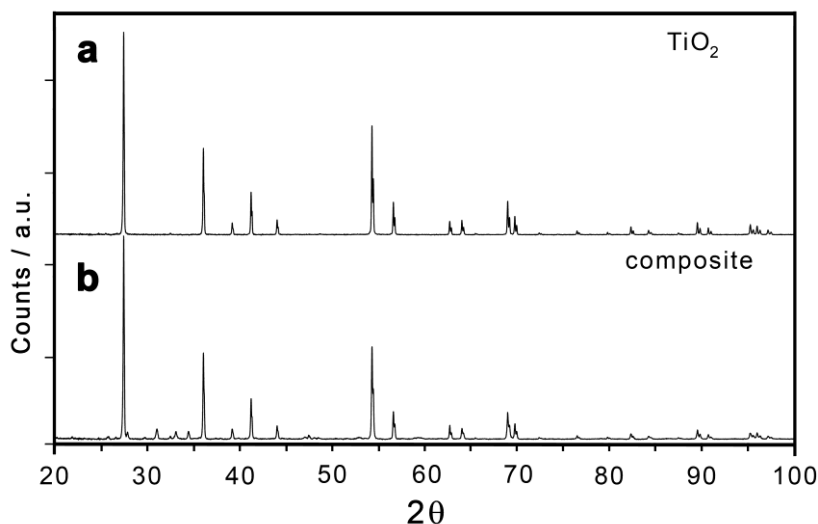


Figure 2 X-ray powder diffraction patterns of (a) TiO_2 scaffolds (Rutile ref. JCPDS 21-1276) and (b) TiO_2/HA scaffolds (β -tricalcium phosphate ref. JCPDS 09-0169, Calcium titanate perovskite ref. JCPDS 42-0423).

The identification of *beta*-tricalcium phosphate ($\beta\text{-TCP}$) in the composite scaffolds has also been confirmed by DRIFT measurements (Fig. 5c₁). The characteristic peaks at 945, 974, 986, 1008, 1026 and 1130 cm^{-1} are diagnostic to PO_4^{3-} ions in TCP.²⁴ The broad absorption band centered at 897 cm^{-1} and 867 cm^{-1} for the TiO_2 (Fig. 4a₁) and the composite scaffold (Fig. 5c₁), respectively, can be assigned to the Ti-O lattice vibrations. This shift of the maxima will be discussed in the section *Discussion*. The mechanical properties of porous scaffolds were determined by micro hardness determinations for quantifying the intrinsic elastic properties of the

investigated specimens. The average indentation modulus of TiO_2 scaffolds was $4.50 \pm 0.24 \text{ GPa}$ as compared to $4.26 \pm 0.68 \text{ GPa}$, the latter determined for the composite scaffolds. The average indentation hardness was $289 \pm 15 \text{ MPa}$ and $167 \pm 15 \text{ MPa}$ for the TiO_2 and the composite scaffolds, respectively, with an elastic part of indentation work corresponding to $39 \pm 2\%$ and $27 \pm 5\%$ of the respective values.

2.6.2.3.2 Electrochemically-assisted depositions and bioactivity tests

SEM analysis

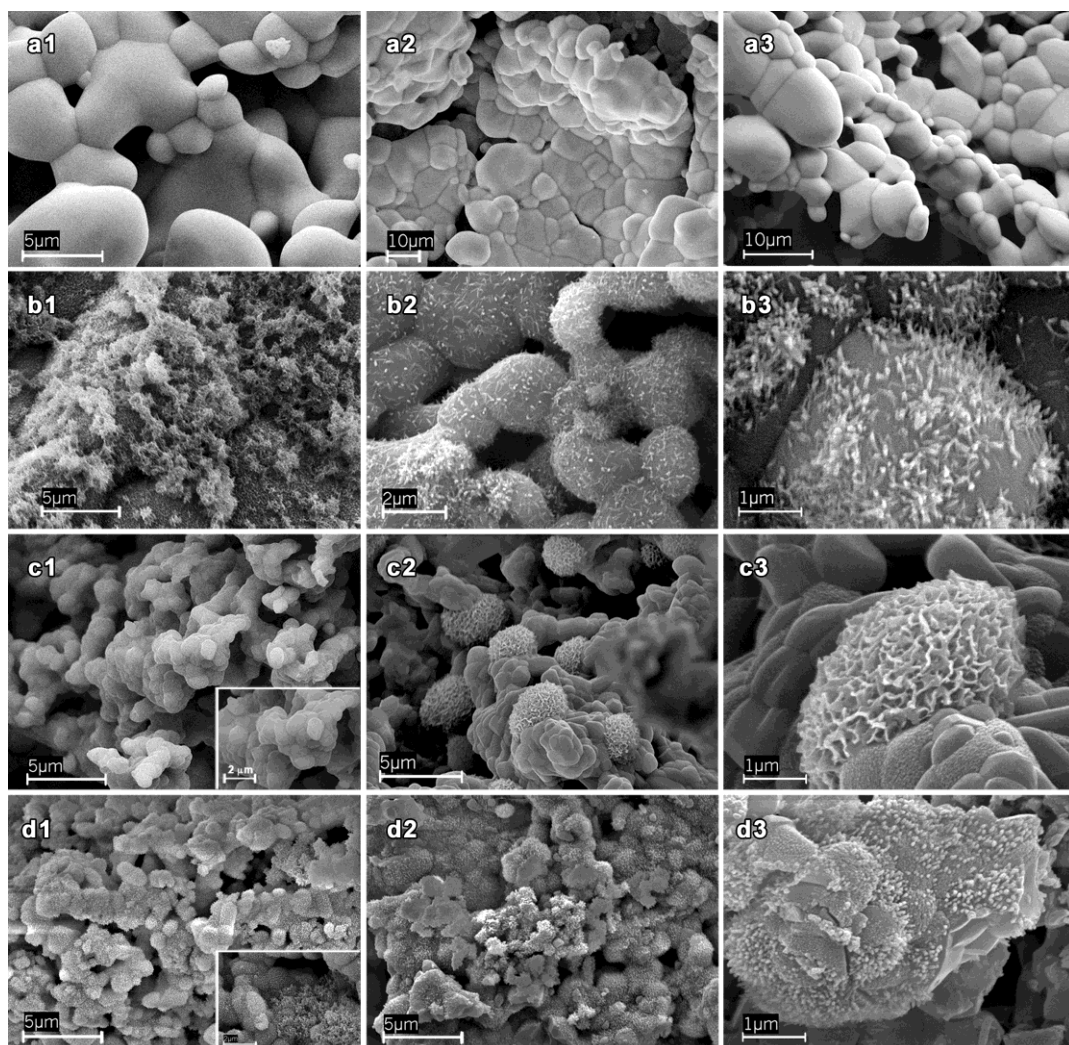


Fig. 3 Mosaic of SEM images of the samples morphology obtained in different experimental conditions. Grains morphology of the (a1) TiO_2 scaffolds and (c1) composite scaffolds. Coating grown after the electrochemically-assisted deposition and the NaOH post-treatment onto the (b1) TiO_2 surfaces and the (d1) composite substrates. The images

a2-a3 represent the TiO₂ scaffolds soaked in SBF for 14 days. The images x2 and x3 (x=, b, c, d) represent the corresponding reference samples soaked in SBF for 14 days, at low and high magnification, respectively.

EDS analysis suggested that the nanostructured coating obtained (in both TiO₂ and composite scaffolds) via electrochemically-assisted deposition was composed by HA crystals (experimental Ca/P=1.6, theoretical Ca/P=1.67). However, the deposition was limited to the outer surface of the TiO₂-based scaffolds, as shown in Fig. SI1 in the Supplementary Information (SI). This effect was likely due to hindrance of reagents diffusion toward the center of the scaffolds.

In order to extend the deposition to the inner surface, HA formation reaction was driven by immersion of the scaffolds in a sodium hydroxide solution (1M) for 22h. This process led to the growth of a new phase onto the inner surfaces of the biomimetic architectures. In the case of TiO₂ scaffolds, the phase presented undefined arrangement and shape (Fig. 3b₁; SI, Fig. SI2), while on the composite scaffolds (Fig. 3d₁; SI, Fig. SI3a), we observed needle-like crystals with an average diameter of about 60 nm. Fig. SI3b shows different degrees of growth of the coating on the composite scaffolds: from tens of nanometers crystal nuclei (SI, Fig. SI3b inset) to large deposits that obstruct the pores.

The *in vivo* bone bioactivity of a scaffold for TE can be predicted from the apatite formation on its surface in SBF.²³ In the present case, the preparation method greatly influenced the behavior of the final porous materials after the immersion in SBF solutions. Figs. 3a₂-a₃ clearly show that TiO₂ scaffolds were not affected by the immersion in SBF; in fact, the grains surface presented the same morphology initially observed in the starting materials. Interestingly, in the electrochemically/chemically treated TiO₂ samples the coating underwent a dramatic change in morphology after being soaked in SBF and the disordered deposited phase (Fig. 3b₁) transformed into crystals with well-defined shape (Figs. 3b₂-b₃). The new deposit was homogeneously distributed over the TiO₂ surface (SI, Fig. SI4); it was composed by acicular nanocrystals with dimension of about 320 nm in length and 60 nm in width.

Composite reference samples showed a completely different activity in SBF, leading to the growth of porous aggregates with “cauliflower-like” morphology (Figs. 3c₂-c₃) and dimension in the order of micrometers. Moreover, the electrochemically deposited composite scaffolds presented a similar morphology before and after immersion in SBF (Figs. 3d₂-d₃), except for the partial surface reconstruction observed.

DRIFT spectra

DRIFT spectroscopy was used to investigate the nature of the phases grown on the scaffolds surface. The DRIFT spectrum of the TiO₂ scaffolds after electrochemically-assisted deposition (Fig. 4b₁) showed typical vibrational bands due to the presence of amorphous calcium carbonates (ACC). They were characterized by a split peak of the asymmetric stretch (ν_3) of the CO₃²⁻ ions at 1473, 1460, 1442, 1433 cm⁻¹. This observation, together with the absence of the in-plane carbonate bending peak at 713 cm⁻¹ (ν_4), indicated the lack of symmetry in the environment of carbonate ions.²⁵ The out-of-plane bending of CO₃²⁻ ions was clearly visible and centered at 883 cm⁻¹ (ν_2), over the TiO₂ structural vibrational band, while the distinct shoulder at 1002 cm⁻¹ revealed the inclusion of phosphate ions in the CaCO₃ structure.²⁶ Moreover, also the peaks at 1774 and 2490 cm⁻¹ (see arrows in Fig. 4b₁ and inset b1) were attributable to carbonate vibrational modes. On the other hand the sharp peak at 3640 cm⁻¹ (Fig. 4b₁, inset b1) was diagnostic of the presence of crystalline Ca(OH)₂ whereas the broad absorption band in the region 2500-3600 cm⁻¹ could be assigned to hydrogen-bonded hydroxyl ions as well as to water absorbed molecules.²⁷

Fig. 4b₂ shows the DRIFT spectrum of the TiO₂ scaffolds after electrochemically-assisted deposition and immersion in SBF for 14 days. The intensity of the asymmetric stretch of the CO₃²⁻ ions decreases compared to Fig. 4b₁ and the peak splits at 1419 and 1458 cm⁻¹. All the additional bands detected suggest that the residual carbonate ions (peak at 1114 cm⁻¹) was trapped into a new forming apatite phase characterized by a structural order as shown in the SEM analysis (Figs. 3b₂-b₃). The peaks located at 564 and 601 cm⁻¹ were assigned to bending mode, ν_{4c} and ν_{4a} , respectively, of the O-P-O bonds in phosphate groups.²⁴ The shoulder at 961 cm⁻¹ was a characteristic of carbonated HA²⁸ and the well-defined peak at 1024 cm⁻¹ was due to the presence of crystal imperfection and HPO₄²⁻ groups in nonstoichiometric HA. Additionally, the peak with low intensity at 3556 cm⁻¹ (Fig. 4b₂, inset b2) was the typical stretching mode, ν_s , of the OH in the HA structure.^{24,29} Fig. 5b₂, inset b3, reports the phosphate ν_4 absorption peak at 560-600 cm⁻¹ after subtraction of spectrum 5a₁. The extent of splitting (splitting factor, SF) of this band has been previously used to evaluate the sample crystallinity;²⁸ in the present case the calculated SF was 5.15 suggesting a high crystallinity for the growing phase.

In the case of composite scaffolds, DRIFT analysis became more complex because of the presence of β -TCP in the structure of the TiO₂ scaffolds. This component dramatically increased the

activity of the samples in SBF. Indeed, whose spectrum (Fig. 5c₂) was different to the reference one (Fig. 5c₁) for the marked increased intensity of the bands at 1008

and 1026 cm^{-1} . This observation suggested that the porous deposits were composed by apatite even though the lack of characteristic bands of HA ($560\text{--}600\text{ cm}^{-1}$, 3560 cm^{-1}). In fact, the presence of HA was identified by the existence of the well-known globular, cauliflower-like shaped crystals (Figs. 3c₂–c₃) already reported for polycaprolattone-based scaffold,³⁰ poly(L-lactic acid) foam³¹ or 45S5 Bioglass®-based scaffold³² after immersion in SBF.

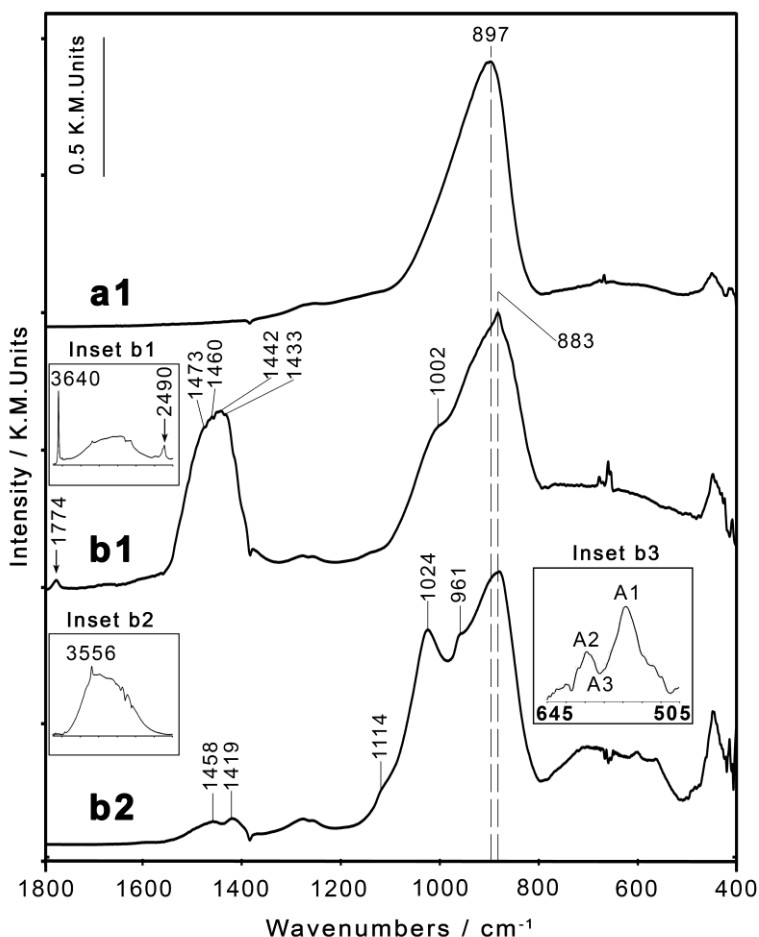


Figure 4 Diffuse Reflectance Infrared Fourier Transformed (DRIFT) spectra of TiO_2 scaffolds (a1) as a reference; (b1, inset b1) after deposition and post-treatment in NaOH; (b2-inset b2,3) sample b1 after immersion in SBF for 14 days. The intensity are normalized to the Ti-O stretching peak at 897 cm^{-1} . The inset b1 was obtained subtracting a1 from b2.

Fig. 5d₁ represents the DRIFT spectrum of the homogeneous coating grown on composite scaffolds after electrochemically-assisted treatment and subsequent immersion in 1 M NaOH solution. This crystals are composed by octacalcium phosphate (OCP) as suggested by the bands located at 1053 and 1076 cm^{-1} and by the prominent shoulder at 1250 cm^{-1} .²⁴ The rose-like crystals morphology observed

by SEM analysis (SI, Fig. SI3b) supports this observation since it was already observed onto titania surface by other authors.³³⁻³⁴ Once the sample mentioned above was immersed in SBF, the vibrational bands of the scaffolds changed. The IR bands of the OCP disappeared and the coating was characterized by the same spectrum of the reference composite scaffolds, albeit the bands related to β -TCP had a lower intensity.

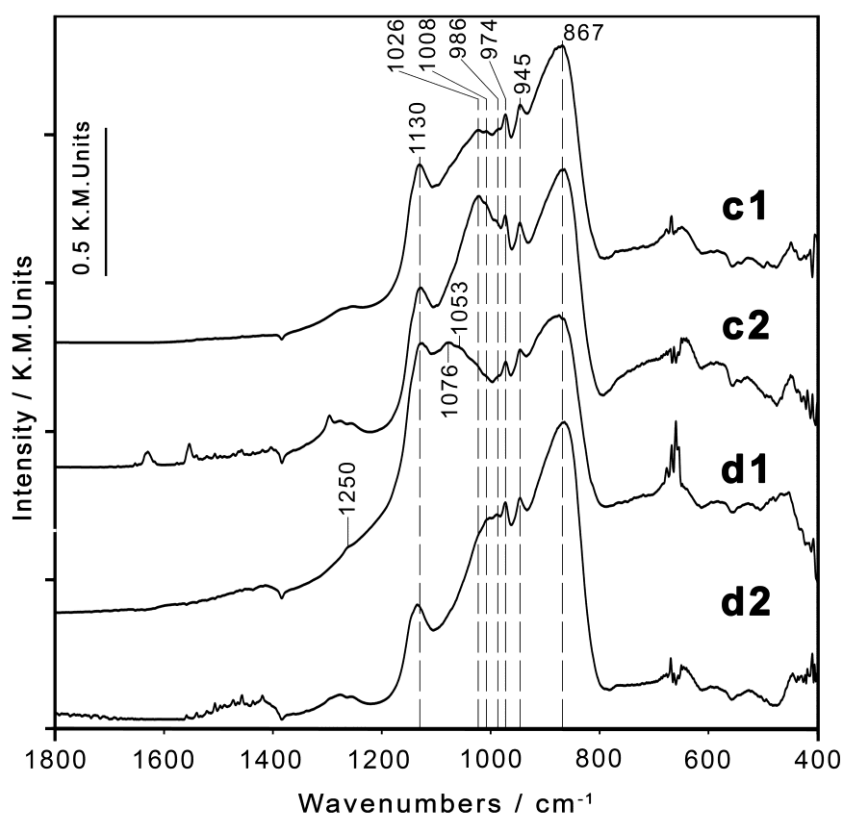


Figure 5 DRIFT spectra of TiO_2 based composite scaffolds (c1) as a reference; (c2) reference soaked in SBF for 14 days; (d1) after deposition and post-treatment in NaOH; (d2) sample d1 after immersion in SBF for 14 days. The intensity are normalized to the Ti-O stretching peak at 867 cm^{-1} .

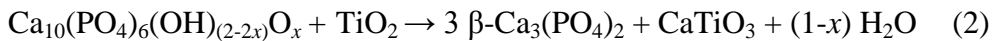
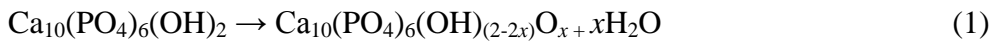
2.6.2.4 Discussion

The conventional polymeric sponge method exploits the rheological properties of an inorganic slurry (e.g. HA, TiO_2) to obtain a morphological complementarity to the structure of the template: porous ceramics obtained through this method have open-celled porosity, programmable pore size and a complex shape.^{8,11,35-37}

Differently, here we used the sponge to direct the nucleation and growth of TiO_2 preferentially along its surface. The hydrolysis/polycondensation reaction of the

TiO₂ precursor occurred both inside the pores inner volume and on their walls, but preferentially on the latter. Thus, the resulting scaffolds had an extensive microporosity strictly resembling the morphological properties of the polymeric backbone and macropores with diameters of suitable sizes to host osteoblasts and the diffusion of the new, growing bone. In addition, microporosity is a fundamental property of biomaterials for TE because it contributes to higher bone-inducing protein adsorption as well as ions dissolution/re-precipitation involved in bone regeneration process. For these reasons, the proposed scaffold synthetic route could be applied also for other materials such as HA, ZrO₂ and polymer/inorganic hybrid materials.

The insertion of biomimetic HA crystals in the synthesis of the TiO₂ scaffolds led to the formation of bioceramic composite materials. The HA phase transformation and decomposition was already reported for the system Ca₁₀(PO₄)₆(OH)₂-ZrO₂.³⁸ We suggest a similar behavior for the HA-TiO₂ composite material according to the following steps:



The loss of water from HA started around 600°C and an oxyhydroxyapatite was thereby formed (1). The process enhanced the reactivity between titanium dioxide and HA creating vacancies in its structure. Since the rate of the beta-tricalcium phosphate (β-TCP) formation (2) increases with temperature, HA was decomposed completely after a treatment of 2h at 1200°C in air, as confirmed by XRD analysis (Figs. 2a-b). The presence of TiO₂ is responsible for the unique behavior of the system since the phase transition temperature from β-TCP to α-TCP is usually around 1100°C.³⁹ The formation of an intimate composite material after HA decomposition was further proved by the shift of 30 cm⁻¹ (Figs. 4a₁ and 5c₁) of the structural peak of the O-Ti-O rutile lattice.

The mechanism mediated by water diffusion, which directed to the formation of tricalcium phosphate and calcium titanate, influenced the growth of the grains during the sintering process, resulting in a great homogeneity and smaller grain size for the composite materials (Figs. 3a₁ and 3c₁).

HA crystals were added in the synthesis with the aim of improving the bioactivity of the TiO₂ scaffolds. The immersion in SBF of the TiO₂ and composite scaffolds was the proof of the effectiveness of our strategy: TiO₂ samples have not shown any deposit growing onto its surface (Figs. 3a₂-a₃); inversely, apatite crystals with a

“cauliflower-like” morphology grown onto the overall porous area of the composite scaffolds (Figs. 3c₂-c₃; SD, Figs. SD5a-b). This finding can be explained by the presence in the crystalline lattice of biologically active phases such as β -TCP and CaTiO_3 .⁴⁰⁻⁴² The mechanical properties of the TiO_2 (elastic modulus and indentation hardness, see the section *Results*) are comparable to the ones of trabecular bone specimens (e.g. trabecular lamellae in the neck of human femur) already reported,⁴³⁻⁴⁴ even though mechanical properties of our samples can be further improved, for example by inclusion of polymeric materials into the TiO_2 network.

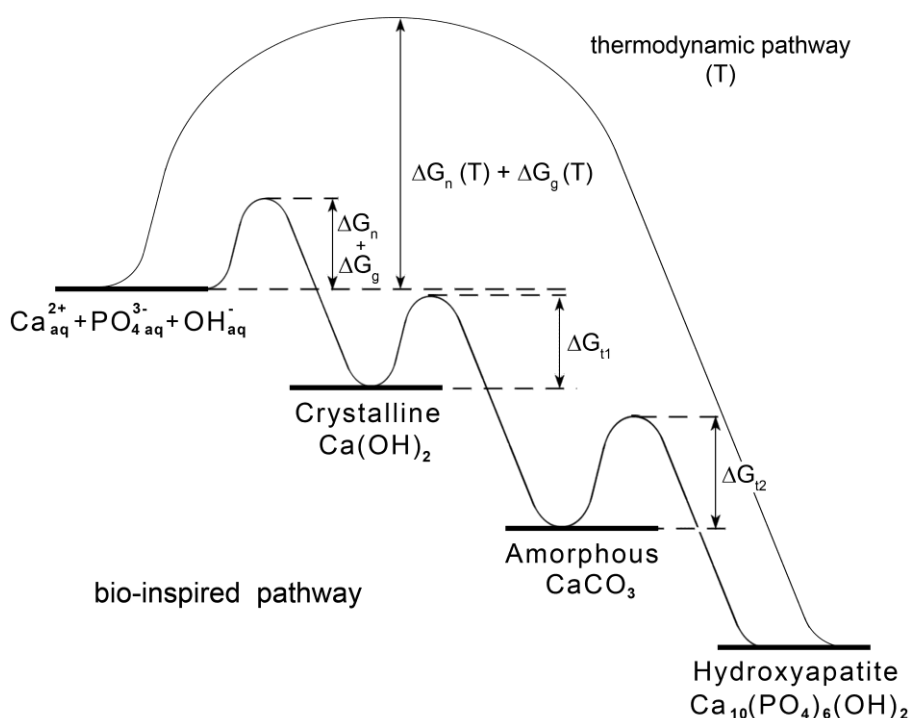
In order to enhance the bioactivity of the TiO_2 scaffolds, we adopted the electrochemically-assisted deposition as deeply described in the section *Experimental*. Unfortunately, the method by its own led to the deposition of HA only onto the outer surface of the scaffolds (Figs. SD1a-b). This indicates that the method is promising for the direct and quick deposition of HA onto non-conductive structures but still needs improvement. In order to allow the growth of HA structures also in the less accessible regions of the scaffolds, they were immersed in NaOH 1M for 22h without washing out from the pores volume the original electrolyte solution.⁴⁵ The experimental evidences showed that, after the whole process, the composite scaffolds presented the β -TCP template growth of octacalcium phosphate (OCP) crystals that dissolved when the scaffolds were immersed in SBF for 14 days. The high solubility of the OCP and β -TCP phases induced the partial dissolution/reconstruction of the surface morphology. Differently, the growing deposit observed on the TiO_2 scaffolds was an amorphous calcium carbonate (ACC) phase that transformed into biomimetic acicular HA nanocrystals after immersion in SBF.

This is the result of a different role played by the electrochemically-assisted deposition technique on non-conductive substrates compared to its effect on metallic electrodes. In the latter case, the electric field reduces the activation energy for the heterogeneous nucleation, and the thermodynamically stable phase (HA) is deposited on the electrode surface.⁴⁶ In this work, the experimental evidences suggest that the modification of the method for non-conductive scaffolds had the major effect of changing the surface state of the sample: the high concentration of electrochemically generated OH^- induced a negative charge (TiO_2 isoelectric point is at a pH of about 6-7) on the scaffolds surface. The platinum coil is also negatively charged. As a consequence, a gradient concentration of the different species was reached. In particular, the presence of phosphates was likely decreased while Ca^{2+} concentration was increased in the volume confined by the Pt coil. The main effects were both a Ca specific adsorption and a local precipitation of calcium

phosphates, in both cases interesting the inner and the outer surface of the scaffold. The following immersion in NaOH had then different effects in dependence on the nature of the scaffolds: in the composite ones, the presence of a calcium phosphate polymorph in the TiO₂ crystalline lattice directed the growth of OCP crystals while for the TiO₂ ones, the formation of a crystalline calcium hydroxide deposit was observed (Scheme 2). Since the alkaline treatment lasted 22h, the CO₂ molecules dissolved in the water have partially replaced the hydroxyl ions in the Ca(OH)₂ lattice, leading to a mixture of crystalline Ca(OH)₂ and hydrated ACC (Fig. 4b₁). ACC is highly soluble and usually rapidly transforms to calcite, vaterite or aragonite, but surprisingly when the TiO₂ scaffolds were immersed in SBF, ACC (Fig. 3b₁) underwent a transformation into biomimetic acicular carbonated HA nanocrystals (Figs. 3b₂-b₃). To the best of our knowledge, this is the first report about the transformation of ACC to biomimetic HA through immersion in SBF; the conversion of crystalline CaCO₃ to HA was already obtained but under different experimental conditions.⁴⁷⁻⁵⁰

It is well known that nature uses ACC as a transient precursor phase for making mineralized skeletal parts: the first-formed deposit is a disordered and hydrated phase that with time transforms into the stable crystalline form. This strategy permits to natural organisms to obtain large single crystals with desired shape starting from a melt amorphous phase.⁵⁴⁻⁵⁷ Similarly, we obtained highly bioactive TiO₂ scaffolds using ACC as a possible precursor phase toward the bioactivity.

In general, electrochemically-assisted deposition permits to obtain the growth of the most thermodynamically stable polymorph (HA) following a single-step pathway. Otherwise, the results obtained for the TiO₂ scaffolds can be summarized as a reported in Scheme 2. We proposed a bio-inspired crystallization pathway that proceeds by a sequential process involving compositional and structural modifications of a crystalline intermediate, Ca(OH)₂, and an amorphous precursor, ACC. The kinetic control of the system is based predominantly on the modification of the activation-energy barrier of nucleation (ΔG_n), growth (ΔG_g) and transformation (ΔG_t). The phase transformations depend on the solubilities of the intermediates, energy of interconversion and presence of additives (e.g. PO₄³⁻ ions). The nucleation of Ca(OH)₂ as well as the transformation of ACC into HA were therefore highly heterogeneous and associated to the scaffolds surface.⁵¹ In particular, the conversion from ACC to HA can be explained by the nanoporous structure of ACC proposed by a theoretical model already reported by other authors.⁵²



Scheme 2 HA bio-inspired crystallization pathways proposed for the TiO_2 scaffolds system and under thermodynamic control. A system follows a one-step route to the final mineral phase (pathway T) or proceeds by sequential precipitation (our pathway) depending on the free energy of activation (ΔG) associated with nucleation (n), growth (g), and phase transformation (t).

Its fundamental feature is the evolution of two distinct percolating structural components: a porous Ca-rich framework and a carbonate/water (Ca-poor regions) “channels” forming interconnected pathways. The dissolution of ACC and the presence of these Ca-poor nanopores can permit the phosphate ions diffusion, facilitating the HA nanocrystals formation template by the TiO_2 surface, a biomimetic process similar to the biomolecules-assisted crystallization of ACC observed in biogenic or synthetic materials.⁵³

2.6.2.5 Conclusions

Titania-based scaffolds with a biomimetic porosity similar to the morphology of the trabecular bone were produced by a modification of the polymeric sponge method. The proposed electrochemically-assisted deposition method represents therefore a promising route for the functionalization of non-conductive surfaces. On one hand, the direct HA deposition was possible (and was observed on the outer surface of the scaffolds), but the motion of ions into sample pores was hindered by the charging of the scaffold surface and by partial pores occlusion. After the

alkaline treatment, the TiO_2 inner surface was predominantly covered by amorphous calcium carbonate that, as observed for the first time, easily converts to hydroxyapatite under nearly physiological conditions. This represents a promising powerful route for the improvement of synthetic materials bioactivity.

2.6.2.6 Supplementary Information

Figure SI1

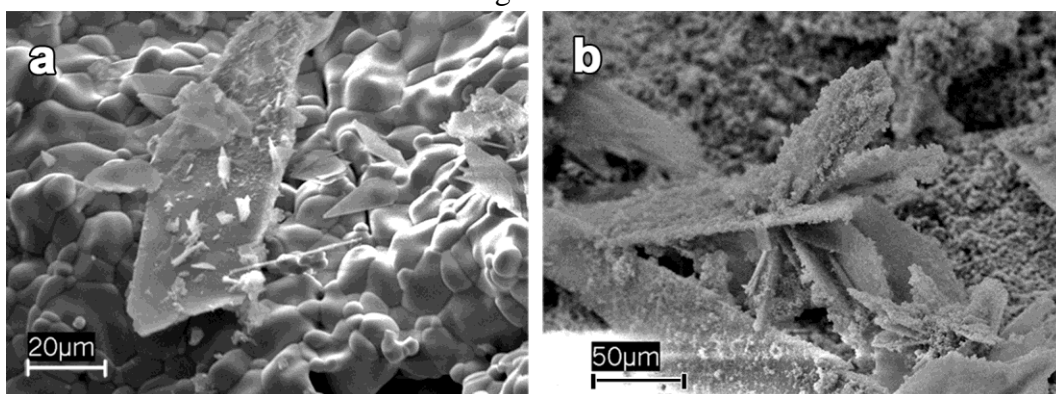


Figure SI1. SEM micrographs shown hydroxyapatite crystals originated through homogeneous nucleation in the electrolytic solution and then deposited onto the outer surface of (a) TiO_2 scaffolds (b) composite scaffolds.

Figure SI2

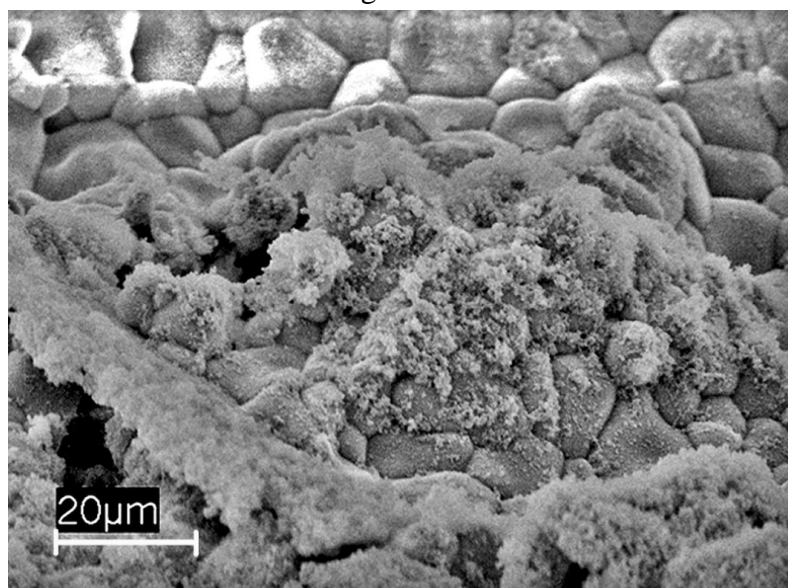


Figure SI2. SEM image of the coating of amorphous CaCO_3 observed onto the TiO_2 scaffolds surface after the electrochemical deposition and alkaline post-treatment.

Figure SI3

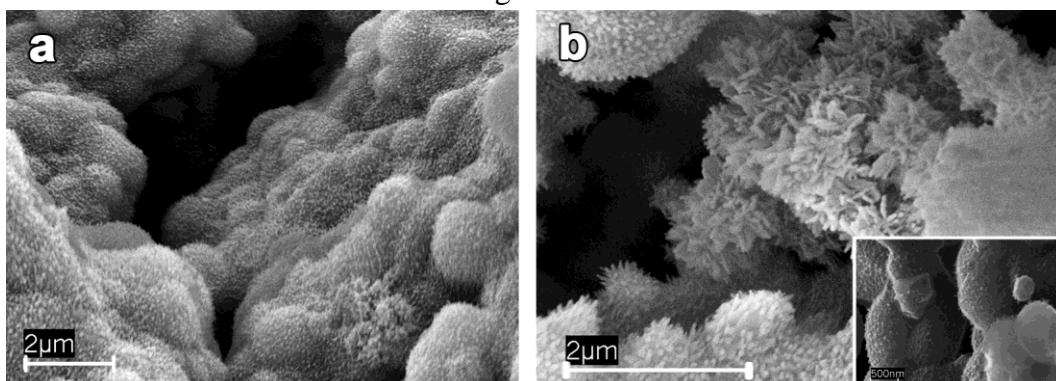


Figure SI3. High magnification SEM images of the composite scaffolds surface after the electrochemical deposition and alkaline post-treatment: (a) the coating obtained onto the inner scaffolds surface is homogeneous (b) and it grows also into the pores. The inset b shows a region where the crystal growth is starting and the dimension of the crystallites is in the range of tens of nanometers.

Figure SI4

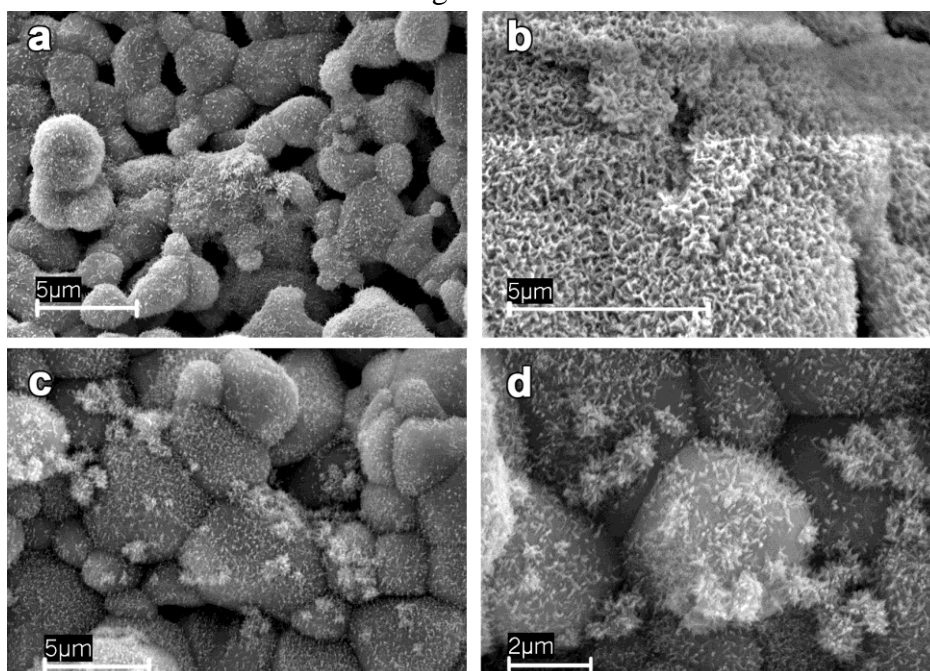


Figure SI4. SEM images of the carbonated hydroxyapatite crystals grown onto the surface of TiO_2 scaffolds deposited and soaked in NaOH after immersion in SBF for 14 days.

Figure SI5

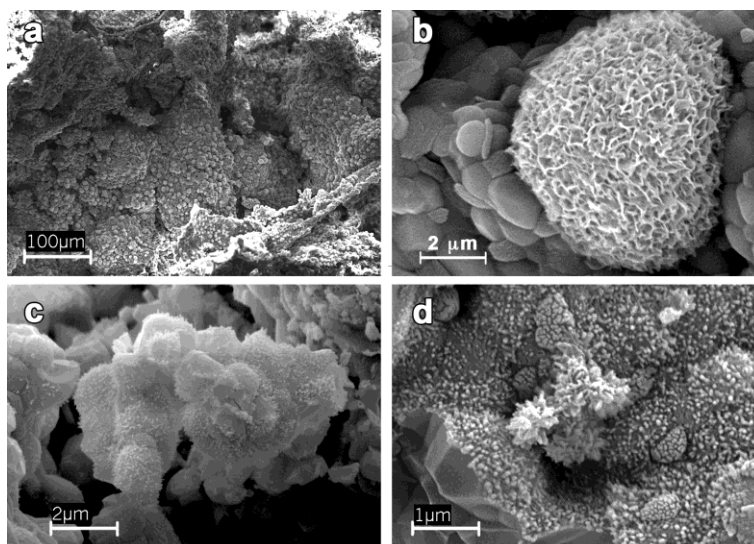


Figure SI5. Composition of SEM images shown the composite scaffolds surface after soaking in SBF for 14 days: (a) the panoramic view attempts that the calcium phosphate deposit grows homogeneously distributed; differently the (b) high magnification image highlights the porous cauliflowers-like morphology of the growing phase. (c) and (d) are SEM images showing the morphology of the coating onto the composite scaffolds after the electrochemical and alkaline treatment and the subsequent immersion in SBF for 14 days.

Figure SI6

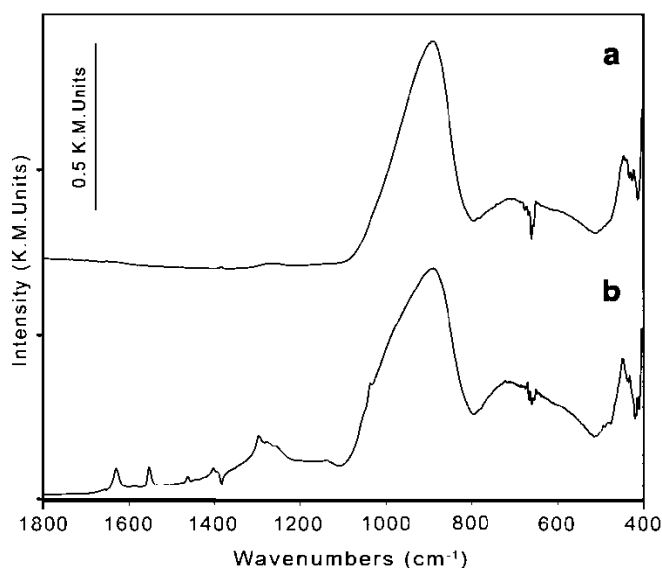


Figure SI6. DRIFT spectra of TiO_2 scaffolds (a) after immersion in $\text{Ca}(\text{NO}_3)_2$ 0.042 M and $\text{NH}_4\text{H}_2\text{PO}_4$ 0.025 M for 3 h and post-treatment in NaOH 1 M for 22 h; (b) soaked in SBF for 14 days, the spectra indicates the presence of tris(hydroxymethyl)aminomethane adsorbed onto the surface of the scaffold. The intensity are normalized to the Ti-O stretching peak at 897 cm^{-1} .

2.6.2.7 References

- 1 P. X. Ma, *Adv. Drug Delivery Rev.* **2008**, *60*, 184.
- 2 J. R. Jones, L. M. Ehrenfried, L. L. Hench, *Biomaterials* **2006**, *27*, 964.
- 3 C. Suwanchawalit, A. J. Patil, R. K. Kumar, S. Wongnawa, S. Mann, *J. Mater. Chem.* **2009**, *19*, 8478.
- 4 V. Karageorgiou, D. Kaplan, *Biomaterials* **2005**, *26*, 5474.
- 5 K. Rezwan, Q. Z. Chen, J. J. Blaker, A. R. Boccaccini, *Biomaterials* **2006**, *27*, 3413.
- 6 C. R. Rambo, F. A. Muller, L. Muller, H. Sieber, I. Hofmann, P. Greil, *Mater. Sci. Eng. C* **2006**, *26*, 92.
- 7 E. S. Ahn, N. J. Gleason, A. Nakahira, J.Y. Ying, *Nano Lett.* **2001**, *1*, 149.
- 8 G. Fostad, B. Hafell, A. Førde, R. Dittmann, R. Sabetrasekh, J. Willc, J. E. Ellingsen, S. P. Lyngstadaas, H. J. Haugen, *J. Euro. Ceram. Soc.* **2009**, *29*, 2773.
- 9 J. Wei, Q. Z. Chen, M. M. Stevens, J. A. Roether, A. R. Boccaccini, *Mat. Sci. Eng. C* **2008**, *28*, 1.
- 10 F. G. Torres, S. N. Nazhat, S. H. S. Md Fadzullah, V. Maquet, A. R. Boccaccini, *Compos. Sci. Technol.* **2007**, *67*, 1139.
- 11 S. Teixeira, M. A. Rodriguez, P. Pena, A. H. De Aza, S. De Aza, M. P. Ferraz, F. J. Monteiro, *Mater. Sci. Eng. C* **2009**, *29*, 1510.
- 12 S. Deville, E. Saiz, A. P. Tomsia, *Biomaterials* **2006**, *27*, 5480.
- 13 E. Landi, A. Tampieri, G. Celotti, R. Langenati, M. Sandri, S. Sprio, *Biomaterials* **2005**, *26*, 2835.
- 14 M. A. Lopez-Heredia, J. Sohler, C. Gaillard, S. Quillard, M. Dorget, P. Layrolle, *Biomaterials* **2008**, *29*, 2608.
- 15 H. Wang, N. Eliaz, Z. Xiang, H. P. Hsu, M. Spector, L. W. Hobbs, *Biomaterials* **2006**, *27*, 4192.
- 16 K. Schwartzwalder, A. V. Somers, *US Patent No.* 3090094, **1963**.
- 17 S. Manara, F. Paolucci, B. Palazzo, M. Marcaccio, E. Foresti, G. Tosi, S. Sabbatini, P. Sabatino, G. Altankov, N. Roveri, *Inorg. Chim. Acta* **2008**, *361*, 1634.

- 18 S. Rößler, A. Sewing, M. Stolzel, R. Born, D. Scharnweber, M. Dard, H. Worch, *J. Biomed. Mater. Res. A* **2003**, 64, 655.
- 19 A. Vertova, R. Barhdadi, C. Cachet-Vivier, C. Locatelli, A. Minguzzi, J. Y. Nedelec, S. Rondinini, *J. Appl. Electrochem.* **2008**, 38, 965.
- 20 Z. H. Huang, Y. S. Dong, C. L. Chu, P. H. Lin, *Mater. Lett.* **2008**, 62, 3376.
- 21 S. Ardizzzone, C. L. Bianchi, G. Cappelletti, A. Naldoni, C. Pirola. *Environ. Sci. Technol.* **2008**, 42, 6671.
- 22 B. Palazzo, M. Iafisco, M. Laforgia, N. Margiotta, G. Natile, C. L. Bianchi, D. Walsh, S. Mann, N. Roveri, *Adv. Funct. Mater.* **2007**, 17, 2180.
- 23 T. Kokubo, H. Takadama, *Biomaterials* **2006**, 27, 2907.
- 24 S. Koutsopoulos, *J. Biomed. Mater. Res. A* **2002**, 62, 600.
- 25 L. Addadi, S. Raz, S. Weiner, *Adv. Mater.* **2003**, 15, 959.
- 26 Y. Politi, T. Arad, E. Klein, S. Weiner, L. Addadi, *Science* **2004**, 306, 1161.
- 27 G. C. Maiti, M. Baerns, *Thermochim. Acta* **1995**, 261, 69.
- 28 J. Mahamid, A. Sharir, S. Weiner, L. Addadi, *Proc. Natl. Acad. Sci. USA* **2008**, 105, 12748.
- 29 J. M. Oliveira, M. T. Rodrigues, S. S. Silva, P. B. Malafaya, M. E. Gomes, C. A. Viegas, I. R. Dias, J. T. Azevedo, J. F. Mano, R. L. Reis, *Biomaterials* **2006**, 27, 6123.
- 30 M. Lebourg, J. Suay Anton, J. L. Gomez Ribelles, *J. Mater. Sci.: Mater. Med.* **2010**, 21, 33.
- 31 R. Zhang, P. X. Ma, *J. Biomed. Mater. Res. A* **1999**, 45, 285.
- 32 Q. Z. Chen, A. R. Boccaccini, *J. Biomed. Mater. Res. A* **2006**, 77, 445.
- 33 W. Wu, G. H. Nancollas, *Langmuir* **1997**, 1, 861.
- 34 M. Szekeres, G. Fodor, A. Fazekas, M. Radnai, K. Turzo, I. Dekany, *Colloid Polym. Sci.* **2005**, 283, 587.
- 35 S. Teixeira, M. P. Ferraz, F. J. Monteiro, *J. Mater. Sci.: Mater. Med.* **2008**, 19, 855.
- 36 I. Sopyan, M. Mel, S. Ramesh, K. A. Khalid, *Sci Tech of Adv. Mater.* **2007**, 8, 116.

- 37 A. Tampieri, G. Celotti, S. Sprio, A. Delcogliano, S. Franzese, *Biomaterials* **2001**, 22, 1365.
- 38 Z. Shen, E. Adolfsson, M. Nygren, L. Gao, H. Kawaoka, K. Niihara, *Adv. Mater.* **2001**, 13, 214.
- 39 X. Yang, Z. Wang, *J. Mater. Chem.* **1998**, 8, 2233-2237.
- 40 M. Wei, M. Uchida, H. M. Kim, T. Kokubo, T. Nakamura, *Biomaterials* **2002**, 23, 167.
- 41 J. Coreno, O. Coreno, *J. Biomed. Mater. Res. A* **2005**, 75, 478.
- 42 M. Manso, M. Langlet, J. M. Martinez-Duart, *Mater. Sci. Eng. C* **2003**, 23, 447.
- 43 P. K. Zysset, X. E. Guo, C. E. Hoffler, K. E. Moore, S. A. Goldstein, *J. Biomech.* **1999**, 32, 1005.
- 44 J. Y. Rho, T. Y. Tsui, G. M. Pharr, *Biomaterials* **1997**, 18, 1325.
- 45 J. Wang, Y. Chao, Q. Wan, Z. Zhu, H. Yu, *Acta Biomater.* **2009**, 5, 1798.
- 46 M. Yousefpour, A. Afshar, X. Yang, X. Li, B. Yang, Y. Wu, J. Chen, X. Zhang, *J. Electroanal. Chem.* **2006**, 589, 96.
- 47 C. M. Zaremba, D. E. Morse, S. Mann, P. K. Hansma, G. D. Stucky, *Chem. Mater.* **1998**, 10, 3813.
- 48 C. Verwilghen, M. Chkir, S. Rio, A. Nzihou, P. Sharrock, G. Depelsenaire, *Mater. Sci. Eng. C* **2009**, 29, 771.
- 49 M. Yoshimura, P. Sujaridworakun, F. Koh, T. Fujiwara, D. Pongkao, A. Ahniyaz, *Mater. Sci. Eng. C* **2004**, 24, 521.
- 50 D. M. Roy, S. K. Linnehan, *Nature* **1974**, 247, 220.
- 51 H. Colfen, S. Mann, *Angew. Chem. Int. Ed.* **2003**, 42, 2350.
- 52 E. M. Pouget, P. H. H. Bomans, J. A. C. G. Goos, P. M. Frederik, G. de With, N. A. J. M. Sommerdijk, *Science* **2009**, 323, 1455.
- 53 A. L. Goodwin, F. M. Michel, B. L. Phillips, D. A. Keen, M. T. Dove, R. J. Reeder, *Chem. Mater.* **2010**, 22, 3197.
- 54 S. Weiner, I. Sagi, L. Addadi, *Science* **2005**, 309, 1027.
- 55 Y. Politi, T. Arad, E. Klein, S. Weiner, L. Addadi, *Science* **2004**, 306, 1161.

- 56 Y. Politi, R. A. Metzler, M. Abrecht, B. Gilbert, F. H. Wilte, I. Sagi, L. Addadi, S. Weiner, P. U. P. A. Gilbert, *Proc. Natl. Acad. Sci. USA* **2008**, *105*, 17362.
- 57 L. Addadi, S. Raz, S. Weiner, *Adv. Mater.* **2003**, *15*, 959.

Chapter 4

Conclusions

This Ph.D. Thesis is mainly focused on the design and application of nanostructured TiO₂ both for photocatalysis in environmental remediation and for biomedical applications.

The findings discussed in the above chapters, highlight the versatility of sol-gel reaction: it is demonstrated that using the same TiO₂ precursor (e.g., an alkoxide) and slightly changing the initial experimental condition, several different morphologies (e.g., nanoparticles, macroporous scaffolds) are obtained.

In the synthesis of TiO₂ catalysts for environmental remediation of pollutants in air, sol-gel synthesis is a powerful tool to control the phase composition, morphological properties, surface area, and surface features (e.g., surface hydrophilicity/hydrophobicity). All these aspects are strictly related to the photocatalytic activity of the samples since they influence the processes involved in photocatalysis such as charge separation, suppression of charge recombination, and reactivity of the surface sites. The importance of the physico-chemical properties of TiO₂ home-made samples on the final photocatalytic activity and on the photodegradation path has been studied. In addition, N-doped titanium dioxide is synthesized using titanium chloride as a starting reagent.

In this Ph.D. Thesis, the study of the chemical/physical effects of ultrasound is another important issue. In a first work, the effect of high intensity ultrasound (e.g., 20 kHz) on the properties of TiO₂ nanoparticles obtained via a sol-gel route is shown. Ultrasound treatment induces the presence of titanium surface defect sites hence inducing a high photocatalytic activity in the degradation of nitrogen oxides. Moreover, the cavitation produced by high intensity ultrasound is exploited in conjunction of the advanced Fenton process in the degradation of ionic surfactants in the liquid phase.

Acoustic waves travelling at the interface of two liquids can generate the nebulization of liquid chemical precursor. This is the main concept behind ultrasonic spray pyrolysis (USP). USP presents many advantages in comparison with traditional synthetic route since it exploits the indirect effects of ultrasound to create micron-sized droplets that act as isolated, individual micron-sized chemical reactors. In this Thesis is reported the USP synthesis of porous TiO₂ microsphere with tunable physical-chemical properties: changing the dimension and amount of colloidal silica templates, it is possible to tune the surface area, phase composition, crystallites dimension, band gap, porosity, photocatalytic activity, and surface character of the resulting TiO₂ microspheres.

Finally, a preliminary study on the possibility to use TiO₂ nanoparticles for drug delivery and an example of the use of macroporous TiO₂ scaffold in biomedical application was reported. The synthesized monoliths have shown a

similar morphology that by trabecular bone and mechanical properties suitable to employ the scaffolds in tissue engineering for bone regeneration. The bioactivity of such samples was improved by an electrochemically-assisted deposition for non-conductive sample. The most important finding was the observation of a new bio-inspired apatite crystallization pathway toward the bioactivity of biomaterials. The latter result highlights the possibility to use TiO_2 as model materials in the study of the interactions among inorganic materials and biological systems.

APPENDIX A

Collaborations in science of biomaterials

The interest in the field of '*science of biomaterials*' has led to fruitful collaborations with other Italian research groups: since we have long experience in X-ray photoelectron spectroscopy analysis, we have contributed in the determination of surface atomic species, understanding of the superficial properties of biomaterials and in their general behavior. We have investigated the role of inorganic biomaterials (e.g. biomimetic hydroxyapatite, bioactive glasses) in fundamental biological process.

In conjunction with the research group of Prof. Norberto Roveri (Department of Chemistry, University of Bologna) we have examined the different effects of biomimetic apatite nanocrystals on the surface enamel remineralization. The characterization of the surface of enamel slabs before and after treatment with carbonated hydroxyapatite (CHA) or fluoride toothpaste have underlined the possibility to obtain an enamel remineralization through the formation of a surface apatite coating which covers the enamel structure avoiding the most probably health dangerous fluoride effects. The documented CHA biomimetic coating formation which is less crystalline than enamel natural apatite represents an enamel repair process corresponding to an apatite deposition inside the demineralized area of enamel surface and may be considered an innovative approach to contrast enamel demineralization.

Differently, in collaboration with the research group of Dr. Enrica Vernè (Department of Materials Science and Chemical Engineering, Politecnico di Torino) we have focused on the functionalization of bioactive glasses, glass-ceramic and ferrimagnetic glass-ceramic. In the first work we have demonstrated that alkaline phosphatase, an enzyme involved in bone formation and mineralization, could be grafted onto different bioactive surfaces while maintaining its activity. Presence of the enzyme *in vitro* enhances the inorganic bioactivity of the materials tested, proving that we have obtained a stable biomimetic surface. Secondly, we have studied a ferrimagnetic glass-ceramic, belonging to the system $SiO_2-Na_2O-CaO-P_2O_5-FeO-Fe_2O_3$ (SC45), as potential carrier for antineoplastic agents (doxorubicin, cisplatinum), in order to exploit the combination of hyperthermia and chemotherapy. The antineoplastic agents were incorporated into the glass-ceramic powders, and the subsequent release behavior was studied.

This research work pointed out the possibility to graft antineoplastic agents on SC45 glass-ceramic surface. This material can be used for both antitumoral implants and magnetic drug targeting, overworking, in this way, the material ability to generate heat and to release chemotherapeutics able to interact with neoplastic cells.

APPENDIX A1: Surface enamel remineralization: biomimetic apatite nanocrystals and fluoride ions different effects

N. Roveri, E. Battistella, C. L. Bianchi, I. Foltran, E. Foresti, M. Iafisco,, M. Lelli, A. Naldoni, B. Palazzo, L. Rimondini, *Journal of Nanomaterials* **2009** , doi:10.1155/2009/746383.

A.1.1 Introduction

Dental erosion is the chemical wear of the dental hard tissue without the involvement of bacteria.¹ Its clinical relevance is becoming wider and wider,²⁻⁶ and it is considered one of the main tooth pathologies able to cause patient discomfort, after periodontal diseases and caries. Its aetiology is related to the enormous increase in consumption of soft drinks, fruit juices and sport drinks consumption.⁷ However, other acid sources such as drugs containing syrups, analgesics and vitamin C intake and environmental acid exposure in working conditions are claimed to be related to enamel erosion.⁸⁻¹² The mechanisms involved in the damage of dental hard tissue are the acid attacks on the outer few micrometers of the enamel, which brings to demineralization and dissolution of the mineral phase.¹³⁻¹⁶ Hydroxyapatite is the main constituent of the dental tissues representing in enamel and dentine the 95 wt% and 75 wt%, respectively. The primary determinant of dissolution rate is the solubility of hydroxyapatite (HA) which is related to pH, and the presence of salivary pellicle also appears to be important.¹⁷⁻¹⁹ Frequent application of a high concentration of topical fluoride may be of some benefit in preventing further demineralization and increasing the abrasion resistance of erosion lesions.²⁰ In vitro studies have shown that synthetic carbonated-hydroxyapatite (CHA) dissolution inhibition is a logarithmic function of the fluoride concentration in solution.²¹ Systemic intake of fluoride during tooth formation has been claimed to be effective in caries prevention just by means of the apatite demineralization inhibition. According to recommended daily allowances (RDAs) panel of the European Food Safety Authority, an intake of 0.1 mg fluoride/Kg body weight/day in children up to the age of eight years can be considered as the dose below which there will be no significant occurrence of moderate forms of fluorosis in permanent teeth.²² However, it is important to consider that fluoridated water, fluoride supplements in diet, fluoride toothpaste, and topical fluoride applications have been identified as sources of enamel fluorosis.²³ Moreover, the “probably toxic dose” of fluoride—the dose which should trigger therapeutic intervention and hospitalization—is 5mg/Kg of body weight, but as currently packaged, many dental products contain sufficient fluoride to exceed the “probably toxic dose” for young children.²⁴ Most of the products and

devices used to contrast enamel and dentine erosion, such as fluoride,²⁵⁻²⁸ behave by reducing apatite dissolution rather than aiming to promote mineralization through apatite crystallization or replacement of the lost mineral. Hydroxyapatite, as well as in bone, is responsible for the mechanical behavior of the dental tissues. Unlike bone, in enamel and dentine, when HA is dissolved or abraded, it cannot spontaneously remineralize because enamel contains no cells and dentine apposition occurs only toward the pulp tissues. Therefore, both enamel and dentine can be reconstructed only by the application of alloplastic materials providing a sort of prosthetic restoration. In view of this situation, the demineralized area and micrometric sized scratches, which normally occur on enamel surface as a consequence of microwear and acid attack,²⁹ cannot be repaired biologically nor prosthetically. Hydroxyapatite has been widely subjected to experiment as bone filler and prosthetic coating due to its biocompatibility and osteoconductivity, representing an elective material covering a wide range of applications for bone substitution and interface.³⁰ Poorly crystalline HA nanocrystals, in addition to the excellent biological properties of HA, such as nontoxicity and lack of inflammatory and immunitary responses, have bioresorption properties under physiological conditions. This property can be modulated by modifying its degree of crystallinity, which is achieved by implementation of innovative synthesis with a nanosize crystals control. In the last decade, advanced technology has been utilized to synthesize a new generation of biomimetic apatitic alloplastic materials which can optimize the interaction with biological entities thanks to their strong surface bioactivity.³¹ The aim of the present study is to highlight the effect of the synthetic biomimetic hydroxyapatite crystals respect the fluoride ions into the remineralization in vitro of human enamel surface.

A.1.2 Materials and Methods

A.1.2.1 Chemicals

All the chemicals reagents used were of high chemical grade from Sigma-Aldrich, Mo, USA.

A.1.2.2 Synthesis of Carbonate-Hydroxyapatite Nanocrystals

Plate-acicular shaped carbonate-hydroxyapatite nanocrystals about 100 nm in size were synthesized according to a modification of the method previously reported³² and patented.³³ CHA nanocrystals about 100 nm in size were precipitated from an aqueous suspension of $\text{Ca}(\text{OH})_2$ (0.17 M) by slow addition of H_3PO_4 (0.15 M). The reaction mixture was stirred at 37 °C for 12 hours, and then stirring was suspended allowing the deposition of CHA nanocrystals. Synthesized CHA 100 nm sized nanocrystals were isolated by filtration of the mother liquor, repeatedly washed

with water and freeze-dried. The fraction of plate-acicular shaped crystals about 100nm in size with a granular dimensions ranging from 100 to 150 μm was selected for the study. Aliquot of plate-acicular shaped crystals about 100 nm in size has been allowed, after synthesis to intergrowth in the reaction mixture up to the formation of clusters having dimension ranging from about 0.5 to 3.0 μm . The cluster aggregation process has been stopped by adding a surfactant (Protelan MST35 8 wt%) in the mother solution. Plate-shaped carbonate-hydroxyapatite nanocrystals about 20 nm sized were synthesized according to the method of Liou et al.³⁴ with some modifications. The nanocrystals were precipitated from an aqueous solution of $(\text{NH}_4)_3\text{PO}_4$ (5.1 mM) by slow addition of an aqueous solution of $\text{Ca}(\text{CH}_3\text{COO})_2$ (8.5 mM) keeping the pH at a constant value of 10 by addition of a NH OH solution. The reaction mixture was kept under stirring at room temperature for 24 hours, and then stirring was suspended allowing the deposition CHA nanocrystals. Synthesized CHA nanocrystals were isolated by filtration of the solution, repeatedly washed with water, and freeze-dried. The fraction of plate shaped crystals about 20 nm in size having granular dimensions ranging from 100 to 150 μm was selected for the study.

A.1.2.3 Morphological Characterization

Transmission electron microscopy (TEM) investigations were carried out using a Philips CM 100 instrument. The powdered samples were ultrasonically dispersed in ultrapure water, and then a few droplets of the slurry deposited on holey-carbon foils supported on conventional copper microgrids. Scanning electron microscopy (SEM) observation was carried out by an SEM (Zeiss EVO, 40 XVP) using secondary electrons at 25 kV and various magnifications.

A.1.2.4 Structural Characterization

X-ray diffraction powder and enamel surface patterns were collected using an Analytical X'Pert Pro equipped with X'Celerator detector powder diffractometer using Cu K_α radiation generated at 40 kV and 40mA. The instrument was configured with a 1° divergence and 0.2 mm receiving slits. The samples were prepared using the front loading of standard aluminum sample holders which are 1 mm deep, 20 mm high, and 15 mm wide. The degree of HA crystallinity was evaluated according to the formula:³⁵

$$\text{crystallinity} = \left(\frac{X}{Y} \right) 100$$

where X = net area of diffracted peaks, and Y = net area of diffracted peaks + background area. Crystal domain size along the c direction was calculated applying Scherrer's formula:

$$L_{(002)} = \frac{0.94\lambda}{\cos \theta \left(\sqrt{\Delta r^2 - \Delta_0^2} \right)}$$

where θ is the diffraction angle for plane (002), Δr and Δ_0 are the widths in radians of reflection (002) at half height for the synthesized and the reference HA materials, respectively, and $\lambda = 1.5405$ Å.

A.1.2.5 Infrared Microscopy Spectral Analysis

ATR-IR spectra were recorded on a Thermo Nicolet 380 FT-IR spectrometer equipped with a commercial ATR accessory. The infrared spectra were registered from 4000 to 400 cm^{-1} at 2 cm^{-1} resolution using a Bruker IFS 66v/S spectrometer using KBr pellets. ATR spectra were recorded with the cell empty to be used as a blank for subsequent experiments. Samples were made by placing the powder sample onto the Ge ATR crystal. Spectra were collected by averaging 32 scans at 4 cm^{-1} resolution.

A.1.2.6 Specific Surface Area Determination.

Measurements were undertaken using a Carlo Erba Sorpty 1750 instrument by measuring N_2 absorption at 77 K and adopting the well-known BET procedure.³⁶

A.1.2.7 Spectrophotometric Analysis

Phosphorus contents were determined spectrophotometrically as molybdovanadophosphoric acid using 1 cm quartz cell.³⁷ Calcium contents were measured using inductively coupled plasma (ICP) optical emission spectrometry (OES) using a Perkin Elmer Optima 4200DV.

A.1.2.8 X-Ray Photoelectron Spectroscopy (XPS)

Analyses were performed in an M-Probe Instrument (SSI) equipped with a monochromatic Al K_α source (1486.6 eV) with a spot size of 200×750 μm and pass energy of 25 eV, providing a resolution for 0.74 eV. With a monochromatic source, an electron flood gun was used to compensate the build up of positive charge on the insulator samples during the analyses. 10 eV electrons were selected to perform measurements on these samples. The accuracy of the reported binding energies (BEs) was estimated to be ± 0.2 eV. The quantitative data were also accurately

checked and reproduced several times (at least ten times for each sample), and the percentage error was estimated to be $\pm 1\%$.

A.1.2.9 Statistics Analysis

Determination of HA crystallite domain size along the *c* direction, bulk and surface Ca/P ratio, and specific surface area were carried out 5 times on the same synthesis product. Data are presented as mean value \pm SD. Differences were considered statistically significant at a significance level of 90%.

A.1.2.10 In Vitro Enamel Remineralization Procedures

Slabs of enamel (3×3 mm) were obtained from interproximal surfaces of premolars extracted for orthodontic reasons. After the extraction, the teeth were cut with diamond disks, and the obtained slabs were sonicated for 10 minutes in 50% ethanol in order to remove any debris. Then, the specimens were etched with 37% phosphoric acid for 1 minute. Etched slabs were washed in distilled water for 10 minutes under stirring and then air dried. Two different in vitro remineralization procedures have been performed. The first in vitro remineralization procedure utilizes a 10 wt% CHA in the range from 100 to 150 μm granules slurries constituted of both 20 nm or 100 nm sized nanocrystals. CHA nanocrystals aqueous slurries were applied for 10 minutes on the surfaces of the enamel slabs at room temperature with 100% relative humidity and then removed by water washing and air dried. The second in vitro remineralization process utilizes toothpaste containing both fluoride ions and CHA 0.5 – 3.0 μm sized clusters constituted by intergrowth of 100 nm sized nanocrystals. Comparable etched enamel slabs were divided into 3-groups of treatment using, respectively, fluoride or CHA-based toothpaste and only water (control). Each slab was brushed three times a day for a period of 15 days. The intervals between brushing sessions were at least 5 hours. Every brushing session has been performed for 30 seconds by an electric toothbrush using constant pressure and a bean sized toothpaste aliquot wetted with tap water, closely resembling the in vivo usual tooth brushing procedure. After every treatment, the single enamel slab was washed with tap water using a cleaned toothbrush in order to remove residual toothpaste.

A.1.3 Results

A.1.3.1 Synthesis and Characterization of Biomimetic Carbonate-Hydroxyapatite Nanocrystals

Biomimetic carbonate- hydroxyapatite nanocrystals have been synthesized with a nearly stoichiometric in bulk Ca/P molar ratio of about 1.6-1.7 and containing 4 ± 1

wt% of carbonate ions replacing prevalently phosphate groups. CHA nanocrystals have been synthesized both about 100 nm and 20 nm sized with an acicular and plate morphology, respectively. TEM images of synthetic 20 nm sized CHA nanocrystals showing the plate-shaped morphology and synthetic 100nm sized CHA nanocrystals showing the acicular morphology are reported in Figures 1(a) and 1(b), respectively. CHA nanocrystals can aggregate in micro-sized crystal clusters, whose dimensions increase prolonging maturation time in mother solution at constant temperature and stirring.³³

Powder X-ray diffraction patterns of plate shaped about 20 nm sized CHA nanocrystals and acicular shaped about 100 nm sized CHA nanocrystals (see Figures 2(b) and 2(c), resp.) show characteristic diffraction maxima of an apatite single phase (JCPDS 01-074-0565). These X-ray diffraction patterns are compared with those collected for natural carbonate hydroxyapatite from deproteinized dentine and enamel reported in Figures 2(a) and 2(d), respectively. The broadening of the diffraction maxima present in the X-ray diffraction patterns reported in Figures 2(a), 2(b), and 2(c) indicates a relatively low degree of crystallinity, which was quantified according to previous.³⁵ The degree of crystallinity of synthesized about 20 nm sized CHA nanocrystals with plate morphology and synthesized about 100 nm sized CHA nanocrystals with acicular morphology is 30% and 50%, respectively.

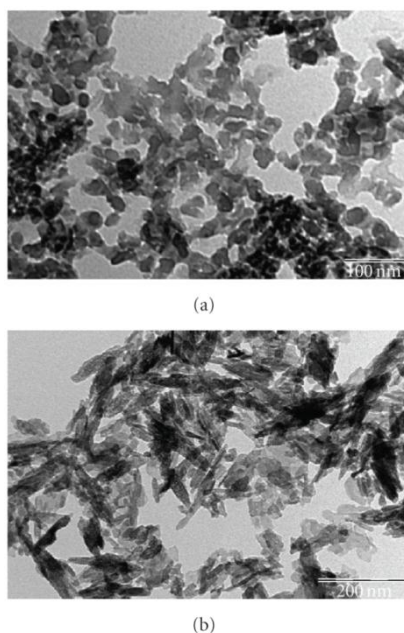


Figure 1: TEM images of (a) synthetic plate-shaped 20 nm sized CHA nanocrystals (scale bar = 100 nm), (b) synthetic plate-acicular 100 nm sized CHA nanocrystals (scale bars = 200 nm).

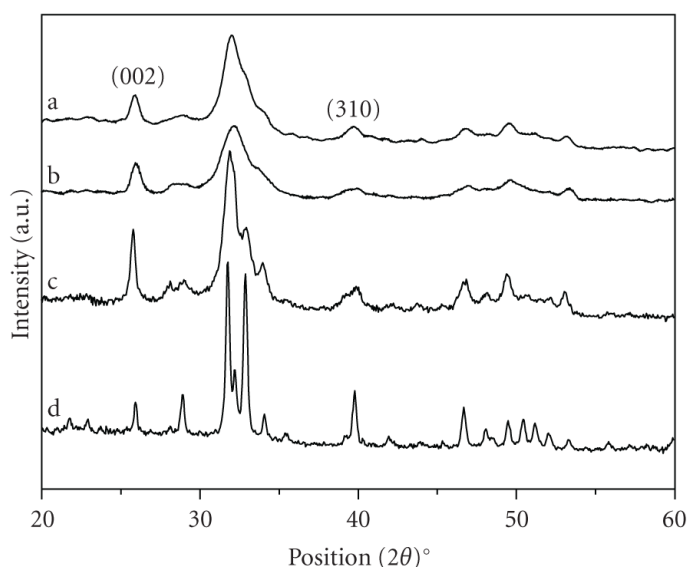


Figure 2: X-ray diffraction patterns of (a) natural carbonate-hydroxyapatite from deproteinized dentine, (b) synthetic plate shaped 20 nm sized CHA nanocrystals, (c) synthetic plate-acicular shaped 100 nm sized CHA nanocrystals, and (d) natural carbonate-hydroxyapatite from enamel.

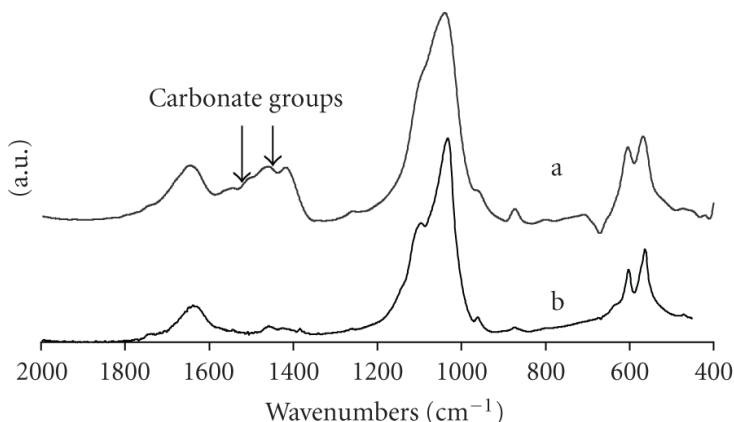


Figure 3: (a) FTIR spectra of synthetic 20 nm sized CHA nanocrystals, (b) natural carbonate-hydroxyapatite from deproteinized dentine.

The crystallinity degree of about 20 nm sized CHA nanocrystals is very close to that one determined from the X-ray diffraction pattern of deproteinized dentine natural carbonate-hydroxyapatite (28%) reported in Figure 2(a). Furthermore, the crystallinity degree of natural hydroxyapatite of deproteinized enamel, reported in Figure 2(d), is 70%. The crystal domain sizes along the *c* direction have been calculated by Scherrer's formula using the $2\theta = 26^\circ$ (002) diffraction peak of the X-ray diffraction patterns reported in Figures 2(a), 2(b), and 2(c). The calculated

crystal domain sizes for 20 nm sized CHA nanocrystals and deproteinized dentine are 250 Å and 213 Å, respectively

These results obtained by X-ray diffraction investigation reveal that the crystal structures of the synthesized CHA nanocrystals are very close to that observed for natural dentine. The same similarity can be observed from the comparison of the FTIR spectra of synthesized CHA nanocrystals and natural apatite of deproteinized dentine reported in Figures 3(a) and 3(b), respectively. In these spectra, the characteristic absorption bands of phosphate and carbonate groups are clearly resolved.

The absorption band at 1468 cm^{-1} is related to the carbonate group substitution to the phosphate one, while the shoulder at 1545 cm^{-1} can be considered the contribution of the carbonate group substituting the hydroxyl group in the apatite structure. This finding reveals that synthesized CHA nanocrystals not only contain a similar carbonate amount, but also underline that the carbonate substitution to the phosphate and/or hydroxyl group is very similar in the synthetic and biological crystals. A surface characterization of the synthetic carbonate-hydroxyapatite nanocrystals has been carried out in order to highlight their surface chemical-physical characteristic which directly interfaces and reacts with exposed dental tissues. The ATR spectra (data not shown) of the synthetic about 20 nm and 100 nm sized CHA nanocrystals reveal a 4% and 3 wt% surface carbonate, respectively. The consistent amount of surface of carbonate percentage present in synthetic CHA is appreciably higher than the surface carbonate percentage present in enamel and dentine about 2 wt%.

Specific surface area of $100\text{ m}^2\cdot\text{g}^{-1}$ and $80\text{ m}^2\cdot\text{g}^{-1}$ has been determined for 20 nm sized CHA nanocrystals with plate morphology and synthesized 100 nm sized CHA nanocrystals with acicular morphology, respectively. These specific surface area values obtained for synthetic nanocrystals are only slightly lower than the $110\text{ m}^2\cdot\text{g}^{-1}$ obtained for biological nanocrystals. The surface Ca/P molar ratio determined by XPS analysis for CHA nanocrystals and CHA crystals microclusters does not reveal appreciable differences and result significantly lower than Ca/P molar ratio determined by ICP analysis in bulk indicating a surface calcium deficiency probably due to surface disorder. In fact, the Ca/P molar ratios of 1.7 determined in bulk for synthetic CHA nanocrystals reduce to a value of 1.4-1.5 when determined on the crystals surface by XPS analysis (see Table 1).

XPS analysis of spectral features of the O 1s region of the synthetic 100 nm sized CHA nanocrystals (see Figure 4(c)) shows a definite O 1s shape fitted by three components: a first, very intense, peak at lower BE attributed to oxygen in phosphate group, a second peak due to OH of the carbonate-hydroxyapatite, and a

final peak at very high BE, which can be attributed to trapped undissociated water and carbonates.

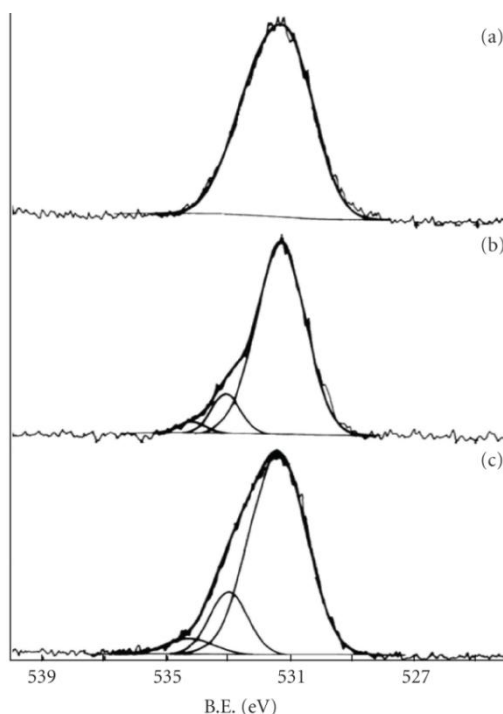


Figure 4: XPS analysis of spectral features of (a) the O 1s region of the enamel demineralized by orthophosphoric acid 37% for 1 min, (b) enamel remineralized by a treatment with synthetic microclusters of CHA nanocrystals 100 nm sized for 10 min, and (c) synthetic microclusters of CHA nanocrystals 100 nm sized.

A.1.3.2 *In Vitro Enamel Surface Remineralization by Biomimetic CHA Nanocrystals*

SEM analysis allows investigating the morphology of both demineralized enamel and the features observed after remineralization procedures induced by biomimetic CHA nanocrystals in vitro application.

The demineralization procedure by orthophosphoric acid 37% for 1 minute removes the aprismatic enamel, and exposed hydroxyapatite prisms became evident. Figure 5(a) shows demineralization of both interprismatic and prismatic enamel structures. After treatment for 10 minutes by aqueous slurry of both synthetic 20 nm and 100 nm sized CHA nanocrystals, the surface of the demineralized enamel appears covered by the CHA phase (see Figures 5(b) and 5(c), resp.) arranged in a thick and homogeneous apatitic layer. XPS analysis of spectral features of the O 1s region of the enamel demineralized by orthophosphoric acid 37% for 1 minute shows a single broad band, in which it is difficult to determine precisely and to quantify the

binding energy (BE) and, therefore, the kind of the surface oxygen components (see Figure 4(a)).

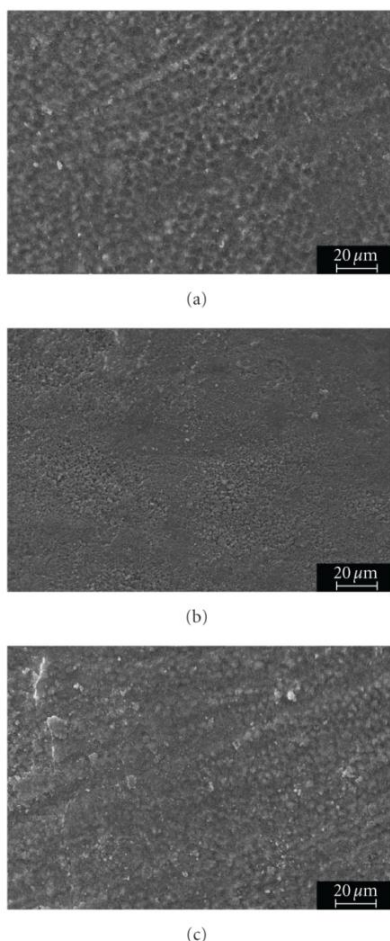


Figure 5: SEM image of enamel surface after application of 37% ortophosphoric acid for 1 min. The etching treatment removed aprismatic layer and exposed prismatic and interprismatic hydroxyapatite structures (a), remineralized enamel surface after treatment by synthetic CHA micro-clusters constituted of nanocrystals 20 nm (b) and 100 nm sized (c) and synthetic CHA microclusters.

Table 1: XPS analysis of CHA nanocrystals, enamel tooth treated with ortophosphoric acid before and after treatment with either CHA 20 or 100 nm sized nanocrystals and after brushing with toothpaste containing booth CHA or fluoride.

Sample	O (%)	C (%)	Ca (%)	P (%)	N (%)	Si (%)	Na (%)	F (%)	Ca/P
20 nm CHA nanocrystals	50.4	17.6	19.4	12.6	—	—	—	—	1.5
100 nm CHA nanocrystals	48.4	18.0	19.6	13.9	—	—	—	—	1.4
Tooth treated with ortophosphoric acid	30.7	49.4	5.4	5.3	5.9	1.9	1.4	—	1.1
Tooth treated with 20 nm CHA nanocrystals	43.3	27.3	13.4	10.1	2.3	—	1.9	—	1.3
Tooth treated with 100 nm CHA nanocrystals	43.7	26.0	14.8	11.2	1.0	—	1.5	—	1.3
CHA containing toothpaste	30.7	51.9	5.5	4.7	1.6	5.6	—	—	1.2
Fluoride containing toothpaste	20.9	63.3	4.1	1.2	2.0	4.9	—	3.6	3.4

On the contrary, the enamel remineralized by synthetic 100 nm sized CHA nanocrystals for 10 minutes shows a definite O 1s shape fitted by three components at different binding energy (see Figure 4(b)). These components correspond to the same three ones used to fit O 1s shape recorded for synthetic 100nm sized CHA nanocrystals (see Figure 4(c)), the first at lower BE very intense peak is attributed to oxygen in phosphate group, the second peak is due to OH of the carbonate-hydroxyapatite, and a final peak at high BE, can be attributed to trapped undissociated water and carbonate groups. These results unequivocally confirm the presence of synthetic CHA at the surface of the treated enamel and the consequent validation of the enamel remineralization. The same finding is pointed out by the ATR spectrum of enamel treated for 10 minutes by synthetic 100 nm sized CHA nanocrystals, showing appreciable higher intensity of the characteristic absorption bands of carbonate ions (1420–1460 and 1680 cm^{-1}) in respect of the same absorption bands present in the demineralized enamel ATR spectrum. No differences are appreciable in the phosphate ions bands (1000–1100 and 530–580 cm^{-1}). ATR spectrum (data not shown) of remineralized enamel reveals that surface apatite is richer in carbonate than natural one, such as synthetic 100 nm sized CHA nanocrystals.

A.1.3.3 In Vitro Enamel Surface Remineralization by Toothpaste Containing either Fluoride or Biomimetic CHA Nanocrystals Microclusters

SEM analysis allowed us to investigate the morphology of both demineralized enamel and the features observed after a remineralization process which utilizes in vitro application of toothpaste containing either fluoride or CHA microclusters constituted of 100 nm in size nanocrystals.

The surfaces of the teeth treated with fluoride (see Figure 6(b)) were not consistently changed respect to that of demineralization by orthophosphoric acid (see Figure 6(c)). Actually both the interprismatic and prismatic enamel structures appear still evident. On the contrary after treatment of the enamel slabs with a toothpaste containing synthesized CHA microclusters constituted of 100 nm sized nanocrystals, the interprismatic and prismatic enamel structures appear to be completely hidden by a thick homogeneous apatitic layer (see Figure 6(a)). The XRD patterns collected on the surface of enamel slabs after treatment with CHA or fluoride toothpaste and water are reported in Figures 7(b), 7(c), and 7(d), respectively, and compared with the XRD pattern (see Figure 7(a)) of CHA microclusters constituted of 100 nm sized nanocrystals utilized to prepare the used CHA toothpaste. The XRD diffraction maxima recorded on the surface of enamel slabs treated with fluoride containing toothpaste appear slightly more sharpened

than those obtained on the enamel etched slabs brushed only with water. This observation reveals an increased crystallinity degree probably due to a partial structural conversion of hydroxyapatite into fluoride substituted hydroxyapatite. On the contrary, the XRD pattern obtained on the surface of enamel slabs brushed with CHA containing toothpaste shows the broadened diffraction maxima characteristic of the synthetic biomimetic CHA, revealing its presence on the enamel surface. The CHA not removed by brushing procedures suggests the formation of chemical bonds between the synthetic CHA microclusters constituted of 100 nm sized nanocrystals and natural enamel apatite crystals. These bonds allow the formation of a persistent CHA coating on the enamel surface whose morphology was detected by SEM analysis.

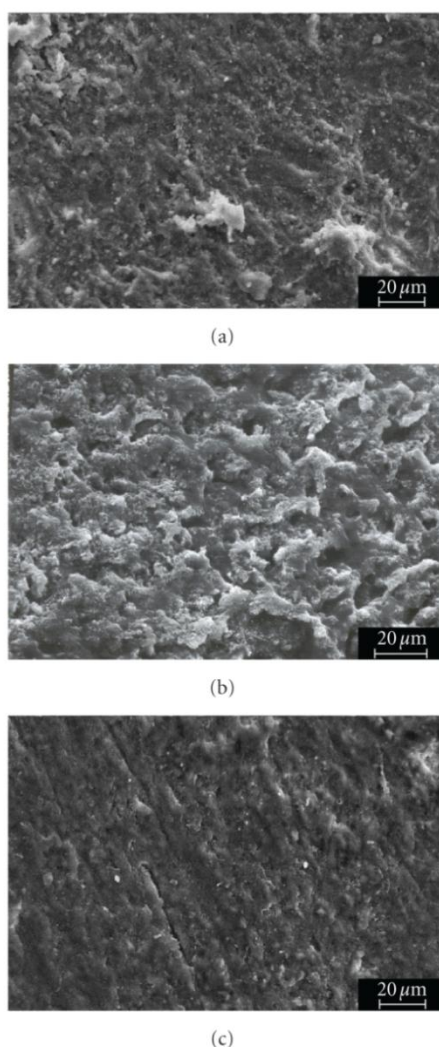


Figure 6: SEM images of enamel after brushing treatment with (a) CHA toothpaste containing, (b) fluoride containing toothpaste, and (c) orthophosphoric acid application.

The surface Ca/P molar ratio determined by XPS analysis for demineralized enamel slabs before and after in vitro remineralization by brushing whit toothpaste containing either fluoride or CHA are compared in Table 1. In this table, a comparison with the Ca/P molar ratio of CHA microclusters constituted of 100 nm sized nanocrystals also present. The enamel surface Ca/P molar ratio changes before and after the brushing treatment with toothpaste containing fluoride, assuming a value of 3.4 very different from the apatite stoichiometric one (Ca/P = 1.7). This finding reveals that the only structural modification of enamel hydroxyapatite induced by fluoride is restricted to a partial hydroxyl groups replacement by fluoride ions without affecting appreciably the Ca and phosphate structural network. On the contrary, enamel slabs treated with the toothpaste containing synthesized CHA microclusters of 100nm sized nanocrystals exhibit a surface Ca/P molar ratio very similar to that one of the synthetic CHA. This coating is highly less crystalline than native enamel apatite, and consists of a new apatitic mineral deposition which progressively fills the scratches and pits. On the contrary, the surface remineralization observed on the specimens treated with fluoride containing toothpaste is mainly based on chemical-physical enamel apatite surface modifications rather than a formation of a new mineral deposition. The CHA biomimetic coating formation is a remineralization process corresponding to a new apatite deposition in the demineralized area of enamel surface.

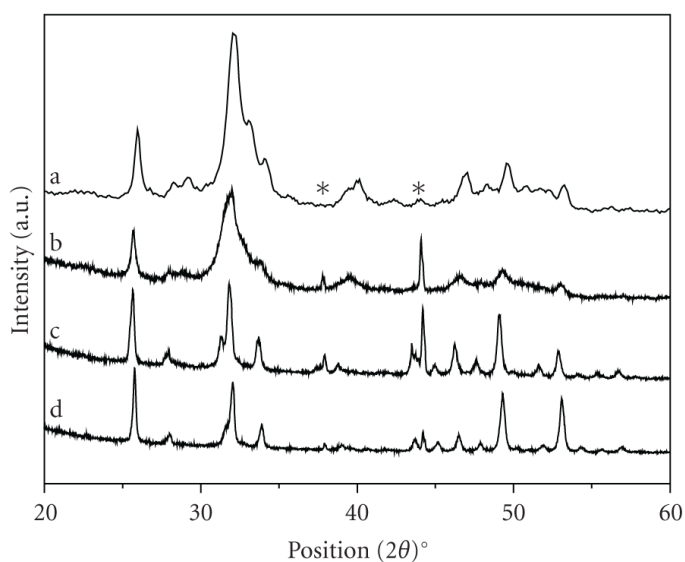


Figure 7: (a) XRD pattern of synthetic CHA, (b) enamel after brushing treatment with CHA containing toothpaste, (c) enamel after brushing treatment with fluoride containing toothpaste, (d) enamel after brushing treatment with water. * indicates Al holder diffraction maxima.

A.1.4 Discussion

Enamel is the hardest and most mineralized tissue of human body. It is structured in order to resist to mechanical injuries, abrasion, and chemical attack. Differently from all the other mineralized tissues, it lacks proteins even if they are essential to its formation. Actually, matrix proteins are cleaved by proteinases secreted by the ameloblasts during tooth formation; hence, the matrix proteins of enamel are not incorporated into enamel prisms.³⁸ Degradation and resumption of enamel matrix proteins is the reason why enamel prisms, once formed, cannot be remodelled. After enamel prism formation, only the amount of hydroxyapatite within the prisms may decrease in consequence of chemical changes into the oral environment.

Acid attack is one of the major causes of enamel hydroxyapatite loss. It may occur even in young age as a consequence of plaque metabolism or simply due to food and beverage intakes.²⁻⁴

In the present paper, synthetic carbonate-hydroxyapatite biomimetic nanocrystals have been chemical-physical characterized and investigated regarding the possibility to obtain an in vitro remineralization of the altered enamel surfaces. The experimental model used in the present investigation was the demineralization by means of orthophosphoric acid of sound enamel of the interproximal surfaces and its subsequent remineralization. This model was chosen because the demineralizing effect of orthophosphoric acid is well known in terms of chemical and microhistological features because it is an essential part of the procedures of adhesive restoration applications. The SEM observations showed that the enamel is characterized by both amorphous and prismatic hydroxyapatite and by an irregular surface even. The use of orthophosphoric acid causes an exposure of prism and a loss of both interprismatic and prismatic substances. The treatment of demineralized enamel only for ten minutes, by synthetic CHA nanocrystals, induces a consistent enamel remineralization through the formation of a surface carbonate-hydroxyapatite coating. This coating is due to the chemical bond of the synthetic CHA nanocrystals biomimetic for composition, structure, size, and morphology on the surface prismatic hydroxyapatite enamel. It can be supposed that the application of CHA nanocrystals 20 nm sized allows a better mineralization in the lower surface fissure, because the interprismatic and prismatic enamel structures appear totally hidden. Using an equal time of treatment, the application of CHA nanocrystals 100 nm sized produces the formation of a homogeneous coating which hides interprismatic and prismatic enamel structures when examined with SEM. In this paper, an in vitro enamel surface remineralization by brushing with toothpaste containing either fluoride or biomimetic CHA nanocrystals microclusters has been also carried out. The XRD

patterns, SEM images, and XPS spectra collected on the surface of enamel slabs before and after treatment with CHA or fluoride toothpaste underline the possibility to obtain an enamel remineralization through the formation of a surface apatite coating which covers the enamel structure avoiding the most probably health dangerous fluoride effects, to contrast the mechanical abrasion and acid attacks to which tooth enamel is exposed. The documented CHA biomimetic coating formation which is less crystalline than enamel natural apatite represents an enamel repair process corresponding to an apatite deposition inside the demineralized area of enamel surface and may be considered an innovative approach to contrast enamel demineralization.

A.1.5 References

- [1] J. D. Eccles, "Dental erosion of nonindustrial origin. A clinical survey and classification," *The Journal of Prosthetic Dentistry*, vol. 42, no. 6, pp. 649–653, 1979.
- [2] C. Deery, M. L. Wagner, C. Longbottom, R. Simon, and Z. J. Nugent, "The prevalence of dental erosion in a United States and a United Kingdom sample of adolescents," *Pediatric Dentistry*, vol. 22, no. 6, pp. 505–510, 2000.
- [3] C. R. Dugmore and W. P. Rock, "The prevalence of tooth erosion in 12-year-old children," *British Dental Journal*, vol. 196, no. 5, pp. 279–282, 2004.
- [4] Y. H. Al-Dlaigan, L. Shaw, and A. Smith, "Dental erosion in a group of British 14-year-old, schoolchildren—part I: prevalence and influence of differing socioeconomic backgrounds," *British Dental Journal*, vol. 190, no. 3, pp. 145–149, 2001.
- [5] I. B. Arnadottir, S. R. Sæmundsson, and W. P. Holbrook, "Dental erosion in Icelandic teenagers in relation to dietary and lifestyle factors," *Acta Odontologica Scandinavica*, vol. 61, no. 1, pp. 25–28, 2003.
- [6] J. H. Nunn, P. H. Gordon, A. J. Morris, C. M. Pine, and A. Walker, "Dental erosion—changing prevalence? A review of British national childrens' surveys," *International Journal of Pediatrics Dentistry*, vol. 13, no. 2, pp. 98–105, 2003.
- [7] British Soft Drinks Association, "A shared responsibility," Annual Report, The British Soft Drinks Association, London, UK, 2002-2003.
- [8] C. C. Costa, I. C. S. Almeida, and L. C. Costa Filho, "Erosive effect of an antihistamine-containing syrup on primary enamel and its reduction by fluoride dentifrice," *International Journal of Pediatrics Dentistry*, vol. 16, no. 3, pp. 174–180, 2006.

- [9] M. Kitchens and B. M. Owens, "Effect of carbonated beverages, coffee, sports and high energy drinks, and bottled water on the in vitro erosion characteristics of dental enamel," *Journal of Clinical Pediatric Dentistry*, vol. 31, no. 3, pp. 153–159, 2007.
- [10] A. Wiegand and T. Attin, "Occupational dental erosion from exposure to acids—a review," *Occupational Medicine*, vol. 57, no. 3, pp. 169–176, 2007.
- [11] A. Lussi, T. Jaeggi, and D. Zero, "The role of diet in the aetiology of dental erosion," *Caries Research*, vol. 38, supplement 1, pp. 34–44, 2004.
- [12] A. Lussi, E. Hellwig, D. Zero, and T. Jaeggi, "Erosive tooth wear: diagnosis, risk factors and prevention," *American Journal of Dentistry*, vol. 19, no. 6, pp. 319–325, 2006.
- [13] N. X. West, A. Maxwell, J. A. Hughes, D. M. Parker, R. G. Newcombe, and M. Addy, "A method to measure clinical erosion: the effect of orange juice consumption on erosion of enamel," *Journal of Dentistry*, vol. 26, no. 4, pp. 329–335, 1998.
- [14] N. X. West, J. A. Hughes, D. M. Parker, R. G. Newcombe, and M. Addy, "Development and evaluation of a low erosive blackcurrant juice drink 2. Comparison with a conventional blackcurrant juice drink and orange juice," *Journal of Dentistry*, vol. 27, no. 5, pp. 341–344, 1999.
- [15] J. A. Hughes, N. X. West, D. M. Parker, R. G. Newcombe, and M. Addy, "Development and evaluation of a low erosive blackcurrant juice drink in vitro and in situ 1. Comparison with orange juice," *Journal of Dentistry*, vol. 27, no. 4, pp. 285–289, 1999.
- [16] J. A. Hughes, N. X. West, D. M. Parker, R. G. Newcombe, and M. Addy, "Development and evaluation of a low erosive blackcurrant juice drink 3. Final drink and concentrate, formulae comparisons in situ and overview of the concept," *Journal of Dentistry*, vol. 27, no. 5, pp. 345–350, 1999.
- [17] A. V. Nieuw Amerongen, C. H. Oderkerk, and A. A. Driessen, "Role of mucins from human whole saliva in the protection of tooth enamel against demineralization in vitro," *Caries Research*, vol. 21, no. 4, pp. 297–309, 1987.
- [18] B. T. Amaechi, S. M. Higham, W. M. Edgar, and A. Milosevic, "Thickness of acquired salivary pellicle as a determinant of the sites of dental erosion," *Journal of Dental Research*, vol. 78, no. 12, pp. 1821–1828, 1999.
- [19] Y. Nekrashevych and L. Stosser, "Protective influence of experimentally formed salivary pellicle on enamel erosion: an in vitro study," *Caries Research*, vol. 37, no. 3, pp. 225–231, 2003.
- [20] D. T. Zero and A. Lussi, "Erosion—chemical and biological factors of importance to the dental practitioner," *International Dental Journal*, vol. 55, no. 4, supplement 1, pp. 285–290, 2005.

- [21] J. D. B. Featherstone, R. Glana, M. Shariati, and C. P. Shields, "Dependence of in vitro demineralization of apatite and remineralization of dental enamel on fluoride concentration," *Journal of Dental Research*, vol. 69, pp. 620–625, 1990.
- [22] European Food Safety Authority, "Opinion of the scientific panel on dietetic products, nutrition and allergies on a request from the Commission related to the tolerable upper intake level of fluoride," *The EFSA Journal*, vol. 192, pp. 1–65, 2005.
- [23] D. G. Pendrys and J.W. Stamm, "Relationship of total fluoride intake to beneficial effects and enamel fluorosis," *Journal of Dental Research*, vol. 69, pp. 529–538, 1990.
- [24] G. M. Whitford, "The physiological and toxicological characteristics of fluoride," *Journal of Dental Research*, vol. 69, pp. 539–549, 1990.
- [25] C. Ganss, J. Klimek, U. Schaffer, and T. Spall, "Effectiveness of two fluoridation measures on erosion progression in human enamel and dentine in vitro," *Caries Research*, vol. 35, no. 5, pp. 325–330, 2001.
- [26] C. Ganss, J. Klimek, V. Brune, and A. Schurmann, "Effects of two fluoridation measures on erosion progression in human enamel and dentine in situ," *Caries Research*, vol. 38, no. 6, pp. 561–566, 2004.
- [27] A. Wiegand and T. Attin, "Influence of fluoride on the prevention of erosive lesions—a review," *Oral Health & Preventive Dentistry*, vol. 1, no. 4, pp. 245–253, 2003.
- [28] A. Young, P. S. Thrane, E. Saxegaard, G. Jonski, and G. R. Olla, "Effect of stannous fluoride toothpaste on erosion-like lesions: an in vivo study," *European Journal of Oral Sciences*, vol. 114, no. 3, pp. 180–183, 2006.
- [29] M. F. Teaford, "A review of dental microwear and diet in modern mammals," *Scanning Microscopy*, vol. 2, no. 2, pp. 1149–1166, 1988.
- [30] N. Roveri and B. Palazzo, "Hydroxyapatite nanocrystals as bone tissue substitute," in *Tissue, Cell and Organ Engineering*, C. S. S. R. Kumar, Ed., vol. 9 of *Nanotechnologies for the Life Sciences*, pp. 283–307, Wiley-VCH, Weinheim, Germany, 2006.
- [31] B. Palazzo, M. Iafisco, M. Laforgia, et al., "Biomimetic hydroxyapatite-drug nanocrystals as potential bone substitutes with antitumor drug delivery properties," *Advanced Functional Materials*, vol. 17, no. 13, pp. 2180–2188, 2007.
- [32] E. Landi, A. Tampieri, G. Celotti, and S. Sprio, "Densification behaviour and mechanisms of synthetic hydroxyapatites," *Journal of the European Ceramic Society*, vol. 20, no. 14–15, pp. 2377–2387, 2000.
- [33] S. P. A. Coswell, G. Gazzaniga, N. Roveri, et al., "Biologically active nanoparticles of a carbonate-substituted hydroxyapatite, process for their preparation and compositions incorporating the same," EU patent no. 005146, 2006.

- [34] S.-C. Liou, S.-Y. Chen, H.-Y. Lee, and J.-S. Bow, "Structural characterization of nano-sized calcium deficient apatite powders," *Biomaterials*, vol. 25, no. 2, pp. 189–196, 2004.
- [35] Z. E. Erkmen, "The effect of heat treatment on the morphology of D-Gun sprayed hydroxyapatite coatings," *Journal of Biomedical Materials Research Part B*, vol. 48, no. 6, pp. 861– 868, 1999.
- [36] S. Brunauer, P. H. Emmett, and E. Teller, "Adsorption of gases in multimolecular layers," *Journal of the American Chemical Society*, vol. 60, no. 2, pp. 309–319, 1938.
- [37] K. P. Quinlan and M. A. DeSesa, "Spectrophotometric determination of phosphorus as molybdovanadophosphoric acid," *Analytical Chemistry*, vol. 27, no. 10, pp. 1626–1629, 1955.
- [38] J. P. Simmer and A. G. Fincham, "Molecular mechanisms of dental enamel formation," *Critical Reviews in Oral Biology and Medicine*, vol. 6, no. 2, pp. 84–108, 1995.

APPENDIX A2: Alkaline phosphatase grafting on bioactive glasses and glass ceramics

E. Vernè, S. Ferraris, C. V. Brovarone, S. Spriano, C. L. Bianchi, A. Naldoni, M. Morra, C. Cassinelli, *Acta Biomaterialia* **2010**, 6, 229–240.

A.2.1 Introduction

Improvements in bone implant integration and bone regeneration at surgical sites are still unresolved problems in orthopaedic and dental surgery. Recently, new strategies to provide an appropriate environment for bone regeneration have been investigated. Among them, the delivery of biomolecules with a specific action on the bone mineralization process has attracted much attention. From the clinical point of view, it is possible to deliver active molecules systemically or locally at the implant site during surgical procedures. These techniques have not been thoroughly investigated because during systemic delivery biomolecules could be rapidly inactivated by serum and a large amount is required to ensure a sufficient level at the site of damage. Moreover, growth factors and proteins locally delivered at surgical sites without a carrier immediately diffuse and can be rapidly washed out by drainage. Finally, both these techniques require a large number of biomolecules and do not allow gradual release at the site of damage.^{1,2} A number of studies have been published on polymeric matrices as carriers of osteogenic growth factors.^{3,4} However, it is possible to graft these molecules onto implanted material surfaces. Functionalization techniques can be classified in terms of type of molecule or strategy of delivery. As far as the first point is concerned, it is also possible to graft cell adhesion molecules, such as proteins from the extracellular matrix (ECM proteins) or derived peptides (e.g. the sequence Arg–Gly–Asp, RGD), growth factors and enzymes. As far as grafting strategies are concerned, there are three main techniques available: simple adsorption, covalent bonding or release from a degradable carrier.^{5,6} In the literature several solutions have been proposed. ECM proteins or peptides are mainly anchored to biomaterial surfaces in order to improve the biological response of implants. Fibronectin has been grafted onto titanium surfaces via tresyl chloride activation⁷ and synthetic peptides have been covalently grafted to oxidized titanium substrates after silanization.⁸ Other research groups have focused their activities on enzymatic grafting onto inert surfaces for analytical purposes, such as sensors.^{9,10} Finally, the possibility of anchoring growth factors to biomaterials has been considered, for example bone morphogenetic proteins (BMP) have been grafted to titanium surfaces via plasma surface modification treatment¹¹ and to bioactive glass surfaces by silanization.¹²

Biomimetism can be defined as the ability to promote both inorganic and biological responses. The inorganic response refers to the ability to induce hydroxyapatite precipitation onto material surfaces after exposure to physiological or simulated body fluids (commonly known as “bioactivity”, and widely studied and documented for bioactive glasses and glass ceramics)¹³. The biological response refers to the ability of the material to directly stimulate cell behaviour via proper biochemical signals. It is widely known that bioactive glasses and glass ceramics are able to induce apatite precipitation in physiological fluids¹³ and, thus, by anchoring to specific surface biomolecules it is possible to improve tissue regeneration around implants, from both a chemical and biological point of view. The aim of the present research work was to graft an enzyme involved in bone formation and mineralization (alkaline phosphatase, ALP) to the surface of bioactive glasses and glass ceramics in order to obtain stable biomimetic surfaces. Bioactive glasses and glass ceramics were chosen because they have good potential as materials for bone defect regeneration. ALP was chosen as the biomolecule for biological functionalization since it was a good model enzyme: it is well known and widely used as a marker of osteoblast differentiation in in vitro tests and the assay is quite simple and relatively inexpensive. At the same time, ALP is of potential interest as it is involved in the bone formation and mineralization processes. A study of the literature¹⁴ underlined that higher ALP activity was detected in mineralization areas of alveolar bone and cellular cementum and, in particular, it showed that there is a relationship between enzyme activity and cementum thickness. Another research work¹⁵ described how ALP application in conjunction with titanium implants improved new bone formation and mineralization around materials. Moreover, it has been suggested¹⁶ that ALP coatings onto surfaces could favour mineralization and attachment of collagen sheets to functionalized substrates. The active role of ALP in the mineralization process was also evident in a study by Golub and Boesze-Battaglia¹⁷ and was investigated by de Jonge et al.,¹⁸ who reported experimental evidence of the ability of ALP grafted surfaces to provide local enrichment of Ca^{2+} and PO_4^{3-} ions.

A.2.2 Materials and methods

A.2.2.1 Materials preparation

Two different biomaterials were considered in this research work. The first was a glass with a simple composition and a low bioactivity index, belonging to the system $\text{SiO}_2\text{--CaO--NaO--Al}_2\text{O}_3$ (SCNA from here on). The second was a more complex glass with a high degree of bioactivity, CEL2, belonging to the system $\text{SiO}_2\text{--P}_2\text{O}_5\text{--CaO--MgO--Na}_2\text{O--K}_2\text{O}$. Glasses were prepared by melting the

precursors in a platinum crucible and quenching the melt on a brass plate, to obtain glass bars, which were subsequently annealed in a furnace to relax the residual stresses. Detailed compositions of the glasses, melting temperatures and annealing conditions are reported in Table 1. Annealed bars were cut in a mechanical cropper and polished with SiC abrasive papers and diamond pastes. SCNA were chosen for their simple composition and high stability, as demonstrated by previous works concerning silver surface enrichment on bulk materials and coatings,^{19,20} as well as surface functionalization with bone morphogenetic proteins.¹² They were investigated only in glassy form, since the foreseen applications (i.e. bioactive coatings) do not need a devitrification treatment. In contrast, CEL2 was investigated in both its glassy and glass ceramic forms. This second step was carried out because CEL2 has been employed in the preparation of highly bioactive glass ceramic scaffolds, as described in previous works.^{21,22}

Table 1: Glass composition (molar percentages), melting temperatures and annealing conditions.

Glass	Glass composition (mol.%)							T_{melt} (°C)	Annealing
	SiO ₂	P ₂ O ₅	CaO	MgO	Na ₂ O	K ₂ O	Al ₂ O ₃		
SCNA	57		34		6		3	1550	10 h at 600 °C
CEL2	45	3	26	7	15	4		1400	12 h at 500 °C

Functionalization of glass ceramic scaffolds is a possible future application of the process described in this paper. In order to prepare CEL2 glass ceramic samples (CEL2-cer) CEL2 samples were subjected to a thermal treatment, 1 h at 950 °C, before polishing. After this process CEL2-cer samples were polished, in the same way as the glass samples.

A.2.2.2 Hydroxyl exposure

The first step of the functionalization process was a cleaning treatment, to promote both surface removal of contaminants and exposure of reactive hydroxyls. The cleaning procedure was determined from a previous study on functionalization of bioactive glasses.¹² In the cited reference different treatments were compared through contact angle measurement and X-ray photoelectron spectroscopy (XPS) analysis in order to study surface modification (hydroxyl exposure and bioactivity). The optimal treatment was chosen as that which allowed high hydroxylation in a controlled and reproducible way. On this basis, a first wash in acetone for 5 min in an ultrasonic bath was carried out and subsequently the samples were washed three times in bidistilled water for 5 min in an ultrasonic bath, to favour –OH group exposure. After this treatment, samples were air dried at room temperature, as reported in Vernè et al.¹² Hydroxylated samples are henceforth designated Glass-wash (Table 2). The presence of hydroxyls groups on the sample surface was

investigated by means of contact angle measurements (Drop Shape Analysis System DSA10, Kruss), since their exposure renders surfaces hydrophilic.

A.2.2.3 Silanization

The second step of the process was the introduction of specific functional groups in order to promote and stabilize bonding between the material and organic molecules. In this research work silanization was chosen, because it is a well-known technique for glass functionalization. In our experiments this technique was adapted to reactive glasses and glass ceramics, as previously described.¹²

Table 2: Names and characteristics of the samples analysed.

Sample name	Material	Treatment
SCNA-wash	SCNA	Hydroxylation ^a
SCNA + sil	SCNA	Hydroxylation and silanization
SCNA + sil + ALP	SCNA	Hydroxylation, silanization and ALP grafting
SCNA + ALP	SCNA	Hydroxylation and ALP grafting
CEL2-wash	CEL2	Hydroxylation ^a
CEL2 + sil	CEL2	Hydroxylation and silanization
CEL2 + sil + ALP	CEL2	Hydroxylation, silanization and ALP grafting
CEL2 + ALP	CEL2	Hydroxylation and ALP grafting
CEL2-cer-wash	CEL2-cer	Hydroxylation ^a
CEL2-cer + sil	CEL2-cer	Hydroxylation and silanization
CEL2-cer + sil + ALP	CEL2-cer	Hydroxylation, silanization and ALP grafting
CEL2-cer + ALP	CEL2-cer	Hydroxylation and ALP grafting

^a Ultrasonic washing: 5 min in acetone and 3 × 5 min in water.

3-Aminopropyl triethoxysilane [$\text{H}_2\text{N}(\text{CH}_2)_3\text{Si}(\text{OC}_2\text{H}_5)_3$] (APTES) (99%, Aldrich) was employed in order to introduce amino groups as functionalities for enzyme grafting. Silanization was carried out using a method analogous that described by Ma et al.²³ and applied by Verné et al.¹² Glass and glass ceramic samples were immersed in a solution containing 150 ml ethanol and 35 μl silane for 6 h at room temperature and then dried for 1 h at 100 °C in a furnace in order to stabilize the silane–surface bond. After cooling the samples were washed three times in ethanol in an ultrasonic bath for 5 min in order to remove non-bonded molecules and dried for 1 h at 100 °C in a furnace. Henceforth silanized samples are indicated by Glass + sil (Table 2). Silanization effectiveness was verified by means of contact angle measurements, as the presence of silane on the materials surfaces induces hydrophobicity. Some samples were ultrasonically washed for 2 min in Tris–HCl solution after silanization and then analysed in order to study the stability of the silane–surface bonding. Tris–HCl was chosen because it is one of the media involved in the following steps of functionalization. Tris–HCl solution was prepared by dissolving 2.42 g Tris [tris(hydroxymethyl)aminomethane, $(\text{HOCH}_2)_3\text{CNH}_2$, >99.9% ultra- pure grade, Aldrich) in 100 ml bidistilled water, pH adjusted to 7.5 by adding 1M HCl. A second technique employed to investigate this step of the process was XPS analysis (Al source, M-Probe, Surface Science

Instruments), as it allows the detection of nitrogen, characteristic of amino groups, on the sample surface.

A.2.2.4 Alkaline phosphatase grafting

The final step of the functionalization process was biomolecule anchoring. In order to covalently graft ALP to glasses and glass ceramics, the samples were immersed in a solution of 5 mg·ml⁻¹ ALP in phosphate-buffered saline (PBS) (Sigma–Aldrich). ALP solution was prepared by dissolving bovine ALP (bovine intestinal mucosa, lyophilized powder, 10–30 DEA U mg solid⁻¹) (Sigma–Aldrich) in PBS, under magnetic stirring. Silanized samples and hydroxylated ones only were immersed in 5 ml ALP solution for 20 h. Different grafting temperatures were tested: 4 °C in a refrigerator, 25 °C in a thermostatic bath and 37 °C in an incubator. At the end of the incubation period samples were washed, without stirring or shaking, in Tris–HCl solution buffered at pH 7.5 and air dried at room temperature. Functionalized samples are henceforth designated Glass + sil + ALP and Glass + ALP, respectively (Table 2). Anchoring temperatures are specified each time. As far as grafting temperature is concerned, the two glasses (SCNA and CEL2) and the glass ceramic (CEL2-cer) were grafted at 4 °C, while glassy SCNA and CEL2 were also studied at different temperatures, in order to compare a more stable glass and a more reactive one. Temperatures were selected on the basis of the functionalization procedures described in the literature.^{7,24} The three temperatures mentioned above were chosen in order to maximize reaction effectiveness, at the same time preserving ALP from inactivation and denaturation. ALP is sensitive to both temperature and pH alterations: it has been shown that at pH 5 and below and temperatures higher than 40 °C inactivation occurs.^{25,26} All treatments were performed in PBS in order to maintain a constant pH of ~7.5. The temperature was kept below 37 °C. In order to verify the effect of temperature on both grafting and protein activity, samples of pure ALP solution were also stored at different temperatures and then analysed to verify their activity, as described below. In order to study the bonding stability between grafted ALP and the material surface some functionalized samples (both directly anchored and silanized) were washed for 2 min in an ultrasonication apparatus¹² in 10 ml Tris–HCl solution and then analysed for enzymatic activity. Washing solutions were also analysed to determine the amount of ALP washed out of the samples. Grafting efficacy was investigated by means of enzymatic activity tests (described below) and by means of XPS analysis. As far as the last technique is concerned, in the survey spectra enrichment of carbon and nitrogen and a decrease in signals characteristic of glass/glass ceramic substrate would be expected as a consequence

of ALP presence on the material surface. A detailed study of the carbon region allowed an investigation of the characteristic peaks of the enzyme at ~286 eV (C–O and C–N bonds) and 292–293 eV (aromatic rings).

A.2.2.5 *Enzyme activity study*

In order to improve bone formation and mineralization, ALP grafted onto material surfaces has to be biologically active. Enzyme activity was studied by monitoring the reaction between ALP and p-nitrophenylphosphate in an alkaline environment. p-Nitrophenylphosphate is hydrolyzed by ALP and produces p-nitrophenol, characterized by a yellow colour. The amount of p-nitrophenol produced is proportional to the amount of ALP present and could be quantified by means of UV–visual spectroscopy. In order to determine enzyme activity, functionalized samples were placed in 1 ml reactive mixture containing equal volumes of 2mM MgCl₂, 2mM p-nitrophenylphosphate and 2 mM 2-amino-2-methyl-1-propanol (AMP) (all reagents from Sigma–Aldrich Fluka). The pH value of the reactive mixture was 10.5. The reaction between ALP grafted onto the sample surface and p-nitrophenylphosphate in solution was stopped after 2 min by the addition of 1 ml 0.1 N NaOH. After removing solid samples from the wells the intensity of the yellow colour produced was quantified by measuring the UV absorbance at 405 nm (Genius Spectra Fluor plus Tecan).

Values of ALP activity for bulk samples were related to sample surface area in order to minimize data dispersion due to differences in sample shape and dimensions. In order to obtain enzymatic specific activities, absorbance values were divided by sample surface area, only the surface exposed to functionalization being considered. Roughness was not considered, as all samples were mirror polished. As far as the washing solutions were concerned, 0.5 ml of the solution was added to 0.5 ml reactive mixture. The reaction was stopped by adding 0.5 ml NaOH after 2 min and then measurements were carried out in the same way as for the solid samples. Enzymatic activity of ALP solutions at defined concentrations from 0.01 to 5.00 mg·ml⁻¹ was evaluated in order to produce a standard reference curve for ALP activity. Tests were carried out using multi-well plates. In order to obtain a reference, for each test plate three measurements on wells containing only reactive mixture and NaOH were carried out. Reference values were subtracted from the sample absorbance values in order to obtain standard and comparable results.

A.2.2.6 Analysis of surface morphology and chemistry during the functionalization procedure

In order to understand surface modifications during the functionalization process, samples at different steps of the treatment (hydroxylation, silanization and enzyme grafting) were investigated by means of scanning electron microscopy and energy-dispersive spectroscopy (EDS) analysis (SEM-FEI, Quanta Inspect 200, EDS-EDAX PV 9900).

A.2.2.7 In vitro bioactivity tests

Samples of both glasses at different stages of the functionalization process (hydroxylation, silanization or enzyme grafting) were soaked in simulated body fluid (SBF) in order to evaluate whether biological modification affects inorganic bioactivity. SBF was prepared as described by Kokubo and Takadama.²⁷ For this test ALP grafting was performed at 4 °C. Samples of the most reactive glass (CEL2) were maintained in SBF for up to 1 week, because at this time the material was able to trigger and exhibit its bioactive behaviour.²¹ As far as SCNA was concerned, 2 weeks dipping was considered as the shortest time because the kinetics are slower.¹⁹ Solution refreshment was performed every 2 days in order to mimic natural turnover of physiological fluids. At each refreshment point the solution pH was registered. At the end of the soaking period samples were washed, without stirring or shaking, in double distilled water and observed by means of scanning electron microscopy (SEM-FEI, Quanta Inspect 200, EDS-EDAX PV 9900). Before scanning electron microscopic (SEM) observation all samples were sputter coated with a thin metal layer in order to make them conductive. Silver was employed for CEL2 samples, while chromium was used for SCNA samples. As far as the most reactive glass (CEL2) was concerned, enzymatic activity tests were carried out before and after SBF soaking, in order to determine whether ALP had been released or still remained on the glass surface in the active state. SBF solution was also analysed at different experimental times in order to individuate ALP presence.

A.2.2.8 Statistical analysis

All tests were performed in triplicate. Data were analysed by means of one-way ANOVA, with a significance level of $P < 0.05$. Data are represented as means \pm standard deviation.

A.2.3 Results

A.2.3.1 Hydroxyl exposure

After acetone and water washing a significant reduction in water contact angle could be observed (Fig. 1). The difference between the contact angle before and after the washing procedure was statistically significant ($P < 0.05$) for all tested materials. This result indicates the high wettability induced by hydroxyl exposure and proves the efficacy of the first step of the functionalization process.

A.2.3.2 Silanization

This step was first investigated by means of contact angle measurements, since a silane layer on the material surface would change its wettability and, in particular, would make the surface hydrophobic. Contact angle measurements after silanization are described in Fig. 1.

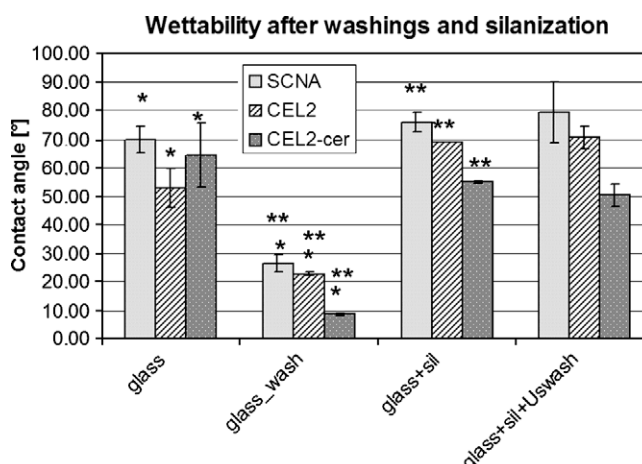


Fig. 1. Contact angles before and after washing and silanization. *,** Statistically significant difference between values marked with the respective symbols ($P < 0.05$).

Table 3: N/Si and C/Si ratios for SCNA, CEL2 and CEL2-cer at different steps in the functionalization process.

	SCNA		CEL2		CEL2-cer	
	N/Si	C/Si	N/Si	C/Si	N/Si	C/Si
Glass-wash	0	4.86	0.11	1.92	0.12	1.95
Glass + ALP	na	na	5.75	35.81	0.70	4.82
Glass + sil	0.21	1.67	0.54	14.56	0.27	3.58
Glass + sil + ALP	na	na	3.60	87.30	1.01	6.20

na, the ratio could not be calculated because silicon was not detectable on the surface.

There was an evident increase in contact angle for all tested materials, due to the anchoring of a hydrophobic molecule on the glass surface, and the difference

between angles was statistically significant in all cases ($P < 0.05$). This means that silanization is effective on all the investigated bioactive materials, despite their intrinsic reactivity. These data are in agreement with previous studies.¹² The resulting silane–surface bonds were stable, as there was no significant decrease ($P > 0.05$) in contact angles values after ultrasonic Tris washing of the silanized samples (last series in Fig. 1). XPS analysis showed an enrichment in nitrogen (characteristic of silane amino groups) after silanization for all materials tested (Table 3, row 3).

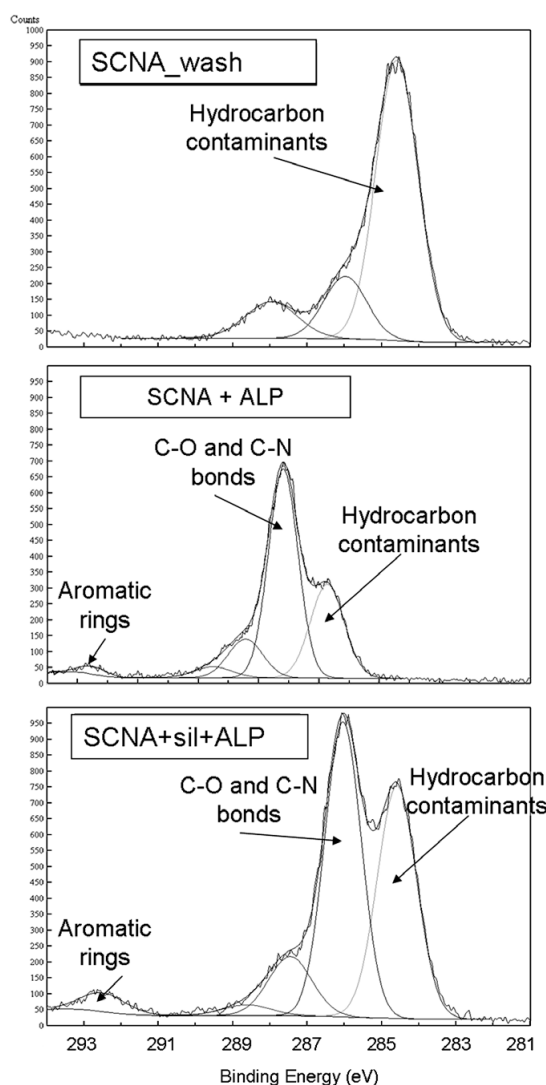


Fig. 2. Carbon region XPS spectra for: (a) washed SCNA; (b) SCNA directly grafted with ALP without silanization; and (c) SCNA silanized and grafted with ALP.

A.2.3.3 Alkaline phosphatase grafting

XPS analysis of functionalized samples showed an enrichment in carbon and nitrogen after grafting and also a decrease in substrate constituents for all the samples (Table 3, rows 2 and 4). XPS spectra (carbon region details) of SCNA samples after the washing procedure (for control purposes) and after functionalization (direct ALP grafting and silanization and ALP grafting) are reported, as examples, in Fig. 2. A detailed analysis of the carbon region showed a peak characteristic of hydrocarbon contaminants (284.6 eV), which is always present, but on ALP grafted samples two other peaks appeared: peak B (286 eV), typical of C–O and C–N bonds present in the enzyme, and peak E (292–293 eV), due to aromatic rings flattened on the surface.

A.2.3.4 Enzymatic activity

Fig. 3 is a graph of the specific enzymatic activity for the tested materials after grafting at 4 °C, showing that ALP has been successfully grafted onto all the substrates considered.

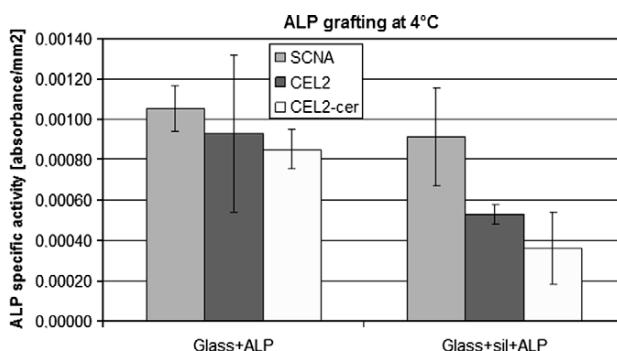


Fig. 3. Enzyme specific activity. Comparison between direct anchoring and silanization for the different materials after grafting at 4 °C.

It should be noted that the amount of ALP is lower on CEL2 glass and CEL2-cer than on SCNA, nevertheless, it is important to note that a significant amount of ALP could be grafted in an active state onto very bioactive materials such as CEL2 and CEL2-cer. In order to evaluate the bonding stability between ALP and the material surfaces, functionalized samples were ultrasonically washed for 2 min in Tris solution. Fig. 4 shows a comparison between enzymatic activity before and after washing of SCNA and CEL2 functionalized at different temperatures with and without silanization. Table 4 reports the percentage decrease in specific enzymatic activity after washing. It can be observed that silanization does not increase the amount of ALP grafted onto both glasses (SCNA and CEL2) at 4 and 37 °C. The difference between the enzymatic activities of Glass + ALP and Glass + sil + ALP was not statistically significant ($P > 0.05$). On the other hand, the amount of ALP

that remained on material surfaces after washing was higher for silanized samples for both glasses if anchoring was performed at 4 rather than 37 °C (Figs. 3 and 4, Table 3).

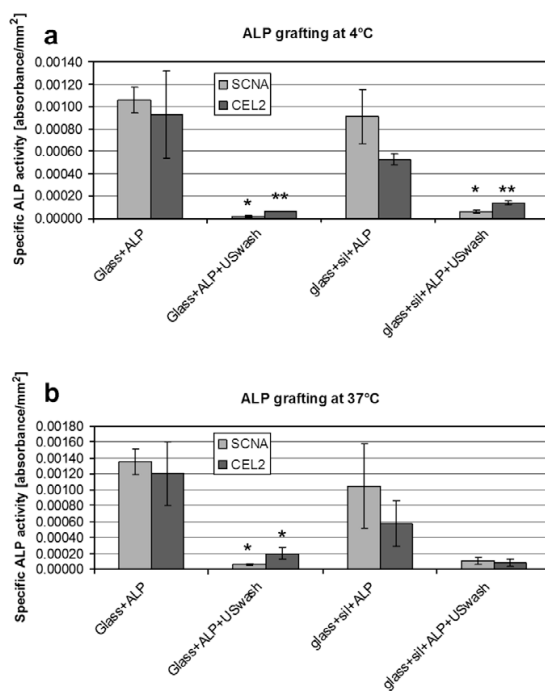


Fig. 4. Enzyme activity. Comparison between direct anchoring and silanization before and after washing. Grafting at: (a) 4 °C; (b) 37 °C. *,** Statistically significant difference between values marked with the respective symbols ($P < 0.05$).

Table 4: Decrease in ALP specific activity after washing (%).

	4 °C anchoring		37 °C anchoring	
	ALP	Sil + ALP	ALP	Sil + ALP
SCNA	98.3	93.5	95.8	90.0
CEL2	93.0	73.7	83.6	86.2

The situation was similar for CEL2-cer: it seems that direct anchoring could be slightly more effective than silanization in grafting ALP at 4 °C.

Considering the grafting temperature, it should be noted that there is no significant difference in the amount of ALP grafted to both glasses (SCNA and CEL2) at 4 or 37 °C, except in the case of direct anchored samples after washing. In this case the amount of ALP maintained on the glass surfaces was higher if grafting was performed at 37 °C. It was verified that an ALP solution maintains its activity after storage at all tested temperatures. The mean values for enzymatic activity of standard solutions after 20 h storage at 4, 25 and 37 °C were 1.4, 1.9 and 2.0, respectively. It seems that low temperature storage could reduce ALP activity.

As far as the type of glass is concerned, it could be observed that the amount of ALP grafted onto the most reactive glass (CEL2) was slightly lower than that grafted onto the more stable one (SCNA) at both 4 and 37 °C, with or without silanization. Differences were not statistically significant and so we can state that ALP could be successfully grafted onto bioactive glasses despite their reactivity. On the other hand, the obtained data underline that after washing CEL2 samples were able to maintain a higher amount of ALP on their surface (both silanized and not at 4 °C but only not silanized at 37 °C).

Considering the washing solutions (Fig. 5), it could be observed that a significant amount of ALP had been washed off the samples and it was present in the solution in an active state. Data for the ALP activity of the samples are related to surface area (specific activity), while data for solutions were measured on the whole solution volume, so they could not be quantitatively compared. After washing there was no significant difference ($P > 0.05$) between the amount of ALP found in solution for directly grafted and silanized samples for every material and anchoring temperature.

A.2.3.5 Analysis of surface morphology and chemistry during the functionalization procedure

Figs. 6–8 show SEM images and EDS spectra for SCNA, CEL2 and CEL2-cer at different steps of the functionalization process. In the EDS analysis the presence of Ag is due to the metallization process and the presence of Cl is due to the use of Tris–HCl. It can be seen that for the most reactive glass (CEL2) the bioactivity reaction (hydroxyl condensation to form silica gel) begins in the functionalization medium (see Fig. 6c and d). In fact, in this case a silica rich gel-like layer is observed in the SEM micrograph and its presence can be confirmed through EDS analysis showing a high Si peak. This behaviour is not shown by CEL2-cer (Fig. 7) and SCNA (Fig. 8).

A.2.3.6 In vitro bioactivity of functionalized samples

Fig. 9 shows SEM micrographs of CEL2 samples (at different steps of the functionalization process) after 1 week in SBF. It can be observed that an evident silica gel layer is present in all samples. EDS analysis underlined an enrichment in calcium and phosphorous for this gel. Looking at ALP grafted samples (Fig. 9c and d, ALP grafted directly to hydroxyls groups; Fig. 9e and f, ALP grafted to a silanized surface), it is clear that a significant number of particles, with the typical morphology of hydroxyapatite, started to precipitate all over the gel. EDS spectra confirmed that they were constituted mainly of Ca and P. Fig. 10 shows SEM micrographs of SCNA (at different stages of the functionalization process) after 2

weeks in SBF. As far as the washed and silanized samples are concerned, no silica gel was present (Fig. 10a and b) and only a few small hydroxyapatite particles could be detected, and their dimensions were $<3\text{ }\mu\text{m}$. Looking at the ALP grafted samples (Fig. 10c, ALP grafted directly to hydroxyls groups; Fig. 10e, ALP grafted to a silanized surface), a significant number of particles with dimensions between 5 and $20\text{ }\mu\text{m}$ could be detected. EDS (Fig. 10d, ALP grafted directly to hydroxyls groups; Fig. 10f, ALP grafted to a silanized surface) analysis confirmed that they were constituted mainly of Ca and P. The pH of the SBF solution showed small variations (pH 7.4–7.6) in the dipping period for both glasses.

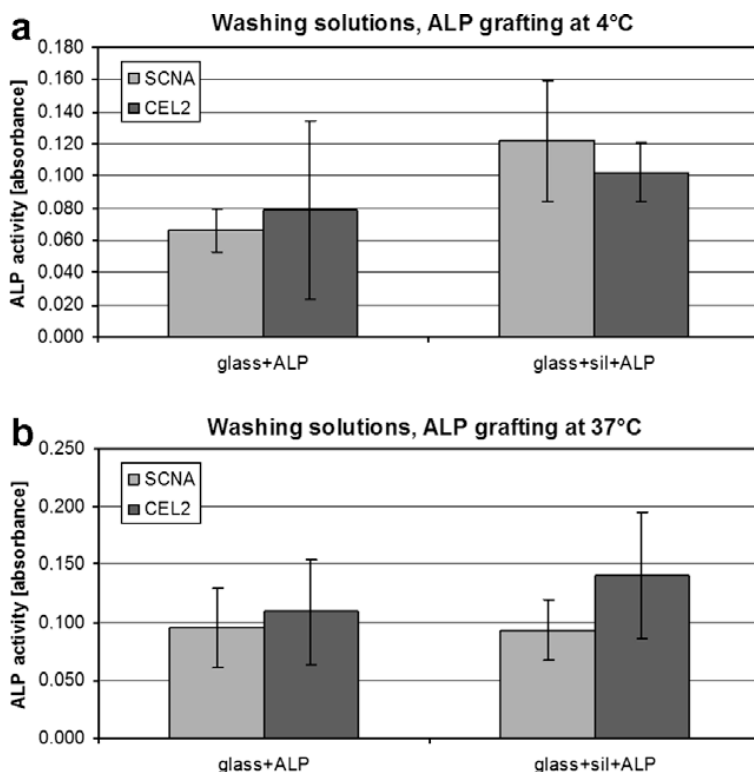


Fig. 5. Enzyme activity in washing solutions. Grafting at: (a) 4 °C; and (b) 37 °C.

A.2.3.7 Enzymatic activity tests after SBF soaking

Fig. 11a shows enzymatic activity measured on functionalized samples, functionalized and ultrasonically washed samples and functionalized samples after 1 week in SBF. It should be noted that SBF soaking significantly reduced the ALP activity of the samples, but less so than ultrasonic washing. Fig. 11b underlines that ALP, gradually released in SBF, maintained its activity, both on the material surface and in solution, for at least 1 week. Since tests were carried out with solution refreshment, it can be observed that enzyme release continued throughout the entire dipping period, even if it was higher in the first days.

A.2.4 Discussion

Surface cleaning, hydroxyl exposure and silanization were successfully carried out by applying a procedure optimized in a previous work.¹² In this research the enzyme ALP was grafted onto two bioactive glasses and a glass ceramic with different degrees of bioactivity, both via silanization and also through direct anchoring to hydroxylated surfaces. In all cases a significant increase in carbon and nitrogen was detected by XPS analysis. At the same time a decrease in those elements characteristic of the glass substrate was observed. These observations suggest the presence of an organic layer on the surface. Enzyme grafting was confirmed by detailed analysis of the carbon region, and specific signals for C–O and C–N bonds (286 eV) and for aromatic rings flattened onto the surface (292–293 eV) were detected. The first is related to typical bonds in proteins, while the second could be attributed to phenylalanine, an amino acid present in ALP.²⁸

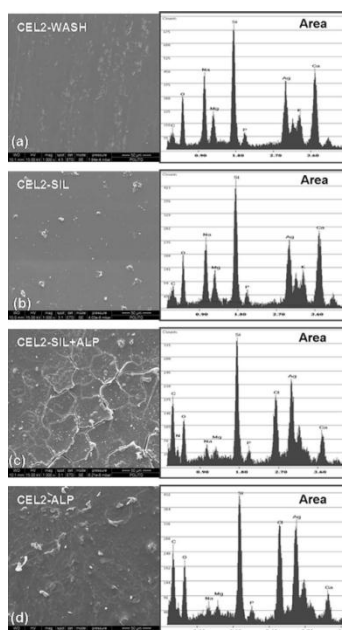


Fig. 6. SEM micrographs of CEL2 at different steps in the functionalization process.

It is recognized that a grafted enzyme should be in an active conformation in order to fulfill its tasks and so, in order to verify ALP activity after anchoring, the reaction between ALP grafted samples and p-nitrophenylphosphate was monitored. From enzymatic activity studies it could be determined that the amount of grafted ALP was lower on CEL2 glass and CEL2-cer than on SCNA, which is probably due to their reactivity in PBS (that has a pH similar to physiological fluids, 7.00), which could interfere with bonding reactions reducing the total amount of enzyme finally attached. Hydroxyl condensation could interfere with bonding reactions, as

described in Fig. 12, in which the presence of well-exposed or condensed hydroxyl groups is shown.

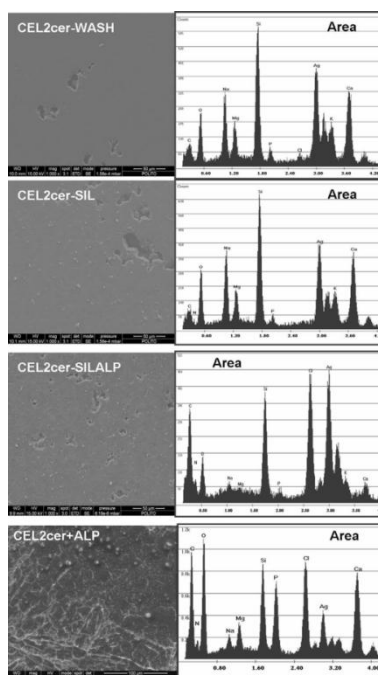


Fig. 7. SEM micrographs of CEL2-cer at different steps in the functionalization process.

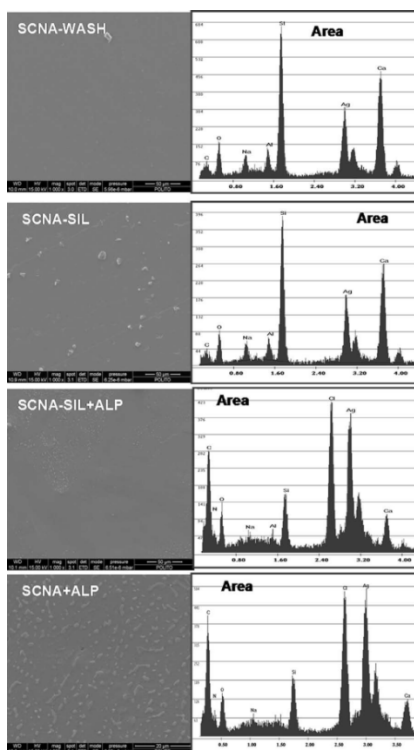


Fig. 8. SEM micrographs of SCNA at different steps in the functionalization process.

In fact, after the washing treatment hydroxyl groups are well exposed and prone to silanization or biomolecule anchoring on the less reactive glass (SCNA), while on the most reactive surface (CEL2) the hydroxyl groups partially condense to form hydrated Si–O–Si species (silica gel). The situation is more complex for CEL2-cer, which is a glass ceramic: in this case only the amorphous phase showed exposed hydroxyl groups whereas, as far as the exposure of –OH groups is concerned, the crystalline phases were inert. In the case of CEL2-cer also, the residual amorphous phase was reactive and the exposed –OH could partially condense, as for amorphous CEL2, leading to a lower surface reactivity towards both silanes and ALP.

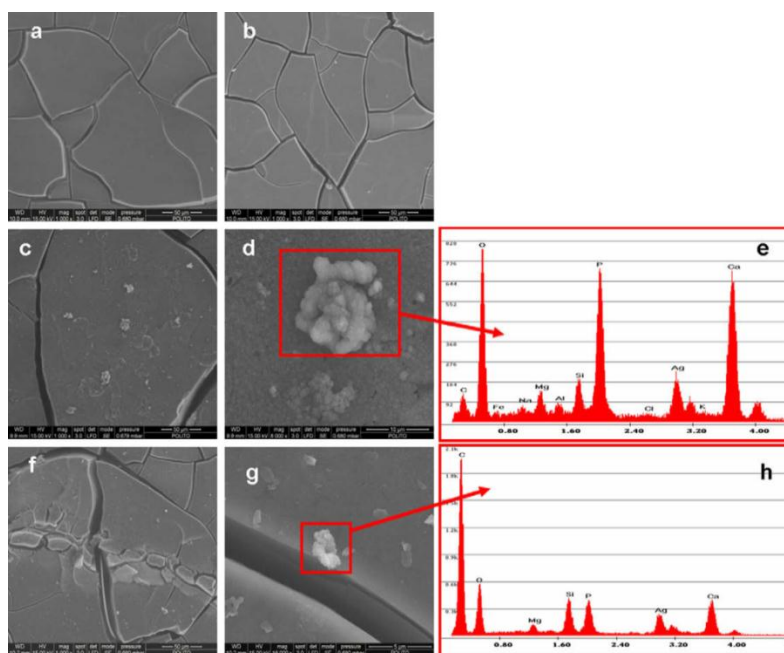


Fig. 9. SEM micrograph of CEL2 samples after 1 week in SBF. (a) Washed sample; (b) silanized sample; (c) ALP directly grafted sample; (d) ALP directly grafted sample at higher magnification; (e) EDS of the particle in (d); (f) silanized and ALP grafted sample; (g) silanized and ALP grafted sample at higher magnification; and (h) EDS of the particle in (g).

This hypothesis was confirmed by SEM observation of functionalized samples, with CEL2 samples showing an evident reaction layer for ALP grafting after 1 day incubation in PBS, while this phenomena did not appear for SCNA samples under the same conditions (Figs. 6 and 8). Surface reactivity (silica gel formation) could also explain the ability of CEL2 to retain a higher amount of ALP after washing, as the silica gel is porous and could adsorb and retain ALP.

Looking at the washing solutions (Fig. 5) it could be observed that the released ALP maintained its activity. This is a very positive feature, as it would induce osteoblast differentiation and bone mineralization, combining this effect with that due to the grafted ALP retained on the material surface after washing. Bioactive glasses are able to induce hydroxyapatite precipitation in SBF solutions via a mechanism, described by Cao and Hench,¹³ that could include, during the early stages of immersion in SBF, silica gel layer formation. As described in a previous work,¹⁹ SCNA showed slower kinetics of bioactive behaviour. This glass contains 3% Al₂O₃ that, as reported in the literature,¹³ inhibits bioactivity. When compared with CEL2 it is clear that the surface reactivity is lower, even after 2 weeks dipping. In vitro bioactivity tests on modified samples underlined that biological functionalization, even if it includes the deposition of a double organic layer, does not inhibit the reactivity of bioactive glasses (Figs. 9 and 10).

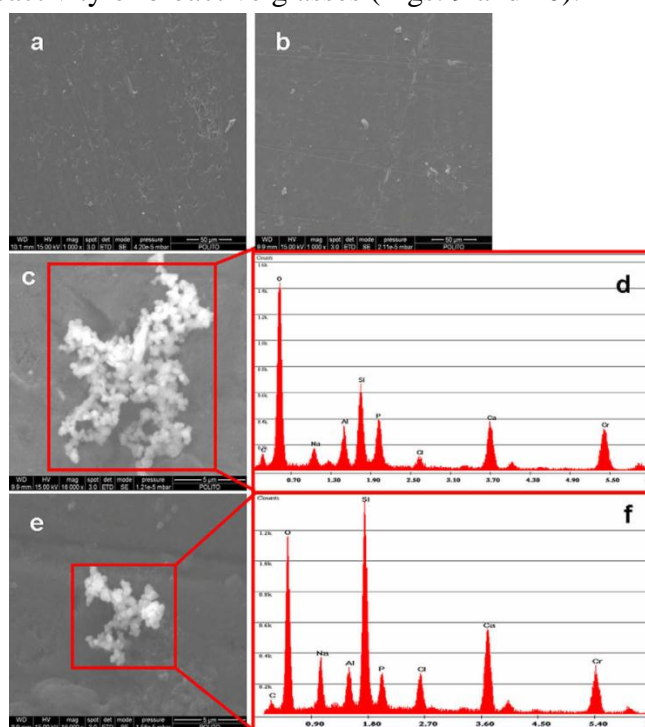


Fig. 10. SEM micrograph of SCNA samples after 2 weeks in SBF. (a) Washed sample; (b) silanized sample; (c) ALP directly grafted sample; (d) EDS of the particle in (c); (e) silanized and ALP grafted sample; and (f) EDS of the particle in (e).

In fact, for the most reactive glass silica gel formation occurred on both the silanized only and silanized and grafted with ALP samples. The presence of the enzyme ALP quickened the reaction kinetics for both the most reactive glass and also for the most stable one. In fact, hydroxyapatite particles precipitated onto both functionalized surfaces in greater numbers and with larger dimensions than onto

non-functionalized samples. Finally, it should be noted that direct anchoring of ALP (without silanization) seemed to be more effective in inorganic bioactivity enhancement, with greater numbers of Ca- and P-rich particles of bigger dimensions (Figs. 9d and 10c) being observed on these samples. ALP is a homodimeric metalloenzyme which catalyzes the hydrolysis of almost any phosphomonoester with the release of phosphate and alcohol. Its properties have been associated with the mineralization process and phosphate homeostasis in bone tissue.²⁹

ALP acts as a nucleation center for hydroxyapatite as it is able to release phosphate and captures calcium ions. In this way, the presence of ALP and its substrate (β-glycerophosphate) or simply of a solution rich in calcium ions induces the deposition of hydroxyapatite crystals and amorphous calcium phosphate. This property has been applied in realizing hydroxyapatite layers on organic substrates.^{16,30} ALP binds the phosphate group of the phosphate ester to form a transient phosphoenzyme, which is subsequently hydrolyzed.³¹ The active site of ALP is characterized by two zinc ions and is a high affinity phosphate-binding site. It has been observed that it is also able to bind phosphates at neutral pH.^{32,33} We suggest that the enzyme, present on a glass surface soaked in SBF, could attract phosphate from the solution to the material surface and, subsequently, calcium ions, thus favouring hydroxyapatite precipitation. It has also been observed that ALP concentration and activity are particularly high in cellular mineralized tissues, such as cellular cementum in the rat molar periodontium.¹⁴ Finally, in vivo experiments in rats¹⁵ have demonstrated that ALP adsorption onto plasma sprayed titanium implants increases bone production around the implant.

Comparing these literature observations with our experimental results, it should be noted that ALP grafting onto the surface of bioactive glasses does not reduce surface reactivity but enhances the ability to induce hydroxyapatite precipitation. So the bioactive behaviour of a biocompatible and slightly reactive glass, such as SCNA, could be improved by biological functionalization. Moreover, presence of the enzyme could also promote new bone formation by stimulating osteoblasts. This last hypothesis will be investigated in a future work with specific cellular tests on functionalized materials. Further investigations should also be planned to assess the role of the silane layer on the early stages of bioactivity, but this is not the primary aim of the present work.

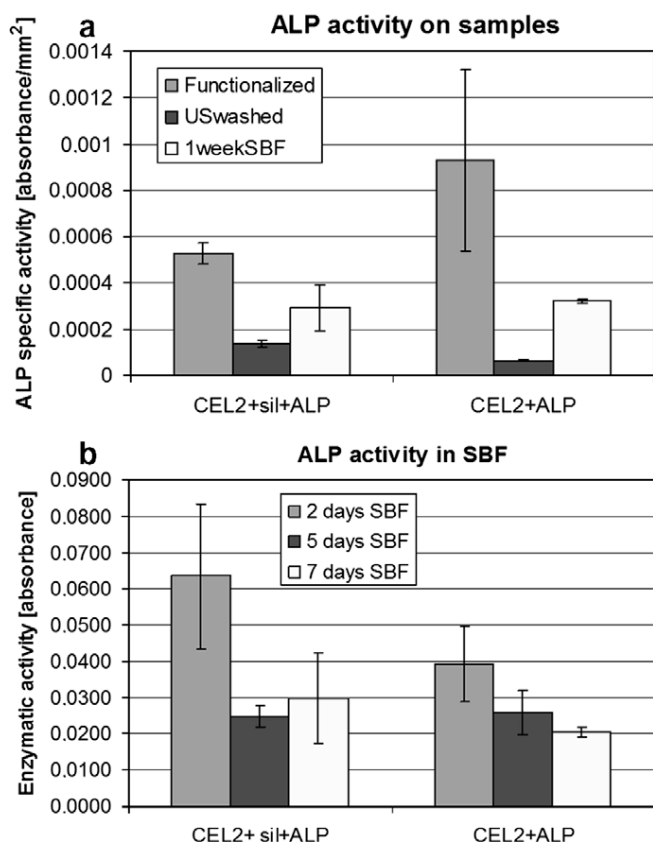


Fig. 11. Enzyme activity on CEL2 samples after functionalization, functionalization and ultrasonic washing, functionalization and SBF soaking (a) and in SBF after sample soaking (b). ALP grafting was performed at 4°C.

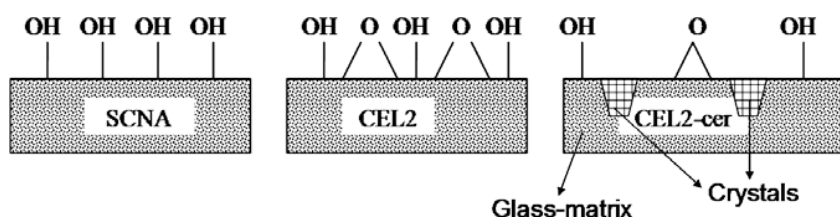


Fig. 12. Hydroxyl exposure on biomaterials with different reactivity.

A.2.5 Conclusions

ALP has been successfully attached to bioactive glasses and glass ceramics with different degrees of bioactivity. Modification was carried out with good results, despite the differences in surface reactivity. ALP maintained its activity after grafting on all the surfaces investigated.

Enzyme anchoring was performed effectively both on silanized surfaces and also by direct anchoring to exposed hydroxyl groups. A fraction of the grafted biomolecules was strongly bonded and remained attached to the surface also after

severe (ultrasonic) washing. ALP released into solution maintained its activity. This is an interesting result as *in vivo* the functionalized materials would be in contact with physiological fluids and it is expected that a certain amount of ALP would be released while the remaining would remain strongly bonded to the surface. Both fractions of ALP would be in their active state, so they could stimulate bone tissue regeneration and implant integration. The amount of ALP released *in vivo* is related to the aggressiveness of the fluid, but should be less than that due to ultrasonic treatment. Finally, it has been observed that ALP is able to enhance and accelerate the kinetics of bioactivity in SBF, so it would seem that biological functionalization has a positive synergic interaction with inorganic bioactivity. Cellular tests are in progress to evaluate how the conjunction between inorganic and biological activity is able to stimulate cell behaviour.

A.2.6 References

- [1] Setti S, Rengachery MD. Bone morphogenetic proteins: basic concepts. *Neurosurg Focus* 2002;13:1–6.
- [2] Kirker-Head CA. Potential applications and delivery strategies for bone morphogenetic proteins. *Adv Drug Deliv Rev* 2000;43:65–92.
- [3] Luginbuehl V, Meinel L, Merkle HP, Gander B. Localized delivery of growth factors for bone repair. *Eur J Pharm Biopharm* 2004;58:197–208.
- [4] Lee S-H, Shin H. Matrices and scaffold for delivery of bioactive molecules in bone and cartilage tissue engineering. *Adv Drug Deliv Rev* 2007;59:339–59.
- [5] Hildebrand HF, Blanchemain N, Mayer G, Chai F, Lefebvre M, Boschini F. Surface coatings for biological activation and functionalization of medical devices. *Surf Coat Technol* 2006;200:6318–24.
- [6] Puleo DA, Nanci A. Understanding and controlling the bone–implant interface. *Biomaterials* 1999;20:2311–21.
- [7] Hayakawa T, Yoshinari M, Nemoto K. Direct attachment of fibronectin to tetracycline-activated titanium. *J Biomed Mater Res* 2003;67A:684–8.
- [8] Bagno A, Piovan A, Dettin M, Chiarion A, Brun P, Gambaretto R, et al. Human osteoblast-like cell adhesion on titanium substrates covalently functionalized with synthetic peptides. *Bone* 2006;40:693–9.
- [9] Bautista FM, Bravo MC, Campelo JM, Garcia A, Luna D, Marinas JM, et al. Covalent immobilization of acid phosphatase on amorphous AlPO₄ support. *J Mol Catal B* 1999;6:473–81.

- [10] Taylor RH, Fournier SM, Simons BL, Kaplan H, Hefford MA. Covalent protein immobilization on glass surface. Application to alkaline phosphatase. *J Biotechnol* 2005;118:265–9.
- [11] Puleo DA, Kissling RA, Sheu MS. A technique to immobilize bioactive proteins, including bone morphogenetic protein-4 (BMP-4), on titanium alloy. *Biomaterials* 2002;23:2079–87.
- [12] Vernè E, Vitale-Brovarone C, Bui E, Bianchi CL, Boccaccini AR. Surface functionalization of bioactive glasses. *J Biomed Mater Res*. doi: 10.1002/jbm.a.32153.
- [13] Cao W, Hench LL. Bioactive materials. *Ceram Int* 1996;22:493–507.
- [14] Groeneveld MC, Everts V, Beertsen W. Alkaline phosphatase activity in the periodontal ligament and gingiva of the rat molar: its relation to cementum formation. *J Dent Res* 1995;74:1374–81.
- [15] Piattelli A, Scarano A, Corigliano M, Piattelli M. Effects of alkaline phosphatase on bone healing around plasma sprayed titanium implants: a pilot study in rabbits. *Biomaterials* 1996;17:1443–9.
- [16] Berendsen AD, Smit TH, Hoebe KA, Walboomers XF, Bronckers ALJJ, Everts V. Alkaline phosphatase-induced mineral deposition to anchor collagen fibrils to a solid surface. *Biomaterials* 2007;28:3530–6.
- [17] Golub EE, Boesze-Battaglia K. The role of alkaline phosphatase in mineralization. *Curr Opin Orthop* 2007;18:444–8.
- [18] De Jonge LT, Leuwemburg SCG, van den Beucken JJJP, Wolke JGC, Jansen A. Electrosprayed enzyme coatings as bioinspired alternative to bioceramic coatings for orthopedic and oral implants. *Adv Funct Mater* 2009;19:1–8.
- [19] Vernè E, Miola M, Vitale Brovarone C, Cannas M, Gatti S, Fucale G, et al. Surface silver-doping of biocompatible glass to induce antibacterial properties. Part I: Massive glass. *J Mater Sci Mater Med* 2009;20(3):733–40.
- [20] Miola M, Ferraris S, Di Nunzio S, Robotti PF, Bianchi G, Fucale G, et al. Surface silver-doping of biocompatible glass to induce antibacterial properties. Part II: Plasma sprayed glass-coatings. *J Mater Sci Mater Med* 2009;20(3):741–9.
- [21] Vitale Brovarone C, Vernè E, Robiglio L, Martinasso G, Canuto RA, Muzio G. Biocompatible glass-ceramic materials for bone substitution. *J Mater Sci Mater Med* 2008;19:471–8.
- [22] Vitale-Brovarone C, Vernè E, Robiglio L, Appendino P, Bassi F, Martinasso G, et al. Development of glass-ceramic scaffolds for bone tissue engineering: characterisation, proliferation of human osteoblasts and nodule formation. *Acta Biomater* 2007;3:199–208.

- [23] Ma M, Zang Y, Yu W, Shen H, Zhang H, Ning N. Preparation and characterization of magnetite nanoparticles coated by amino silane. *Colloid Surf A Physiochem Eng Aspects* 2003;212:219–26.
- [24] Puleo DA. Biochemical surface modification of Co–Cr–Mo. *Biomaterials* 1997;17:217–22.
- [25] De La Fournière L, Nosjean O, Buchet R, Roux B. Thermal and pH stabilities of alkaline phosphatase from bovine intestinal mucosa: a FTIR study. *Biochim Biophys Acta* 1995;1248:186–92.
- [26] Bortolato M, Besson F, Roux B. An infrared study of the thermal and pH stabilities of the GPI-alkaline phosphatase from bovine intestine. *Biochem Biophys Res Commun* 2002;292:874–9.
- [27] Kokubo T, Takadama H. How useful is SBF in predicting in vivo bone bioactivity. *Biomaterials* 2006;27:2907–15.
- [28] Nilsen IW, Øverbø K, Olsen RL. Thermolabile alkaline phosphatase from northern shrimp (*Pandalus borealis*): protein cDNA sequence analyses. *Comp Biochem Phys* 2001;129B:853–61.
- [29] Balcerzak M, Hamade E, Zhang L, Pikula S, Azzar G, Radisson J, et al. The roles of annexins and alkaline phosphatase in mineralization process. *Acta Biochim Polon* 2003;50(4):1019–38.
- [30] Yamauchi K, Goda T, Takeuchi N, Einaga H, Tanabe T. Preparation of collagen/calcium phosphate multilayer sheet using enzymatic mineralization. *Biomaterials* 2004;25:5481–9.
- [31] Zhang L, Buchet R, Azzar G. Phosphate binding in the active site of alkaline phosphatase and the interactions of 2-nitrosoacetophenone with alkaline phosphatase-induced small structural changes. *Biophys J* 2004;86:3873–81.
- [32] Applebury ML, Johnson BP, Coleman JE. Phosphate binding to alkaline phosphatase. *J Biol Chem* 1970;245:4968–76.
- [33] Holtz KM, Stec B, Kantrowitz ER. A model of the transition state in the alkaline phosphatase reaction. *J Biol Chem* 1999;274:8351–4.

APPENDIX A3: Surface Activation of a Ferrimagnetic Glass–Ceramic for Antineoplastic Drugs Grafting

E. Vernè, M. Miola, S. Ferraris, C. L. Bianchi, A. Naldoni, G. Maina, O. Bretcanu, *Advanced Engineering Materials* **2010**, 12, B309-B319.

A.3.1 Introduction

The malignant tumors development and their care is one of the most critical problems of this century, connected to modern medicine. Up today, the main techniques used to treat tumors are radiotherapy and chemotherapy, which, respectively, overwork the ionizing radiation and the systemic administration of anticancer drugs, in addition to the surgical treatment. Hyperthermia is another technique recently used to treat solid tumors, which involves the exposition of body's tissue to a controlled heat, normally included between 41 and 46 °C. In fact, tumoral cells are genetically more sensitive to heat; the cancer neovascularization is sluggish and abnormal, and is characterized by a poor blood flow, unable to disperse heat.¹⁻³

Hyperthermia can be associated to classical chemotherapy, limiting in this way the collateral effects such as gastrointestinal absorption and toxicity induced by a chemotherapeutic administration, by a faster drug action and a better distribution of the drug inside the tumor site.⁴ Heat administration increases the sensitivity of malignant cells toward different drugs or radiotherapy, inducing a decrease in drugs dosage and as a consequence, reducing their side effects on human body. Hyperthermia can be induced by several magnetic implants, such as metallic alloy particles, magnetic fluids, ferromagnetic bone cements, and ferrimagnetic glass–ceramics, which have been deeply studied in the literature.⁵⁻¹⁰ In particular, ferrimagnetic biocompatible/bioactive glass–ceramic materials have been investigated as candidates for bone cancer treatment, since they combine the possibility to be used as bone filler (and thus their ability to osteointegrate and form a chemical bond with bone tissue), with their quality to act as local hyperthermic implant, due to their specific ferrimagnetic properties.¹¹⁻¹⁷ In previous research works, structural, thermal, and magnetic properties, together with the in vitro reactivity of ferrimagnetic glass–ceramics belonging to the system $\text{SiO}_2\text{--Na}_2\text{O--CaO--P}_2\text{O}_5\text{--FeO--Fe}_2\text{O}_3$ were investigated.¹⁸⁻²⁰ As other silica-based bioactive glass–ceramics, these materials could be surface activated in order to expose active sites, prone to the bonding to several kinds of molecules, including antineoplastic agents. There are several works in literature where surface functionalization of silica-based glasses (both inert and bioactive) are described.²¹⁻

²⁵ Bioactive glasses and glass–ceramics are well known for their peculiar surface reactivity when they are in contact with water or aqueous solutions, as simulated body fluid, TRIS buffer, physiological media, etc.²⁶⁻³¹ The aim of this work is to study the surface modifications which occur by soaking a $\text{SiO}_2\text{--Na}_2\text{O--CaO--P}_2\text{O}_5\text{--FeO--Fe}_2\text{O}_3$ glass–ceramic in different washing solution, in order to activate its surface to the exposition of functional groups able to bond with therapeutic agents. After the surface activation, the grafting of two different antineoplastic agents onto the functionalized ferrimagnetic glass–ceramic was investigated, and a preliminary release study was done. The final idea is to combine hyperthermia with chemotherapy, exploiting the therapeutic effect of an antitumoral drug bound to the magnetic glass–ceramic surface. Therefore, the drug could be released directly on the desired tumor site using the ferrimagnetic glass–ceramic microparticles as drug carrier. The selected antineoplastic agents, doxorubicin and cisplatin, belong to two different drug classes and a different bonding mechanism can be hypothesized. They were selected due to their molecular structure, which allows them to bond with the chemical species present on the functionalized glass–ceramic surface. Cisplatin, a water soluble drug, is a planar complex of platinum, which reacts with cell's DNA, altering its structure and inhibiting the repair system of the organism. Such as all platinum derivatives, it has mutagenic properties and produces the total or partial regression of different cancers such as lung, stomach, testicle, ovary, uterus, cervix, or acts on epidermis carcinoma and melanoma. It can be used in combination with other oncostatic chemotherapeutics, depending on the cancer typology.^{32,33} Doxorubicin belongs to anthracycline family and it is characterized by a planar tetra-cyclic part, on which two active sites from a therapeutic point of view (daunosamine and adriamycinone) are linked; it is known to interact with DNA by intercalation and inhibition of macromolecular biosynthesis. This inhibits the progression of the enzyme topoisomerase II, which unwinds DNA for transcription. Doxorubicin stabilizes the topoisomerase II complex after it broke the DNA chain for replication, preventing the DNA double helix from being resealed and thereby stopping the process of replication.³⁴

This paper is focused on the surface treatments on the ferrimagnetic bioactive glass–ceramic to make it prone to functionalization, in order to bind doxorubicin and cisplatin. The uptake and release of these drugs have been preliminarily investigated in aqueous solutions at 37 °C. The paper presents the results concerning functionalization of these glass–ceramics, aiming to explore their potentiality as magnetic drug carrier.

A.3.2 *Materials and Methods*

A glass–ceramic material, named SC45, with the composition 24.7 SiO₂, 13.5 Na₂O, 13.5 CaO, 3.3 P₂O₅, 14 FeO, and 31 Fe₂O₃ (wt%), was prepared by traditional melting and quenching of commercial reagents, at 1550 °C for 30min in air, as described in previous works.^{18,19} A part of the melt was cast in a brass mold to obtain bars and another part was milled and sieved to powders, with the grain size below 20 µm. The obtained bars were annealed at 600 °C for 12h and then were cut in slices of 10×10×1.5 mm³. Each slice was polished with SiC abrasive papers, up to 1200 grit and then with 6 mm diamond paste. SC45 samples were analyzed by scanning electron microscopy (SEM—FEI, QUANTA INSPECT 200), energy dispersion spectrometry (EDS—EDAX PV 9900), and X-ray diffraction (XRD—X’Pert Philips diffractometer), to confirm the presence of the crystalline phase, magnetite (which was identified in a previous research¹⁸), and to observe its morphology.

A.3.2.1 *In Vitro Bioactivity Test*

To evaluate the material reactivity, SC45 slices were dipped in a simulated body fluid (SBF-Kokubo³⁵) up to one month. Samples were removed from SBF at specific time points (1, 3, 7, 14, and 28 days) and their surface was observed by SEM and EDS. The SBF solution was changed every 3 days, to simulate the natural replacement of fluids in the human body. The pH was measured before and after SBF refresh, during all the soaking period. Slices have been chosen as testing samples, and SBF as soaking solution, in order to collect both structural and morphological data about the surface reactivity of this glass–ceramic with an easy and very common approach. The step concerning the optimization of the surface treatment in order to induce only the first reactions of the bioactivity mechanism and lead to free –OH group on top of the glass–ceramic was subsequently optimized, by investigating the different pre-treatments reported below, where dipping time and washing solutions have been selected taking into account the bioactivity kinetics already assessed by the bioactivity test.

A.3.2.2 *Samples Pre-Treatment*

In order to bond with the drugs, the glass–ceramic surface should be firstly activated. The surface of a silica-based glass–ceramic can be functionalized by activating the –OH groups after the contact with an aqueous medium.^{24,25} On the basis of literature and taking into account the bioactivity of this glass–ceramic, investigated in this work, three different pre-treatments were set out in order to expose the –OH functional groups to the glass–ceramic surface: (i) ultrasonic

washing of the samples, (ii) soaking the samples in distilled water, and (iii) soaking the samples in SBF solution.

The first pre-treatment consists in washing the slice samples firstly in acetone (95 vol% pure) for 5min (to degrease the samples) and then three times in distilled water, each for 5 min, by using ultrasounds, at room temperature. This treatment leads to the formation of –OH groups on top of the samples surface. For the other two pre-treatment processes, the samples were immersed in distilled water and, respectively, in SBF for 1, 3, and 7 days, at 37 °C (without the refreshing of the solutions).

After pre-treatment the samples were analyzed by SEM, EDS, and X-ray photoelectron spectroscopy (XPS). XPS spectra were registered by using Al-source Surface Science Instrument (M-Probe) The survey spectra and the detailed spectra of oxygen and silicon regions were analyzed. The survey spectra presents atomic percentages of elements in the first surface layer (40Å) while the detailed spectra allow the evaluation of specific bonds between atoms from bonding energies. The evaluation of materials surface wettability before and after pre-treatment was carried out by contact angle measurements, using water as wettable fluid. Both static and dynamic angle measurements were performed using drop shape analysis system (DSA 10, Kruss) with an accuracy of $\pm 5^\circ$. This characterization approach was already successfully used by some of the authors in order to assess the early stage reactivity of silica-based bioactive glasses and the surface activation for functionalization purposes.^{24,26} This step was still optimized on slices for their easy characterization.

A.3.2.3 Drugs Uptake

The drug uptake test was made on glass–ceramic powders pre-treated in the medium which gave the best results in terms of –OH group exposition. Powders have been used in this step, since this could be the final morphology of this material for *in vivo* applications. For this test, 100 mg of pre-treated glass–ceramic powders (with particles size less than 20 μm) were immersed in 10 mL drug aqueous solution at 37 °C (Sigma–Aldrich Chemical Company). After 1 day and, respectively, 2 days, the solutions were filtered and the obtained powders were dried at 40 °C in an oven. The quantity of drug grafted on materials surface was calculated indirectly, by difference, measuring the amount of drug which remains in solution and using a calibration curve. The dried powders were analyzed by XRD. Cisplatin solution was prepared with a concentration of 0.5 $\text{mg}\cdot\text{mL}^{-1}$, since its solubility in water is 1 $\text{mg}\cdot\text{mL}^{-1}$.³⁶ The solution was stirred for 20 min, using a magnetic stirrer, to allow a complete solubilization of the drug.

Doxorubicin has a very low solubility in water and the concentration of $0.1 \text{ mg}\cdot\text{mL}^{-1}$ was selected using the literature reference.³⁷ Also in this case the solution was stirred for 20 min, using a magnetic stirrer. The quantity of drug which remains in solution (not bonded with the glass–ceramic surface) was measured by using a graphite furnace atomic adsorption spectrometer (GF-AAS, Perkin-Elmer 4100 ZL)³⁸ for cisplatinum and a UV–Visible spectrophotometer (UV–Vis, Varian 500SCAN), in absorbance conditions, for doxorubicin. Doxorubicin has a characteristic absorbance wavelength at 480 nm.[4] The calibration curves were obtained by using different solutions with the concentration varying in the range ($0.01\text{--}0.5 \text{ mg}\cdot\text{mL}^{-1}$). All drug uptake tests were performed in triplicate and an average value was calculated. The solutions pH was monitored during these experiments.

A.3.2.4 *Drugs Release*

The drugs release kinetics was registered up to 14 days, by using aqueous solutions. For doxorubicin it was used bidistilled water, since literature does not reports any particular indication on this matter. For a very preliminary characterization water seems to be the easier medium in which the release of a so complex molecule should be investigated, in order to avoid any interference from a more complex solution, as SBF or PBS. On the contrary, for cisplatinum a saline solution of 0.9% w/v NaCl was used. Cisplatinum requires chloride ions in order to be released from the glass–ceramic surface. As reported in literature,³⁹ Cl^- ions move the bond between cisplatinum and oxygen of OH^- groups toward the reconstruction of chlorine and platinum bonding, characteristic of this molecule. The dried powders obtained after the uptake test were first rinsed in distilled water, to eliminate the drug eventually absorbed and not bond to the material surface, then dipped into 10 mL aqueous solution (bidistilled water or saline solution) at 37°C . After different time points (12 h, 1, 3, 7, 10, and 14 days), the concentration of the drug released into the solution was measured using GF-AAS for cisplatinum and UVS for doxorubicin. The time points were selected from the literature review.^{36,39–41} Three samples were analyzed for each data point and an average value was calculated. The pH of the drugs release solutions was also evaluated.

A.3.3 Results and Discussion

A.3.3.1 Glass–Ceramic Characterization

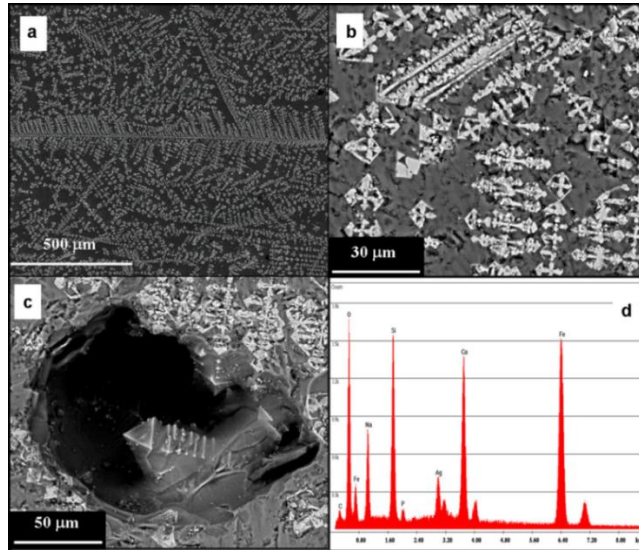


Fig. 1. (a–c) SEM micrographs (back scattering condition) of the glass ceramic samples; (d) EDS analysis of the whole area of figure a.

SEM micrographs of the glass–ceramic slices are shown in Figure 1. Small columns of magnetite crystals with octahedral shape are uniformly distributed throughout the glass matrix [Fig. 1(a)]. The magnetite crystals size is lower than 10 μm [Fig. 1(b, c)]. The EDS spectrum of the whole area of Figure 2(a) is illustrated in Figure 1(d). The peaks corresponding to the elements of the SC45 composition (Na, Ca, Si, P, Fe, and O) are identified. The Ag peak comes from the sample preparation. All the samples were coated with Ag before SEM analysis. XRD analysis of the glass–ceramic samples demonstrated the presence of a unique crystalline phases, magnetite. The residual amorphous halo can be observed in the range of 2θ between 25° and 40° (Fig. 2).

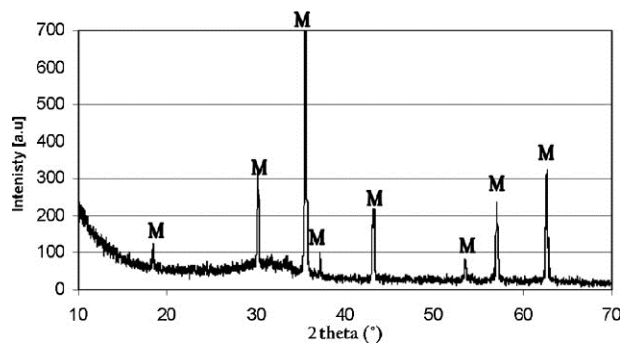


Fig. 2. Diffraction pattern of SC45 (M = magnetite).

A.3.3.2 In Vitro Test

In vitro mechanism of hydroxylapatite (HA) formation during the SBF soaking consists in ionic exchange between the samples surface and surrounding solution, formation of a silica gel layer followed by precipitation of carbonated HA on the samples surface. The silica rich layer acts as nucleation center for HA. The presence of magnetite and trace of residual iron ions into the glassy matrix could cause a slow bioactive behavior of this glass–ceramic, so its bioactivity was investigated with attention. After few days of immersion in SBF solution the amorphous matrix starts to erode and as a consequence, the magnetite crystals come out on the surface. No other significant phenomena were observed during the first week of SBF soaking. After 14 days of treatment the surface dissolution of glassy matrix was observed, as confirmed by EDS analysis. After 28 days of dipping, a discontinuous silica gel layer is formed on the glass–ceramic samples. During drying, the gel loses the water molecules and forms cracks on its surface.

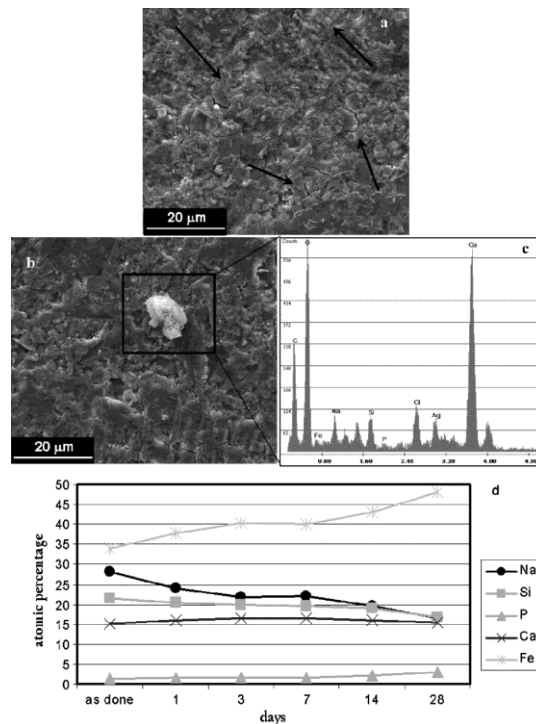


Fig. 3. SEM micrographs of sample surfaces after 28 days of SBF treatment, where it can be observed the silica gel [black arrows], (a) a particle of calcium carbonate (b), and its respective EDS (c). Atomic percentages variations of SC45 elements during in vitro test (d).

These cracks characteristic to the dried silica gel layer are clearly visible on SEM images [see black arrows in Fig. 3(a)]. On the samples surface calcium carbonate

particles, precursors of hydroxycarbonate apatite (HCA) start to precipitate [Fig. 3(b, c)]. The silica gel formation and the precipitation of calcium carbonate on the glass–ceramic samples are an indicator of the first step of the bioactivity process.^{15,26} Figure 3(d) presents the variation of atomic percentage of samples elements during 1 month of soaking in SBF. The data points were obtained from EDS analyses performed on glass–ceramic surfaces of about $2.5 \times 2 \text{ mm}^2$ area. As can be observed, during 28 days of dipping, the concentration of Na and Si decreases, while the amount of Ca and P slightly increases. The trend of Fe shows a continuous increase, probably due to the higher emergence of magnetite crystals during the glass phase etching. The pH measurements put in evidence a slow shift toward basic values (about 7.6), due to ion-exchange between Na^+ ions coming from the glass–ceramic and H_3O^+ ions present in the solution. However the values remain within the range of the physiological variability. Since the bioactivity investigation revealed that the silica gel and apatite formation start after 7 days of soaking in SBF, the samples pre-treatment for the surface activation (exposing the • OH groups) was investigated up to 7 days.

A.3.3.3 Sample Pre-treatment

The efficiency of the three pre-treatment methods was analyzed by contact angle measurements, SEM/EDS observation, and XPS scanning. The results of the wettability test are reported in Figure 4.

By washing pre-treatments in ultrasounds, distilled water and SBF, both static and dynamic contact angles decrease. After 7 days of soaking in SBF, the materials surface appeared totally wettable (contact angle closed to zero). A lower contact angle corresponds to a higher hydrophilic behavior, due to the formation of the –OH functional groups on the material surface. It seems that the efficiency of the surface activation increases in the following order: ultrasounds washing, water dipping, and SBF dipping. The ultrasounds washing pre-treatment was considered irrelevant for the surface activation and it was dismissed. The highest hydrophilic surface is obtained after 7 days of immersion in SBF at 37 °C. For these reasons, the XPS analyses were carried out only on the samples pre-treated 7 days in distilled water and SBF.

Table 1 shows constituent rates of elements after different pre-treatments. Ca/Si rate is an indicator of pre-treatment aggressiveness and of earlier bioactivity stages. It reaches its maximum value for 7 days soaking in SBF; the increase in calcium content is due to the formation of precipitates onto material surface. An analogous behavior could be observed for P/Si rate. Fe/Si rate reaches its maximum values for

7 days soaking in each medium. This result confirms SEM and EDS observations which underline that 1 week of treatment causes a high removal of glassy phase. In order to study the hydroxyls exposition after pre-treatments, a detailed analysis of oxygen and silicon regions was performed. The XPS spectra of the oxygen region before and after 7 days of pre-treatment in distilled water and SBF are shown in Figure 5, while the ones of silicon region are presented in Figure 6. During the soaking of the samples in the two aqueous fluids (SBF and distilled water), a rapid ionic exchange between the alkaline ions from the glass surface and the hydrogen ions from the solution takes place, with the formation of silanols, which undergo polycondensation developing a silica gel layer. This layer promotes the diffusion of Ca^{2+} and PO_4^{3-} ions from the solution, that crystallize into hydroxyapatite.²⁷ The deconvoluted oxygen peak presents three contributions: one at about 529.9–530.6 eV, characteristic of oxygen in different oxides, another one at 531.8–532.1 eV typical of oxygen in silica and the last one at 532.8–533.3 eV which can be attributed to hydroxyls or to silica gel. For this last term the correct identification of characteristic bonds can be done comparing oxygen and silicon regions. Generally, silicon peak is monoenergetic at about 101 eV. Contributions at low energy can be ascribed to SiC contaminations from polishing process, while signals at higher energy (103–104 eV) are typical of silica gel. So the presence of a peak at about 532.8–533.3 eV in oxygen region and one at about 103 eV in silicon region is an indicator of silica gel formation on the material surface.

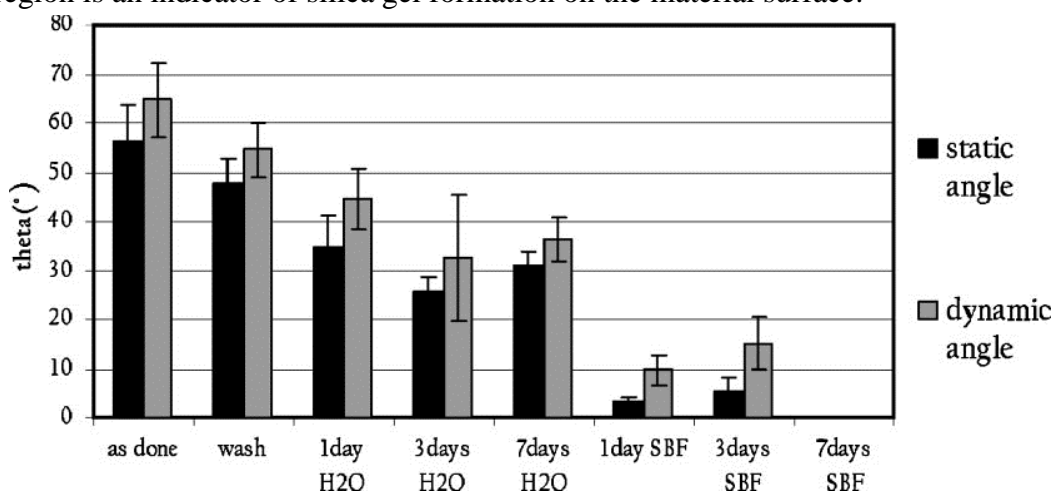


Fig. 4. Static and dynamic contact angles after the three pre-treatment processes.

Considering the Figure 5, it can be observed that all the oxygen spectra have the 532.8–533.3 eV contribution. For the untreated sample this signal is small and can be due to humidity absorption, while on the water pre-treated sample the deconvoluted peak increases due to the hydroxyls formation. In fact, after both pre-

treatments, the ratio between the intensities of hydroxyls/silica gel peak and those of silica and oxides, is higher in comparison with the one before pre-treatment, suggesting an increase in the –OH concentration on the samples surface. As far as the SBF pre-treated samples is concerned, also a contribution at about 534 eV (attributable to carbonates) appears.

In order to better understand the nature of 532.8–533.3 peaks, a detailed analysis of silicon peak is essential. Considering the silicon region (Fig. 6), it can be noticed that after 7 days of soaking in distilled water [Fig. 6(b)], the silicon peak is monoenergetic (around 102 eV), while after 7 days of soaking in SBF [Fig. 6(c)], the silicon peak presents two contributions (102 and 104 eV). The 102 eV signal corresponds to silica, while the 104 eV signal is characteristic to the silica gel.

Therefore, during the water pre-treatment only the formation of –OH groups took place, whereas for the SBF pre-treatment also silica gel formation occurred. Precipitation of HA precursors is confirmed by carbonate's signals in oxygen region. The XPS results suggest that the best pre-treatment is dipping for 7 days in distilled water, in order to obtain effective hydroxyls exposition and to avoid the silica gel formation on the samples surface.

SEM and EDS analyses were performed only on the samples pre-treated up to 7 days in distilled water and SBF, without solutions refreshing. SEM observations of samples dipped in distilled water showed a progressive dissolution of the amorphous phase and a consequent emergence of the crystalline phase.

Table 1. *Constituent rates of elements after different pre-treatments.*

Sample	Ca/Si	Na/Si	P/Si	Fe/Si
As done	0.5	0.8	0.2	0.2
7 days H ₂ O	0.2	0.8	0.3	0.4
7 days SBF	0.9	0.7	1.5	0.4

The variation of the atomic concentration (%) of the SC45 elements during 7 days of water pre-treatment is represented in Figure 7(a). The data were obtained from EDS analyses of the whole samples surface, using 50× magnification. It can be observed a decrease of sodium ion concentration and an increase of iron ions amount especially after 7 days of soaking, probably due to the emergence of the magnetite crystals during the glass dissolution. For the SBF pre-treated samples, no particular changes of the surface were noticed. The variation of the atomic concentration (%) of the SC45 elements after the pre-treatment in SBF solution, during 7 days of soaking is presented in Figure 7(b). Also in this case the data were

obtained from EDS analyses of a surface of about $2.5 \times 2 \text{ mm}^2$. A slightly increase in phosphorus ions concentration is observed, suggesting the initiation of the bioactivity mechanism. Iron concentration still increases but with a lower rate confronted with the water treated samples. Even though the 7 days SBF pre-treatment leads to a completely hydrophilic surface, XPS and SEM/EDS analyses indicate a faster surface reactivity of these samples to the SBF solution, confronted with the distilled water.

The reaction kinetics is still slow, but it is not well controllable and can provoke, even for short time, a preliminary precipitation and/or silica gel condensation. Afterward, the 7 days water pre-treatment at 37°C was selected, in order to guarantee good hydroxyls exposition, which will trigger the grafting of the chemotherapeutic agents. The pH values begin to increase immediately during the powders pre-treatments. After 7 days of immersion in distilled water the values ranges from 7.37 (pH of water at 37°C) to 10.1, due to the fast ion exchange between the glass–ceramic surfaces and water solution.

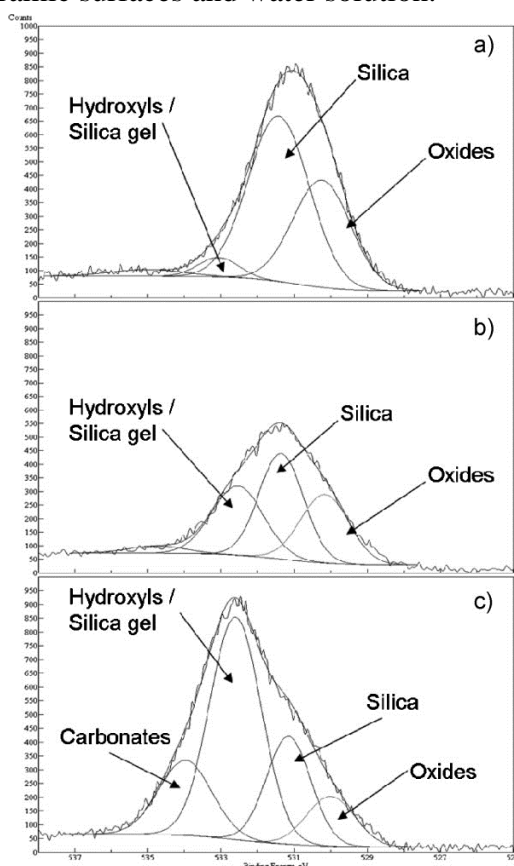


Fig. 5. XPS spectra of oxygen region (a) before pre-treatment, (b) after 7 days in distilled water, and (c) after 7 days in SBF. Graphs ordinates represent counts.

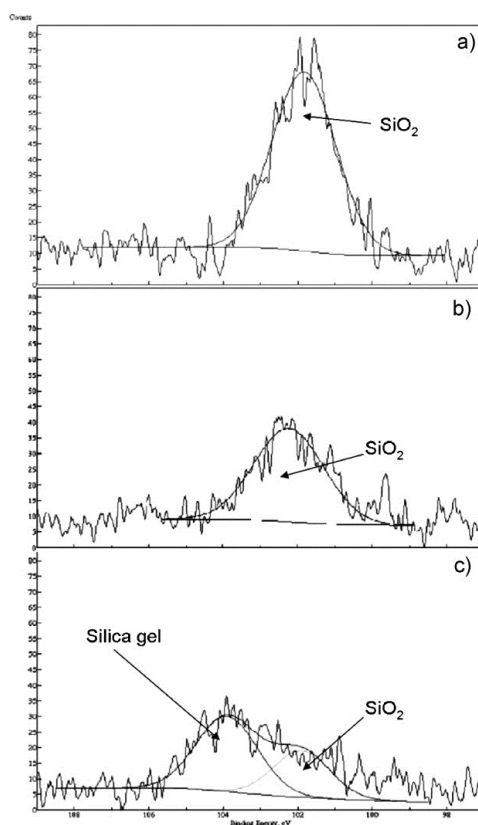


Fig. 6. XPS spectra of silicon region (a) before pre-treatment, (b) after 7 days in distilled water, and (c) after 7 days in SBF. Graphs ordinates represent counts.

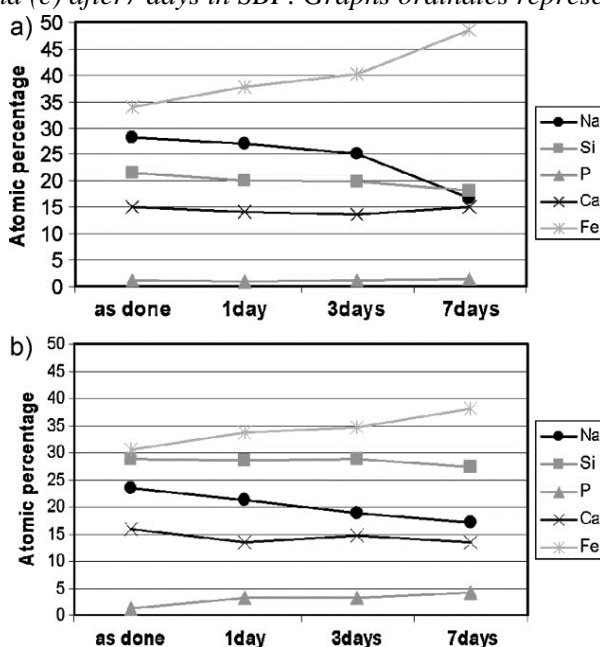


Fig. 7. Variations of the atomic concentration (at%) of the SC45 elements after pre-treatment (a) in water and (b) in SBF solution, during 7 days of soaking.

A.3.3.4 Drugs Uptake

In order to graft drugs on glass–ceramics surface, the approach investigated in this research was to overwork the ability of glasses and glass–ceramics to expose reactive groups. SC45 has a residual amorphous phase (equivalent to Bioglass one) and a ceramic phase (magnetite), both able to expose hydroxyl groups and to bond to silicon and/or iron.^{42,43} Both phases (amorphous or crystalline) could be exploited to functionalize the ferrimagnetic glass–ceramic with antineoplastic agents. Cisplatin could bind covalently with –OH groups, here exposed by the amorphous phase, by losing the Cl[−] ion. As reported in literature, the Cl[−] ions can bond with H⁺ ions leached from the –OH groups of the amorphous phase, forming hydrochloric acid molecules [Fig. 8(a)].²⁸ Doxorubicin could realize a covalent bond with the –OH groups of the glass phase, by removing water molecules [Fig. 8(b)] [after demethylation of the methoxy group (electron donor) of the planar tetra-cyclic part, with formation of a –OH group, a condensation with the acid ≡Si–OH group exposed by the glass–ceramic surface can be hypothesized]. Another possible bonding mechanism of the doxorubicin is the link with the –OH groups exposed by the magnetite in a basic medium.⁴⁰ The investigation of the bonding mechanism is not possible at this stage of the work, but the stability of the grafting can be assessed indirectly. As previously mentioned, the antitumor drugs uptake was carried out in aqueous solutions, by using 7 days water pre-treated glass–ceramic powders (with particles size less than 20 μm). Therefore, SC45 powders were previously pre-treated in water for one week and then were dipped in the drug aqueous solution for 1 and 2 days at 37 °C.

The doxorubicin amount grafted on SC45 surface was calculated from the calibration curve, using solutions with different concentrations in the range (0.01–0.1 mg·ml^{−1}). The samples absorbance was measured by UV–Vis spectroscopy. A linear dependence was obtained between absorbance values (a) and doxorubicin concentration (c), such as:

$$a = 18.29c - 0.0459 (R^2 = 0.997) \quad (1)$$

The amounts of doxorubicin grafted on the SC45 surface, after one and two uptake days are displayed in Figure 9(a). There are not significant differences between the quantities of drug incorporated (77±7 wt% after 1 day and 75±9 wt% after 2 days). For this reason the release tests were made after 1 day of uptake. The pH of the doxorubicin aqueous solution at 37 °C is about 6.77, but after 1 day of uptake it increases to basic values, about 9.5. This behavior can be explained by the interaction phenomena which take place between SC45 powders and the drug

solution, including partial dissolution of the glassy phase and in particular, sodium ions release.

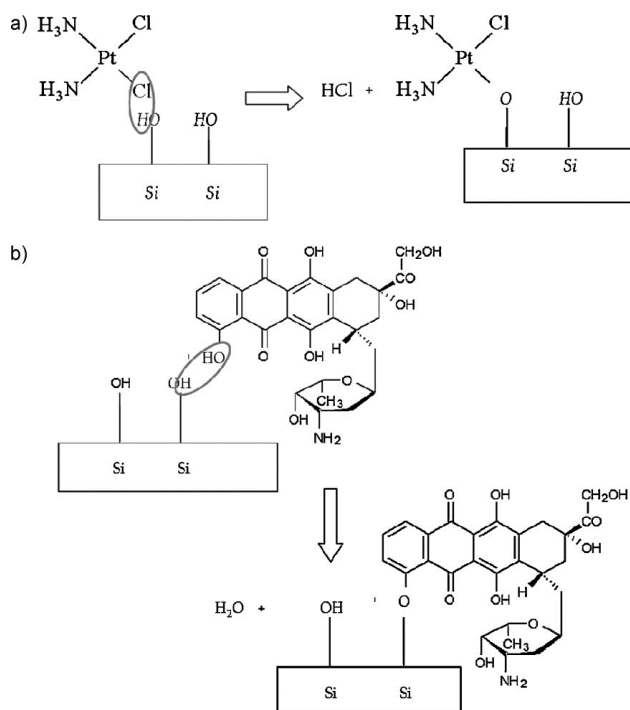


Fig. 8. Possible bond mechanism of (a) cisplatin and (b) doxorubicin with the activated $-\text{OH}$ groups of the glass-ceramic surface.

The pH trend is important to understand the charge of the drug molecule; in fact doxorubicin is neutral in lightly basic ambient, while it is positive in the acid one. The cisplatin amount grafted on SC45 surface was calculated from the calibration curve, using solutions with the concentration in the range ($0.05\text{--}0.5 \text{ mg}\cdot\text{ml}^{-1}$). The samples absorbance was measured by GF-AAS. The obtained curve is not linear; it has an exponential trend, such as:

$$y = ax^{1.3} \quad (R^2 = 0.999) \quad (2)$$

where y is the platinum amount detected by the instrument, x is the initial drug solution concentration and a is a multiplying coefficient. Figure 9(b) shows the quantity of cisplatin grafted on the SC45 surface, after one and two uptake days. Also in this case there are not significant differences between the concentration of drug incorporated ($42 \pm 9.6 \text{ wt\%}$ after 1 day and $50 \pm 3.4 \text{ wt\%}$ after 2 days) and therefore the release tests were made after 1 day of uptake.

The pH of the cisplatin solution slowly increases from 6.04 before uptake to 7.3 after 1 day of uptake. In this case the pH variation is lower than for doxorubicin

due to the H^+ released during the cisplatinum condensation reaction. In fact, during condensation, cisplatinum liberates HCl which is completely dissociated in an aqueous solution. The released hydrogen ions will compensate the pH increase (due to the ionic exchange between the glass–ceramic powders and drug solution), lowering the pH. XRD analyses (not reported) on samples after the uptake treatments did not show any significant modification.

A.3.3.5 *Drugs Release*

The doxorubicin release was performed in 10mL of distilled water, at 37 °C, for different periods of time up to 14 days, by analyzing the solutions concentration with UV–Vis spectroscopy. The quantity of doxorubicin released at different time points is presented in Figure 10(a). As can be seen, the drug released concentration is very low (less than 15.5 wt%). Moreover, the variation of the drug released in time is not linear, being impossible to describe the reaction kinetics.

The glass–ceramic powders release a very few percentage of doxorubicin, which varies between 5.9 ± 5 and 15.3 ± 9.6 wt%. This behavior is probably due to a strong covalent bonding between the drug molecule and the hydroxyl groups exposed on materials surfaces, which allows the release of a small amount of adsorbed drug, explaining also the high data dispersion.

The cisplatinum release was measured with a GF-AAS, by using 10 ml of 0.9% w/v NaCl saline solution, since the drug needs Cl^- ions to be released. Figure 10(b) shows the variation of the drug released up to 14 days of soaking at 37 °C. The concentration of the released drug reaches a maximum of almost 50 ± 6.8 wt% after 1 day of immersion, but also in this case the amount of drug released varies randomly in time, being impossible to describe the cisplatinum release kinetics. However, the amount of drug released is higher than for doxorubicin, varying between 25 and 50 wt%. In this case, as suggested by literature, the presence of Cl^- ions in the solution could affect the drug release, by changing the equilibrium reaction of cisplatinum toward drug recombination [see Fig. 8(a) with the equilibrium reaction to the left instead of the right direction; HCl could combine with the drug grafted on the glass–ceramic surface to reform the drug molecule].

However, the Cl^- ions concentration is probably not high enough to carry out a complete release of the drug. It seems that the maximum amount of drugs is released during the first hours of immersion in the aqueous solutions at 37 °C for both doxorubicin and cisplatinum agents. The pH of the both drug released solutions belongs to the basic field. During the release test of the doxorubicin, the solution pH varies in the range (9–10.2), reaching the 9.7 value after 12 h. Similar results were obtained for the cisplatinum release test, where the pH was almost

stable (around 10 value) after 12 h. These first results let only asses that a strong bonding to the activated glass–ceramic surface was achieved for both drugs, which is the goal of the present work, and that their release is connected with the composition of the leaching medium. For doxorubicin, water is not able to break its bonding to the glass–ceramic surface.

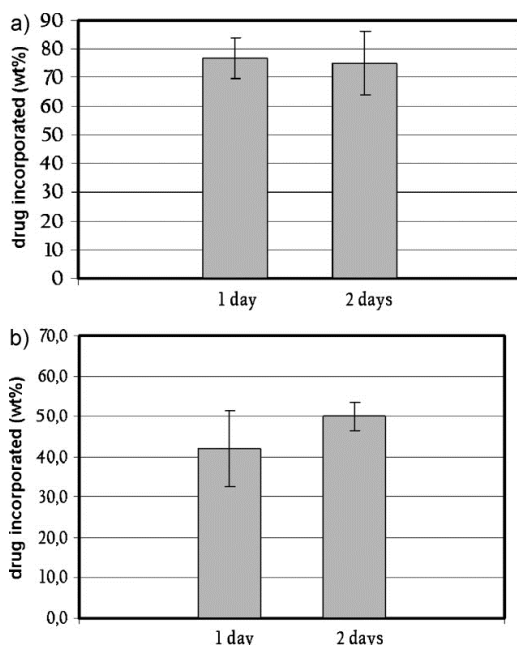


Fig. 9. Amounts (wt%) of doxorubicin (a) and cisplatin (b) grafted on SC45 surface, after one and two uptake days.

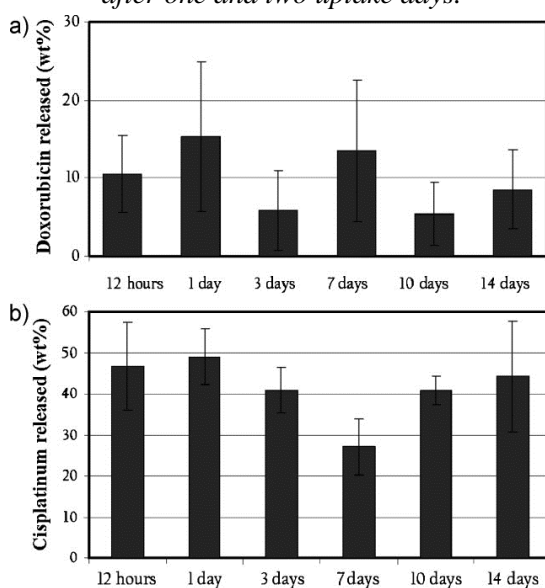


Fig. 10. Amounts (wt%) of doxorubicin (a) and cisplatin (b) released after different soaking periods.

The hypothesis of a covalent bonding between the drug and the glass–ceramic (likely between the hydrolyzed methyl group of doxorubicin and the –OH groups on top of the glass–ceramic) at the moment is only supported by the evidence of a very few release. It is to be considered that the active groups of doxorubicin are represented by the daunosamine and adriamycinone connected to the tetra-cyclic planar group³⁷ so a few release of this drug should not be a drawback of a functionalized device, if the bonding does not involve these two groups. On the contrary, the action of cisplatin is related to the displacement of the two chloride ligands^{32,33} so they must be restored via release in chloride-rich aqueous solutions. It is not possible, with the data collected in this work, to make any comparison between the release kinetics of the two different drugs, both because of the different media chosen for the leaching test and for the different bonding mechanisms that could be hypothesized. A better understanding of both bonding and release mechanisms will be object of a future work, where different media, in different condition of temperature, are going to be investigated.

A.3.4 Conclusions

A ferrimagnetic glass–ceramic belonging to the system $\text{SiO}_2\text{--Na}_2\text{O--CaO--P}_2\text{O}_5\text{--FeO--Fe}_2\text{O}_3$, has been studied as a drug carrier material for cancer treatment. This ferrimagnetic glass–ceramic has a unique crystalline phase (magnetite) and shows slow bioactivity kinetics. Two different anticancer drugs were considered: cisplatin and doxorubicin. In order to bond with the drugs, the glass–ceramic surface was firstly activated, by exposing the –OH functional groups. Treatments performed to expose the –OH groups reveal that one week of immersion in distilled water is the best treatment which guarantees the exposition of superficial hydroxyls. Both antineoplastic agents used in this work are able to bind with exposed groups of SC45. After 1 day of immersion, 77 ± 7 wt% of doxorubicin were incorporated into the glass–ceramic powders, while the cisplatin amount loaded into the glass–ceramics is about 42 ± 9.6 wt%. The antitumoral drugs release has an opposite behavior, since a very low doxorubicin amount (less than 15.5 wt%) is released during the 14 days of immersion in water, probably due to a strong covalent bonding with the glass–ceramic surface. The amount of cisplatin released in 1 day in a saline physiological solution is instead about 50 ± 6.8 wt%. Future works will investigate and analyze thoroughly the mechanism of drugs attachment and release. A study of the drugs uptake and release kinetics at higher temperature (in the range of hyperthermic treatment) and in different solutions which simulate the in vitro behavior (such as phosphate buffered saline PBS and SBF) is in progress. Nevertheless this research work points out the possibility to

graft antineoplastic agents on SC45 glass–ceramic surface. This material can be used for both antitumoral implants and magnetic drug targeting, overworking, in this way, the material ability to generate heat and to release chemotherapeutics able to interact with neoplastic cells.

A.3.5 References

- [1] P. Wust, B. Hildebrandt, G. Sreenivasa, B. Rau, J. Gellermann, H. Riess, R. Felix, P. M. Schlag, *Lancet Oncol.* 2002, 3, 487.
- [2] C. W. Song, *Cancer Res.* 1984, 44, 4721.
- [3] S. Ryu, S. L. Brown, S. Kim, M. S. Khil, J. H. Kim, *Int. J. Radiat. Oncol. Biol. Phys.* 1996, 34, 133.
- [4] I. Takahashi, Y. Emi, S. Hasuda, Y. Kakeij, Y. Maehara, K. Sugimachi, *Surgery* 2002, 131, S78.
- [5] T. C. Cetas, E. J. Gross, Y. Contractor, *IEEE Trans. Biomed. Eng.* 1998, 45, 68.
- [6] A. Jordan, R. Scholz, P. Wust, H. Fahling, R. Felix, J. Magn. Mater. 1999, 201, 413.
- [7] S. A. Gomez-Lopera, R. C. Plaza, A. V. Delgado, J. Colloid Interface Sci. 2001, 240, 40.
- [8] Y. K. Lee, D. H. Kim, Y. J. Lee, K. N. Kim, I. B. Shim, Synthesis of Sr and Cr doped barium ferrite micro- spheres for hyperthermic cancer treatment by sol–gel process, *Ceramics, cells and tissues, Eighth Annual Seminar and Meeting Faenza* 2003.
- [9] K. Takegami, T. Sano, H. Wakabayashi, J. Sonoda, T. Yamazaki, S. Morita, T. Shibuya, A. Uchida, *Biomed. Mater. Res.* 1998, 43, 210.
- [10] N. F. Borrelli, A. A. Luderer, J. N. Panzarino, US Patent 4323056, (1982).
- [11] T. Kokubo, T. Yamamuro, Y. Ebisawa, K. Ohura, European Patent 361797 (1990).
- [12] Y. Ebisawa, F. Miyaji, T. Kokubo, K. Ohura, T. Nakamura, *Biomaterials* 1997, 18, 1277.
- [13] S. H. Oh, S. Y. Choi, Y. K. Lee, K. N. Kim, J. Biomed. Mater. Res. 2001, 54, 360.
- [14] Y. Ebisawa, F. Miyaji, T. Kokubo, K. Ohura, T. Nakamura, *J. Ceram. Soc. Jpn.* 1997, 105, 947.
- [15] D. Arcos, R. P. Del Real, M. Vallet-Regi, *Biomaterials* 2002, 23, 2151.
- [16] Th. Leventouri, A. C. Kis, J. R. Thomson, I. M. Anderson, *Biomaterials* 2005, 26, 4924.

- [17] N. I. Papanearchou, Th. Leventouri, A. C. Kis, A. Hotiu, I. M. Anderson, *Mater. Res. Soc. Symp. Proc.* 2005, 839, 3.7.1.
- [18] O. Bretcanu, E. Vernè, M. Coisson, P. Tiberto, P. Allia, J. Magn. Magn. Mater. 2006, 300, 412.
- [19] O. Bretcanu, E. Vernè, M. Coisson, P. Tiberto, P. Allia, J. Magn. Magn. Mater. 2006, 305, 529.
- [20] M. Ferraris, O. Bretcanu, E. Vernè, Italian Patent TO2002 A000994, 2002.
- [21] J. J. Cras, C. A. Rowe-Taitt, D. A. Nivens, F. S. Ligler, *Biosens. Bioelectron.* 1999, 14, 683.
- [22] Q. Z. Chen, K. Rezwan, D. Armitage, S. N. Nazhat, A. R. Boccaccini, *J. Mater. Sci.: Mater. Med.* 2006, 17, 979.
- [23] E. Verne`, S. Ferraris, C. Vitale-Brovarone, S. Spriano, C. Bianchi, M. Morra, C. Cassinelli, *Key Eng. Mater.* 2008, 361, 593.
- [24] E. Verne`, C. Vitale-Brovarone, E. Bui, C. L. Bianchi, A. R. Boccaccini, *J. Biomed. Mater. Res. Part A* 2009, DOI: 10.1002/jbm.a.32153.
- [25] E. Vernè, S. Ferraris, C. Vitale-Brovarone, S. Spriano, C. L. Bianchi, A. Naldoni, M. Morra, C. Cassinelli, *Acta Biomater.* 2009, DOI: 10.1016/j.actbio.2009.06.025.
- [26] E. Verne`, O. Bretcanu, C. Balagna, C. L. Bianchi, M. Cannas, S. Gatti, C. Vitale-Brovarone, *J. Mater. Sci.: Mater. Med.* 2009, 20, 75.
- [27] L. L. Hench, *Bioactive Glasses*, in: *An Introduction to Bioceramics*, Vol. 1 (Eds: L. L. Hench, J. Wilson), World Scientific Pub, 1993, pp. 41–62.
- [28] T. Kokubo, *J. Non-Cryst. Solids* 1990, 120, 138. [29] O. Peitl, E. Zanotto, L. L. Hench, *J. Non-Cryst. Solids* 2001, 292, 115.
- [30] T. Kokubo, H. Kushitai, C. Ohtsuki, S. Sakka, T. Yamamuro, *J. Mater. Sci.: Mater. Med.* 1992, 3, 79.
- [31] T. R. Zeitler, A. N. Cormack, *J. Cryst. Growth* 2006, 294, 96.
- [32] D. Lebolwhol, R. Canetta, *Eur. J. Cancer* 1998, 34, 1522.
- [33] P. M. Takahara, C. A. Frederick, S. J. Lippard, *J. Am. Chem. Soc.* 1996, 118, 12309.
- [34] R. L. Momparler, M. Karon, S. E. Siegel, F. Avila, *Cancer Res.* 1976, 36, 2891.
- [35] T. Kokubo, H. Takadama, *Biomaterials* 2006, 27, 2907.
- [36] X. Yan, R. Gemeinhardt, *J. Controlled Release* 2005, 106, 198.
- [37] N. Tang, G. Du, N. Wang, C. Liu, H. Hang, W. Liang, *J. Natl. Cancer Inst.* 2007, 99, 1004.

- [38] H. Ye, L. Jin, R. Hu, Z. Yi, J. Li, Y. Wu, X. Xi, Z. Wu, *Biomaterials* 2006, 27, 5958.
- [39] A. Barroug, M. J. Glimcher, *J. Orthop. Res.* 2002, 20, 274.
- [40] W. Ke, Y. Zhao, R. Huang, C. Jiang, Y. Pei, *J. Pharm. Sci.* 2007, 12, 107.
- [41] G. Kang, S. Cheon, S. Song, *Int. J. Pharm.* 2006, 319, 29.
- [42] M. Ma, Y. Zhang, W. Yu, H. Shen, H. Zhang, N. Gu, *Colloids Surf., A: Physicochem. Eng. Aspects* 2003, 212, 219.
- [43] K. Woo, J. Hong, J. Ahn, *J. Magn. Magn. Mater.* 2005, 293, 177.

APPENDIX B

Physico-Chemical characterizations

APPENDIX B1: X-Ray Powder Diffraction technique

X-ray powder diffraction is a non-destructive technique widely applied for the characterization of crystalline materials.¹⁻⁴ This method has been traditionally used for phase identification, quantitative analysis and the determination of structure imperfections. Illustrated examples are given to highlight the importance of this technique. More detailed information on recent developments can be obtained from references.⁵⁻⁹

B.1.1 Introduction

Some solids can be prepared only as micro crystalline powders and hence their structure cannot be determined using single crystal diffraction techniques. In such cases it is necessary to analyze the structure of the material using powder diffraction data. The ability to determine crystal structures using powder diffraction promises to open up many avenues in structural sciences. It is possible to determine the orientation, unit cell dimensions, stress/strain, crystal structure, etc. from the information obtained in the powder diffraction pattern. The steps involved in this process are¹⁻⁴:

- unit cell determination;
- decomposition of powder pattern into integrated intensities;
- assignment of space group from systematic absences;
- refinement of the structure, typically by the Rietveld method.¹⁰⁻¹³

However the determination of structures using powder diffraction data is much more difficult than from single crystal data. This problem arises due to the collapse of the three dimensional crystallographic information into a single dimensional one which is the powder diffraction pattern. This ambiguity creates problems in the determination of the unit cell. However with the improvements in the instrument and algorithmic developments it is now possible to solve different structures from powder diffraction data alone. Now powder diffraction has become the promising technology in the characterization of crystalline materials.¹⁰⁻¹³

B.1.2 Bragg's condition

Consider a beam of wavelength striking a line of atoms spaced at equal distances. The radiated beam that is in the form of spherical wavefronts will be of maximum intensity when the path difference between the incident and the reflected beam is equal to an integer number of wavelengths.¹⁻⁴ Taking a picture where each atom is giving off a spherical wave front, the directions of scattering thus constitute a series of cones. If we take a 2-D net, in which there is another line of atoms independent

from the first line of atoms, another series of cones is generated. Thus a 2-D net produces two families of intersecting cones. Thus a constructive interference is seen only in some specific well defined directions in space. Also when the axes of the cones are non-linear, the intersections of the cones give a series of lines.

Extending this idea to three dimensions, strong constructive interference will occur only for some specific conditions of interference and specific directions. But it is difficult to picture this in three dimensions. However Bragg proposed that the condition for constructive interference is equivalent to that of a simple plane, which can be described by the Miller indices. Now the plane is $(h\ k\ l)$ and the spacing between the planes are considered but not the spacing between the atoms or lattice points as was considered previously. A 3-D scattering of X-rays can be seen in Fig. B.1.

Consider a crystal lattice whose interplanar spacing is d . Also the incident radiation strikes the planes $(h\ k\ l)$ at an angle θ as shown. The condition for constructive interference is now:¹⁻⁴

$$n\lambda = 2d \sin \theta$$

where λ = incident light wavelength, n = multiple number (0,1,2,3, etc.), d = interplane spacing, θ = angle between the incident radiation and the planes $(h\ k\ l)$.

The incident angle is chosen by rotating the crystal relative to the beam, the wavelength is fixed and thus the interplanar spacing d is obtained (see Fig. B.2). The conclusion is that any set of planes in a crystal will reflect an X-ray beam if the set of planes is at right angle ($\theta = 90$) to the incident beam. But there arises another question whether the planes will reflect the beam strongly or not.

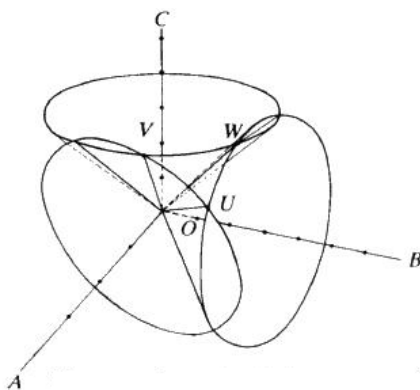


Fig. B.1: The general case for the intersection of diffraction cones coaxial with three non-coplanar.

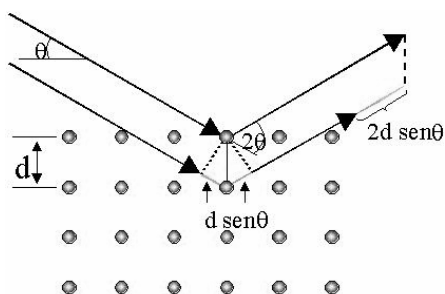


Fig. B.2: Explanation of Bragg's condition.

The intensity of the reflected beam is proportional to the product of the intensity of the incident beam and the concentration of electrons in the reflecting plane. Thus if the unit cell dimensions are known and, subsequently, the atomic number of each of the atoms, it is possible to calculate the concentration of electrons and hence the intensity of the reflected beam.

Now considering the reverse situation, if the size of the unit cell and the intensities of the reflections are known, the positions of atoms and also the relative number of electrons per atom are found. It is obvious that all compounds with different formula or unit cells have different collections of d -spacings and different intensities of reflections. The observed patterns of spacings and intensities can thus be used to identify an unknown compound in a specific crystalline phase.

B.1.3 Powder diffraction

If monochromatic X-ray radiation is taken instead of white light and the crystal is placed in front of the beam, there will be only one reflected beam for one particular angle of incidence. If the crystal is now rotated around the incident ray direction without changing the incident angle, the reflected beam will describe a cone with the crystal at the apex of the cone as shown in Fig. B.3.

When there are hundreds of crystals, there are many reflected beams and when the crystals are rotated about their axes of incident X-ray beam, a series of cones are formed as shown in Fig. B.4. If a powdered sample is placed in the path of x-rays there will be a continuous series of point reflections lying along the arc of the cone.¹⁻⁴ This is the basis of powder method that is used in X-ray crystallography to determine the unknown samples. For every set of crystal planes, one or more crystals will satisfy Bragg's condition.

The main methods of studying powders have led to the investigation of the atomic arrangements. The methods employed are the Debye Scherrer method and Diffractometry .

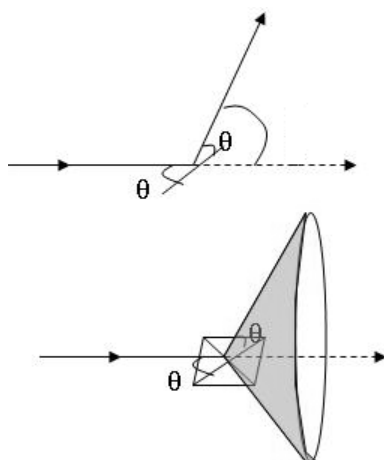


Fig. B.3: The cone of the reflected beam

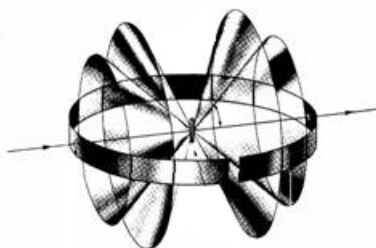


Fig. B.4: Series of cones of the reflected beams.

○ Debye Scherrer Camera

One of the simplest ways of determining unit cell parameters is the Debye Scherrer method. To understand the principles involved, consider a particular $(h\ k\ l)$ reflection. One or more particles will be oriented so that their $(h\ k\ l)$ planes obey Bragg reflection condition. Fig B.3 shows one plane in the set. If the plane is now rotated such that the angle of incidence is kept constant, the reflected beam travels over the surface of the cone with the axis coinciding with the transmitted beam. Though this rotation does not occur in powder method, combined effects of some reflections from the $(h\ k\ l)$ planes make the correct Bragg angle with the incident beam and thus have the form of a cone of diffracted radiation. Thus the $(h\ k\ l)$ reflection from a powder produces many cones.

In the Debye Scherrer method a narrow strip of film is curved in a short cylinder with the specimen placed on the axis and the incident beam is directed at right angles to the axis. The cones of diffracted radiation intersect the cylindrical strip in lines and when the strip is laid straight the resulting pattern is as shown in the Fig. B.4. Each pattern is made up of small spots each from one particle and the spots are so close to each other that they appear as a continuous line. These lines are

generally curved and when $2\theta = 90^\circ$, they form a straight line. From the measured position of a given diffraction line, θ can be determined and if the wavelength λ is known, it is possible to calculate the d -spacings of the lattice planes.

If the shape and size of the unit cell are known, the position of all the possible diffraction lines can be predicted. The Debye Scherrer method is widely used especially in metallurgy.

○ *The Powder Diffractometer (Bragg-Bentano)*

Modern X-ray techniques give a series of peaks instead of diffraction intensities as in Debye Scherrer method. In this method a detector is used instead of the film.

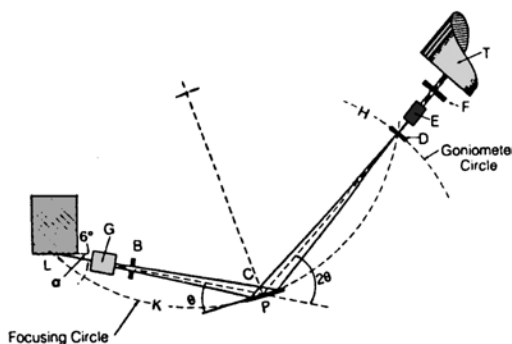


Fig. B.5: *The Powder Diffractometer (Bragg-Bentano).*

A convergent incident ray is used to give a good peak resolution. The powder is filled in the hole of a sample holder. The set up requires that if reflection is obtained when the beam is incident at an angle θ with the lattice plane, the reflected beam is recorded at an angle of 2θ in what is referred to as θ - 2θ scan, as shown in Fig. A.5. The peak positions and the intensities are readily obtained from the chart. The powder diffractometer uses an X-ray detector like a Proportional or Scintillation Counter to measure the positions of the diffracted beams.

B.1.4 Application

X-ray powder diffraction has opened up new avenues in the studies of structures. It has a number of applications.

- Qualitative analysis: from the pattern, the d -spacings are recorded and the relative intensities are measured and are compared with the patterns of the known compounds. This comparison is done with the help of a powder diffraction file that contains the patterns of some standard compounds divided into subdivisions-minerals, inorganic, organic;

- Quantitative Analysis: for a multi-component mixture the relative concentration of each of the components can be obtained by using a fitting program based on Rietveld refinement¹⁰⁻¹²;
- *Structure of alloys*: an alloy is a mixture of two or more elements. If the composition is uniform it produces a typical powder diffraction pattern. If one of the components precipitates, it produces separate lines on the powder pattern corresponding to the component;
- *Stress Determination in metals*: if there is a stress in a metal then the angle of the diffraction cone changes because of a change in the d-spacing due to stress. By measuring the changes in the cone angle accurate measurements of stress can be made. In addition, stress invariably broadens diffraction peaks unless it is absolutely uniform on an atomic scale;
- *Determination of crystallite size*: as the size of the crystallite decreases, the angular spread of the reflection increases. The full width at half maximum can be used as a measure of the mean particle size of the sample;
- *Identification and raw material evaluation*: for some complex materials, it is difficult to analyze the pattern. But since similar materials exhibit similar patterns, we can for example determine the structure of different clays as a cement material by comparing with acceptable clay and thus relate structure to properties.

B.1.5 Limitation

- Single crystal methods depend upon mathematical algorithms and accurate peak intensities to solve structures. Such accuracy is sometimes difficult to obtain.
- The individual peak intensities are difficult to obtain because in powder diffraction, a 3-D pattern is reduced to a 1-D pattern and analysis is done. This leads to both accidental and exact peak overlap.
- The symmetry of crystals cannot be obtained accurately in powder diffraction pattern.
- Preferred orientation can lead to inaccurate peak intensities. But both rotating the sample about its normal and rocking it about each data point can overcome this.

B.1.6 Informations obtained by a diffraction line

Tab. B.1 shows the main qualitative information¹⁻⁴ obtained by a diffraction pattern. The positions of the peaks are directly related to the dimensions of the unit cell. The intensities are related to the contents of the unit cell. The *d*-spacings are

taken because they are independent of the wavelength of the light used. Normally relative intensities are used in order to normalize the intensities. The normalization of intensities is done by taking a reference for the strongest peak and other intensities are scaled accordingly. The Full Width at Half Maximum (FWHM) of the most intensive peak ($I = 100\%$) is used to calculate the average diameter of the particles; the broad lines underline the presence of amorphous phase in the sample.

The X-ray powder diffraction pattern of a mixture containing two or more compounds is the weighted sum of the individual patterns. Although a powder diffraction pattern is used as a finger print for identifying a material, other important information is obtained in it.

Tab. B.1: General information obtained by a diffraction line.

Feature	Information obtained
Peak positions (2θ values)	Unit cell dimensions and symmetry.
Peak intensity	Unit cell contents (basis vectors) and thermal vibrations
FWHM	Average particle size/strain
Peak shapes	Stacking faults, layer defects
Broad lines	Amorphous phase
Non –indexable lines	Presence of a crystalline impurity

B.1.7 Structure refinement and quantitative phase analysis of powder diffraction patterns

The structure refinement is a method to get the exact structure from the data obtained in structure solution method. Thus if the structure solution is a good approximation to the original structure, a good quality structure may be obtained by structure refinement.¹⁰⁻¹³ Structure refinement is generally carried out by the Rietveld method, the best refinement to obtain an exact structure even if there are peak overlaps. This method is also the most powerful tool to extract quantitative information from a multiphase polycrystalline sample.

The main sources of error for quantitative phase analysis (QPA) are the well-known peak overlapping, extinction, preferred orientation and microabsorption effects.

The Rietveld method,¹⁰ being a full-pattern fitting technique, offers great advantages, among which:

- (a) the calibration curves are not needed;

- (b) it does not require the pattern decomposition in integrated intensity values;
- (c) overlapping of reflections is generally not problematic (except for low concentrations of low-scattering-power phases);
- (d) it exploits the whole pattern information;
- (e) it allows microabsorption and preferred orientation effects to be modelled;
- (f) it can deal with complex mixtures;
- (g) it supplies more accurate results.

The method requires, for each phase, the prior knowledge of the structural model, which is usually kept fixed during refinement; approximate models can be refined if the experimental information is sufficient. The mixture pattern is calculated by taking into account the contributing pattern of each phase according to

$$Y_c(i) = \sum_j Y_{cj}(i) + Y_b(i)$$

where the summation is over the number of phases in the mixture, $Y_c(i)$ is the total calculated pattern for each step i ; $Y_b(i)$ is the calculated background model for each step i ; $Y_{cj}(i)$ is the calculated pattern for the phase j for each step i ; and $Y_c(i)$, $Y_b(i)$, $Y_{cj}(i)$, according to

$$Y_{cj}(i) = S_j \sum_h I_h P(i, h) A(i, h) O(h)$$

S_j is the scale factor; Σ takes into account the contribution of each reflection to the value of $Y_{cj}(i)$ at the point i ;

$$I_h = m_h |F_{hc}|^2 Lp_h$$

is the integrated intensity of reflection h , including the multiplicity (m_h), the structure-factor modulus ($|F_{hc}|$) calculated from the model (occupancy factors are taken into account, more complicated structures like mixed crystals are not considered) and the Lorentz-polarization correction (Lp_h); $P(i, h)$ is the profile shape function; $A(i, h)$ is the asymmetry function; $O(h)$ is the preferred orientation correction.

Each contributing pattern is a function of the phase weight fraction in the mixture; this information is derived from the refined scale parameter S_j ,¹⁴⁻¹⁵ according to

$$W_i = \frac{S_i \rho_i}{\sum_{j=1}^n S_i \rho_i}$$

ρ_i = is the density of the phase j .

Several efficient Rietveld programs are nowadays available for structure refinement; most of them are able to treat multiphase systems and can be run for QPA applications, but usually require substantial intervention by expert users. More automatic approaches are mainly supplied by commercial programs.

APPENDIX B2: Surface area and pore structure by gas adsorption

B.2.1 Introduction

A relatively great proportion of the atoms of a fine powder are at or near the surface. If, in addition, the powder particles have cracks, crevices, or pores within their structure, the proportion of exposed atoms is still greater. This causes powders to exhibit distinctly different properties from the same material in bulk form and to do so in a manner strongly dependent on the magnitude of their surface areas and the nature of their porosity. A fine powder is more reactive than the same material in bulk; it shows enhanced solubility; it sinters at lower temperature; it has more adsorptive capacity; and it exhibits greater catalytic activity. The influence is so pronounced in some instances that surface area and structure appear almost as important as chemical composition. Gas adsorption on solid surface and in the pore spaces is a complex phenomenon involving mass and energy interaction and phase changes. Depending upon the strength of the interaction, all adsorption processes can be divided into the two categories of chemical or physical adsorption. The former, also called irreversible or chemisorption, is characterized mainly by large interaction potentials, which lead to high heats of adsorption often approaching the values of chemical bonds. This fact, coupled with other spectroscopic, electron spin resonance, and magnetic susceptibility measurements confirms that chemisorption involves true chemical bonding of the gas or vapour with the surface. Because chemisorption occurs through chemical bonding it is often found to occur at temperatures above the adsorbates critical temperature. Strong bonding to the surface is necessary, in the presence of higher thermal energies, if adsorption is to occur at all. Also, as it is true for most chemical reactions, chemisorption is usually associated with an activation energy. In addition, chemisorption is necessarily restricted to, at most, a single layer of chemically bound adsorbate at the surface. Another important factor relating to chemisorption is that the adsorbed molecules are localized on the surface. Because of the formation of a chemical bond between an adsorbate molecule and a specific site on the surface the adsorbate is not free to migrate along the surface. This fact, often enables the number of active sites on catalysts to be determined by simply measuring the quantity of chemisorbed gas. The second category, reversible or physical adsorption, exhibits characteristics that makes it most suitable for surface area determinations as indicated by the following:

- Physical adsorption is accompanied by low heats of adsorption with no violent or disruptive structural changes occurring to the surface during the adsorption measurements.
- Unlike chemisorption, physical adsorption may lead to surface coverage by more than one layer of adsorbate. Thus, pores can be filled by the adsorbate for pore volume measurements.
- At elevated temperatures physical adsorption does not occur or is sufficiently slight that relatively clean surfaces can be prepared on which to make accurate surface area measurements.
- Physical adsorption equilibrium is achieved rapidly since no activation energy is required as in chemisorption. An exception here is adsorption in small pores where diffusion can limit the adsorption rate.
- Physical adsorption is fully reversible, enabling both the adsorption and desorption processes to be studied.
- Physical adsorbed molecules are not restrained to specific sites and are free to cover the entire surface. For this reason surface areas rather than number of sites can be calculated.

The kinetics and thermodynamics of adsorption have been extensively studied, but, when surface area and pore structure are the subject of interest, the investigative procedure is first to establish what is known as an adsorption (desorption) isotherm. This is a measure of the molar quantity of gas n (or standard volume V_a , or general quantity q) taken up, or released, at a constant temperature T by an initially clean solid surface as a function of gas pressure P . Most frequently the test is conducted at a cryogenic temperature, usually that of liquid nitrogen (LN_2) at its boiling point (77.35 K at one atmospheric pressure). Convention has established that the quantity of gas adsorbed is expressed as its volume at standard conditions of temperature and pressure (0°C and 760 torr and signified by STP) while the pressure is expressed as a relative pressure which is the actual gas pressure P divided by the vapour pressure P_0 of the adsorbing gas at the temperature of which the test is conducted. Plots of V_a as the ordinate against P/P_0 as the abscissa reveal much about the structure of the adsorbing material (called the adsorbent) simply from their shape. Adsorption isotherms generally follow one of six forms, the first five of which originally were assigned type number by Brunauer, Deming, Teller.¹⁶ The sixth is a recent addition;¹⁷ all are reproduced in Fig. B.6.

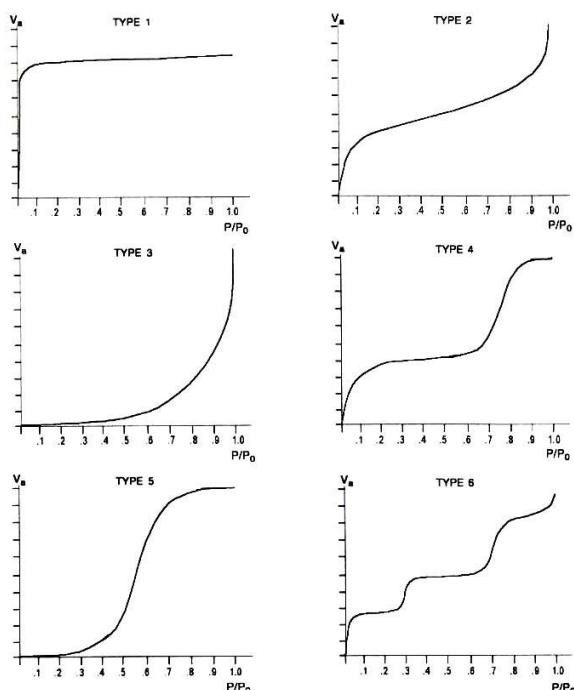


Fig. B.6: The six basis adsorption isotherm types.

○ *Type 1* isotherms are encountered when adsorption is limited to, at most, only a few molecular layers. This condition is encountered in chemisorption where the asymptotic approach to a limiting quantity indicates that all of the surface sites are occupied. In the case of physical adsorption, Type 1 isotherms are encountered with microporous powders whose pore size does not exceed a few adsorbate molecular diameters. A gas molecule, when inside pores of these small dimensions, encounters the overlapping potential from the pore walls which enhances the quantity adsorbed at low relative pressures. At higher pressures the pore are filled by adsorbed or condensed adsorbate leading to the plateau showing little or no additional adsorption after the micropores have been filled. Physical adsorption that produces the type 1 isotherm indicates that the pores are microporous and that the exposed surface resides almost exclusively within the micropores which, once filled with adsorbate, leave little or no external surface for additional adsorption.

○ *Type 2* isotherms are most frequently encountered when adsorption occurs on nonporous powder or on powders with pore diameters larger than micropores. The inflection point of the isotherm usually occurs near the completion of the first adsorbed monolayer and, with increasing relative pressure, second and higher layers are completed until at saturation the number of adsorbed layers becomes infinite.

- *Type 3* isotherms are characterized principally by heats of adsorption that are less than the adsorbate heat of liquefaction. Thus, as adsorption proceeds, additional adsorption is facilitated because the adsorbate interaction with an adsorbed layer is greater than the interaction with the adsorbent surface; condition that is valueless in surface and pore analysis.
- *Type 4* isotherms occur on porous adsorbents possessing pores in the radius range of approximately 1.5-100 nm. The slope increase at higher pressures indicates an increased uptake of adsorbate as the pores are being filled. As is true for the *Type 2* isotherms, the knee of the *Type 4* isotherm generally occurs near the completion of the first monolayer.
- *Type 5* isotherms result from small adsorbate-adsorbent interaction potentials similar to the *Type 3* isotherm. However, *Type 5* isotherms are also associated with pores in the same range as those of the *Type 4* isotherms.
- *Type 6* isotherms is indicative of a nonporous solid with a stepwise monolayer.

B.2.2 Adsorption theory and methods of extracting information from the adsorption isotherm

The success of equilibrium theories directed toward the measurements of surface areas depends upon their ability to predict the number of adsorbate molecules required to exactly cover the solid with a single molecular layer. Equally important is the cross-sectional area of each molecule or the effective area covered by each adsorbed molecule on the surface. The surface area then, is the product of the number of molecules in a completed monolayer times the effective cross-sectional area of an adsorbate molecule.

B.2.2.1 Langmuir theory

The Langmuir¹⁸ development more properly applies to chemisorption situations than to physical adsorption ones because its first assumption is that gases form only one molecular layer on a solid. Collision of a gas molecule with a solid is taken to be inelastic, so that the gas molecule remains in contact with the solid for a time before returning to the gas phase. This time delay is taken as responsible for the phenomenon of adsorption. The equation

$$V_a = \frac{V_m b P}{1 + b P} \quad (1)$$

was obtained by relating the rate at which molecule strike a surface to the rate at which they leave the surface. Here V_a is the quantity of gas adsorbed at pressure P , V_m the quantity of gas adsorbed when the entire surface is covered with a

monolayer, and b is an empirical constant. Equation (1) can be rearranged to the linear form

$$\frac{P}{V_a} = \frac{1}{V_m b} + \frac{P}{V_m} \quad (2)$$

Thus, if the equation applies and values of P/V_a are plotted against P values, a straight line should result. Some sets of data obtained using nitrogen as the adsorptive gas and adsorbing it at LN₂ temperature plot a straight line only in limited regions, allowing b and V_m to be evaluated from the slope and intercept of the line. The specific surface area S_L of the adsorbent is then calculated from V_m by

$$S_L = \frac{V_m \sigma N_A}{m V_0} \quad (3)$$

where σ is the area of surface occupied by a single adsorbed gas molecule (16.2 Å² in the case of nitrogen), N_A the Avogadro constant, m the mass of the adsorbing sample, and V_0 the molar volume of the gas. When nitrogen is the adsorptive, equation (3) becomes

$$S_L (m^2 g^{-1}) = \frac{4.35 V_m (cm^3 \text{ at STP})}{m(g)} \quad (4)$$

B.2.2.2 BET theory

A major advance in adsorption theory generalized the treatment of Langmuir and incorporated the concept of multimolecular layer adsorption. It is known as the BET theory from the surnames of its originators, Brunauer, Emmett and Teller.¹⁶ The fundamental assumption is that the forces active in the condensation of gases also are responsible for the binding energy in multimolecular adsorption. By equating the rate of the condensation of gas molecules onto an already adsorbed layer to the rate of the evaporation from that layer and summing for an infinite numbers of layers, the expression

$$V_a = \frac{V_m C P}{(P_0 - P) \left[1 + (C - 1) \frac{P}{P_0} \right]} \quad (5)$$

is obtained, where C is a constant, P_0 the saturation pressure of the gas, and other terms as previously defined. The value of C in simplest terms is

$$C \propto \exp \frac{q_1 - q_L}{RT} \quad (6)$$

where q_l is the heat of adsorption of the first layer, q_L the heat of liquefaction of the adsorptive, R the gas constant and T the absolute temperature. Equation (5) also can be written in the linear form

$$\frac{P}{V_a(P_0 - P)} = \frac{1}{V_m C} + \frac{C-1}{V_m C} \left(\frac{P}{P_0} \right) \quad (7)$$

From which, if applicable, a plot of $P/[V_a(P_0-P)]$ versus P_0/P should yield a straight line with intercept $1/V_m C$ and slope $(C-1)/V_m C$, as shown in Fig. B.7.

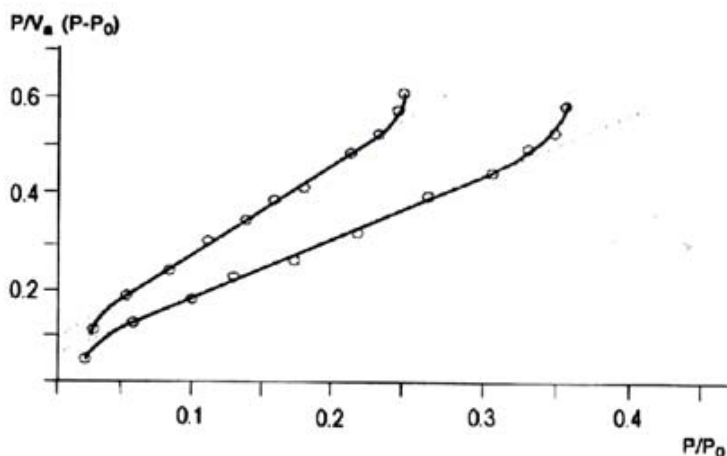


Fig. B.7: BET transform plot ,each with a regression line through the linear region.

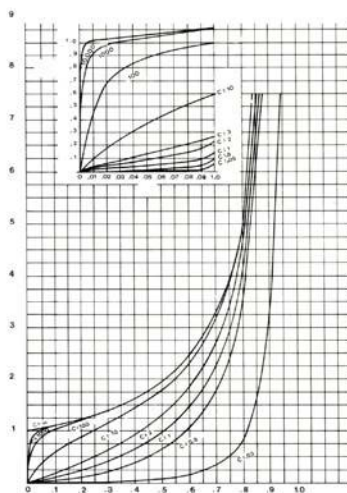


Fig. 6.8: Isotherm shapes as a function of BET C values.

The values of V_m and C may then be obtained from a plot of a straight line, or a regression line, through the points. Isotherm data for most solids when using nitrogen as the adsorptive and plotting them in accordance to equation (6) yield a

straight line between P_0/P values from about 0.05 to 0.3, but the upper limit is sometimes as low as 0.2 and occasionally even lower. The value of C is most frequently between 50 and 300 when using nitrogen at 77 K (Fig. B.8). A high or negative C value is indicative of micropores and their measurements is not amenable to analysis by this BET model without modification.

B.2.2.3 The meaning of monolayer coverage

Hill¹⁹ has shown that when sufficient adsorption has occurred to cover the surface with exactly one layer of molecules, the fraction of surface, θ_0 , not covered by any molecules is dependent on the BET C value and is given by

$$\theta_0 = \frac{C^{1/2}-1}{C-1} \quad (8)$$

From the preceding equation it is evident that when sufficient adsorption has occurred to form a monolayer there is still always some fraction of surface unoccupied. Indeed, only for C values approaching infinity will θ_0 approach zero and in such cases the high adsorbate-surface interaction can only result from chemisorption.

B.2.2.4 The BET constant and site occupancy

Equation (8) is used to calculate the fraction of surface unoccupied when $V_a=V_m$, that is, when just a sufficient number of molecules have been adsorbed to give monolayer coverage. Lowell²⁰ has derived an equation that can be used to calculate the fraction of surface covered by adsorbed molecules of one or more layers in depth. Lowell's equation is

$$(\theta_i)_m = C \left[\frac{C^{1/2}-1}{C-1} \right]^{i+1} \quad (9)$$

where θ_i represents the fraction of surface covered by layers i molecules deep. The subscript m denotes that eq. (9) is valid only sufficient adsorption has occurred to make $V_a=V_m$.

B.2.3 Methods for characterizing mesoporous and macroporous materials

Mesopores generally are defined as those having widths between 2 and 50 nm and macropores those with greater than 50 nm. It is well established that the pore space of a mesoporous solid fills with condensed adsorbate at pressure somewhat below the prevailing saturated vapour pressure of the adsorptive. When combined with a correlating function that relates pore size with critical condensation pressure, this knowledge can be used to characterize the mesopore size distribution of the

adsorbent. Adsorption studies leading to measurements of pore size and pore size distributions generally make use of the Kelvin²¹ equation which relates the equilibrium vapour pressure of a curved surface, such as that of liquid in a capillary or pore, to the equilibrium pressure of the same liquid on a plane surface. The Kelvin equation is usually written

$$\ln \left(\frac{P}{P_0} \right) = - \left(\frac{2\gamma v \cos \theta}{RT r} \right) \quad (10)$$

where P is the equilibrium vapour pressure of the liquid contained in a narrow pore of radius r and P_0 is the equilibrium pressure of the same liquid exhibiting a plane surface. The term γ and v are the liquid surface tension and the molar volume, respectively, and θ is the contact angle at which the liquid meets the pore wall. In a pore, the overlapping potentials of the walls more readily overcome the translational energy of an adsorbate molecule so that condensation will occur at a lower pressure than is normally required on an open or plane surface. Thus, as the relative pressure is increased condensation will occur first in pores of smaller radii and will progress into the larger pores until, at a relative pressure of unity, condensation will occur on those surfaces where the radius of curvature is essentially infinite. Conversely, as the relative pressure decreases, evaporation will occur progressively out of pores with decreasing radii.

Of six isotherms classification in Fig. B.6 the Types 1, 4, 5 are associated with porosity. The Type 1 isotherm usually corresponds to microporosity, that is, pores of diameters only slightly larger than adsorbate molecules. The types 4, 5 isotherms are associated with pore ranging from about 1.5-100 nm with the Type 4 isotherm far from more frequently encountered. Fig. B.9 shows the hysteresis which is typical of Type 4 isotherms.

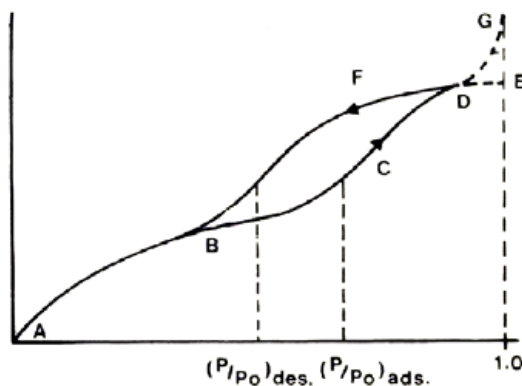


Fig. B.9: Typical Type 4 adsorption and desorption isotherms showing hysteresis.

The line BCD indicates the path traversed along the adsorption isotherm as the relative pressure is increased, whereas the line DFB shows the path followed along the desorption isotherm as the relative pressure is reduced. The presence of the hysteresis loop introduces a considerable complication, in that within the region of the hysteresis loop there are two relative pressure values corresponding to a given quantity adsorbed with the lower value always residing on the adsorption isotherm. As shown in Fig. B.9, the quantity V_a is adsorbed at a lower relative pressure on the desorption isotherm than on the adsorption curve. The pore radius corresponding to the quantity adsorbed must be single-valued and some criteria have to be established as to which value of relative pressure is to be employed in the Kelvin equation. The molar free energy change accompanying the condensation of vapour into a pore during adsorption is given by

$$\Delta G_{ads} = RT(\ln P_{ads} - \ln P_0) \quad (11)$$

For the same quantity on the desorption isotherm the corresponding free energy change

$$\Delta G_{des} = RT(\ln P_{des} - \ln P_0) \quad (12)$$

Since $P_{des} < P_{ads}$ it follows that $\Delta G_{des} < \Delta G_{ads}$, therefore, the desorption value of relative pressure corresponds to the more stable adsorbate condition and the desorption isotherm should, with certain exceptions, be used for pore size analysis. Several theories have been formulated to explain the difference between the state of the adsorbate during adsorption and desorption. Zsigmondy²² postulated that hysteresis was caused by a difference of contact angle during adsorption and desorption. McBain²³ accounted for hysteresis by assuming the pores contained a narrow opening and a wide body, the so-called “bottle-neck” shape. His model assert that during adsorption the wide inner portion of the pore is filled at high relative pressures but cannot empty until the narrow neck of the pore empties at lower relative pressure during desorption. It follows, therefore, that for “bottle-neck” pores the adsorption isotherm corresponds to the equilibrium condition. Cohan²⁴ assumed that condensation occurs by filling the pore from the wall inward which, for a cylindrical pore, would give a cylindrical shaped meniscus whereas evaporation occurs from a hemispherical meniscus once the pore is filled. Foster²⁵ explained hysteresis by considering the pores to fill by adsorption on the walls while emptying by evaporation from a spherical meniscus. These or other theories²⁶ may each describe a unique condition leading to hysteresis and indeed there may be no single mechanism that can universally explain hysteresis. De

Boer²⁷ has identified five types of hysteresis loop, as shown in Fig. B.10, which he has correlated with various pore shapes.

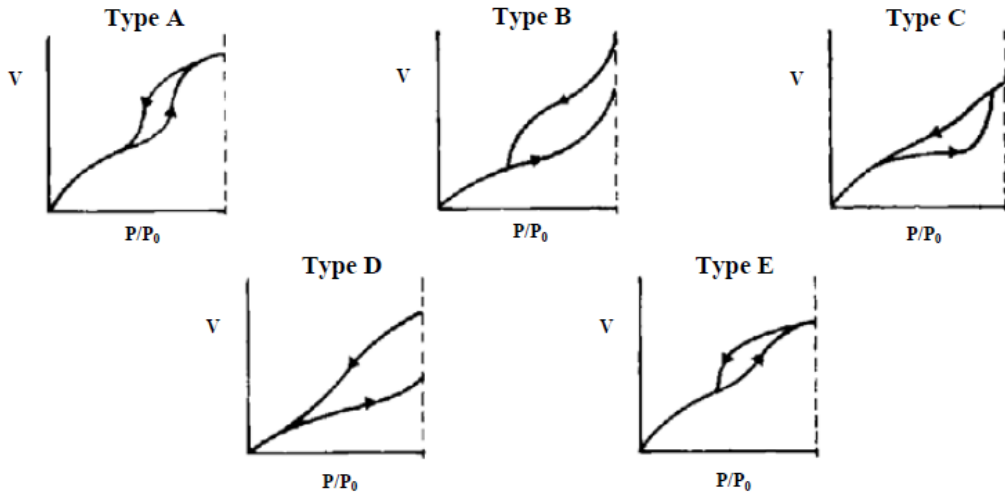


Fig. B.10: De Boer's five types of hysteresis.

- *Type A hysteresis* is due principally to cylindrical pores open at both ends (Fig. B.11). According to Cohan,⁴³ type A hysteresis is caused by condensation producing a cylindrical meniscus with one radius of curvature equal to the pore radius, less the thickness of previously condensed film, and the other radius is the length of the pore or essentially infinite.
- *Type B hysteresis* curve is associated with slit-shaped pores or the space between parallel plates.
- *Type C hysteresis* is produced by a mixture of tapered or wedge-shaped pores with open ends.
- *Type D* are also produced by tapered or wedge-shaped pores but with narrow necks at one or both open ends.
- *Type E hysteresis* results from McBain's "bottle-neck" pores. In pores of this shape, emptying of the wide portion will be delayed during desorption until the narrow neck can evaporate. Therefore, the desorption curve exhibits a small slope at high relative pressures and a large slope where the wide part of the pore evaporates.

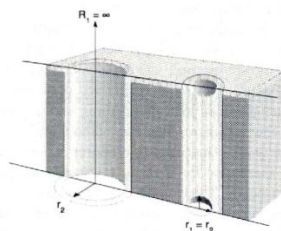


Fig. B.11: An image of cylindrical pores open at both ends.

APPENDIX B3:X-ray Photoelectron Spectroscopy

B.3.1 Introduction

Photoelectron spectroscopy^{28,29} utilizes photo-ionization and energy-dispersive analysis of the emitted photoelectrons to study the composition and electronic state of the surface region of a sample. Traditionally, when the technique has been used for surface studies it has been subdivided according to the source of exciting radiation into:

- X-ray Photoelectron Spectroscopy (XPS) using soft x-ray (200-2000 eV) radiation to examine core levels;
- Ultraviolet Photoelectron Spectroscopy (UPS) using vacuum UV (10-45 eV) radiation to examine valence levels;
- The development of synchrotron radiation sources has enabled high resolution studies to be carried out with radiation spanning a much wider and more complete energy range (5-5000 eV) but such work is, and will remain, a very small minority of all photoelectron studies due to the expense, complexity and limited availability of such sources.

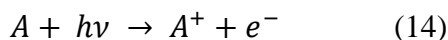
B.3.2 Physical Basis

Photoelectron spectroscopy is based upon a single photon in/electron out process and from many viewpoints this underlying process is a much simpler phenomenon than the Auger process. The energy of a photon is given by the Einstein relation:

$$E = h\nu \quad (13)$$

where h is the Planck constant (6.62×10^{-34} J s), and ν is the frequency (Hz) of the radiation. Photoelectron spectroscopy uses monochromatic sources of radiation (i.e. photons of fixed energy). In XPS the photon is absorbed by an atom in a molecule or solid, leading to ionization and the emission of a core (inner shell) electron. By contrast, in UPS the photon interacts with valence levels of the molecule or solid, leading to ionisation by removal of one of these valence electrons. The kinetic

energy distribution of the emitted photoelectrons (i.e. the number of emitted photoelectrons as a function of their kinetic energy) can be measured using any appropriate electron energy analyser and a photoelectron spectrum can thus be recorded. The process of photoionization can be considered in several ways: one way is to look at the overall process as follows



Conservation of energy then requires that:

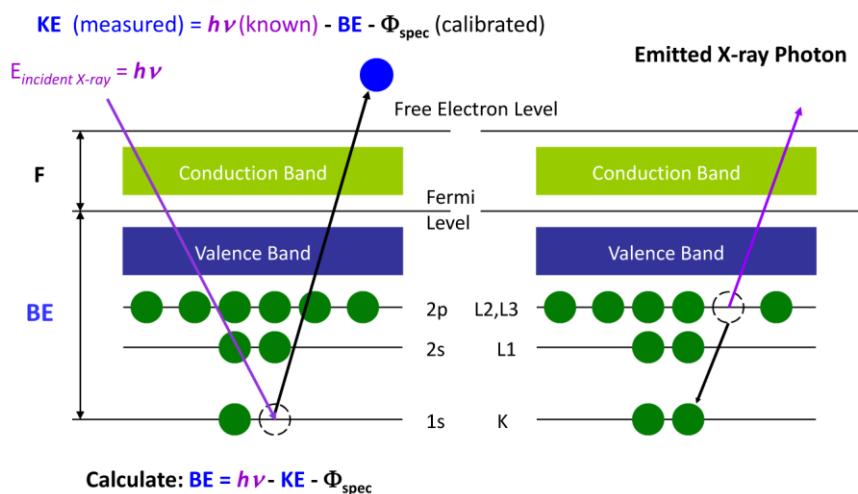
$$E(A) + h\nu = E(A^+) + E(e^-) \quad (15)$$

Since the electron's energy is present solely as kinetic energy (KE) this can be rearranged to give the following expression for the KE of the photoelectron:

$$KE = h\nu - E(A^+) - E(A) \quad (16)$$

The final term in brackets, representing the difference in energy between the ionized and neutral atoms, is generally called the *binding energy* (BE) of the electron; this then leads to the following commonly quoted equation:

$$KE = h\nu - BE \quad (17)$$



BE – binding energy depends on Z, i.e. characteristic for the element

Fig. B.12: The electron energy levels.

The BE is now taken to be a direct measure of the energy required to just remove the electron concerned from its initial level to the vacuum level and the KE of the photoelectron is again given by eq. (16). The *binding energies* (BE) of energy levels in solids are conventionally measured with respect to the Fermi-level of the

solid, rather than the vacuum level. This involves a small correction to the equation given above in order to account for the work function (Φ) of the solid, but for the purposes of the discussion below this correction will be neglected.

B.3.3 XPS: the general features

The basic requirements for a photoemission experiment (XPS or UPS) are:

- a source of fixed-energy radiation (an X-ray source for XPS or, typically, a He discharge lamp for UPS);
- an electron energy analyser (which can disperse the emitted electrons according to their kinetic energy, and thereby measure the flux of emitted electrons of a particular energy);
- a high vacuum environment (to enable the emitted photoelectrons to be analysed without interference from gas phase collisions).

Such a system is illustrated schematically in Fig. B.13. There are many different designs of electron energy analyser but the preferred option for photoemission experiments is a concentric hemispherical analyser (CHA) which uses an electric field between two hemispherical surfaces to disperse the electrons according to their kinetic energy.^{28,29}

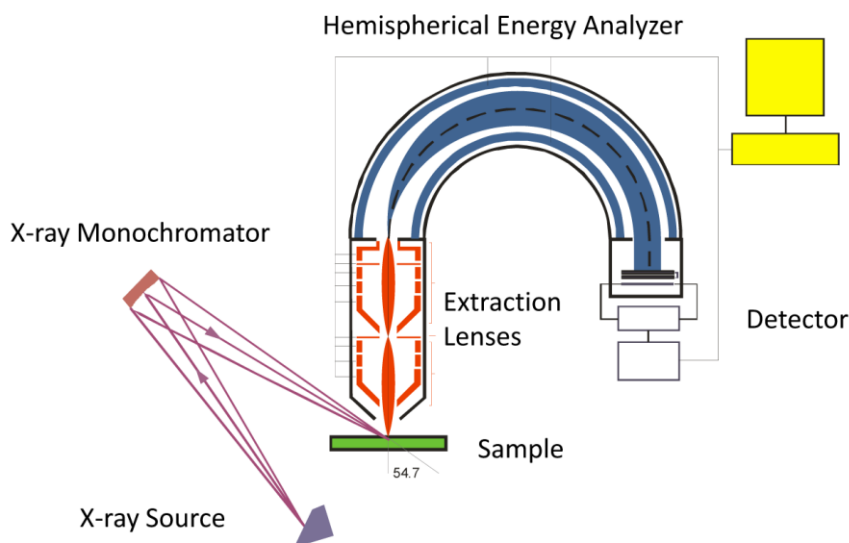


Fig. B.13: The scheme of the instrument.

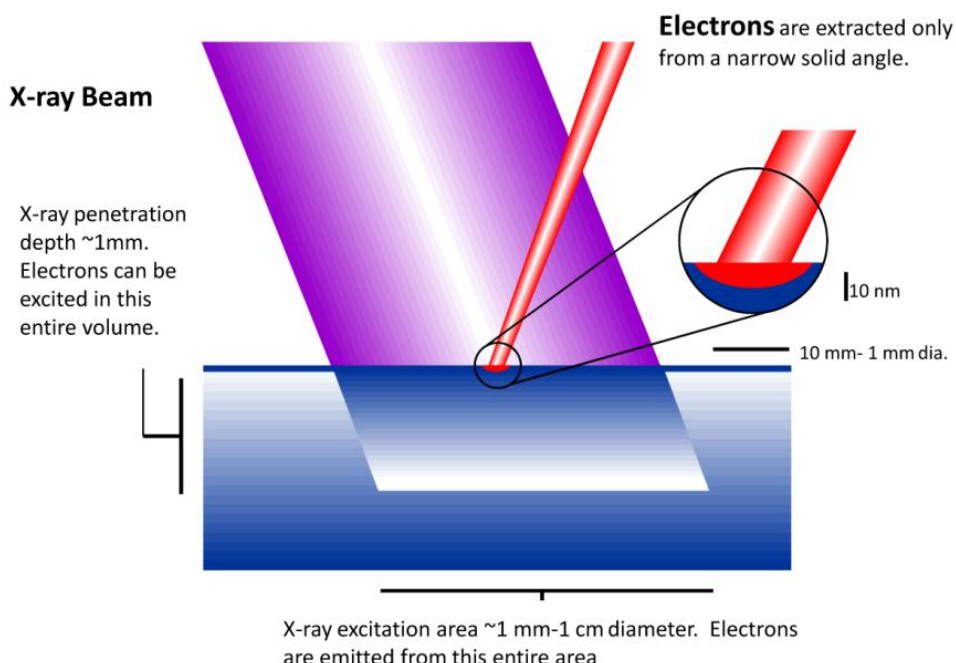


Fig B.14: *electrons extraction from the solid excited from the X-ray source.*

For each and every element, there will be a characteristic binding energy associated with each core atomic orbital i.e. each element will give rise to a characteristic set of peaks in the photoelectron spectrum at kinetic energies determined by the photon energy and the respective binding energies. The presence of peaks at particular energies therefore indicates the presence of a specific element in the sample under study. Furthermore, the intensity of the peaks is related to the concentration of the element within the sampled region. Thus, the technique provides a quantitative analysis of the surface composition and is sometimes known by the alternative acronym, ESCA (Electron Spectroscopy for Chemical Analysis). The most commonly employed X-ray sources are those giving rise to:

- Mg K_{α} radiation: $h\nu = 1253.6 \text{ eV}$
- Al K_{α} radiation: $h\nu = 1486.6 \text{ eV}$

The emitted photoelectrons will therefore have kinetic energies in the range of ca. 0- 1250 eV or 0-1480 eV. Assuming inelastic scattering only, from the Lambert-Beer equation can be deduced that the maximum path an electron can travel is of a few nm (Fig 6.14).

B.3.4 Spin-Orbit Splitting

The emission from some levels (most obviously $3p$ and $3d$) does not give rise to a single photoemission peak, but a closely spaced doublet. It is possible to underline this more clearly if, for example, we consider the spectrum of Pd in the region of the $3d$ emission, as shown as in Fig. B.15.

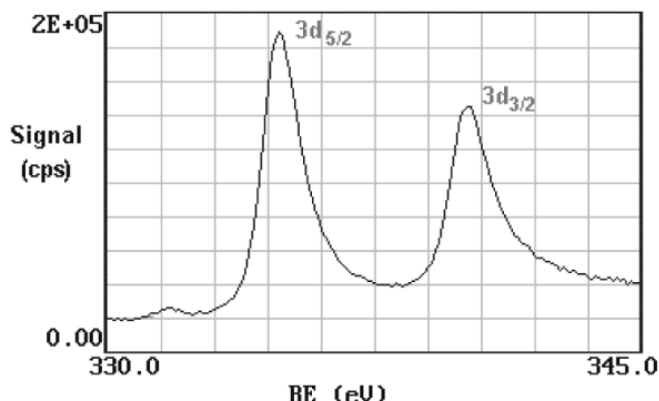


Fig. B.15: XPS experimental spectra of a Pd metal sample in the region of $3d$ emission.

The $3d$ photoemission is in fact split between two peaks, one at 334.9 eV BE and the other at 340.2 eV BE, with an intensity ratio of 3:2. This arises from spin-orbit coupling effects in the final state. The inner core electronic configuration of the initial state of the Pd is $(1s)^2(2s)^2(2p)^6(3s)^2(3p)^6(3d)^{10}....$ with all sub-shells completely full. The removal of an electron from the $3d$ sub-shell by photo-ionization leads to a $(3d)^9$ configuration for the final state; since the d -orbitals ($l = 2$) have non-zero orbital angular momentum, there will be coupling between the unpaired spin and orbital angular momenta. Spin-orbit coupling is generally treated using one of two models which correspond to the two limiting ways in which the coupling can occur; these being the LS (or *Russell-Saunders*) coupling approximation and the $j-j$ coupling approximation. If consider the final ionised state of Pd within the *Russell-Saunders* coupling approximation, the $(3d)^9$ configuration gives rise to two states (ignoring any coupling with valence levels) which differ slightly in energy and in their degeneracy:

$$^2D_{5/2} \quad g_J = 2x \left\{ \frac{5}{2} \right\} + 1 = 6 \quad (18)$$

$$^2D_{3/2} \quad g_J = 2x \left\{ \frac{3}{2} \right\} + 1 = 4 \quad (19)$$

These two states arise from the coupling of the $L = 2$ and $S = 1/2$ vectors to give permitted J values of $3/2$ and $5/2$. The lowest energy final state is the one with maximum J (since the shell is more than half-full), i.e. $J = 5/2$, hence this gives rise

to the "lower binding energy" peak. The relative intensities of the two peaks reflects the degeneracies of the final states ($g_J = 2J + 1$), which in turn determines the probability of transition to such a state during photoionization.

The Russell-Saunders coupling approximation is best applied only to light atoms and this splitting can alternatively be described using individual electron l - s coupling. In this case the resultant angular momenta arise from the single hole in the d -shell; a d -shell electron (or hole) has $l = 2$ and $s = 1/2$, which again gives permitted j -values of $3/2$ and $5/2$ with the latter being lower in energy (Fig. B.15). This spin-orbit splitting is of course not evident with s -levels ($l = 0$), but is seen with p , d and f core-levels which all show characteristic spin-orbit doublets.

B.3.5 Chemical Shifts

The exact binding energy of an electron depends not only upon the level from which photoemission is occurring, but also upon:

- the formal oxidation state of the atom;
- the local chemical and physical environment.

Changes in this conditions give rise to small shifts in the peak positions in the spectrum - so- called *chemical shifts*. An example of the effect of the oxygen on the C $1s$ binding energy is reported in Fig. B.16.

Electronegativity Effects

Carbon-Oxygen Bond

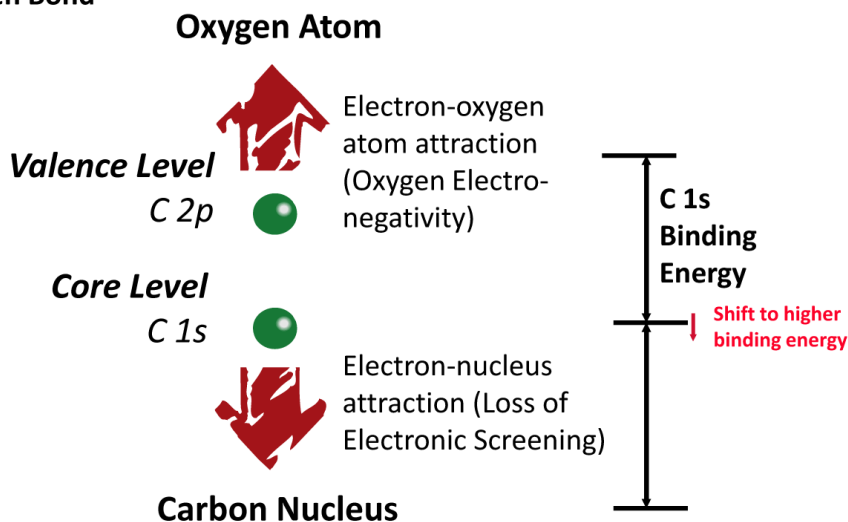


Fig B.16: electronegativity effects on the C $1s$ binding energy.

Tab B.2: Effect of functional groups on the shift of the BE of C 1s.

Functional Group		C 1s Binding Energy (eV)
hydrocarbon	<u>C</u> -H, <u>C</u> -C	285.0
amine	<u>C</u> -N	286.0
alcohol, ether	<u>C</u> -O-H, <u>C</u> -O-C	286.5
Cl bound to C	<u>C</u> -Cl	286.5
F bound to C	<u>C</u> -F	287.8
carbonyl	<u>C</u> =O	288.0

APPENDIX B4: Scanning Electron Microscopy

B.4.1 Introduction

The scanning electron microscope (SEM) is a type of electron microscope that images the sample surface by scanning it with a high-energy beam of electrons in a raster scan pattern. The electrons interact with the atoms that make up the sample producing signals that contain information about the sample's surface topography, composition and other properties such as electrical conductivity. The types of signals produced by an SEM include secondary electrons, back-scattered electrons (BSE), characteristic X-rays, light (cathodoluminescence), specimen current and transmitted electrons. Secondary electron detectors are common in all SEMs, but it is rare that a single machine would have detectors for all possible signals. The signals result from interactions of the electron beam with atoms at or near the surface of the sample. In the most common or standard detection mode, secondary electron imaging or SEI, the SEM can produce very high-resolution images of a sample surface, revealing details about less than 1 to 5 nm in size. Due to the very narrow electron beam, SEM micrographs have a large depth of field yielding a characteristic three-dimensional appearance useful for understanding the surface structure of a sample. This is exemplified by the micrograph of pollen shown to the right. A wide range of magnifications is possible, from about 10 times (about equivalent to that of a powerful hand-lens) to more than 500,000 times, about 250 times the magnification limit of the best light microscopes. Back-scattered electrons (BSE) are beam electrons that are reflected from the sample by elastic scattering. BSE are often used in analytical SEM along with the spectra made from the characteristic X-rays. Because the intensity of the BSE signal is strongly related to the atomic number (Z) of the specimen, BSE images can provide information about the distribution of different elements in the sample. For the same reason, BSE imaging can image colloidal gold immuno-labels of 5 or 10 nm diameter which would otherwise be difficult or impossible to detect in secondary electron images in biological specimens. Characteristic X-rays are emitted when the electron beam removes an inner shell electron from the sample, causing a higher energy electron to fill the shell and release energy. These characteristic X-rays are used to identify the composition and measure the abundance of elements in the sample.

B.4.2 How does the SEM work?

In a typical SEM (schematic representation in Fig. B.17) an electron beam is thermionically emitted from an electron gun fitted with a tungsten filament cathode

(*W-Hairpin*). Tungsten is normally used in thermionic electron guns because it has the highest melting point and lowest vapour pressure of all metals, thereby allowing it to be heated for electron emission, and because of its low cost. Other types of electron emitters include lanthanum hexaboride (LaB_6) cathodes, which can be used in a standard tungsten filament SEM if the vacuum system is upgraded and field emission guns (FEG), which may be of the cold-cathode type using tungsten single crystal emitters or the thermally-assisted Schottky type, using emitters of zirconium oxide.

The electron beam, which typically has an energy ranging from 0.5 keV to 40 keV, is focused by one or two condenser lenses to a spot about 0.4 nm to 5 nm in diameter. The beam passes through pairs of scanning coils or pairs of deflector plates in the electron column (B.18), typically in the final lens, which deflect the beam in the x and y axes so that it scans in a raster fashion over a rectangular area of the sample surface.

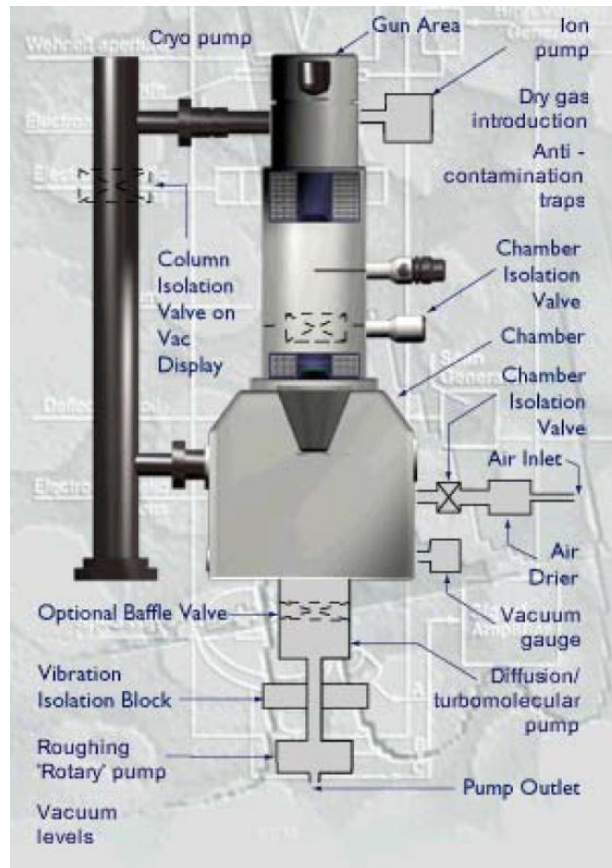


Fig. B.17: schematic representation of all the structural elements of a SEM.

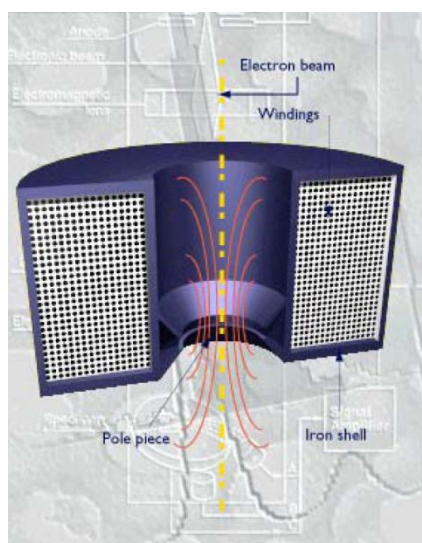


Fig B.18: *schematic representation of the deflection of the electron passing through a SEM electron column.*

When the primary electron beam interacts with the sample, the electrons lose energy by repeated random scattering and absorption within a teardrop-shaped volume of the specimen known as the interaction volume, which extends from less than 100 nm to around 5 μm into the surface. The size of the interaction volume depends on the electron's landing energy, the atomic number of the specimen and the specimen's density. The energy exchange between the electron beam and the sample results in the reflection of high-energy electrons by elastic scattering, emission of secondary electrons by inelastic scattering and the emission of electromagnetic radiation, each of which can be detected by specialized detectors. The beam current absorbed by the specimen can also be detected and used to create images of the distribution of specimen current. Electronic amplifiers of various types are used to amplify the signals which are displayed as variations in brightness on a cathode ray tube. The raster scanning of the CRT display is synchronized with that of the beam on the specimen in the microscope, and the resulting image is therefore a distribution map of the intensity of the signal being emitted from the scanned area of the specimen. The image may be captured by photography from a high resolution cathode ray tube, but in modern machines is digitally captured and displayed on a computer monitor and saved to a computer's hard disk

B.4.3 Sample preparation

For conventional imaging in the SEM, specimens must be electrically conductive, at least at the surface, and electrically grounded to prevent the accumulation of electrostatic charge at the surface. Metal objects require little special preparation

for SEM except for cleaning and mounting on a specimen stub. Nonconductive specimens tend to charge when scanned by the electron beam, and especially in secondary electron imaging mode, this causes scanning faults and other image artifacts. They are therefore usually coated with an ultrathin coating of electrically-conducting material, commonly gold, deposited on the sample either by low vacuum sputter coating or by high vacuum evaporation. Conductive materials in current use for specimen coating include gold, gold/palladium alloy, platinum, graphite, etc. Coating prevents the accumulation of static electric charge on the specimen during electron irradiation. Two reasons for coating, even when there is enough specimen conductivity to prevent charging, are to increase signal and surface resolution, especially with samples of low atomic number (Z). The improvement in resolution arises because backscattering and secondary electron emission near the surface are enhanced and thus an image of the surface is formed. Non conducting specimens may be imaged uncoated using specialized SEM instrumentation such as the "Environmental SEM" (ESEM) or field emission gun (FEG) SEMs operated at low voltage. Environmental SEM instruments place the specimen in a relatively high pressure chamber where the working distance is short and the electron optical column is differentially pumped to keep vacuum adequately low at the electron gun. The high pressure region around the sample in the ESEM neutralizes charge and provides an amplification of the secondary electron signal. Low voltage SEM of non-conducting specimens can be operationally difficult to accomplish in a conventional SEM and is typically a research application for specimens that are sensitive to the process of applying conductive coatings. Low-voltage SEM is typically conducted in an FEG-SEM because the FEG is capable of producing high primary electron brightness even at low accelerating potentials. Operating conditions must be adjusted such that the local space charge is at or near neutral with adequate low voltage secondary electrons being available to neutralize any positively charged surface sites. This requires that the primary electron beam's potential and current be tuned to the characteristics of the sample specimen.

B.4.4 X-Ray microanalysis

B.4.4.1 Introduction

X-ray microanalysis and digital image analysis are powerful, yet easy to use, techniques for revealing information from a small area of a specimen. X-ray microanalysis in an electron beam instrument such as a scanning electron microscope is capable of analyzing elements heavier than or equal to beryllium with spatial resolution of a few cubic micrometers. Although there are other

microanalytical techniques each with its own specific advantages, none are better than X-ray microanalysis for routine chemical analysis of small volumes. When X-ray analysis is combined with digital image analysis, one has a potent tool for understanding the composition and structure of materials or biological specimens.

The technique consists of detecting the characteristic X-rays that are produced by bombarding a solid specimen with high-energy electrons. Detection of these X-rays can be accomplished by an energy dispersive spectrometer, which is a solid-state device that discriminates among X-ray energies. Or it can be done with a crystal spectrometer that uses a diffracting crystal to select the wavelength of interest. The former method is called *energy-dispersive spectroscopy (EDS)*, and the latter is called wavelength-dispersive spectroscopy (WDS), referring to the manner in which X-rays are distinguished.

It is possible to use either technique on any electron beam instrument capable of forming a probe;

however, WDS is used primarily on electron microprobes, while EDS is dominant on scanning and transmission electron microscopes, including analytical electron microscopes. Both spectroscopic methods are capable of performing analysis of elements beginning with beryllium or boron in the periodic table, provided a suitable light element X-ray window is used.

The low-energy limit is determined by the entrance window material and interference from noise, and the high-energy limit is determined by the energy in the electron beam.

One feature of electron beam microanalysis that describes the power of the technique is its absolute

mass sensitivity. For example, it is often possible to detect less than 10^{-19} grams of an element in a thin sample and less than 10^{-13} grams in a microvolume of a bulk sample. Suitable quantification routines are available to convert the raw X-ray counts into elemental concentration, by use of standards or standardless methods. Moreover, since it is performed on a microscope, the chemical analysis can be related to other imaging signals and thus is complementary to image analysis.

X-ray microanalysis is routinely used by materials scientists for both qualitative and quantitative analysis of microstructures. It is also used by biologists to localize elements such as calcium, potassium and phosphorus, and to measure their concentration.

B.4.4.2 Electron-specimen interaction and X-ray generation

B.4.4.2.1 Electron scattering

Electrons in the primary beam can interact with atoms in the specimen in many ways, which can be used to gain information through spectroscopy. These interactions can be divided into elastic and inelastic scattering of the electrons. Elastic scattering refers to a change in trajectory without loss of energy. Backscattering of electrons, for example, is such an event. Inelastic scattering refers to a loss of energy of the electron with little change of direction. The production of secondary electrons, X-rays (both characteristic and continuum), and Auger electrons, for example, are such events.

When an electron of sufficient energy strikes an atom, an inner shell electron may be ejected. To return the atom to its lowest energy state, an outer shell electron (of greater energy) fills the vacancy in the lower energy shell. In so doing, energy equal to transitions that occur within the atom is released either as an X-ray or Auger electron. The rest of the energy is deposited by other inelastic interactions with the specimen such as continuum X-ray generation and phonon excitation resulting in specimen heating.

B.4.4.2.2 Ionization Cross Section

The probability that an energetic electron will ionize an atom depends on the atom, the line to be excited, and the overvoltage. For high overvoltages, the probability (ionization cross section) can be quite small; consequently, few atoms are ionized, thus few X-rays or Auger electrons are produced. The units of cross section are area, usually cm^2 , but this concept should not be confused with atomic or ionic radius.

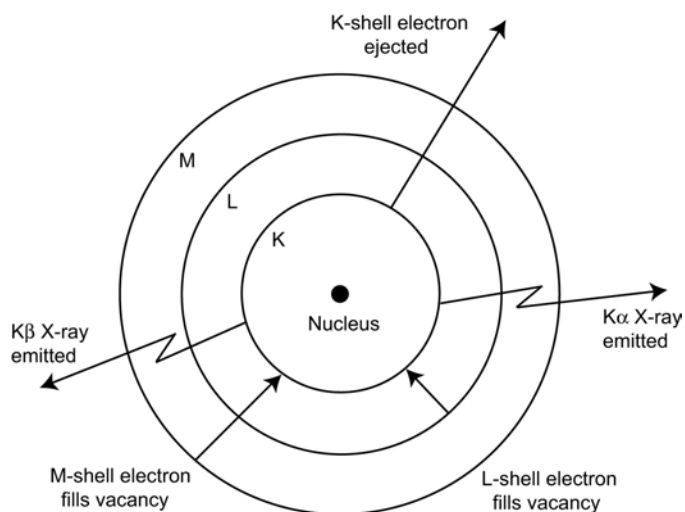


Fig. B.19: X-ray production using Bohr model of the atom.

B.4.4.2.3 Characteristic X-rays

Figure 6.19 illustrates characteristic X-ray generation using a simplified model of the atom. When an electron of sufficient energy, commonly a few kilovolts, strikes the atom and ejects a tightly bound *K*-shell electron, an electron from a higher shell may drop to fill the *K*-shell. When this happens, for example, an *L*-shell electron may drop to fill the *K*-shell, lowering the energy of the atom and emitting *Kα* X-radiation in the process. If an electron from the *M*-shell fills the *K*-shell vacancy, *Kβ* X-radiation will be emitted. Similarly, if an *L*-shell electron is ejected and an electron from the *M*-shell fills the vacancy, *L* radiation will be emitted. Within a given shell, there may be electrons in orbitals that do not possess exactly the same energy because of bonding effects. Accordingly, small variations in energy called chemical shifts occur within *α* or *β* radiation. The *Kα* peak actually comprises the *Kα1* and *Kα2* X-rays. These are very close together and unresolved in an EDS system so that a *Kα1,2* doublet is seen as the *Kα* peak at an energy between the two individual components and an intensity corresponding to a weighted average as follows:

$$\frac{2K\alpha_1 + 1K\alpha_2}{3} \quad (20)$$

The most probable transition when a *K*-shell vacancy is created is the *L* to *K* transition, because these are adjacent energy shells. Therefore *Kα* radiation will always be more intense than *Kβ* radiation. It also follows that *Kβ* radiation will be of higher energy than *Kα* radiation, inasmuch as the energy difference between the *M* and *K* shells (*Kβ* radiation) is greater than the energy difference between the *L* and *K* shells (*Kα* radiation). To ionize an atom, the incoming electron or ionizing radiation must possess a minimum amount of energy. That energy is the binding energy of the particular inner shell electron, which is a specific, characteristic energy for each electron in the atom. The binding energy for a *K*-shell electron, for example, is greater than that of an *L*-shell electron, since the *K*-shell electron is closer to the nucleus and more tightly bound. Therefore, if sufficient energy exists in the incident beam to excite *K* X-rays, *L* and *M* X-rays will also be excited if these shells and the one above them are occupied. The discrete and specific energy requirement necessary to excite any given X-ray line is called the absorption edge energy, or critical excitation potential. It is always slightly greater in energy than the corresponding X-ray emission line. As a consequence, one must select an accelerating voltage on the microscope that is greater than the absorption edge energy of the line intended for analysis. In practice, one must exceed this minimum energy by a comfortable margin, preferably by a factor of 1.5 to 3, to efficiently

excite the X-ray line with an electron beam. The energy difference between adjacent electron shells becomes less, progressing outward from the nucleus. It follows that the energy released upon electron transitions between adjacent shells in the outer shells is less than that released for inner shell transitions. That is, for a given atom, $M\alpha$ radiation will be of lower energy than $L\alpha$ radiation, which in turn will be of lower energy than $K\alpha$ radiation.

B.4.4.2.4 Moseley's Law

The energy of the characteristic radiation within a given series of lines varies monotonically with atomic number. This is Moseley's Law (Moseley, 1913), expressed by Equation 21:

$$\sqrt{E} = C_1(Z - C_2) \quad (21)$$

where E = energy of the emission line for a given X-ray series (e.g. $K\alpha$), Z = atomic number of the emitter C_1 and C_2 are constants.

For qualitative chemical analysis, if the energy of a given K , L or M line is measured, then the atomic number of the element producing that line can be determined. The energies for K , L and M lines are plotted as a function of atomic number in Fig. B.20 Figure B.21 shows a series of K lines from Na to Zn in which the intensities are typical of what one would see in an EDS spectrum.

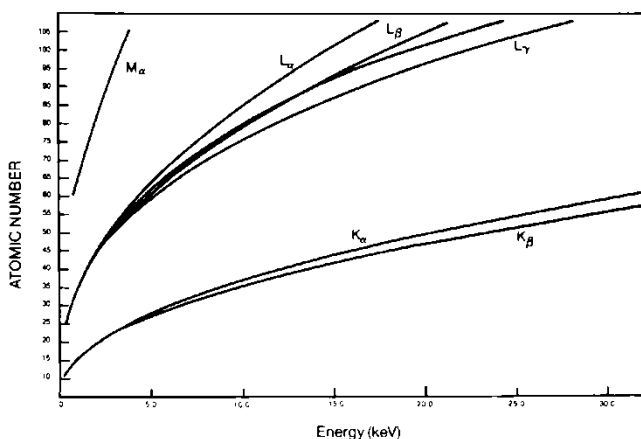


Fig. B.20: Variation of energy of characteristic X-ray lines as a function of atomic number.

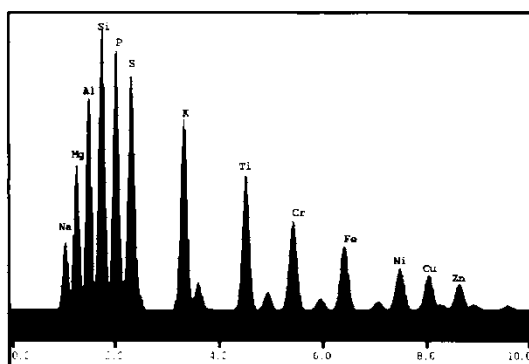


Fig. B.21: Synthetic EDS spectrum showing the relative intensities of the $K\alpha$ lines of elements from Na to Zn.

B.4.4.2.5 Continuum Generation

Besides characteristic X-rays, inelastic scattering of the beam electrons produces continuum X-rays. When electrons strike solids, they can undergo a deceleration in steps, with each deceleration causing the emission of an X-ray with an energy equal to that lost by the electron. The range of energies of these X-rays is from nearly zero to the maximum energy of the electron beam. This latter energy is called the short wavelength limit (SWL), or the Duane-Hunt limit. This type of radiation is called continuous or white radiation. The white radiation spectrum is called the continuum or Bremsstrahlung, meaning “braking radiation.” The continuum is the major source of background in the electron beam-excited X-ray spectrum. And this background under the characteristic peaks consists of real X-rays detected at the crystal, not electronic noise. Continuum X-rays are detected up to the beam energy, which in intermediate voltage electron microscopes can be 300 or 400 keV. Just because the microanalysis system is not calibrated beyond 20 or 30 keV, or the display shows 0-10 keV, does not mean that these X-rays are not being detected and processed by the pulse processing system, and contributing to dead time. Fig. B.22 shows a spectrum measured on pure molybdenum represented in black superimposed on the continuum shown in gray.

Note the presence of a sharp change in the continuum intensity at approximately 2.6 keV. This sudden change is due to the significant difference in ability of Mo atoms to absorb X-rays above and below the critical excitation potential (absorption edge) for the Mo L line. The intensity of the continuum generated at any energy is directly proportional to atomic number and beam energy. But the shape of the background seen in the spectrum includes the detector efficiency and detector-specimen geometrical effects.

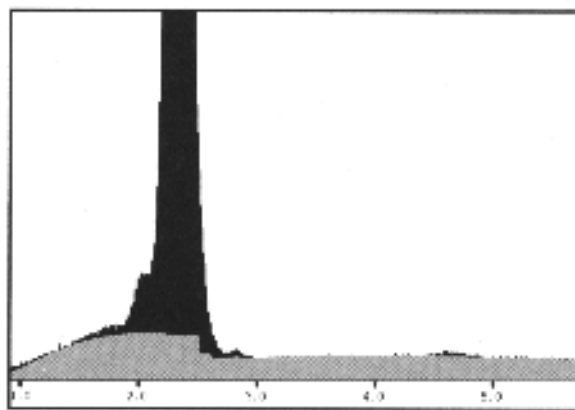


Fig. B.22: Spectrum of molybdenum showing $L\alpha$ line superimposed on the continuum showing L absorption edges.

B.4.4.3 Energy Dispersive Spectroscopy

In an energy dispersive spectrometer, X-rays of all energies are detected by a detecting material, most commonly a lithium-drifted silicon ($\text{Si}(\text{Li})$) crystal. On their way to the detecting crystal, X-rays may be absorbed by a window, a metallic contact layer on the crystal and a silicon dead layer. The active area in the silicon crystal is typically 10 mm^2 or 30 mm^2 , though it may be larger, such as 60 or 80 mm^2 , and it is about $3\text{--}5 \text{ mm}$ thick. The X-rays produce charge pulses in the crystal that are proportional to their energy, and X-rays of all energies are detected virtually simultaneously. In Si , an electron-hole pair is created for every 3.76 eV of incoming X radiation. For a germanium detector, the number is 2.96 eV . EDS detectors require no focusing of the X-rays, so all are detected if they are present within the solid angle subtended by the crystal. The electron-hole pairs created by the incoming X-rays are swept away by the bias voltage of several hundred volts and converted to a voltage pulse in the FET located within the X-ray detector. The pulse then enters the external stages of the preamplifier.

Although $\text{Si}(\text{Li})$ and HpGe are the most common EDS detectors, others are used, though they are seen infrequently in X-ray microanalysis applications.

A photograph of a typical EDS spectrometer is shown in Fig. B.23, in which the most prominent feature is the liquid nitrogen dewar. A field-effect transistor (FET) is located directly behind the detecting crystal and provides the first stage of signal amplification. The actual charge induced in the detector is extremely small. Therefore, to minimize noise, the FET must be located as close to the detector as possible, and must be operated at liquid nitrogen temperature (except in the case of a silicon drift detector). To achieve the required temperature, the detector and FET are connected through an efficient heat conductor to a liquid nitrogen Dewar. The

metal tube housing the detector assembly and cold finger is called the endcap, which must be evacuated to prevent heat loss through its walls.



Fig. B.23: Energy-dispersive spectrometer.

A very thin window of low atomic number material is used to enclose the endcap to ensure its vacuum integrity while providing high X-ray transmission. This window may be 7.5 μm beryllium or $<0.25 \mu\text{m}$ carbon- or boron-based material. Completely windowless detectors are also available, but these must have a window that can be closed for sample changes in the microscope.

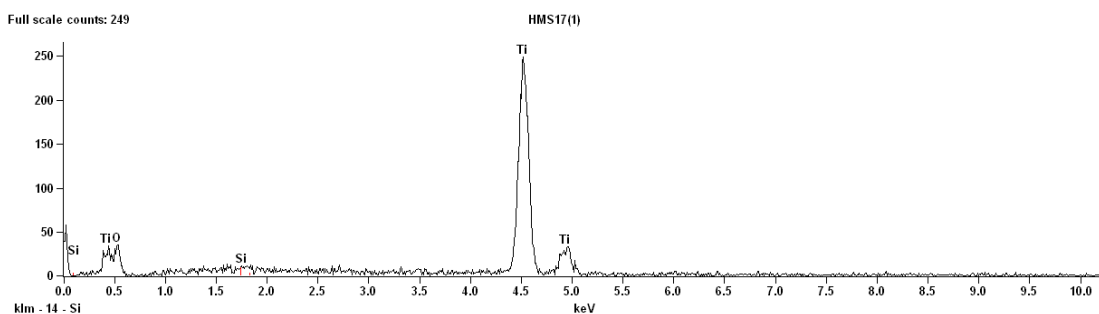


Fig. B.24: a representative EDS spectrum of nanostructured TiO_2 microsphere.

APPENDIX B5: Transmission Electron Microscopy

The transmission electron microscope (TEM-see Fig. B.25-B.26) operates on the same basic principles as the light microscope but uses electrons instead of light. A light microscope is limited by the wavelength of light, instead TEMs use electrons as "light source" and their much lower wavelength makes it possible to get a resolution a thousand times better than with a light microscope. You can see objects to the order of a few angstrom (10^{-10} m). For example, you can study small details in the cell or different materials down to near atomic levels. The possibility for high magnifications has made the TEM a valuable tool in both medical, biological and materials research. A "light source" at the top of the microscope emits the electrons that travel through vacuum in the column of the microscope. Instead of glass lenses focusing the light in the light microscope, the TEM uses electromagnetic lenses to focus the electrons into a very thin beam. The electron beam then travels through the specimen you want to study. Depending on the density of the material present, some of the electrons are scattered and disappear from the beam. At the bottom of the microscope the unscattered electrons hit a fluorescent screen, which gives rise to a "shadow image" of the specimen with its different parts displayed in varied darkness according to their density. The image can be studied directly by the operator or photographed with a camera.

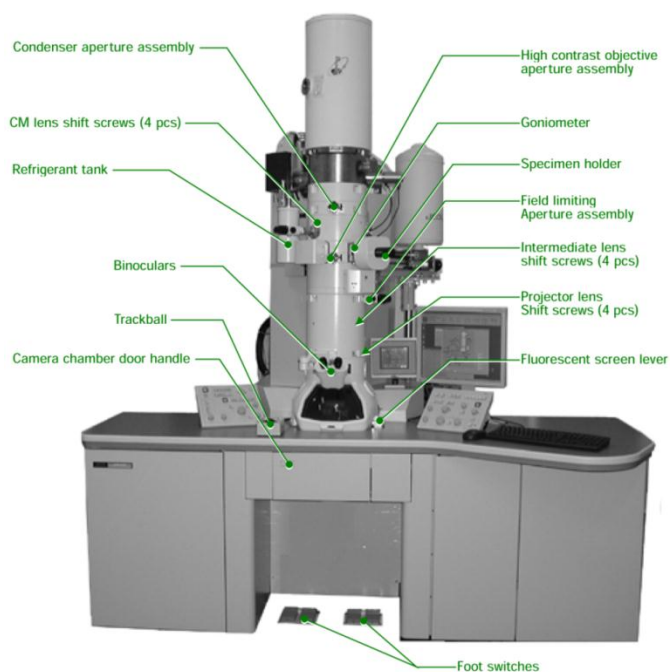


Fig. B.25: A picture of a typical TEM apparatus.

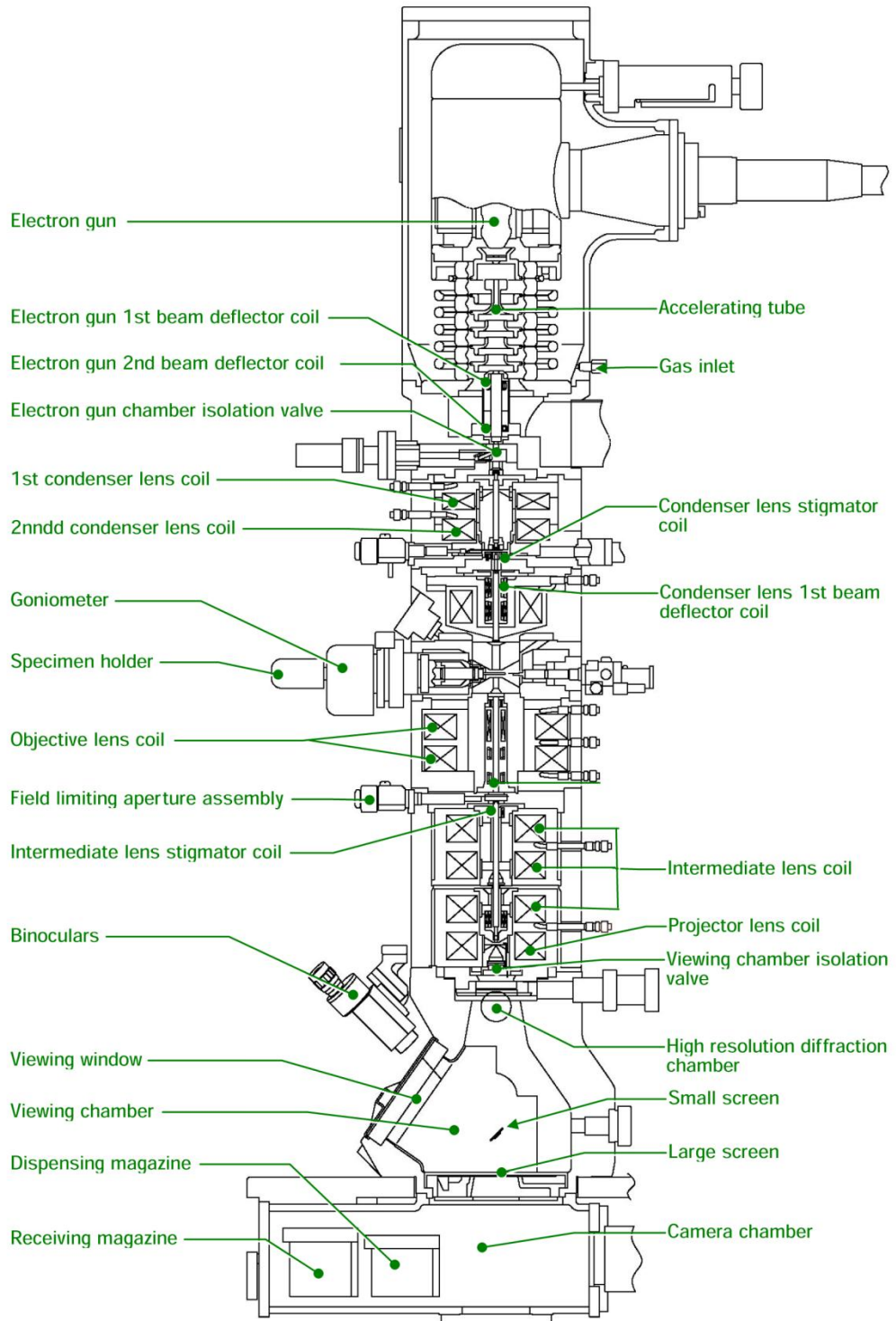


Fig. B.26: a schematic representation of all components inside a transmission electron microscope.

APPENDIX B6: Others characterization techniques

Many other characterization techniques have been employed to analyse the physico-chemical properties of nanomaterials in the research works presented:

- Diffuse Reflectance Infrared Fourier Transformed Spectroscopy (DRIFTS)
- Electron Paramagnetic Resonance (EPR) Spectroscopy
- UV-Vis Diffuse Reflectance Spectroscopy (DRS)
- UV-Vis Spectroscopy
- Total Organic Carbon (TOC) analysis
- High Performance Liquid Chromatography (HPLC)
- Micro Hardness measurements
- Thermogravimetric analysis (TGA)
- Chemiluminescent analyser for NO_x determination

APPENDIX B7: References

- [1] David, W.I.F.; Shankland, K.; McCusker, L.B.; Baerlocher C. *Structure Determination from Powder Diffraction Data* Oxford Science Publications **1992**.
- [2] Bish, D.L.; Post, J.E. *Modern Powder Diffraction* published by The Mineralogical Society of America.
- [3] Azaroff, L.V.; Buerger, M.J. *The Powder Method in X-ray Crystallography* McGraw Hill Book Company, Inc, **1975**.
- [4] Buerger, M.J.; X-ray Crystallography J. Wiley, New York, **1942**, 20.
- [5] Cheetam, A.K.; Wilkinson, A.P.; *Angew. Chemie Int. Ed. Engl.* **1992**, 31, 1557.
- [6] Harris, K.D.M. *Tremayne Chern. Mater.* **1996**, 8, 2554.
- [7] Langford, J.I.; Louer, D.; *Rep. Progr. Phys.* **1996**, 59, 131.
- [8] Poorjay, D.M.; Clearfield, A. *Acc. Chern. Res.* **1997**, 30, 414.
- [9] Harris, K.D.M.; Tremayne, M.; Kariuki, B.M.; *Angew. Chemie Int. Ed.* **2001**, 40, 1626.
- [10] Rietveld, H.M. *J. Appl. Cryst.* **1969**, 2, 65.
- [11] McCusker, L.B.; Von Dreele, R.B.; Cox, D.E.; Louer, D.; Scardi, P. *J. Appl. Cryst.*, **1999**, 32, 36.
- [12] Hill, R.J.; Howard, C.J. *J. Appl. Cryst.* **1987**, 20, 467.
- [13] Altomare, A.; Burla, M.C.; Giacovazzo, C.; Guagliardi, A.; Moliterni, A.G.G.; Polidori, G.; Rizzi, R. *J. Appl. Cryst.* **2001**, 34, 392.
- [14] Bish, D.L.; Howard, S.A. *J. Appl. Cryst.* **1988**, 21, 86.
- [15] Hill, R.J.; Howard, C.J. *J. Appl. Cryst.* **1987**, 20, 467.
- [16] Brunauer, S.; Emmet, P.H.; Teller, E. *J. Am. Chem. Soc.* **1938**, 60, 309.
- [17] Webb, P.A.; Orr, C. *Analytical Methods in Fine Particle Technology* Micromeritics Instrument Corporation, Norcross, USA, **1997**.
- [18] Langmuir, I. *J. Am. Chem. Soc.* **1918**, 40, 1631.
- [19] Hill, T.L.; *J. Chem. Phys.* **1946**, 14, 268.
- [20] Lowell, S. *Powder Technol.* **1975**, 12, 291.
- [21] Thomson, W.T. *Phylos. Mag.* **1871**, 42, 448.
- [22]. Zsigmondy, A. *Z. Anorg. Che.* **1911**, 71, 356.
- [23] McBain, J.W. *J. Am. Chem. Soc.* **1935**, 57, 699.
- [24] Cohan, L.H. *J. Am. Chem. Soc.* **1938**, 60, 433.

- [25] Foster, A.G. *J. Chem. Soc.* **1952**, 1806.
- [26]. Broekhoff, J.C.P.; Linsen, B.G. *Physical and Chemical Aspects of Adsorbents and Catalysts* Academic, New York **1970**.
- [27] De Boer, J.H. *The Structure and Properties of Porous Materials* Butterworth, London **1958**.
- [28] Briggs, D.; Seah, M.P. *Practical Surface Analysis* (2nd edition) Wiley, Volume1.
- [29] Cardona, M.; Ley, L. *Photoemission in Solids 1, general principles* Springer-Verlag.